CHALMERS
UNIVERSITY OF TECHNOLOGY

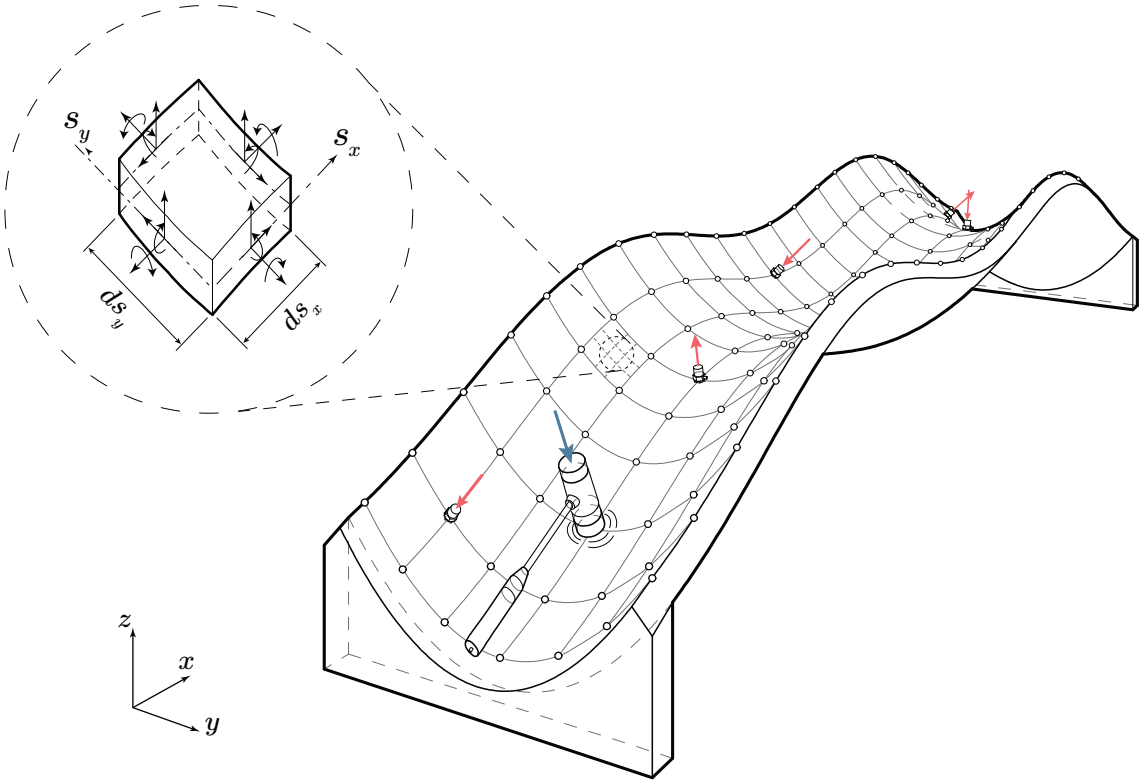

Dynamic and static response of beam-like hyperbolic paraboloid concrete elements

A numerical, analytical, and experimental study

Master's thesis in the Master's Programme Structural Engineering and Building Technology

David Selse, Erik Wigh

DEPARTMENT OF ARCHITECTURE AND CIVIL ENGINEERING
DIVISION OF STRUCTURAL ENGINEERING

CHALMERS UNIVERSITY OF TECHNOLOGY
Gothenburg, Sweden 2025
www.chalmers.se

MASTER'S THESIS ACEX30

Dynamic and static response of beam-like hyperbolic paraboloid concrete elements

A numerical, analytical, and experimental study

Master's thesis in the Master's Programme Structural Engineering and Building Technology

DAVID SELSE
ERIK WIGH

CHALMERS
UNIVERSITY OF TECHNOLOGY

Department of Architecture and Civil Engineering
Division of Structural Engineering
Rasmus Rempling
Alexander Sehlström
CHALMERS UNIVERSITY OF TECHNOLOGY
Gothenburg, Sweden 2025

Dynamic and static response of beam-like hyperbolic paraboloid concrete elements
A numerical, analytical, and experimental study

Master's Thesis in the Master's Programme Structural Engineering and Building Technology

DAVID SELSE
ERIK WIGH

Examensarbete ACEX30
Institutionen för Arkitektur och Samhällsbyggnadsteknik
Chalmers Tekniska Högskola, 2025

Department of Architecture and Civil Engineering
Division of Structural Engineering
Chalmers University of Technology
SE-412 96 Göteborg
Sweden
Telephone +46 31 772 1000

Cover:
Illustration of modal excitation applied to a hyperbolic paraboloid element
Department of Architecture and Civil Engineering
Göteborg, Sweden, 2025

Dynamic and static response of beam-like hyperbolic paraboloid concrete elements
A numerical, analytical, and experimental study

Master's thesis in the Master's Programme Structural Engineering and Building Technology

DAVID SELSE
ERIK WIGH
Department of Architecture and Civil Engineering
Division of Structural Engineering
Chalmers University of Technology

ABSTRACT

Beam-like hyperbolic paraboloid (HP) elements carry loads primarily through membrane action, enabling thinner cross-sections and up to 70% less material compared to bending-active slabs and beams. Their doubly ruled geometry permits reinforcement and prestressing with straight elements, simplifying construction and lowering cost relative to other shell typologies. Experimental verification of their structural response remains limited—yet it is essential to support a broader adoption of these elements.

This thesis investigates the static and dynamic behaviour of an existing HP prototype element using analytical modelling, finite element analysis (FEA), experimental modal analysis (EMA), and static load testing. Dynamic properties, including natural frequencies, damping ratios, and mode shapes, were identified using a roving hammer test. Static behaviour was evaluated under uniform pressure loading and a four-point bending test to failure, with strain data obtained via distributed fibre optic sensing (DFOS) and digital image correlation (DIC).

EMA identified six flexural modes below 220 Hz, with a fundamental frequency of 50.9 Hz and damping ratios between 0.56% and 1.1%. Numerical sensitivity studies explored the effects of boundary conditions, reinforcement, and modelling approaches on modal characteristics. Calibrated numerical models predicted resonance frequencies within 3% of experimental values and demonstrated strong mode shape correlation.

Strain data obtained from DFOS and DIC provided insight into the strain evolution under static loading conditions. Non-linear FEA enabled the prediction of deformations, crack patterns, and ultimate load capacity. Sensitivity studies were performed to assess the influence of boundary conditions, reinforcement configurations, and concrete–reinforcement interface modelling. The degree of longitudinal restraint was found to significantly affect both the structural response and the load-bearing capacity. Preliminary comparisons indicated that the numerical models reasonably captured the observed strain and crack patterns.

Through these static and dynamic assessments the thesis contributes to a deeper understanding of the structural behaviour of HP elements. It provides experimental validation and builds confidence in how these elements can be reliably modelled.

Key words: Hyperbolic paraboloid (HP) shell structures, Reinforced concrete, Experimental modal analysis (EMA), Experimental stress analysis (ESA), Non-linear finite element analysis (NLFEA), Roving hammer testing, Distributed fibre optic strain sensing (DFOS), Digital image correlation (DIC)

Dynamiskt och statiskt beteende hos balkliknande betongelement med hyperbolisk paraboloidgeometri
En numerisk, analytisk och experimentell studie

Examensarbete inom masterprogrammet Structural Engineering and Building Technology

DAVID SELSE
ERIK WIGH
Institutionen för arkitektur och samhällsbyggnadsteknik
Avdelningen för Konstruktionsteknik
Chalmers tekniska högskola

SAMMANFATTNING

Balkliknande hyperboliska paraboloid (HP) element bär laster främst genom membranverkan, vilket möjliggör tunnare tvärsnitt och upp till 70% lägre materialanvändning jämfört med plattor och balkar. Den dubbelkrökta regelytan möjliggör armering och förspänning med helt raka element, vilket förenklar tillverkningsprocessen i jämförelse med andra skaltyper. För att dessa HP element ska kunna tillämpas i större utsträckning krävs en djupare förståelse för deras strukturella beteende. Specifikt fordras experimentell verifiering av deras strukturella respons.

Detta examensarbetet undersöker det statiska och dynamiska beteendet hos HP-element genom att jämföra analytiska modeller och finita elementanalyser (FEA) med resultat från experimentell modalanalys (EMA) och statiska belastningstester. Ett test med impulshammare används för att identifiera egenfrekvenser, modaldämpning och modformer. Statiska tester utförs under jämnt fördelad last samt under fyrpunktsböjning upp till brott, där fiberoptik och digital bildkorrelation används för att mäta töjningar.

EMA identifierade sex böjmoder under 220 Hz, med en fundamental frekvens på 50,9 Hz och dämpningskvoter mellan 0,5% och 1,1%. Numeriska parameterstudier undersökte hur randvillkor, armering och modelleringsstrategier påverkar modala egenskaper. Kalibrerade numeriska modeller uppskattade resonansfrekvenser inom 3% felmarginal av experimentella värden och uppvisade stark överensstämmelse i modformer.

Töjningsdata från DFOS och DIC gav detaljerad inblick i töjningsutvecklingen under last. Icke-linjära FEM-analyser erbjöd uppskattning av deformationer, sprickbildningsmönster och brottlast. Därtill genomfördes parameterstudier av randvillkor, armeringslayouter och interaktionsmodeller mellan betong och armering. Graden av longitudinell inspänning visade sig ha en avsevärd inverkan på både den strukturella responsen och bärförmågan. Preliminära jämförelser visade att de numeriska modellerna relativt väl kunde återge de observerade töjnings- och sprickmönstren.

Genom dessa statiska och dynamiska analyser bidrar arbetet till en fördjupad förståelse för HP-elementens strukturella beteende. Den tillhandahåller experimentell validering och stärker förtroendet för hur dessa element kan modelleras på ett tillförlitligt sätt.

Nyckelord: Hyperboliska paraboloidskal, Armerad betong, Experimentell modalanalys (EMA), Experimentell spänningsanalys (ESA), Icke-linjär finita elementmetodsanalys (NLFEM), Impulshammartest, Distruberad fiberoptisk töjningsmätning (DFOS), Digital bildkorrelation (DIC)

Acknowledgements

The completion of this thesis was made possible through the support, guidance, and encouragement of many individuals. We would like to extend our heartfelt thanks to all who made this journey both rewarding and enjoyable.

First and foremost, we would like to express our sincere gratitude to our supervisor Dr. Alexander Sehlström, and examiner, Assoc. Prof. Rasmus Rempling. Their guidance, expertise, and thoughtful feedback has been invaluable throughout this work. We wish to thank Ju-Hung Pai, Dr. Johan Jonsson, Dr. Claes Fredö, and Tekn. Lic. Penka Dinkova for their profound interest, expertise, and generous support during the modal analysis. Additionally, we thank Assoc. Prof. Ignasi Fernandez, Dr. Carlos Gil Berrocal, Sebastian Almfeldt, Sebastian Daniec, Anders Karlsson, Max Dombrowski and Tekn. Lic. August Jansson for their support and invaluable expertise during the static assessments.

Our appreciation extends to Prof. Jens Ahrens, Dr. Astrid Pieringer, and Prof. Krister Larsson at the Department of Applied Acoustics for providing measurement equipment. We also thank Assoc. Prof. Peter Folkow and Assoc. Prof. Håkan Johansson at the Department of Applied Mechanics for laboratory access and for warmly welcoming us into their research environment.

We would also like to thank Erik Arlinger, Dr Nilla Ollson, and Johan Eriksson who were involved in the design and casting of the prototype element prior to the thesis work.

Finally, we extend our gratitude to our opponents, Erik Gustafsson and Sebastian Oguz, for their constructive feedback and engagement throughout the thesis journey.

David Selse, Gothenburg, June 2025
Erik Wigh, Gothenburg, June 2025

Contents

1 Introduction

This chapter presents the background of the thesis work, along with the aim, objectives, delimitations, and method.

1.1 Background

Sweden aims to achieve net negative greenhouse gas emissions by 2045 (The Swedish Environmental Protection Agency, 2024). The construction sector plays an important role in this effort, accounting for approximately 8% of Sweden's annual territorial greenhouse gas emissions (Ministry of the Environment and Government Offices of Sweden, 2020).

Despite the evident need to reduce climate impact, rising demands for infrastructure and housing can be observed globally. In Sweden, for instance, the government has proposed a 20% increase in infrastructure investments, allocating 1,171 billion SEK to transport infrastructure between 2026 and 2037 (Government Offices of Sweden, 2024). Additionally, the country is expected to need approximately 523,000 new homes between 2024 and 2033 (Swedish National Board of Housing, Building and Planning, 2025). Meeting these demands without compromising climate targets requires a shift toward more efficient and sustainable construction practices. A crucial aspect of this transition involves rethinking construction materials and their application in structural systems.

Concrete remains fundamental to modern construction, yet it is also one of the most carbon-intensive materials, primarily due to emissions from cement production. The concrete industry alone contributes to roughly 8% of global CO_2-eq emissions (Ramsden, 2020). A considerable share of this concrete is used in slab and beam elements, which often have higher embodied carbon and energy than other structural components (Broyles et al., 2023). As shown by Foraboschi et al. (2014), conventional flat slabs can account for up to 70% of the total embodied energy in high-rise buildings.

Doubly curved shell structures could serve as an efficient and sustainable substitute for traditional concrete slab systems found in buildings and bridges. These thin structures predominantly resist load through membrane action—a combination of compressive, tensile, and shear stresses within the surface plane (Sehlström, 2021). By minimising bending action, shell structures enable thinner cross-sections, thereby reducing material usage and environmental impact. According to Arlinger (2023), doubly curved shells have the potential to reduce CO_2-eq emissions by up to 70% compared to hollow core deck elements, and 80% compared to TT-elements.

However, the production of doubly curved concrete shells is typically labour-intensive and costly due to the complex formwork required (Cocco et al., 2024). The oblong beam-like hyperbolic paraboloid (HP) element, for instance found in the systems developed in the 1950's by Wilhelm J. Silberkuhl and Herbert Müller (see Figure 1.1), offers improved constructibility. The geometry is derived from a doubly ruled surface and has a constant parabolic cross-section along its length. Consequently, the element can be reinforced and prestressed with exclusively straight elements, potentially leading to substantial cost savings during production (Osman-Letelier et al., 2017).

The HP element forms a convex parabolic arch along its primary span. Due to this curvature, a significant portion of the applied loads can be transferred through in-plane membrane compressive stresses, provided that the compressive thrust is adequately transferred at the springing points. This reduces the need for reinforcement, minimises the risk of cracking, and enhances the overall durability of the structure compared to traditional slab elements.

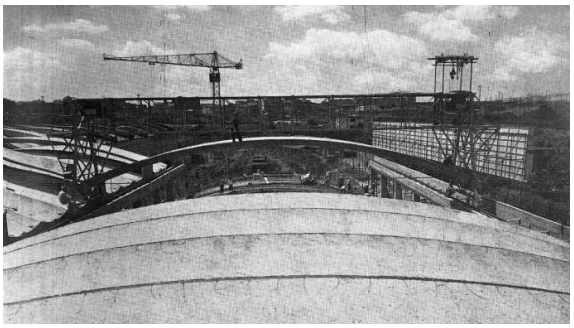

(a) *Silberkuhl system* installed at *Magazzino Merci Rinascente*, Rome, Italy (1962).

(b) Herbert Müller's *HP-Delta shells* in Halle-Neustadt, Germany (1968).

Figure 1.1: Two similar prefabricated HP shell systems were developed on opposite sides of the Iron Curtain after World War II: by Wilhelm J. Silberkuhl in West Germany (left) and by Herbert Müller in East Germany (right) (Scheffler, 2017).

The Silberkuhl and Müller systems have traditionally been employed in roof structures (Scheffler, 2017). Expanding their application to residential flooring and bridge decking introduces more stringent performance requirements, including improved control of vibrations, deflections, and long-term behaviour. Addressing these challenges necessitates a deeper understanding of the systems' static and dynamic responses. Crucially, experimental validation is essential to ensure the reliability of modelling approaches.

To the best of the authors' knowledge, no detailed experimental studies are currently available that verify the static and dynamic behaviour of HP elements. This thesis seeks to address this gap by conducting experimental investigations on a prototype HP element. The prototype element was designed and cast prior to the thesis through a collaboration between Chalmers University of Technology, WSP, and NCC. Its design was based on the earlier thesis work of Arlinger (2023).

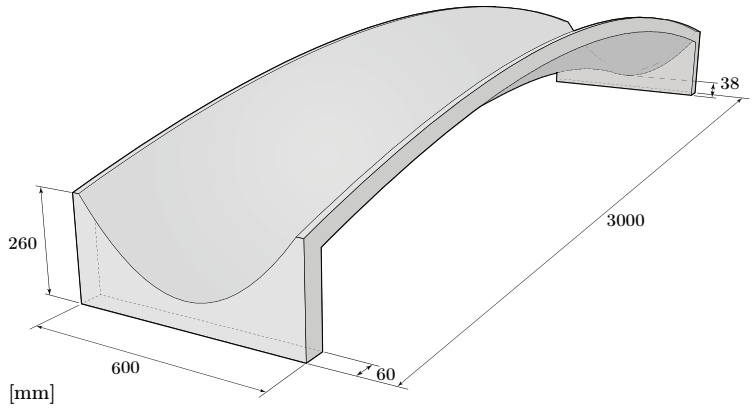

Figure 1.2: Rendered perspective view of the HP prototype element.

1.2 Aim

The aim of this thesis is to investigate the static and dynamic behaviour of oblong, beam-like hyperbolic paraboloid (HP) concrete elements through full-scale testing, and to evaluate the accuracy of analytical and numerical models in predicting their structural response.

1.3 Objectives

The following objectives have been formulated for the thesis work:

- **Review existing research and historical applications** of HP elements to gain a comprehensive understanding of their development, construction methods, performance, and current research topics. This includes reviewing analytical methods for estimating the dynamical and statical response of the elements.
- **Characterise material properties** of the concrete used in the HP prototype element by performing cube strength tests and wedge splitting tests.
- **Conduct experimental modal analysis (EMA)** on the existing prototype element to determine its mode shapes, natural frequencies, and modal damping ratios.
- **Conduct static load tests** on the prototype element to capture global deformations and local strain development under incremental loading up to failure, and document the failure mechanism.
- **Develop numerical finite element models** that simulate both the dynamic and static test setups, replicating loading and boundary conditions.
- **Validate the finite element models and analytical models** by comparing their outputs against results from experimental testing.
- **Perform sensitivity studies** to evaluate how boundary conditions, material properties, and modelling of reinforcement affect the element's static and dynamic response.
- **Assess model calibration strategies**, particularly for adjusting support conditions and material properties to improve the accuracy of numerical models.
- **Evaluate practical implications**, such as how the experimental findings could inform the design of future HP elements.

1.4 Delimitations

This thesis is delimited to the study of doubly curved beam-like concrete elements conforming to the hyperbolic paraboloid surface. The experimental tests are conducted on a single specimen, reinforced with traditional steel reinforcement, without prestressing.

1.5 Methodology

The work is structured into four main phases, as illustrated in Figure 1.3.

Phase 1: A literature review is conducted to establish a theoretical foundation for assessing the static and dynamic behaviour of HP elements using experimental, analytical, and numerical methods.

Phase 2: The dynamic behaviour of the HP prototype element is characterised through modal analysis. Experimental modal analysis (EMA) is performed using a single-input, multiple-output (SIMO) roving hammer test. Complementary numerical modal analyses are carried out to assess the influence of material properties, boundary conditions, and reinforcement through parametric studies. The numerical models are calibrated against experimental data, and the resulting modal characteristics are compared with those obtained from the tests.

Phase 3: The static response of the HP prototype element is investigated through two full-scale load tests: a uniform pressure test using cement bags, and a four-point bending test to failure using a hydraulic test rig. Strain development is monitored using embedded fibre optic sensors and digital image correlation (DIC). The experimental setups are replicated in finite element software for both linear and non-linear analyses, enabling assessment of stress and strain distributions, crack development, failure modes, and load-bearing capacity. The models are validated by comparing their results with both experimental data and analytical predictions. Parametric studies explore the influence of boundary conditions, crack modelling, and reinforcement representation on the static response.

Phase 4: This phase synthesises the findings from the dynamic and static investigations. Methodological limitations are discussed, and recommendations are made for future research.

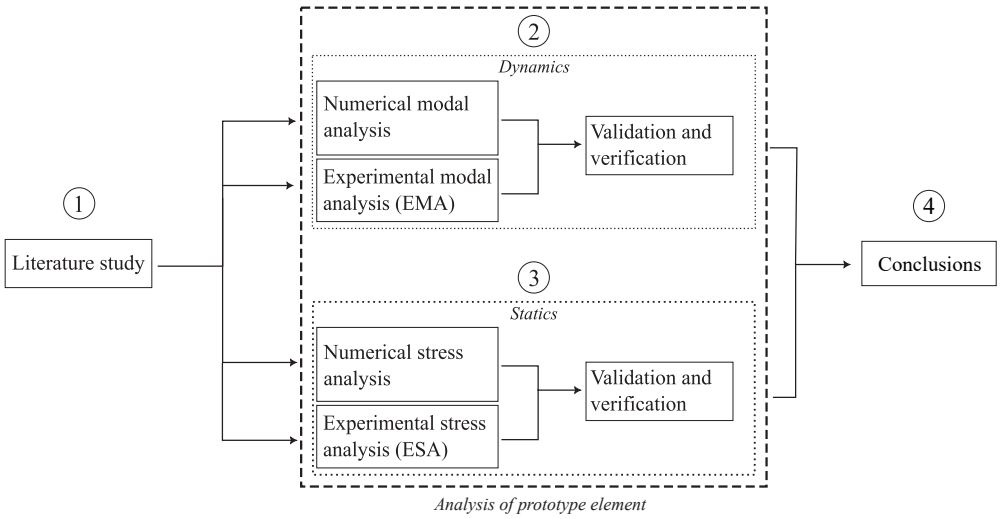

Figure 1.3: Overview of work process.

2 Theory

The response of a structure is governed by the interaction between external stimuli and the inherent properties of the structure. Stimuli such as loads, vibrations, and temperature fluctuations act as external forces that induce structural response. The nature of this response is governed by key properties of the structure, including material composition, geometry, and boundary conditions. How these properties may influence the structural behaviour of hyperbolic paraboloid (HP) elements will be explored further throughout this chapter.

Specifically, the chapter aims to establish a theoretical foundation for assessing the static and dynamic behaviour of HP elements using experimental, analytical, and numerical methods. It is divided into six main parts:

- **Section 2.1** — Introduces mathematical concepts essential for representing the geometry of HP elements.
- **Section 2.2** — Provides an overview of theoretical frameworks for analysing HP elements under static loads, with a focus on beam and shell theories.
- **Section 2.3** — Introduces experimental methods for assessing the static behaviour of HP elements, establishing the theoretical background for strain measurement techniques such as *distributed fibre optic sensing* (DFOS) and *digital image correlation* (DIC).
- **Section 2.4** — Covers fundamental principles of structural dynamics, with emphasis on *modal analysis* and analytical approaches for approximating the natural frequencies of HP elements.
- **Section 2.5** — Introduces *experimental modal analysis* (EMA) as a method for empirically characterising dynamic behaviour of HP elements.
- **Section 2.6** — Discusses numerical approaches for modelling HP elements, including an overview of the *finite element method* and strategies for simulating reinforced concrete in finite element software.

2.1 Geometry of curved surfaces

Establishing a theoretical foundation for analysing the static and dynamic response of HP elements requires an understanding of the hyperbolic paraboloid (HP) surface geometry to which they conform. This section introduces the mathematical background needed to describe curved surfaces, focusing on key geometric concepts such as *Gaussian curvature* and *ruled surfaces* as tools to describe HP surfaces.

In 1827, Carl Friedrich Gauss published the *Theorema Egregium* ('The Remarkable Theorem'), demonstrating that the curvature at a point on a surface can be described by a scalar quantity known as the *Gaussian curvature*, denoted by K (Domokos, 1989). Gauss showed that the Gaussian curvature is an *intrinsic property* of the surface. To illustrate, imagine a rope that is bent and twisted in space. Regardless of its shape or configuration, its total length remains unchanged. The length is intrinsic to the rope it is independent of the rope's position or orientation in space. Likewise, a surface can be bent and twisted in space, but as long as it is not stretched or otherwise distorted, the Gaussian curvature at any given point remains unchanged (Do Carmo, 2016). The Gaussian curvature evaluated at a point $\mathbf{P}$ on a differentiable surface $\mathcal{S}$ can be defined as the product of the two *principal curvatures* κ_1 and κ_2 (Do Carmo, 2016):

$$K = \kappa_1 \kappa_2. \tag{2.1}$$

Figure 2.1 illustrates how the two principal curvatures are defined on a differentiable surface. At any point $\mathbf{P} \in \mathcal{S}$, there exists a unique normal vector $\mathbf{N}$ perpendicular to the surface. A plane containing this normal vector is called a *normal plane*. The intersection of the surface with a normal plane forms a curve known as a *normal section*. A circle with radius r can be fitted to this curve at $\mathbf{P}$, tangent to the normal section. The curvature κ is then defined as the reciprocal of the circle's radius, i.e., $\kappa = 1/r$. The curvature is assigned a positive sign if the curve is convex with respect to the normal vector and a negative sign otherwise. Since infinitely many normal planes pass through the normal vector, there exist infinitely many normal sections at $\mathbf{P}$. The principal curvatures κ_1 and κ_2 are found from the two normal planes containing the circles with maximum and minimum curvature, respectively (Do Carmo, 2016).

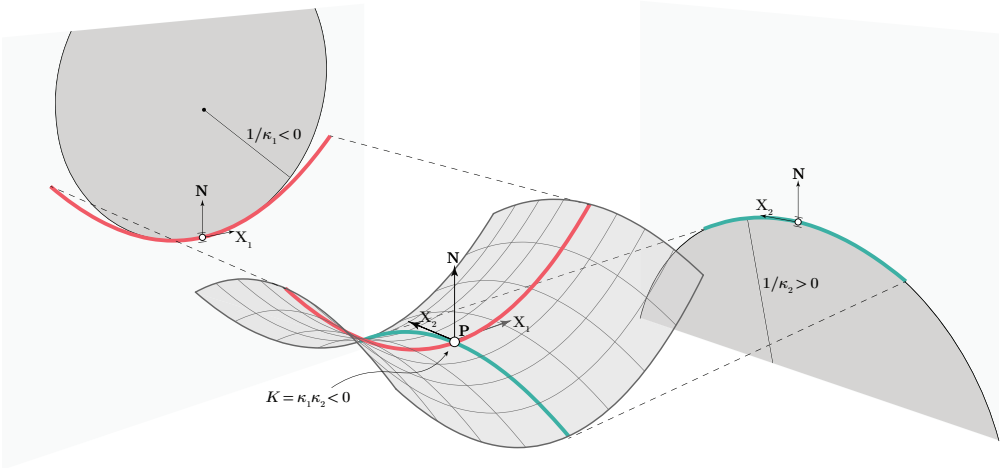

Figure 2.1: Principal curvatures κ_1 and κ_2 evaluated on a surface at a point $\mathbf{P}$.

2.1.1 Classification of surfaces

Surfaces can be classified depending on the properties of the Gaussian curvature. If at least one of the principal curvatures is zero at every point, the Gaussian curvature will also be zero on the entire surface ($\kappa_1\kappa_2 = 0$). Such a surface is called a *developable surface* as it can be unfolded or developed into a flat planar surface (Williams, 2014). Examples include cylinders and cones. If both principal curvatures have the same sign at all points ($\kappa_1\kappa_2 > 0$), the surface is called an *elliptical surface* and is said to have *synclastic curvature*. Examples include spheres and dome-like surfaces. Conversely, if the principal curvatures have opposite signs at all points ($\kappa_1\kappa_2 < 0$), the surface is said to have *anticlastic curvature* and is often referred to as a *hyperbolic surface* (Do Carmo, 2016). Notable examples of such surfaces include catenoid cooling towers and hyperbolic paraboloids.

Furthermore, some surfaces are *ruled surfaces*, meaning that a straight line can be drawn through every point on the surface while remaining entirely on it. For example, on a flat sheet of paper, straight lines can be drawn in all directions. On a vertical cylinder, however, straight lines can only be drawn in the vertical direction, making it a *singly ruled* surface. In contrast, the hyperbolic paraboloid is a *doubly ruled* surface, meaning that there are two distinct directions along which straight lines can be drawn on the surface (Do Carmo, 2016).

2.1.2 Hyperbolic paraboloid surfaces

Hyperbolic paraboloid surfaces, often referred to as *hypar surfaces* or *HP surfaces*, can mathematically be described as a *translation surface* where a parabolic curve (*generatrix*) is translated along an inverted parabolic curve (*directrix*), represented by the Cartesian surface equation:

$$z = \frac{y^2}{h_2} - \frac{x^2}{h_1}, \tag{2.2}$$

where h_1 and h_2 are positive constants that describe the level of curvature in the xz- and yz-planes, respectively (Farshad, 1992). The larger the values of h_1 and h_2, the flatter or less curved the HP surface will appear. The HP elements that are considered in this thesis are found by projecting an oblong rectangle onto a HP surface, as illustrated in Figure 2.2. Any intersection with a vertical plane parallel to the xz- and yz-planes results in planar parabolic curves. Meanwhile, intersections with horizontal planes generate hyperbolas.

It can be shown that the HP surface is a doubly ruled surface (Farshad, 1992, pp. 217–219). Thus, it is possible to construct the surface from straight, albeit twisted, members oriented in the two generator directions, as illustrated in Figure 2.3. The doubly ruled property of the surface enables relatively simple construction procedures and broad applicability in architecture. Felix Candela utilised the HP surface to construct the *Los Manantiales* restaurant building in Xochimilco, Mexico City, in 1958. HP surfaces were also employed by David Jawerth in the conference and restaurant building *Svalan* in Örebro, constructed in the 1970s (Örebroporten, 2025), as well as in the *Scandinavium Arena* in Gothenburg, designed by engineers Gunnar Kärrholm and Alf Samuelsson, completed in 1971 (Kärrholm & Samuelsson, 1972).

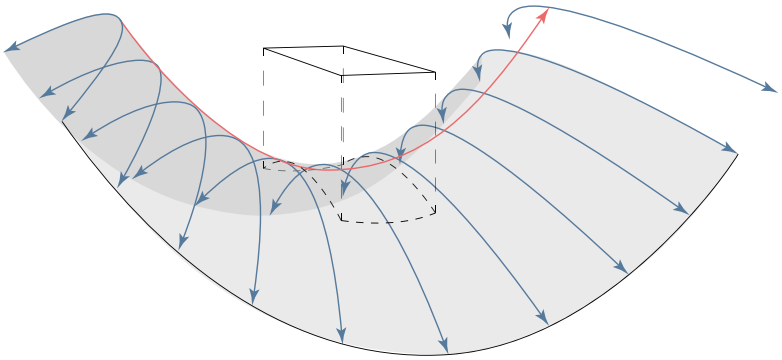

Figure 2.2: Hyperbolic paraboloid surface generated by translating a parabolic generatrix (blue) along an inverted parabolic directrix (red). The HP element considered in this thesis is found by projecting an oblong rectangle onto the HP surface.

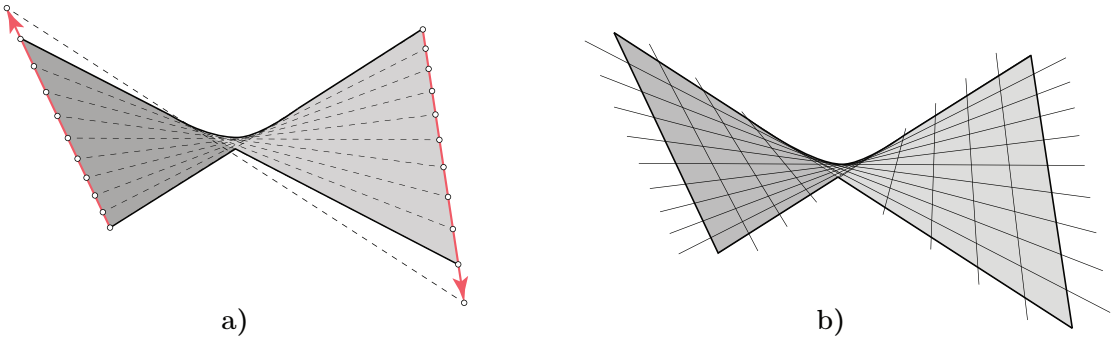

Figure 2.3: Hyperbolic paraboloid surfaces. a) Surface generation by drawing straight lines between points at two non-coplanar edges. b) Straight lines can be drawn in two directions since the surface is doubly ruled.

2.2 Statics of HP elements

This section discusses a theoretical framework for assessing the expected static response of HP elements. Two primary modelling approaches are considered: treating HP elements as either a *shell* or a *beam*. If the element exhibited no curvature along the primary spanning direction, it is reasonable to believe that the structural behaviour would align more closely with that of a thin-walled beam. However, the presence of curvature introduces additional complexities, potentially shifting the behaviour more toward that of a shell. Section 2.2.1 discusses the static response of shells. The *membrane theory* of shells is introduced and a general mathematical formulation of the stress state in arbitrary membrane shells, originally developed by Pucher (1934), is presented. Adopting Pucher's methodology, an expression for the membrane stress state in HP shells is presented. Section 2.2.2 introduces the classical *Euler-Bernoulli beam theory*. The theory is extended to include transverse stresses present in HP elements, as suggested by Dombrowski et al. (2021).

2.2.1 Shell theory

A shell structure is formed by materialising a spatially curved surface, such as the HP surface, with a thin profile. While there are no strict criteria defining the thickness of a shell, reinforced concrete shells typically exhibit a thickness-to-span ratio of approximately 1/200 (Farshad, 1992). Similar to plates, shells can be defined by specifying a middle surface and a thickness that may vary across the shell. Structural elements such as beams, plates, and shells exhibit high flexibility under transverse load and are much easier to bend than to elongate or compress. Unlike beams and plates, which primarily carry transverse loads through bending, shells have the unique ability to transfer a substantial portion of applied loads through *membrane action*. This load-carrying efficiency is inherently linked to their geometric properties, allowing them to achieve highly effective structural performance (Williams, 2014). The following subsections introduce fundamental concepts of shell theory, providing a potential analytical basis for interpreting the expected static response of HP elements.

2.2.1.1 Stress state in shells

The equilibrium of forces in an arbitrary shell body can be expressed as a balance between the divergence of the Cauchy stress tensor $\underline{\boldsymbol{\sigma}}$ and the body force $\mathbf{f}$ given by:

$$\mathbf{f} + \nabla \underline{\boldsymbol{\sigma}} = 0. \tag{2.3}$$

This three-dimensional stress state of the continuum can be reduced to a two-dimensional representation on the middle surface. Consider an infinitesimally small element extracted from the shell geometry, as illustrated in Figure 2.4. This element is defined by two pairs of principal plane sections, separated by distances ds_x and ds_y. The principal radii of curvature of the element are denoted by r_x and r_y. When subjected to external loads or deformation constraints, internal stresses develop within the element. By integrating these stresses over the shell thickness t, the corresponding *stress resultants* are obtained, measured as force per unit width of the cross-section, here denoted with lowercase letters. In most classical shell theories, stress components normal to the shell surface are neglected, meaning $\sigma_z = 0$ (Farshad, 1992). Figure 2.4 expresses the remaining stress resultants in terms of their Cartesian components (normal stress

resultants n_x, n_y, shear stress resultants n_{xy}, n_{yx}, q_x, q_y, and bending stress resultants, m_x, m_y, m_{xy}, m_{yx}). The relationship between internal stresses and the stress resultant is given in Equation (2.4). If the stress is assumed uniform through the thickness, the stress resultant simplifies to the product between the stress and thickness, for example $n_x = \sigma_x \cdot t$. This assumption is particularly relevant for thin shells (Timoshenko & Krieger, 1959).

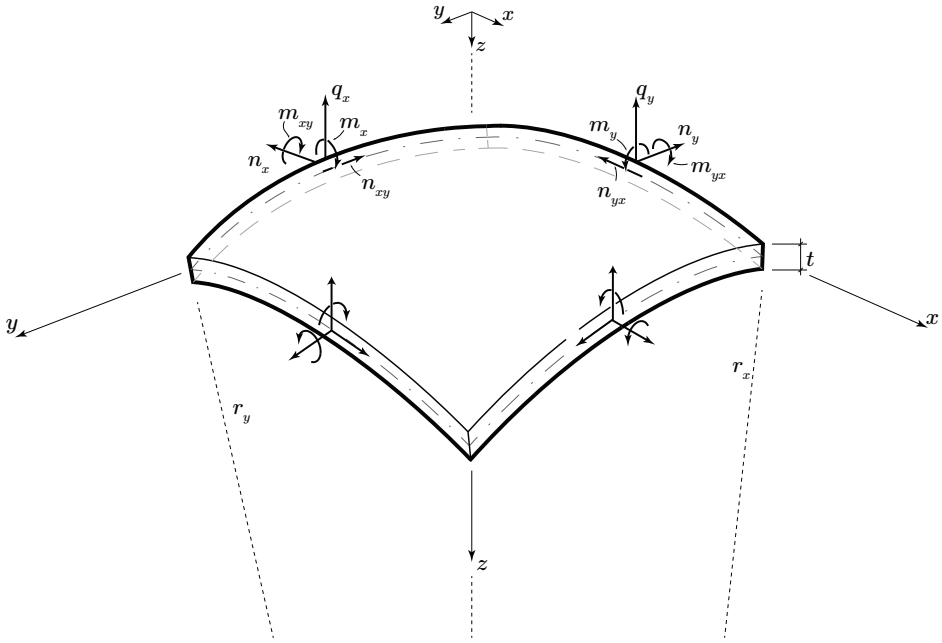

Figure 2.4: Stress resultants per unit cross-section width on an infinitesimally small shell element. The stress resultants are decomposed in Cartesian components and are assumed to act in the middle surface of the shell. Illustration adopted from Farshad (1992).

$$
\begin{aligned}
q_x &= \int_{-\frac{t}{2}}^{\frac{t}{2}} \tau_{xz} \left(1 + \frac{z}{r_y}\right) dz, \qquad & q_y &= \int_{-\frac{t}{2}}^{\frac{t}{2}} \tau_{yz} \left(1 + \frac{z}{r_x}\right) dz, \\
n_x &= \int_{-\frac{t}{2}}^{\frac{t}{2}} \sigma_x \left(1 + \frac{z}{r_y}\right) dz, \qquad & n_y &= \int_{-\frac{t}{2}}^{\frac{t}{2}} \sigma_y \left(1 + \frac{z}{r_x}\right) dz, \\
n_{xy} &= \int_{-\frac{t}{2}}^{\frac{t}{2}} \tau_{xy} \left(1 + \frac{z}{r_y}\right) dz, \qquad & n_{yx} &= \int_{-\frac{t}{2}}^{\frac{t}{2}} \tau_{yx} \left(1 + \frac{z}{r_x}\right) dz, \\
m_x &= \int_{-\frac{t}{2}}^{\frac{t}{2}} z\sigma_x \left(1 + \frac{z}{r_y}\right) dz, \qquad & m_y &= \int_{-\frac{t}{2}}^{\frac{t}{2}} z\sigma_y \left(1 + \frac{z}{r_x}\right) dz, \\
m_{xy} &= \int_{-\frac{t}{2}}^{\frac{t}{2}} z\tau_{xy} \left(1 + \frac{z}{r_y}\right) dz, \qquad & m_{yx} &= \int_{-\frac{t}{2}}^{\frac{t}{2}} z\tau_{yx} \left(1 + \frac{z}{r_x}\right) dz.
\end{aligned}
\tag{2.4}
$$

Integrating the stress resultants along the shell's span directions yields the *internal forces*, here denoted with uppercase letters, manifesting as either forces or moments.

In shell structures, internal forces are traditionally categorized into two groups: *membrane forces* and *bending forces* (Farshad, 1992), as illustrated in Figure 2.5. Membrane forces (N_x, N_y, and $N_{xy} = N_{yx}$) act tangentially to the middle surface, inducing in-plane shearing as well as elongation or contraction of the element. In contrast, bending forces include transverse shear forces (Q_x, Q_y), torsional moments (M_{xy}, M_{yx}), and bending moments (M_x, M_y). To distinguish between these two behaviours, Calladine (1983) introduced the terms *stretching surface* (S-surface) and *bending surface* (B-surface).

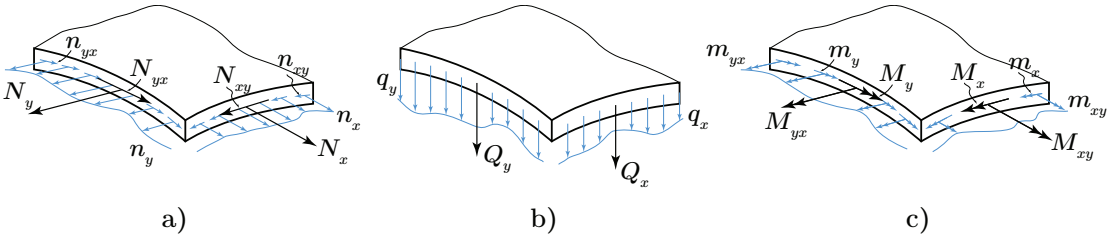

Figure 2.5: Internal forces in shells (black), found by integrating the field of stress resultants (blue) along the span directions. a) Membrane forces, b) and c) bending forces.

For the shell to be in static equilibrium, it must satisfy the three force equilibrium equations ($F_x = 0$, $F_y = 0$, $F_z = 0$) and the three moment equilibrium equations ($M_x = 0$, $M_y = 0$, $M_z = 0$). However, since there are more than six force resultants, it follows that the element is statically indeterminate. Kinematical and constitutive relations are needed to solve for the unknown stress field. A complete solution to the internal forces of the shell must also consider boundary conditions.

2.2.1.2 Membrane behaviour

To simplify the assessment of shells, the bending stresses are commonly disregarded. If only membrane stresses n_x, n_y, and $n_{xy} = n_{yx}$ are present, all global moment equations will be equally satisfied ($M_x = 0$, $M_y = 0$ and $M_z = 0$). The remaining three force equilibrium equations can be used to determine the unknown membrane field, and the system is statically determinate. The shell is said to have a pure membrane behaviour, which can only occur provided that specific conditions related to applied loads, geometric properties, and boundary conditions are fulfilled.

There are three common cases where membrane theory is violated:

i) application of concentrated loads, causing large local deformations of the shell;

ii) incompatible boundary conditions;

iii) presence of kinks or other geometric discontinuities in the shell.

The cases are illustrated in Figures 2.6 and 2.7. Under any of these circumstances, the membrane stress field cannot alone satisfy statical equilibrium and/or displacement requirements. Thus, bending occurs in the shell, confined around the regions where the membrane theory is violated (Farshad, 1992). This is important; the bending action is localised, while the majority of the shell still can behave as a true membrane. The

localisation of bending stresses is enabled by the shell's inherent curvature, contributing to its overall structural efficiency. Depending on the geometry of the shell and the nature of the applied loads, the membrane regions of the shell will be in pure compression and/or tension and only deform 'in-plane'.

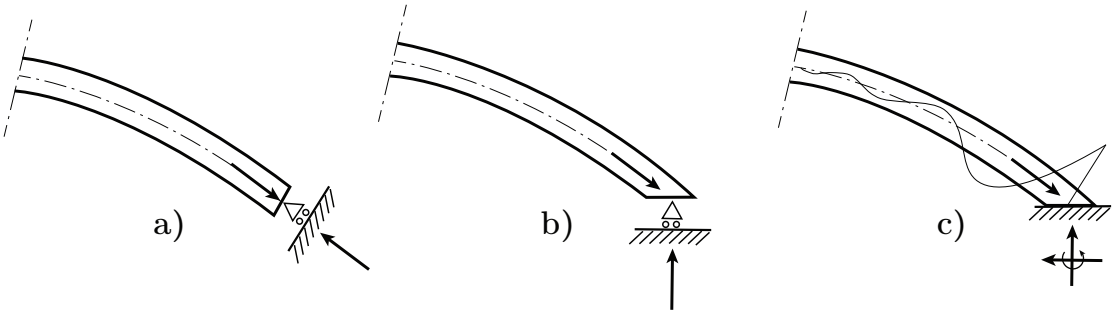

Figure 2.6: Membrane compatibility and incompatible boundary conditions: a) compatible, b) incompatible, c) incompatible.

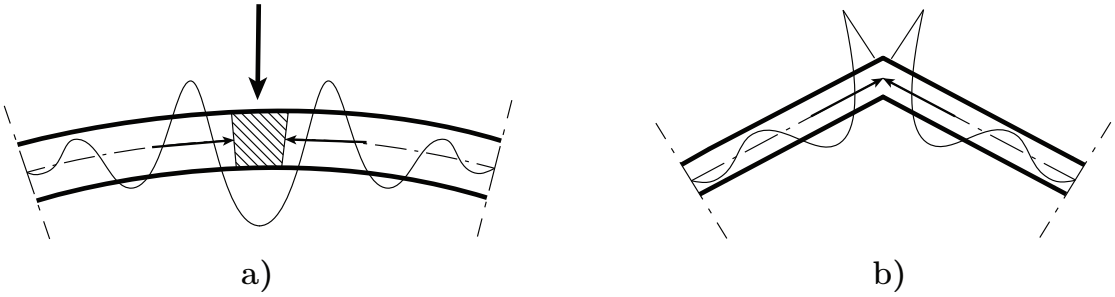

Figure 2.7: Discontinuities violating membrane action: a) concentrated load, b) geometric discontinuity.

2.2.1.3 Membrane stresses in HP shells

George Biddell Airy introduced the *Airy stress function* in 1862 as a method to simplify the calculations of stress components in a two-dimensional elastic body subjected to in-plane forces (Airy, 1863; Timoshenko & Krieger, 1959). The key idea is to define the stress components (σ_x, σ_y, and $\tau_{xy} = \tau_{yx}$) in terms of a *stress function* $\Phi(x, y)$ such that the equilibrium equations are automatically satisfied. This approach reduces the task of determining the full two-dimensional stress distribution to solving a single governing equation for $\Phi(x, y)$. Building on this foundation, Pucher (1934) developed a method to compute the membrane stress field in arbitrary shell structures (Almegaard, 2014; Pucher, 1934; Timoshenko & Krieger, 1959). Instead of directly analysing the spatial shell, he employed a plane stress formulation, which is significantly easier to solve analytically. His approach considered an infinitesimally small rectangular projection of the middle surface onto the *xy*-plane, as illustrated in Figure 2.8. The membrane stress resultants n_x, n_y, and n_{xy} are linked to their corresponding projected in-plane stresses $\bar{n}_x$, $\bar{n}_y$, and $\bar{n}_{xy}$ through the surface geometry. Likewise, the applied distributed loads p_x, p_y, and p_z are associated with their projected counterparts $\bar{p}_x$, $\bar{p}_y$, and $\bar{p}_z$. The stress field is determined for the projected problem and then transformed back onto the original shell geometry.

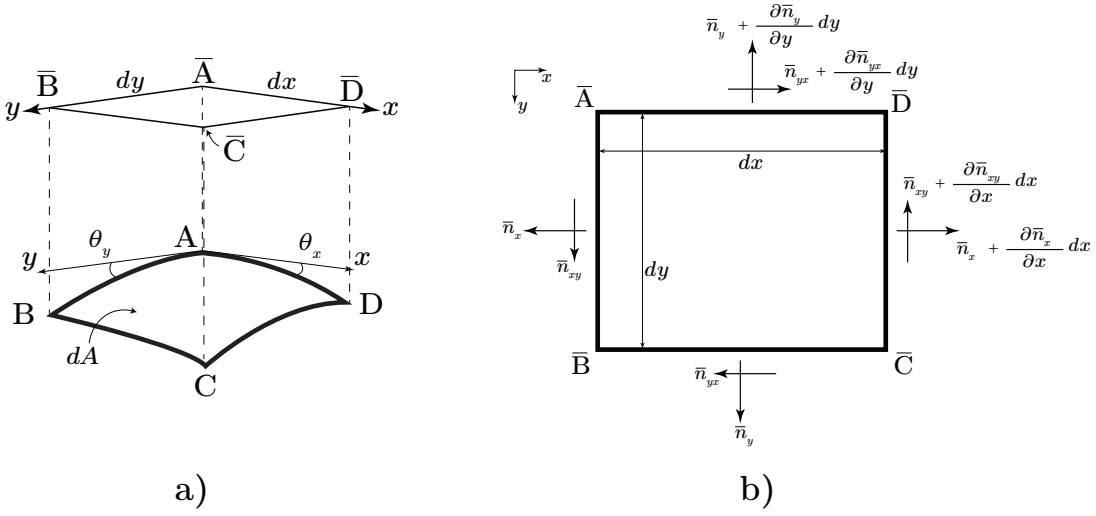

Figure 2.8: Pucher's method for computing membrane forces in arbitrary shells. a) projection of mid-surface onto *xy*-plane, b) free body diagram of projected element.

The three governing equilibrium equations can be formulated based on the equilibrium conditions $\sum \mathrm{f}_x = 0$, $\sum \mathrm{f}_y = 0$, and $\sum \mathrm{f}_z = 0$, per unit width of the cross-section as:

$$\begin{cases} \sum \mathrm{f_x} = \dfrac{\partial \bar{n}_x}{\partial x} + \dfrac{\partial \bar{n}_{xy}}{\partial y} + \bar{p}_x = 0 \\ \sum \mathrm{f_y} = \dfrac{\partial \bar{n}_y}{\partial y} + \dfrac{\partial \bar{n}_{xy}}{\partial x} + \bar{p}_y = 0 \\ \sum \mathrm{f_z} = \bar{n}_x \dfrac{\partial^2 z}{\partial x^2} + 2\bar{n}_{xy} \dfrac{\partial^2 z}{\partial x \partial y} + \bar{n}_y \dfrac{\partial^2 z}{\partial y^2} + \bar{p}_z - \bar{p}_x \dfrac{\partial z}{\partial x} - \bar{p}_y \dfrac{\partial z}{\partial y} = 0, \end{cases} \tag{2.5}$$

(Timoshenko & Krieger, 1959). It is possible to satisfy the equilibrium of the first two statements in Equation (2.5) by introducing the Airy stress function Φ such that

$$\bar{n}_x = \frac{\partial^2 \Phi}{\partial y^2} - \int \bar{p}_x \, dx, \quad \bar{n}_y = \frac{\partial^2 \Phi}{\partial x^2} - \int \bar{p}_y \, dx, \quad \bar{n}_{xy} = -\frac{\partial^2 \Phi}{\partial x \partial y}. \tag{2.6}$$

Inserting Equation (2.6) into Equation (2.5) reduces the problem to one equilibrium equation:

$$\frac{\partial^2 \Phi}{\partial x^2} \frac{\partial^2 z}{\partial y^2} - 2 \frac{\partial^2 \Phi}{\partial x \partial y} \frac{\partial^2 z}{\partial x \partial y} + \frac{\partial^2 \Phi}{\partial y^2} \frac{\partial^2 z}{\partial x^2} = \bar{q}, \tag{2.7}$$

where $\bar{q}$ is defined as

$$\bar{q} = -\bar{p}_z + \bar{p}_x \frac{\partial z}{\partial x} + \bar{p}_y \frac{\partial z}{\partial y} + \frac{\partial^2 z}{\partial x^2} \int \bar{p}_x \, dx + \frac{\partial^2 z}{\partial y^2} \int \bar{p}_y \, dx. \tag{2.8}$$

Equation (2.7) is a second-order partial differential equation in which the stress function Φ should be solved for. By specifying the parametrisation of the middle surface $z(x, y)$,

Φ should be determined such that boundary conditions and equilibrium are satisfied (Farshad, 1992).

Flügge (1962) presents an approach for deriving the membrane stress resultants in a hyperbolic paraboloid shell, whose middle surface is given by the surface equation in Equation (2.2). A portion of this middle surface, enclosed by the rectangular boundary $-l/2 \leq x \leq l/2$ and $-b/2 \leq y \leq b/2$, is shown in Figure 2.9. The surface's straight-line generators are oriented at an angle $\pm\gamma$ relative to the x-axis when projected onto the xy-plane, where $\tan\gamma = \sqrt{h_2/h_1}$. In the special case of $h_1 = h_2$, the generators meet at 90° angles, and appear rotated with 45° to the global coordinate system.

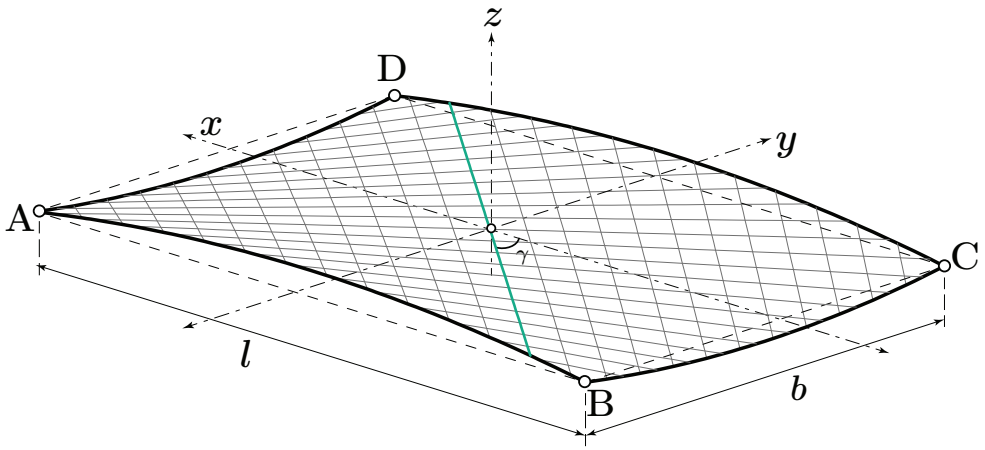

Figure 2.9: Surface parametrisation adopted from Flügge (1962, pp. 184).

Assuming pure vertical loading ($\bar{p}_z = -q$, $\bar{p}_x = \bar{p}_y = 0$) and by evaluating the second-order derivatives of $z(x, y)$ in Equation (2.2), the governing differential equation in Equation (2.7) can be written as

$$\frac{2}{h_1}\frac{\partial^2\Phi}{\partial y^2} - \frac{2}{h_2}\frac{\partial^2\Phi}{\partial x^2} = -q. \tag{2.9}$$

This equation will automatically be satisfied if the Airy stress function is, for example, chosen as

$$\Phi = -\frac{1}{8}q(h_1 y^2 - h_2 x^2). \tag{2.10}$$

Inserting this stress function into Equation (2.6) yields

$$\bar{n}_x^{\mathrm{h}} = -\frac{q\,h_1}{4}, \quad \bar{n}_y^{\mathrm{h}} = \frac{q\,h_2}{4}, \quad \bar{n}_{xy}^{\mathrm{h}} = 0, \tag{2.11}$$

where the superscript h is used to indicate that the solution refers to a homogeneous solution. As seen, the stress field is characterised by compressive normal stresses ($\bar{n}_x^{\mathrm{h}} \leq 0$) in the x-direction and tensile normal stresses ($\bar{n}_y^{\mathrm{h}} \geq 0$) in the y-direction. These normal stresses remain constant across the projected surface and are proportional to the

curvature of the reference surface. A shell with greater curvature, meaning a greater rise and/or smaller span, demonstrates higher reserved strength (Farshad, 1992). Any vertical loads applied to the shell can be understood as being transferred through an inherent system of 'arches' and 'cables' toward the shell's edges, where they must be counteracted by external forces, as shown in Figure 2.10.

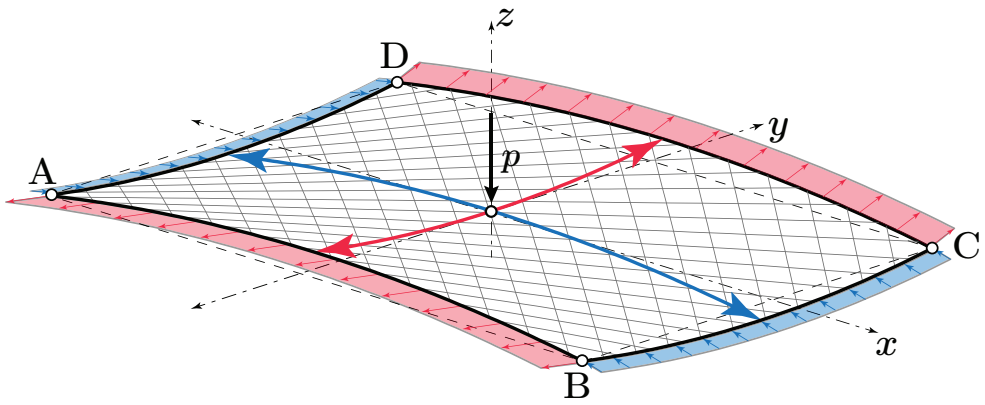

Figure 2.10: A vertical load p is transferred through tensile action (red) and compressive action (blue) toward the edges, where an external force must be applied to maintain equilibrium.

For the HP element analysed in this thesis, edges AB and CD are intended to be designed as free edges, while edges AD and BC may accommodate both shear and thrust. To remove stress at the edges, an internal stress field can be imposed (Flügge, 1962), i.e., a particular solution Φ^{p}, such that the stress state is given by $\Phi = \Phi^{\mathrm{p}} + \Phi^{\mathrm{h}}$. When combined with the existing homogeneous solution, this internal stress field counteracts the existing stresses, effectively cancelling them out along desired boundaries.

Consider a HP middle surface which projection onto the xy-plane is illustrated in Figure 2.11a. The two generators are denoted with directions u and v. At an arbitrary point P_1 situated along edge CD, the homogenous solution yields tensile stresses $\bar{n}_y$ per unit length dx, resulting in a force $\bar{N}_y = \bar{n}_y\, dx$. The force can be resolved into components $\bar{N}_u$ and $\bar{N}_v$ that are parallel with the generators, given as

$$\bar{N}_v = \bar{N}_u = \frac{q\, h_2}{8\, \sin\, \gamma} dx. \tag{2.12}$$

To rid the point of these forces, apply equal but opposite forces, i.e., compressive forces, intersecting the edges at points Q_1 and R_1. Along the edges AD and BC, the stress will be distributed over a distance $ds = dx\, \tan\, \gamma$, giving the stress intensity

$$-\frac{q\, h_2}{8\, \sin\, \gamma} dx = \bar{n}_u^{\mathrm{p}}\, ds = \bar{n}_v^{\mathrm{p}}\, ds \implies \bar{n}_u^{\mathrm{p}} = \bar{n}_v^{\mathrm{p}} = -\frac{q\, h_1}{8\, \cos\, \gamma}. \tag{2.13}$$

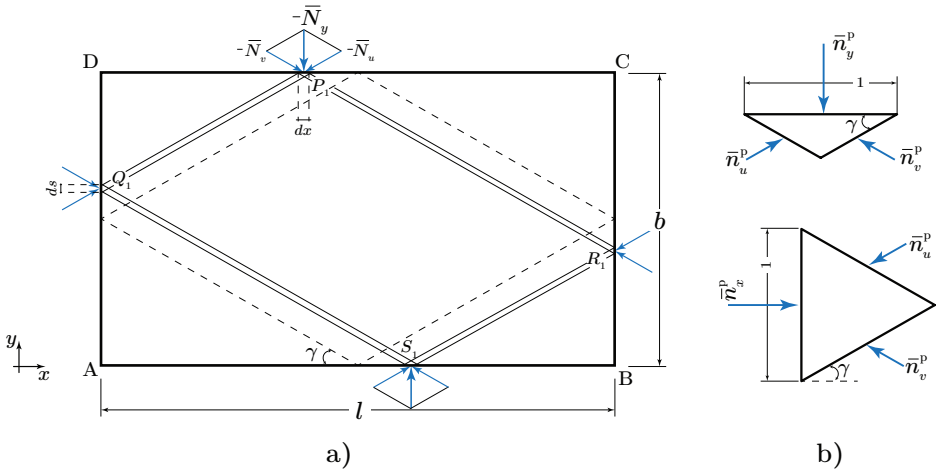

Figure 2.11: Superposition of boundary conditions. a) A compressive force is applied at point P_1 to cancel the existing tensile force from the homogenous solution. b) Transformation of stress resultants in generators to global directions.

Point Q_1 is located on a supported edge. The boundary condition can be enforced by applying a new external force at this point in the direction of the second generator. If a different direction is chosen, a component of the force would propagate back to P_1, disrupting the equilibrium that was just established. The sign of this new force can be chosen such that either its y-component cancels the existing shear $\bar{N}_{xy}$ or its x-component cancels the thrust $\bar{N}_x$. Here, the former case is chosen, resulting in a compressive thrust in the strip Q_1S_1. The same logic applies at R_1, resulting in a compressive thrust in the strip R_1S_1. A closed loop has been formed; at S_1 there are two new external forces that, when added up, cancel the existing tensile force $\bar{N}_y$. The same procedure can be applied to all points along CD, yielding compressive stresses in all generator strips and cancelling all tension along edges AB and CD. These stresses can be transformed back into global components as shown in Figure 2.11b, giving

$$\bar{n}_x^{\mathrm{p}} = -\frac{q\,h_1}{4}, \quad \bar{n}_y^{\mathrm{p}} = -\frac{q\,h_2}{4}, \quad \bar{n}_{xy}^{\mathrm{p}} = 0. \tag{2.14}$$

Adding the particular solution in Equation (2.14) to the homogenous solution in Equation (2.11) gives a shell that is in full compression with stresses occurring only in the x-direction ($\bar{n}_x = -\frac{q\,h_1}{2}$, $\bar{n}_y = \bar{n}_{xy} = 0$), as shown in Figure 2.12. This solution can alternatively also be found directly by choosing the Airy stress function as $\Phi = -\frac{1}{4}qh_1y^2$.

In the studied case, a closed force path was found. For some ratios $h_1 : h_2$, the path runs endlessly over the shell without returning to the starting position. In these cases, a pure membrane stress state is not possible in the shell (Beleș & Soare, 1971). The particular solution that was found imposes additional compressive forces along the supported edges, which must be counteracted by stiffer supports and/or prestressing. Beles and Soare (1971) demonstrates how the thrust at the support AD may be reduced by introducing external tensile forces along the edge, as depicted in Figure 2.13. As no thrust can be transferred at edges AB and CD, all forces along these edges must be reflected, inducing shearing.

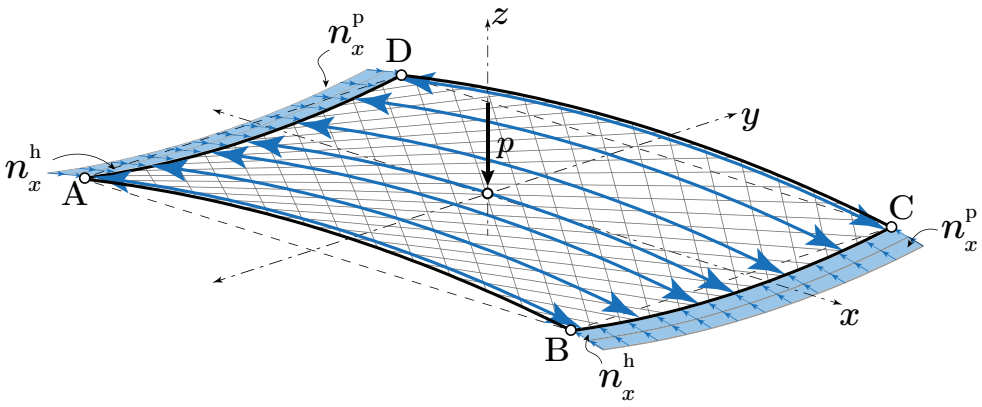

Figure 2.12: Shell in pure compression along the primary span direction as a result of imposed boundary conditions.

If a closed force path is found, there are four possible scenarios that may develop:

a) Two compressive generators meet at edge BC generating additional compressive force.

b) Two tensile generators meet at edge BC, eliminating the existing compressive force.

c) Two generators with opposite signs meet at edge BC, resulting in a shear force. If an equal tensile force is applied along BC, only shear forces must be transferred along the edges.

d) If none of these three cases develop, a mixed form will occur (Beleș & Soare, 1971).

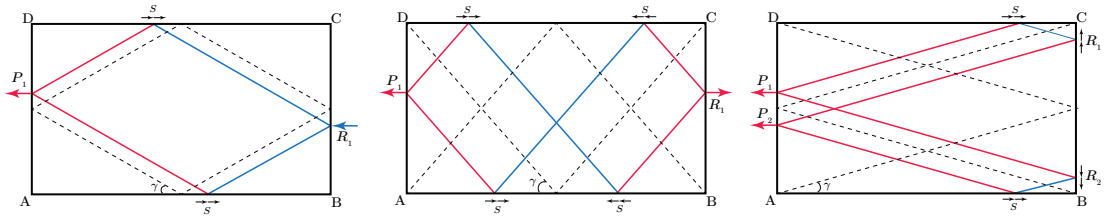

Figure 2.13: Three cases that may develop when applying a tensile force at P_1, depending on the angle γ: a) compression at R_1, b) tension at R_1, c) shear at R_1.

As a consequence of enforcing shearing along edges AB and CD, there are different zones within the shell where the two generators are either both in tension or compression, or have opposite signs. Considering case b) in Figure 2.13, the shell can be divided into seven zones, as shown in Figure 2.14. In zones marked I, both generators are in tension and will cancel the existing compressive normal stress in the x-direction; in zones marked II, the generators have opposite signs, resulting in shearing; and in zone III, both generators are in compression. Figure 2.15 shows the resulting distribution of

stress resultants when adding the imposed boundary conditions in Figure 2.13b onto the previous solution in Figure 2.12.

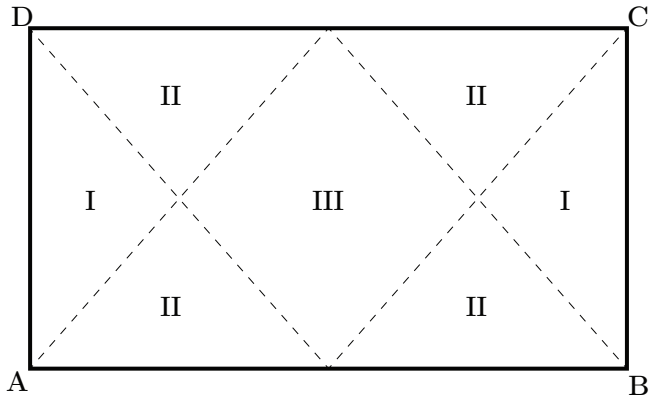

Figure 2.14: Both generators in zone I are in tension, in zone III in compression, and in zone II, they have opposing signs.

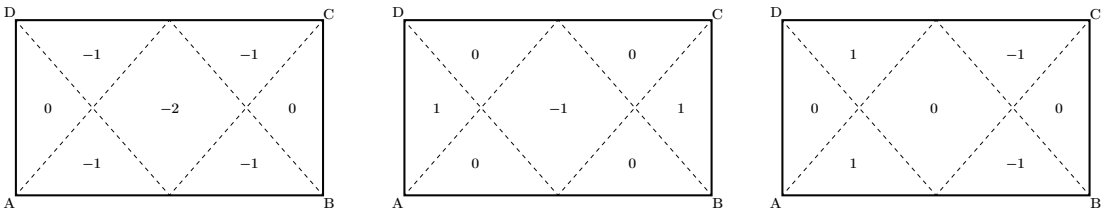

a) Normal stress $\bar{n}_x$ b) Normal stress $\bar{n}_y$ c) Shear stress $\bar{n}_{xy}$

Figure 2.15: Projected stress state in shell when removing the thrust from edges AD and BC.

The solution exhibits severe discontinuities along certain generator lines, where the sign of the stresses changes abruptly. This phenomenon is inherent to problems governed by hyperbolic differential equations, such as the one in Equation (2.9), where solution discontinuities are a known characteristic. As a result, membrane theory alone should be applied with caution when studying HP shells, as it can lead to unrealistic stress predictions (Flügge, 1962), i.e., the equilibrium depend on bending action as well.

2.2.2 Beam theory

Beam theories provide a potentially simpler approach to stress analysis in elastic elements compared to the membrane theory of shells. Both theories satisfy equilibrium, which, according to the *lower limit theorem of plasticity*, ensures that collapse is prevented as long as yielding does not occur, regardless of the actual stress distribution in the element (Hodge, 1959). The accuracy of different beam theories depends on their underlying assumptions. The classical *Euler-Bernoulli* beam theory, developed in the mid-18$^{\text{th}}$ century, is one of the simplest and most widely used. It assumes small deformations and that the neutral axis undergoes pure bending without stretching. Additionally, it postulates that all cross-sections perpendicular to the neutral axis remain planar and perpendicular after deformation. Consequently, shear deformations are neglected, which can lead to underestimated deflections in beams with a span-to-depth ratio of less than 10 (Sehlström et al., 2022). In contrast, the *Timoshenko-Ehrenfest* beam theory accounts for shear deformations, improving accuracy at the cost of increased complexity.

If the curvature along the primary span direction of the HP element is neglected, the element reduces to a parabolic cylinder, closely resembling a cylindrical shell. Based on Euler-Bernoulli beam theory, Lundgren (1949) developed a beam model applicable to simply supported cylindrical shells with a length exceeding twice their width (G. S. Ramaswamy, 1984). More recently, Dombrowski et al. (2021) expanded Lundgren's work to incorporate the effects of HP shells' doubly curved geometry. Their approach is summarised here, while the full derivations can be found in the original publication.

Dombrowski et al. (2021) consider a HP element whose coordinate system originates at the centre of the middle surface, as depicted in Figure 2.16. The local directions, s_x and s_y, align with the principal curvature directions of the surface. The beam is subjected to a uniformly distributed vertical load, p_z, and the internal stresses are assumed to remain constant through the beam's thickness, t. Analogous to the methodology in Section 2.2.1, the stress resultants can be expressed per unit width of the cross-section. In the longitudinal direction, the membrane normal stress, n_x, and shear stress, n_{xs_y}, are given by

$$n_x(x,y) = \frac{N(x)}{A_c}t + \frac{M_y(x)}{I_{yy}}(z_c(x) - z(x,y))t, \tag{2.15}$$

$$n_{xs_y}(x) = \frac{Q(x)S_y}{2\,I_{yy}}, \tag{2.16}$$

where S_y is the first moment of area, I_{yy} is the second moment of area, and z_c denotes the centroid of the cross-section at position x (G. S. Ramaswamy, 1984). If the cross-section remains constant along the beam, only the external moment $M_y(x)$ and shear force $Q(x)$, induced by the transverse load p_z, vary along its length. These forces can be determined using equilibrium conditions, as the simply supported beam is statically determinate. Dombrowski et al. neglect moments m_x, stating that 'their influence on the stress distribution is small in comparison to n_x' (Dombrowski et al., 2021).

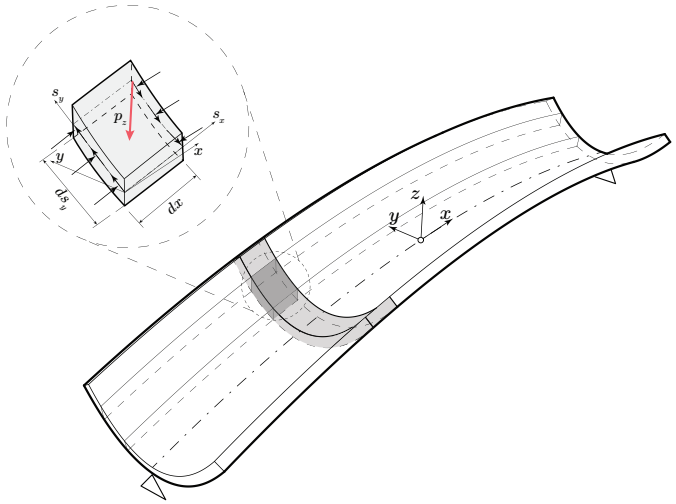

Figure 2.16: Illustration of HP element adopted from Dombrowski et. al (2021). The strips in the transverse direction are supported by adjacent strips through shear and normal forces.

In the transverse direction, the authors consider a series of parabolically shaped strips, dx wide, as shown in Figure 2.16. These strips are supported by adjacent strips through the membrane normal stresses n_x and shear stresses n_{xs_y}, which counteract the external load p_z. The shear stress n_{xs_y} can be decomposed into components n_{xy} and n_{xz}, resulting in four global load-bearing effects (p_z, n_x, n_{xy}, and n_{xz}), summarised in load functions denoted by f in Dombrowski et al. (2021). Each load function is illustrated in Figure 2.17.

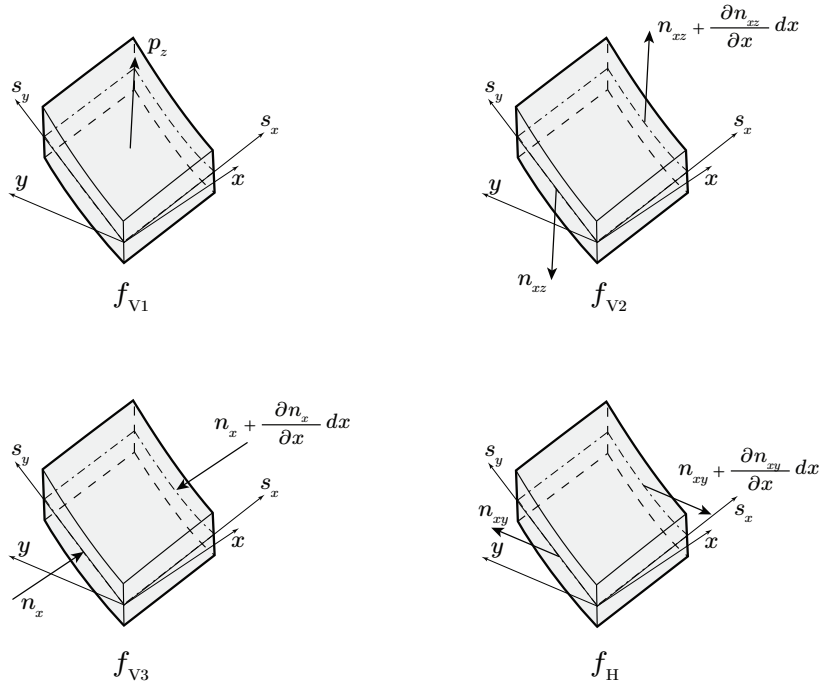

Figure 2.17: Illustration of load-bearing forces acting on an infinitesimally small element of the HP element, adopted from Dombrowski et. al (2021).

The load functions f_{V1}, f_{V2}, f_{V3} and f_{H} are defined as

$$\begin{aligned} f_{\mathrm{V1}} &= -p_z, & f_{\mathrm{V2}} &= \frac{\partial n_{xz}}{\partial x}\,dx, \\ f_{\mathrm{V3}} &= -n_x\frac{\partial^2 z}{\partial x^2} - \frac{\partial n_x}{\partial x}\frac{\partial z}{\partial x} - \frac{\partial n_x}{\partial x}\frac{\partial^2 z}{\partial x^2}, & f_{\mathrm{H}} &= \frac{\partial n_{xy}}{\partial x}\,dx. \end{aligned} \tag{2.17}$$

If a strip is cut in the longitudinal direction, internal stresses n_{s_y}, q_{s_y}, and m_{s_y} must exist, defined in accordance with Figure 2.18. The magnitudes of these stresses are given as the sum of the individual contributions from the four load functions (Dombrowski et al., 2021):

$$n_{s_y} = n_{s_y,\mathrm{V1}} + n_{s_y,\mathrm{V2}} + n_{s_y,\mathrm{V3}} + n_{s_y,\mathrm{H}} \tag{2.18}$$

$$q_{s_y} = q_{s_y,\mathrm{V1}} + q_{s_y,\mathrm{V2}} + q_{s_y,\mathrm{V3}} + q_{s_y,\mathrm{H}} \tag{2.19}$$

$$m_{s_y} = m_{s_y,\mathrm{V1}} + m_{s_y,\mathrm{V2}} + m_{s_y,\mathrm{V3}} + m_{s_y,\mathrm{H}} \tag{2.20}$$

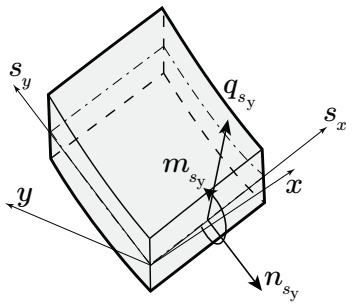

Figure 2.18: Illustration of internal stresses in the transverse direction, adopted from Dombrowski et. al (2021).

Dombrowski et al. (2021) examine how load functions f influence the individual components of internal stresses in the transverse direction through a qualitative assessment. Their findings are summarised in Figure 2.19. As seen, f_{V1} produces a negative moment that opens up the cross-section. The vertical component of the beam shear force, f_{V2}, has the opposite effect, bending the cross-section inwards. Tensile normal stresses, n_{s_y}, are generated by f_{H}, inducing a negative moment in the cross-section. Both f_{V2} and f_{H} are solely governed by the geometry of the cross-section and do not depend on the longitudinal curvature. In contrast, f_{V3} is governed by the longitudinal curvature and produces a positive moment. To minimise the bending moments m_{s_y}, the longitudinal curvature should preferably be chosen such that the negative moments due to f_{V1} and f_{H} balance the positive moments from f_{V2} and f_{V3} (Dombrowski et al., 2021).

Dombrowski et al. (2021) provides numerical expressions for computing the transverse stresses (n_{s_y}, q_{s_y}, and m_{s_y}) at a point $k \in [1, n-1]$, where n is the number of discretisation points along the strip. Figure 2.20 illustrates how the different quantities in Equations (2.21) to (2.23) are defined.

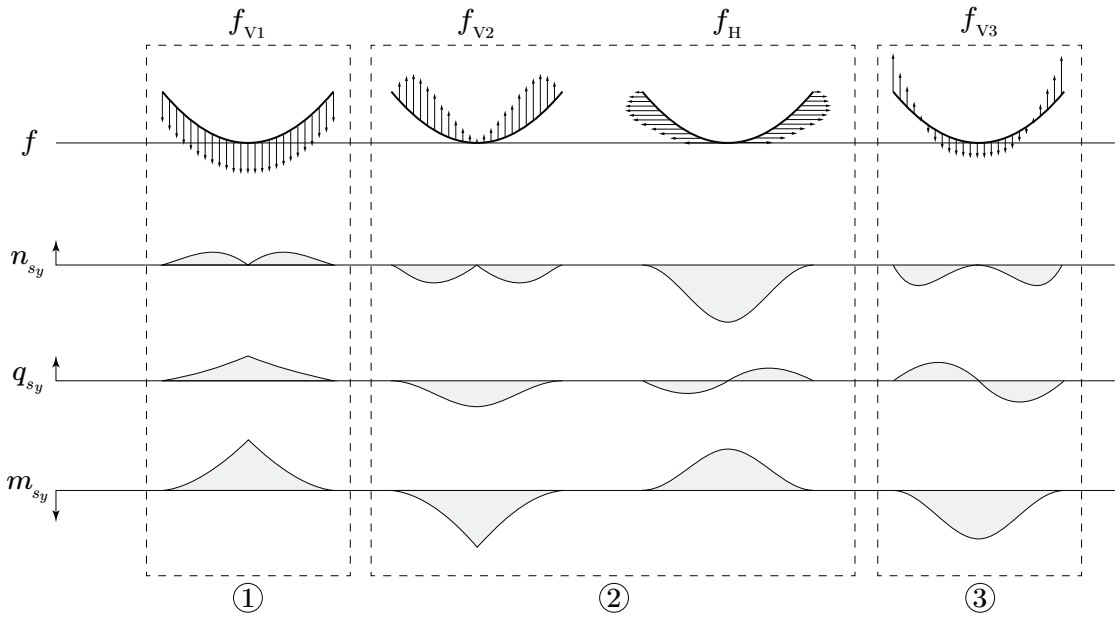

Figure 2.19: Qualitative assessment of internal stress distribution in the transverse direction, adopted from Dombrowski et. al (2021). Stresses associated with part ① are governed by external loading p_z; part ② by the shape of the cross-section; and part ③ by the curvature along the longitudinal direction of the beam (Dombrowski et al., 2021).

$$n_{s_y}(k) = \sum_{i=0}^{k-1} \Delta y_i \left[\left(f_{\mathrm{V1},i} + f_{\mathrm{V2},i} + f_{\mathrm{V3},i} \right) \frac{\Delta z_k}{\Delta s_{y,k}} + f_{\mathrm{H},i} \frac{\Delta y_k}{\Delta s_{y,k}} \right] \tag{2.21}$$

$$q_{s_y}(k) = \sum_{i=0}^{k-1} \Delta y_i \left[\left(f_{\mathrm{V1},i} + f_{\mathrm{V2},i} + f_{\mathrm{V3},i} \right) \frac{\Delta y_k}{\Delta s_{y,k}} + f_{\mathrm{H},i} \frac{\Delta z_k}{\Delta s_{y,k}} \right] \tag{2.22}$$

$$m_{s_y}(k) = \sum_{i=0}^{k-1} \Delta y_i \left[\left(f_{\mathrm{V1},i} + f_{\mathrm{V2},i} + f_{\mathrm{V3},i} \right) (y_i - y_k) + f_{\mathrm{H},i} (z_i - z_k) \right] \tag{2.23}$$

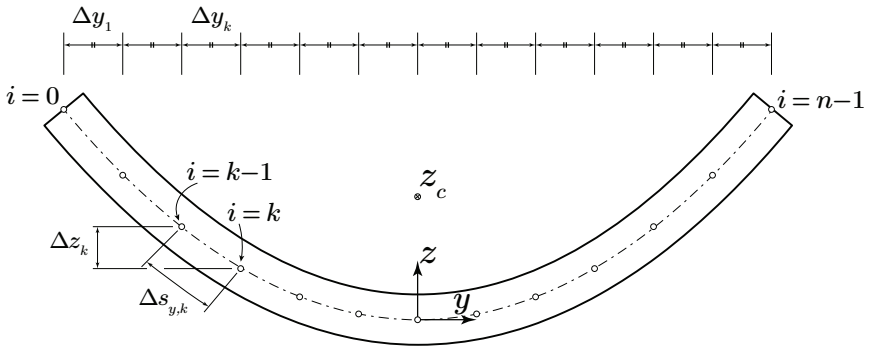

Figure 2.20: Discretisation of beam element in the transverse direction.

2.3 Experimental stress analysis

Up to this point, analytical methods for assessing stresses in HP elements have been presented. In practical applications, stresses cannot be measured directly; instead, strains and deformations are recorded to evaluate the structural response. Several experimental techniques are available to obtain strain and displacement data during static load testing. Point-wise strain measurements use sensors such as strain gauges, while techniques like *distributed fibre optic sensing* (DFOS) and *digital image correlation* (DIC) provide strain fields over larger areas or continuous paths, offering richer spatial information.

This section summarises the fundamental principles underlying DFOS and DIC, highlighting their operational concepts. Both methods were employed in the static testing of the HP prototype element (see Section 3.4.2).

2.3.1 Digital image correlation

Digital image correlation (DIC) is a non-destructive optical technique used to obtain full-field strain and displacement measurements on the surface of a test specimen (Wang et al., 2025). As illustrated in Figure 2.21, the method is based on tracking the deformation of a greyscale stochastic speckle pattern applied to the specimen surface. By comparing a reference image to a deformed image captured at a given load step, relative displacements of pixel subsets can be determined (Wang et al., 2025).

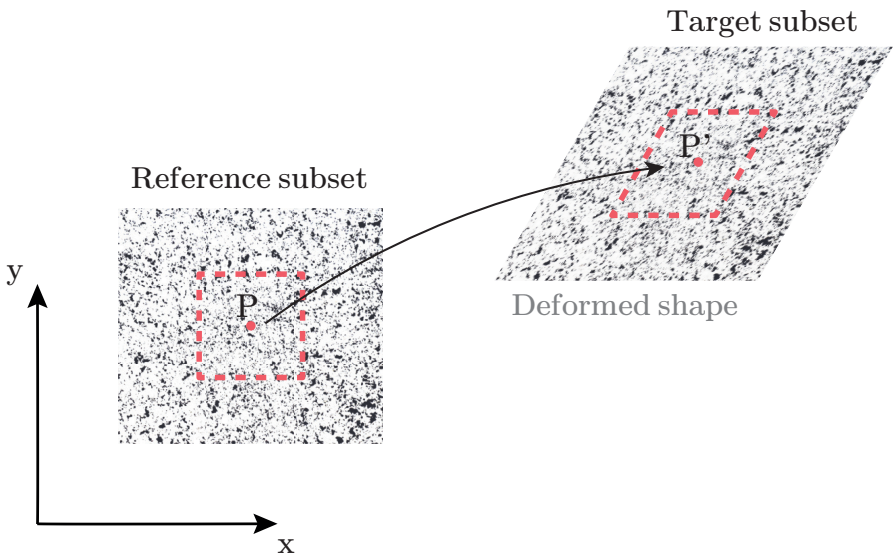

Figure 2.21: Basic principle of displacement and strain field computation using DIC. Adopted from Wang et al. (2025).

Advanced software uses correlation algorithms to compute 2D or 3D displacement vectors and strain maps (McCormick & Lord, 2010). Image acquisition typically employs *charge-coupled device* (CCD) cameras; using multiple synchronised cameras enables three-dimensional measurements (*3D-DIC*) (Wang et al., 2025). Calibration of the camera system is required prior to testing and is typically conducted using markers or objects of known geometry, such as a calibration cross.

2.3.2 Distributed fibre optic sensing

Fibre optic sensing is a monitoring technique that uses optical fibres to detect variations in physical quantities such as strain and temperature along a structure. In contrast to conventional sensors, which measure at discrete points, fibre optic sensors allow for quasi-continuous data collection along the fibre length, enabling high spatial resolution. This makes the technology particularly effective for structural health monitoring applications (Bao & Chen, 2012).

A widely used approach is *distributed fibre optic sensing* (DFOS), which provides spatially resolved strain or temperature measurements along a single optical fibre. Among the various DFOS techniques, *optical frequency domain reflectometry* (OFDR) offers exceptionally high sensitivity and spatial resolution—often on the sub-millimetre scale. OFDR relies on the principle of *Rayleigh scattering*, whereby each fibre exhibits a unique and stable backscatter pattern along its length. When the fibre is subjected to strain or temperature changes, local shifts occur in this reflection pattern. By analysing these spectral shifts, the strain distribution along the fibre can be accurately determined (Bao & Chen, 2012; Kreger et al., 2016).

The basic measurement setup using OFDR is illustrated in Figure 2.22. A tunable laser generates a variable frequency signal that defines spatial resolution. The beam is divided into a measurement path, directed through the sensing fibre, and a reference path. Light reflected from the sensing fibre is recombined with the reference signal at an optical coupler, and the resulting interference pattern is split into orthogonal components by a beam splitter, which are then recorded by detectors (Kreger et al., 2016).

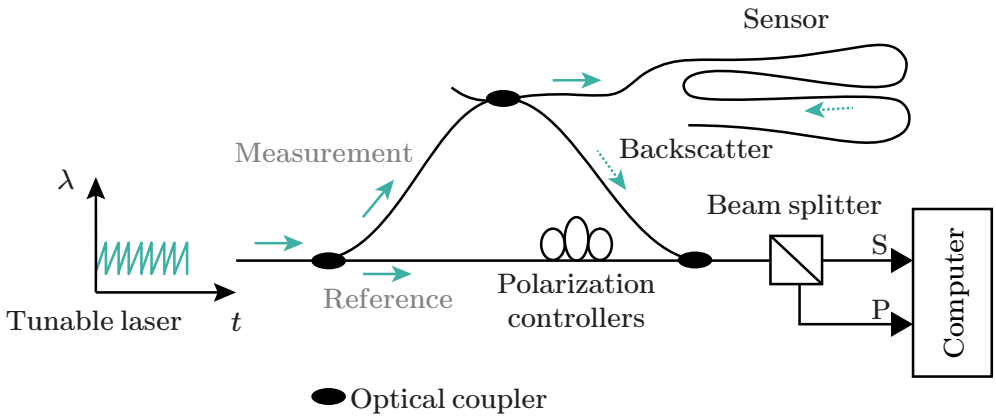

Figure 2.22: Schematic representation of the optical frequency domain reflectometry (OFDR) setup used in distributed fibre optic sensing (DFOS). A tunable laser emits light with a variable wavelength (λ), which is split into two paths by an optical coupler: a reference path and a measurement path. The measurement light travels through the sensing fibre, where Rayleigh backscattering occurs. The backscattered signal is routed back and recombined with the reference signal. Polarization controllers are used to optimize signal coherence. A beam splitter separates the recombined signal into orthogonal polarization components (S and P), which are recorded by photodetectors and processed by a computer. The resulting interference pattern enables reconstruction of the reflection profile along the fibre, from which local strain or temperature variations can be determined. Illustration adopted from Kreger et al. (2016).

The resulting interference pattern encodes both phase and amplitude information, which is extracted through a Fourier transform (see mathematical formulation in Section 2.5.3). This enables reconstruction of the reflection profile along the fibre, allowing local strain values to be determined.

2.4 Dynamics of HP elements

So far, the theoretical behaviour of HP elements has been examined under the assumption of static equilibrium, meaning the structure remains at rest under constant loading. In practice, however, structures are often subjected to time-varying loads that induce dynamic responses like oscillations and vibrations. Common sources of such loads include wind, traffic, and seismic loads. Neglecting dynamic effects in structures can lead to underestimated stresses, unexpected deformations, discomfort, or even structural failure (Ewins, 2000). A notable historical example is the collapse of the *Tacoma Narrows Bridge* in 1940 (see Figure 2.23), which experienced large oscillations and twisting movements due to aeroelastic flutter (Rogers, 2023).

Figure 2.23: The collapse of the Tacoma Narrows Bridge in 1940. This failure exemplifies the importance of dynamic analysis in structural design.

To avoid unexpected motion or failure due to dynamic loading, it is essential to evaluate the dynamic characteristics of HP elements. A common way to characterise a structure's dynamic behaviour is through *modal analysis*. At its core lies a mathematical model that describes the dynamic response of the system through the *system poles* (which contain information about the natural frequencies and damping ratios) and corresponding *mode shapes*.

Performing experimental modal analysis (EMA) involves applying external excitation to a structure and measuring its vibrational response. The objective is to identify the modal parameters that best characterise the system by fitting a mathematical model to the measured input (excitation) and output (response) data, as illustrated in Figure 2.24. A fundamental understanding of structural dynamics is essential for conducting modal

analysis effectively. In particular, it is important to understand the role of the *frequency response function* (FRF), which is directly governed by the underlying modal parameters, i.e., system poles and mode shapes.

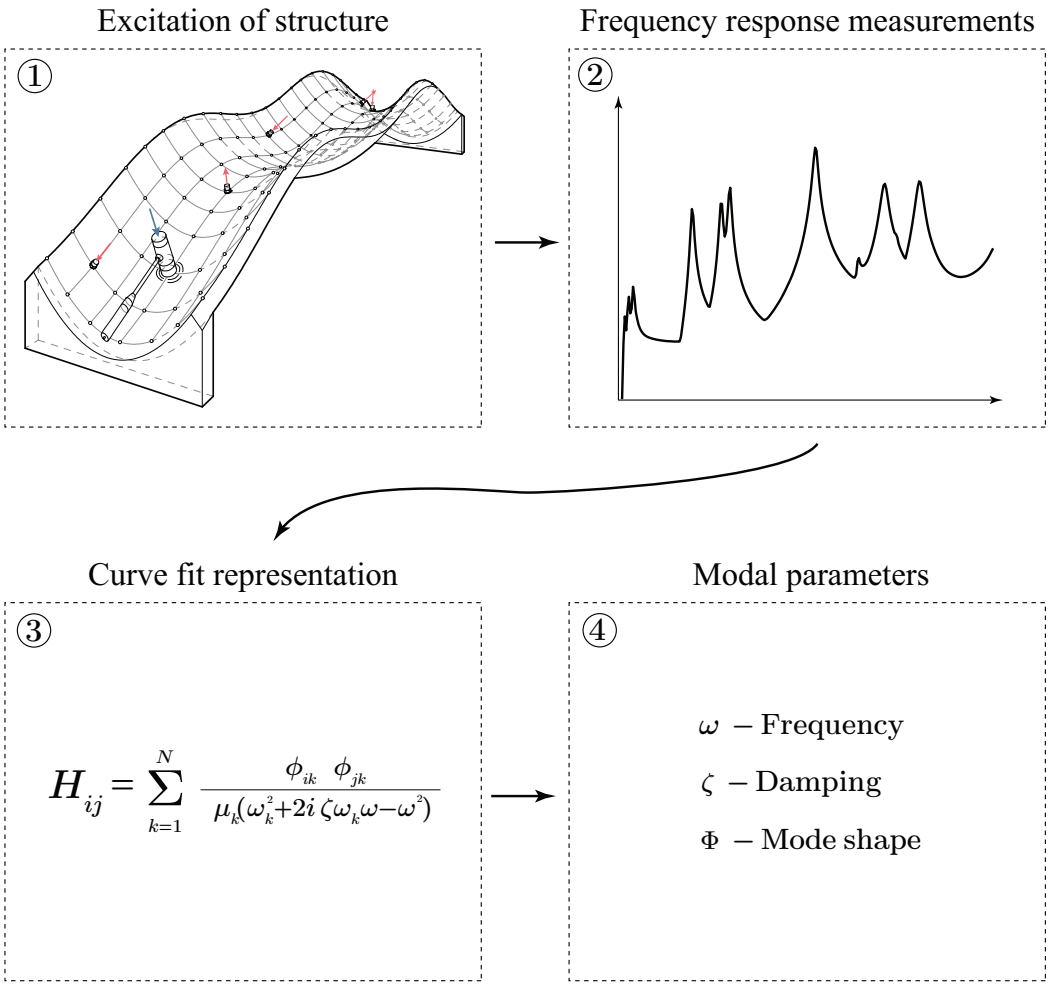

Figure 2.24: Overview of the steps in experimental modal analysis.

This section introduces fundamental concepts of structural dynamics and modal analysis. To understand the frequency response function (FRF), it is necessary to first understand the concepts of *modal parameters* and *modal transformation*. Section 2.4.1 introduces modal parameters in the context of a single degree of freedom (SDOF) system. Section 2.4.2 extends the discussion to multiple degree of freedom (MDOF) systems, from which the modal transformation is derived. The FRF is introduced in Section 2.4.3. Together, the modal parameters and FRF data form the basis for the dynamic characterisation of the HP elements. For continuous systems, such as beams and shells, analytical solutions are available for estimating natural frequencies. These models can also be used to approximate the dynamic behaviour of HP elements, as further detailed in Section 2.4.4.

2.4.1 Dynamics of a single degree of freedom system

Most physical structures, including HP elements, are continuous systems with, in theory, infinitely many degrees of freedom. In many practical contexts, such as in numerical applications, it is necessary to simplify the system into a discrete multiple degree of freedom (MDOF) system. In some cases, the system can be further reduced and modelled as a single degree of freedom (SDOF) system.

An illustrative case of a SDOF system is the motion of a swing. Imagine a person pushing on the swing, as depicted in Figure 2.25. If the person times the pushing motion correctly, synchronising it with the natural motion of the swing, the swing will accelerate, gain speed, and swing higher. Energy is added to the system from external excitation at just the right moments, amplifying the motion. The swing traces a circular trajectory governed by the length of its cords. At the peak of its arc, the swing's kinetic energy is zero while its potential energy is maximised. Due to gravity, it then swings back down, converting potential energy into kinetic energy, and return to the starting position where the person can push again, repeating the cycle.

Throughout each oscillation, the system loses energy due to, e.g., friction, air resistance, and acoustic radiation. These energy losses are collectively termed *damping*.

The swing has a natural frequency, denoted by ω_{n}, determined by its physical properties such as the length of its cords and mass distribution. In reality, due to damping, the swing oscillates at a slightly lower frequency known as the *damped natural frequency*, ω_{d}, which represents the actual number of oscillations per unit time. When the frequency of the external excitation matches ω_{d} (also called the *resonance frequency*), resonance occurs, leading to a significant amplification of motion.

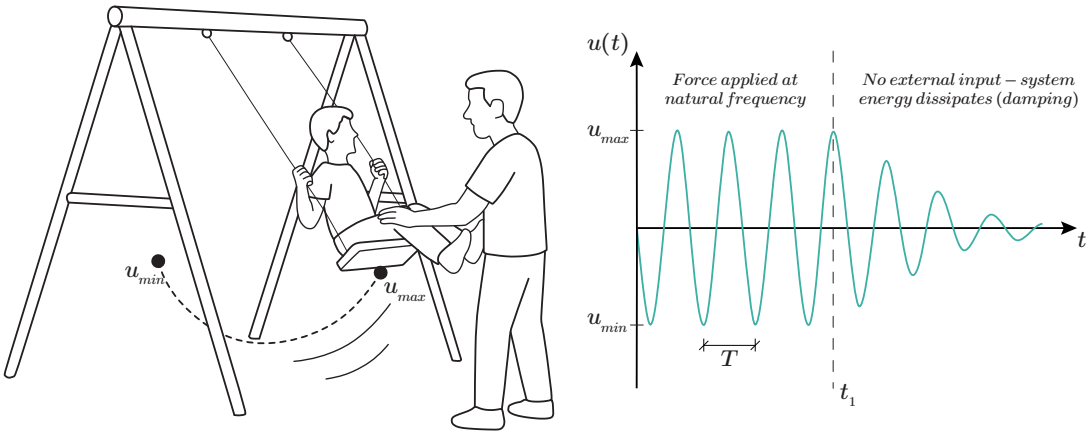

Figure 2.25: The swing analogy effectively illustrates the concepts of resonance, mode shapes, and damping. Energy is supplied to the system by a person pushing the swing at its resonance frequency, resulting in amplified motion—a phenomenon known as resonance. Assuming the system is in steady-state resonance, the energy input during each cycle balances the energy dissipated by damping, causing the amplitude of oscillation to remain constant. At time t_1, the external excitation is removed, and the system gradually returns to rest as the motion decays due to damping. When oscillating at its resonance frequency, the swing moves as a single rigid body, corresponding to its fundamental mode shape.

The time required to complete a full oscillation is called the *period*, denoted T. In the absence of energy losses, that is, in an ideal undamped system, the period is a constant that depends solely on the system's distribution of mass and stiffness. If the amplitude of the swing increases, the distance travelled during each cycle becomes larger, but so does the average speed, such that the period T remains unchanged. This implies that regardless of how hard the person pushes, the system will continue to oscillate at the same natural frequency. However, if the external force is applied at a frequency different from the system's resonance frequency, the energy input will not efficiently reinforce the motion, and resonance will not occur.

The shape a structure naturally assumes while vibrating at a particular resonance frequency is known as a *mode shape*. In the case of the SDOF swing, the entire system moves as a rigid body along a single arc. A guitar string, by contrast, resonates at multiple frequencies. Each resonance frequency is associated with a mode shape, which describes the spatial deformation pattern of the string, as illustrated in Figure 2.26.

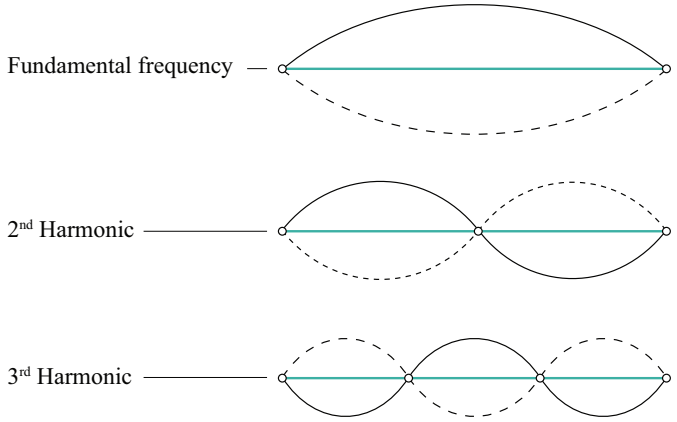

Figure 2.26: Mode shapes of the first three resonance frequencies in a guitar string.

If energy losses are disregarded in a SDOF system, it is commonly referred to as a *simple harmonic oscillator*. This idealised system undergoes sinusoidal oscillations with constant amplitude and frequency (Abrahamsson, 2019). If energy dissipation is introduced, the system is referred to as a *damped harmonic oscillator*, as illustrated in Figure 2.27. The model consists of a mass m [kg], a spring with stiffness k [N/m], a damper with damping coefficient c [Ns/m], and an external excitation $f(t)$ [N] that causes a displacement response $u(t)$ [m], velocity response $\dot{u}(t)$ [m/s] and acceleration response $\ddot{u}(t)$ [m/s^2]. In this model, energy is stored in the system both kinetically, through the motion of the mass, and elastically, through the deformation of the spring.

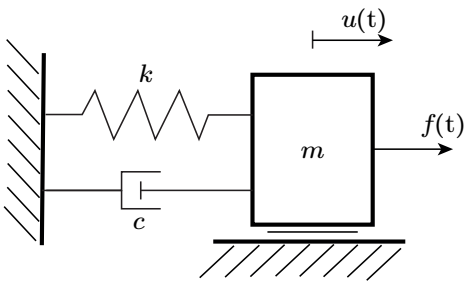

Figure 2.27: Idealised model of a damped harmonic oscillator.

An equation that governs the motion of the system, commonly referred to as the *equation of motion* (EoM), can be expressed using Newton's Second Law:

$$m\ddot{u}(t) + c\dot{u}(t) + ku(t) = f(t). \tag{2.24}$$

This is a second-order, inhomogeneous differential equation. If the system is subjected to a stationary harmonic excitation, the external force can be expressed as $f(t) = \hat{f}\mathrm{e}^{i\omega t}$, where ω is the angular frequency [rad/s]. According to the Fourier assumption, the system's response can be assumed to be harmonic as well, with the form $u(t) = \hat{u}\mathrm{e}^{i\omega t}$ (Abrahamsson, 2019). This implies that the system oscillates at the same frequency as the applied excitation. The homogenous part of the solution, corresponding to $f(t) = 0$ (free-vibrations), can be expressed as:

$$(k + i\omega c - \omega^2 m)\hat{u}\mathrm{e}^{i\omega t} = 0. \tag{2.25}$$

A non-trivial solution exists only when the term within parentheses, known as the *dynamic stiffness*, equals zero: $z = k + i\omega c - \omega^2 m = 0$. The system parameters k, m, and c are assumed known, and the objective is to determine the unknown roots ω. In the literature, these roots are often described as complex poles, known as the *system poles*, commonly denoted by s rather than ω. Each pole consists of a real part and an imaginary part, such that $s = -\sigma \pm i\omega_\mathrm{d}$, where σ is the decay rate (indicating how quickly the vibrations decay) and ω_d is the damped natural frequency (representing how fast the system oscillates under damping) (Hewlett-Packard Company, 1986).

To relate the system poles to the physical parameters of the structure (k, m and c), the following definitions are introduced:

- **Natural frequency:** $\omega_\mathrm{n} = \sqrt{k/m}$, which represents the frequency at which the system would oscillate in the absence of damping.
- **Damping ratio:** $\zeta = \frac{c}{2\sqrt{km}}$, which quantifies the level of damping relative to critical damping.
- **Damped natural frequency:** $\omega_\mathrm{d} = \omega_\mathrm{n}\sqrt{|1 - \zeta^2|}$, which represents the oscillation frequency when damping is present (Abrahamsson, 2019).

In the theory of linear second-order systems, three damping regimes are distinguished based on the value of the damping ratio: the system is said to be *underdamped* when $\zeta < 1$, *critically damped* when $\zeta = 1$, and *overdamped* when $\zeta > 1$. In most engineering applications, however, only the underdamped case is of practical relevance (Hewlett-Packard Company, 1986).

2.4.2 Dynamics of a multiple degree of freedom system

The MDOF system with n degrees of freedom can simply be viewed as an assembly of n idealised SDOF systems, as illustrated in Figure 2.28. The corresponding equation of motion in Equation (2.26) is formulated in matrix notation, where the diagonal elements represent the contributions of individual degrees of freedom (DOFs), and the off-diagonal elements capture the dynamic coupling between them.

The system is characterised by three fundamental matrices: the *mass matrix* ($\underline{\mathbf{M}}$), the *stiffness matrix* ($\underline{\mathbf{K}}$), and the *damping matrix* ($\underline{\mathbf{V}}$). Displacement, velocity, and acceleration are represented as vectors ($\mathbf{u}(t)$, $\dot{\mathbf{u}}(t)$, and $\ddot{\mathbf{u}}(t)$, respectively), with each component corresponding to a particular degree of freedom.

$$\underline{\mathbf{M}}\ddot{\mathbf{u}}(t) + \underline{\mathbf{V}}\dot{\mathbf{u}}(t) + \underline{\mathbf{K}}\mathbf{u}(t) = \mathbf{f}(t). \tag{2.26}$$

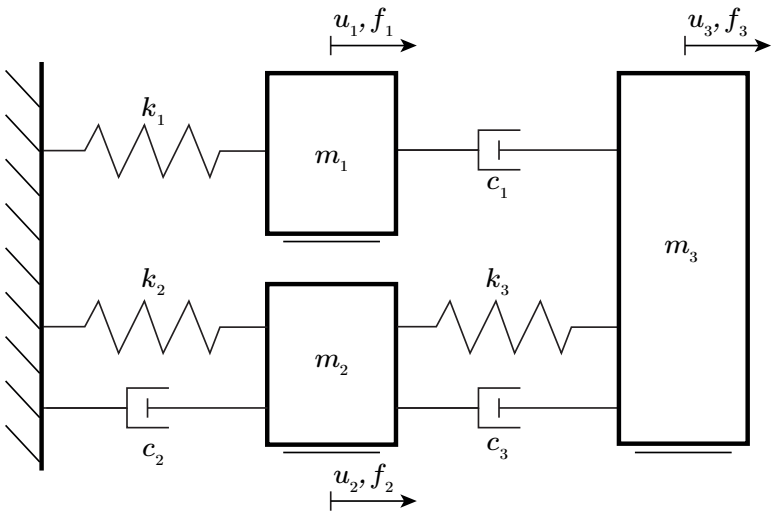

Figure 2.28: Illustration of discrete MDOF system.

Consider the system under free vibration in harmonic stationarity with no energy dissipation ($\mathbf{f}(t) = \mathbf{0}$, $\mathbf{u}(t) = \hat{\mathbf{u}}\mathrm{e}^{i\omega t}$, and $\underline{\mathbf{V}} = \underline{\mathbf{0}}$):

$$\left(\underline{\mathbf{K}} - \omega^2\underline{\mathbf{M}}\right)\hat{\mathbf{u}} = \mathbf{0}. \tag{2.27}$$

This represents a linear system of equations that admits a non-trivial solution ($\hat{\mathbf{u}} \neq \mathbf{0}$) provided that the determinant of the *dynamic stiffness matrix* (also called *impedance matrix*) $\underline{\mathbf{Z}} = \underline{\mathbf{K}} - \omega^2\underline{\mathbf{M}}$ is zero, i.e., $\det(\underline{\mathbf{Z}}) = 0$. A system with n degrees of freedom has n distinct roots ω_k^2, $k = 1, \ldots, n$, that satisfy this condition. These roots are the *eigenvalues* of the system, and the corresponding values $\omega_k = \sqrt{\omega_k^2}$ are the *natural frequencies*.

It can be shown that if the dynamic stiffness matrix is *positive semi-definite*, the eigenvalues are guaranteed to be *real and non-negative*. Furthermore, the set of eigenvectors ($\hat{\mathbf{u}}_k \triangleq \boldsymbol{\phi}_k$) associated with the eigenvalues ω_k^2 forms a complete basis for the system (Abrahamsson, 2019). This implies that all possible solutions to the system of equations

(displacements, velocities, or accelerations) can be expressed as a linear combination of the eigenvectors. For example:

$$\mathbf{u} = \eta_1\boldsymbol{\phi}_1 + \cdots + \eta_n\boldsymbol{\phi}_n = \sum_{k=1}^{n} \eta_k\boldsymbol{\phi}_k = \boldsymbol{\eta}\underline{\boldsymbol{\Phi}}, \tag{2.28}$$

where $\mathbf{u}$ is the displacement vector, $\boldsymbol{\eta}$ is a vector of *modal displacements* (amplitudes indicating each mode's contribution to the overall displacement), and $\underline{\boldsymbol{\Phi}}$ is the *mode shape matrix*, whose columns are the eigenvectors ($\underline{\boldsymbol{\Phi}} = [\boldsymbol{\phi}_1 \cdots \boldsymbol{\phi}_n]$) (Abrahamsson, 2019). Similar transformations apply to physical velocities and accelerations.

Moreover, it can be shown that the eigenvectors are *mutually orthogonal* (Abrahamsson, 2019). According to the *modal decomposition theorem*, this orthogonality allows the application of an orthogonal transformation to the system, effectively mapping it to a linear space where the eigenvectors form the basis. This yields a *diagonalised* (uncoupled) system. In other words, the MDOF system can be transformed into n decoupled SDOF systems. The equations of motions takes the following form:

$$\underline{\boldsymbol{\Phi}}^{\mathrm{T}}\underline{\mathbf{M}}\,\underline{\boldsymbol{\Phi}}\ddot{\boldsymbol{\eta}}(t) + \underline{\boldsymbol{\Phi}}^{\mathrm{T}}\underline{\mathbf{K}}\,\underline{\boldsymbol{\Phi}}\boldsymbol{\eta}(t) = \mathrm{diag}(\mu_k)\ddot{\boldsymbol{\eta}}(t) + \mathrm{diag}(\gamma_k)\boldsymbol{\eta}(t) = \underline{\boldsymbol{\Phi}}^{\mathrm{T}}\mathbf{f}(t) \triangleq \boldsymbol{\Psi}(t), \tag{2.29}$$

where μ_k is the modal masses, γ_k the modal stiffnesses and $\boldsymbol{\Psi}(t)$ the physical loading projected onto the modal basis. Equation (2.29) can be expanded into its decoupled format

$$\begin{cases} \mu_1\ddot{\eta}_1(t) + \gamma_1\eta_1(t) = \psi_1(t) = \boldsymbol{\phi}_1^{\mathrm{T}}\mathbf{f}(t) \\ \mu_2\ddot{\eta}_2(t) + \gamma_2\eta_2(t) = \psi_2(t) = \boldsymbol{\phi}_2^{\mathrm{T}}\mathbf{f}(t) \\ \qquad\qquad\qquad \vdots \\ \mu_n\ddot{\eta}_n(t) + \gamma_n\eta_n(t) = \psi_n(t) = \boldsymbol{\phi}_n^{\mathrm{T}}\mathbf{f}(t) \end{cases} \tag{2.30}$$

Using the modal masses μ_k and modal stiffnesses γ_k, the eigenvalues can be expressed through the *Rayleigh quotient*:

$$\omega^2 = \frac{\underline{\boldsymbol{\Phi}}^{\mathrm{T}}\underline{\mathbf{K}}\,\underline{\boldsymbol{\Phi}}}{\underline{\boldsymbol{\Phi}}^{\mathrm{T}}\underline{\mathbf{M}}\,\underline{\boldsymbol{\Phi}}}, \quad \omega_k^2 = \frac{\boldsymbol{\phi}_k^{\mathrm{T}}\underline{\mathbf{K}}\boldsymbol{\phi}_k}{\boldsymbol{\phi}_k^{\mathrm{T}}\underline{\mathbf{M}}\boldsymbol{\phi}_k}. \tag{2.31}$$

Modal decomposition may be applied only in the absence of damping or under the assumption of proportional damping (Abrahamsson, 2019). Proportional damping refers to cases where the damping matrix is expressed as a linear combination of the mass and stiffness matrices. Two commonly used models are Caughey damping and Rayleigh damping (Caughey & O'Kelly, 1965; Rayleigh, 1877). These models are primarily mathematical constructs that facilitate modal decomposition, with limited physical interpretation.

2.4.3 Transfer functions and frequency response functions

The *transfer function* and *frequency response function (FRF)* are fundamental concepts in modal analysis. Both describe the vibration response of a system at one degree of freedom (DOF) due to an excitation applied at another DOF (Brandt, 2011). While these terms are sometimes used interchangeably in the literature, they are not mathematically equivalent. The distinction between them lies in their definitions and the domains in which they are expressed.

The *transfer function*, denoted $\underline{\mathbf{H}}(s)$, is defined in the *complex frequency-domain* (also known as the *s-domain* or *Laplace domain*). It characterises the complete dynamic behaviour of the system, including both transient and steady-state responses. Specifically, it captures the system's initial response to an input and its behaviour over time as the transients decay. This broader description makes the transfer function particularly useful for mathematical modelling and system identification.

By contrast, the *frequency response function*, $\underline{\mathbf{H}}(\omega)$, is the quantity actually obtained in experimental modal analysis (EMA). During EMA, excitation and response signals are recorded in the time-domain and transformed into the frequency-domain using a Fourier transform (cf. Section 2.5.3). This transformation assumes that the system is in harmonic steady-state, meaning any transient dynamics have dissipated. As a result, the FRF reflects the system's steady-state response to sinusoidal excitation at various frequencies. Mathematically, the FRF is obtained by evaluating the transfer function along the imaginary axis, $s = \pm i\omega$, in the complex plane, as illustrated in Figure 2.29.

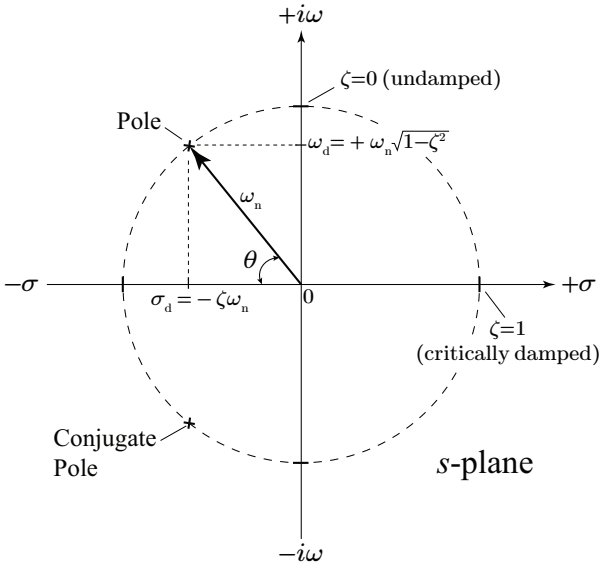

Figure 2.29: Complex plane representation of a system pole.

The transfer function can be obtained from a forced response analysis, assuming harmonic excitation. To illustrate, consider the inhomogeneous equation of motion in Equation (2.26). Assume that the system is in harmonic stationarity, meaning $\mathbf{f}(t) = \hat{\mathbf{f}}\mathrm{e}^{i\omega t}$ and $\mathbf{u}(t) = \hat{\mathbf{u}}\mathrm{e}^{i\omega t}$. Substituting these expressions into Equation (2.26), rearranging terms, and dividing both sides by the common exponential term $\mathrm{e}^{i\omega t}$, the following frequency-domain expression is obtained:

$$\hat{\mathbf{f}} = (\underline{\mathbf{K}} + i\omega\underline{\mathbf{V}} - \omega^2\underline{\mathbf{M}})\hat{\mathbf{u}} = \underline{\mathbf{Z}}(\omega)\hat{\mathbf{u}}. \tag{2.32}$$

Applying a *Laplace transform* ($\underline{\mathbf{Z}}(\omega) \rightarrow \underline{\mathbf{Z}}(s)$), this relation generalises to the complex frequency-domain. The dynamic stiffness matrix in the Laplace domain is according to Brandt (2011) defined as:

$$\underline{\mathbf{Z}}(s) = \underline{\mathbf{K}} + s\underline{\mathbf{V}} + s^2\underline{\mathbf{M}}. \tag{2.33}$$

Inverting the dynamic stiffness matrix $\underline{\mathbf{Z}}(s)$ yields the transfer function $\underline{\mathbf{H}}(s)$:

$$\hat{\mathbf{u}} = \underline{\mathbf{Z}}^{-1}(s)\hat{\mathbf{f}} \triangleq \underline{\mathbf{H}}(s)\hat{\mathbf{f}}. \tag{2.34}$$

In the specific case of displacement response, the transfer function $\underline{\mathbf{H}} \triangleq \underline{\mathbf{H}}_{\mathrm{d}}$ is referred to as the system's *receptance* (Abrahamsson, 2019).

Modal decomposition can be applied to Equation (2.32). If the damping is of Caughey type, complete decoupling can be expressed as:

$$\operatorname{diag}\left(\mu_k(s - s_k)(s - \bar{s}_k)\right)\hat{\boldsymbol{\eta}} = \underline{\boldsymbol{\Phi}}^{\mathrm{T}}\hat{\mathbf{f}}, \tag{2.35}$$

where the product $(s - s_k)(s - \bar{s}_k)$ is equivalent to $s^2 + 2\zeta_k\omega_k s + \omega_k^2$, with system poles $(s_k, \bar{s}_k) = \omega_k\left(-\zeta \pm i\sqrt{1 - \zeta_k^2}\right)$. If a mode is undamped ($\zeta_k = 0$), the poles are purely imaginary, $(s_k,\, \bar{s}_k) = \pm i\omega_k$. For an underdamped mode ($0 < \zeta_k < 1$), the poles are complex-valued scalars, meaning they comprise both real and imaginary components (see Figure 2.29).

Transforming the modal displacements to physical displacements via $\hat{\mathbf{u}} = \underline{\boldsymbol{\Phi}}\hat{\boldsymbol{\eta}}$, the receptance is obtained as:

$$\begin{aligned}
\hat{\mathbf{u}} &= \underline{\boldsymbol{\Phi}}\ \operatorname{diag}\left(\frac{1}{\mu_k(s - s_k)(s - \bar{s}_k)}\right)\underline{\boldsymbol{\Phi}}^{\mathrm{T}}\hat{\mathbf{f}} \\
\implies \underline{\mathbf{H}}_{\mathrm{d}}(s) &= \underline{\boldsymbol{\Phi}}\ \operatorname{diag}\left(\frac{1}{\mu_k(s - s_k)(s - \bar{s}_k)}\right)\underline{\boldsymbol{\Phi}}^{\mathrm{T}}
\end{aligned} \tag{2.36}$$

Since the eigenvectors $\boldsymbol{\phi}_k$ are the columns of the modal matrix $\underline{\boldsymbol{\Phi}}$, the receptance can also be expressed using the following *pole-residue representation*:

$$\underline{\mathbf{H}}_{\mathrm{d}}(s) = \sum_{k=1}^{n} \frac{\boldsymbol{\phi}_k\boldsymbol{\phi}_k^{\mathrm{T}}}{\mu_k(s - s_k)(s - \bar{s}_k)}. \tag{2.37}$$

This expression is equivalent to Equation (6.107) in Brandt (2011), though it uses slightly different notation. The representation allows the isolation of individual terms

of the receptance matrix (Abrahamsson, 2019). For example, the element $H_{ij,\mathrm{d}}$, which relates the displacement at DOF i due to excitation at DOF j, is given by:

$$H_{ij,\mathrm{d}}(s) = \sum_{k=1}^{n} \frac{\phi_{ik}\phi_{jk}}{\mu_k(s - s_k)(s - \bar{s}_k)}. \tag{2.38}$$

For the special case of an undamped system the poles are given as $(s_k,\, \bar{s}_k) = \pm i\omega_k$, which gives:

$$H_{ij,\mathrm{d}}(s) = \sum_{k=1}^{n} \frac{\phi_{ik}\phi_{jk}}{\mu_k(\omega_k^2 + s^2)}. \tag{2.39}$$

The frequency response function $H_{ij,\mathrm{d}}(\omega)$ in the frequency-domain ($s = \pm i\omega$), is consequently found as:

$$H_{ij,\mathrm{d}}(\omega) = \sum_{k=1}^{n} \frac{\phi_{ik}\phi_{jk}}{\mu_k(\omega_k^2 - \omega^2)}. \tag{2.40}$$

It follows that when excitation frequencies ω approaches natural frequencies ω_k of the system ($\omega \to \omega_k$), the receptance tend to $\pm\infty$, i.e., resonance occurs.

The transfer function and FRF may also describe system responses other than displacement, such as velocity $\underline{\mathbf{H}}_{\mathrm{v}}$ or acceleration $\underline{\mathbf{H}}_{\mathrm{a}}$. The FRF is generally a complex quantity, comprising both real and imaginary components, or equivalently, a magnitude and phase when expressed in polar form. Consequently it cannot be fully represented on a single two-dimensional plot. Several formats exist for visualising FRF data. A common approach in the literature is the *Bode plot*, which consists of two separate plots: one showing the magnitude of the frequency response (typically on a logarithmic scale), and another showing the corresponding phase shift. An example of a Bode plot for a SDOF system is shown in Figure 2.30.

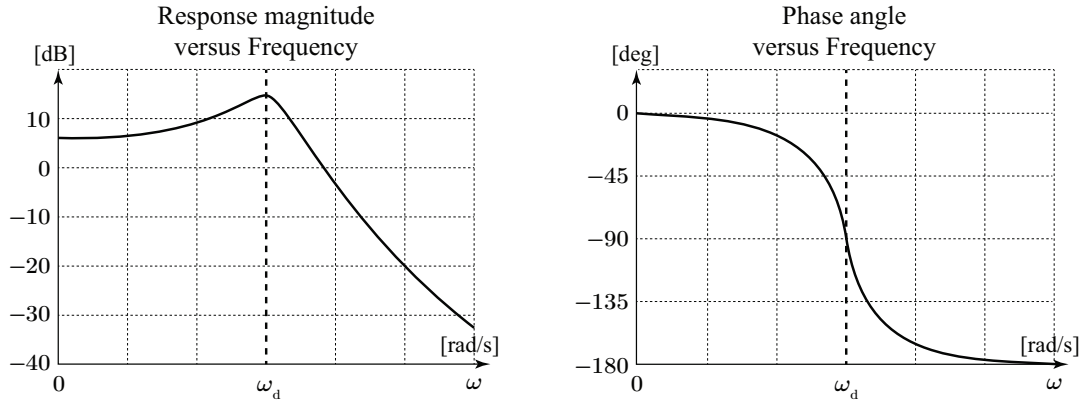

Figure 2.30: Bode plot for a SDOF system. The plot on the left shows the response magnitude versus frequency, while the plot on the right shows the phase angle versus frequency. At low frequencies, the response magnitude is more or less proportional to the excitation magnitude and in phase. Near the resonance frequency ω_d, the response magnitude increases sharply, with the phase shifting by *–90°*. At high frequencies, the response magnitude diminishes and the phase shift approaches *–180°*.

In MDOF systems, all modes contribute to the response across the frequency range. Near particular resonance frequencies, only one or a few modes dominate, as illustrated in Figure 2.31.

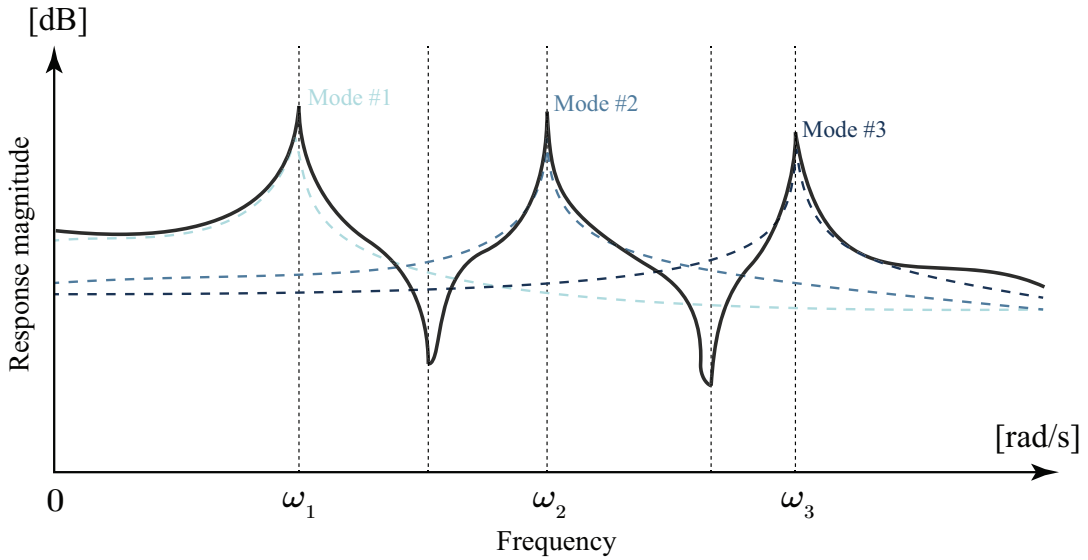

Figure 2.31: The magnitude of the frequency response in a MDOF system results from the combined contributions of each individual mode.

2.4.4 Dynamics of a continuous system

An important aim of this thesis is to validate numerical predictions of the dynamic response of HP elements. While theoretical models may offer some insight, they are insufficient for rigorous validation due to the complexity and variability of the real-world behaviour. The primary focus in this thesis is on validation through experimental modal analysis. To interpret and verify the experimental results accurately, a solid understanding of the underlying theoretical behaviour is, however, still essential. Significant discrepancies between theoretical predictions and experimental data may point to issues in the experimental setup, such as faulty accelerometers, inappropriate boundary conditions, or signal processing errors.

As in the static case, various continuum theories, such as beam, plate, and shell theories, can be used to estimate the dynamic response of HP elements. Unlike discrete SDOF or MDOF systems, which represent mass and elasticity using idealised lumped parameters, continuum models assume that mass and stiffness are continuously distributed throughout the structure (Abrahamsson, 2019). While discrete systems are governed by second-order ordinary differential equations (ODEs), continuous systems are described by partial differential equations (PDEs) that depend on both time and spatial coordinates. This generally results in more complex analytical formulations and solution methods.

Perhaps the simplest theory suitable for predicting the dynamic response of HP elements is again the *Euler–Bernoulli beam theory*. This model relies on several simplifying assumptions, including prismatic geometry, constant material properties, and the neglect of shear deformation and rotary inertia. As a result, it is applicable only to bending modes and cannot be used to analyse torsional behaviour. Assuming free vibrations

(i.e., no external excitation), the equilibrium of the beam is governed by the following partial differential equation:

$$EI\frac{\partial^4 w(x,t)}{\partial x^4} + \rho A\frac{\partial^2 w(x,t)}{\partial t^2} = 0, \tag{2.41}$$

where E is the modulus of elasticity, I is the moment of inertia, ρ is the density, A is the cross-section area, and $w(x,t)$ denotes the transverse deflection of the beam (Abrahamsson, 2019). Solving the equation, assuming *free-free* boundary conditions, results in a characteristic equation from which the natural bending frequencies can be derived:

$$\omega_n = \frac{v_n^2}{2\pi}\sqrt{\frac{EI}{\rho AL^4}}, \quad v_n = [0,\ 4.73,\ 7.853,\ 11.0,\ \ldots]. \tag{2.42}$$

Alternatively, the HP element can be modelled as a plate or a shell. Leissa (1973) conducted a comprehensive study on the vibrational response of plates and shells, highlighting that the dynamic behaviour of shells is significantly more complex than that of plates due to a strong coupling between stretching and bending deformations. As a consequence, membrane theory—which simplifies the governing equations by neglecting bending effects—is not suitable for accurately describing shell dynamics. Leissa also noted that shells tend to exhibit more closely spaced natural frequencies compared to plates, making experimental identification more challenging, particularly for the fundamental (first) natural frequency (Leissa, 1973).

2.5 Experimental modal analysis

Much of the theoretical foundation necessary to understand modal analysis was established in Section 2.4. This section shifts the focus to the practical aspects of experimental modal analysis (EMA). Section 2.5.1 provides an overview of the EMA procedure, while Sections 2.5.2 to 2.5.4 address key considerations related to experimental setup, signal analysis, and signal processing, respectively. Section 2.5.5 presents methods for identifying modal parameters from experimental FRF data. Finally, Section 2.5.6 discusses methods for comparing these parameters with those obtained from numerical analysis.

2.5.1 Experimental modal analysis in a nutshell

The goal of EMA is to determine a modal system model from measured system properties. More specifically, the objective is to estimate modal parameters from measured frequency response functions (FRFs).

As outlined in Section 2.4.3, the transfer function provides a mathematical model that relates the system's response to an applied excitation. Recall from Equation (2.38) that the total receptance can be expressed as a sum of contributions from all n modes in the system. The expression comprises unknown modal parameters such as the mode shape vectors $\boldsymbol{\phi}_k$, and system poles s_k, which in turn encoded parameters including the modal damping ratios ζ_k and the damped frequencies ω_k.

Performing EMA involves sampling responses $X(t)$ and excitations $Y(t)$ at discrete time intervals. The FRF $H(\omega)$ is obtained directly by dividing the response signal (commonly measured as acceleration [m/s^2]) with the excitation signal (commonly measured as force [N]) expressed in the frequency-domain, i.e., $H(\omega) = X(\omega)/Y(\omega)$. Subsequently, system modal parameters should be fitted, such that the approximation error between the measured FRF and the mathematical transfer function model is minimised. This is generally referred to as *system identification* and is achieved through a *curve-fitting procedure*.

Depending on the accuracy and complexity required for the analysis, different experimental configurations can be used to obtain the FRFs. These are generally classified as: *single-input single-output* (SISO), *single-input multiple-output* (SIMO), *multiple-input single-output* (MISO), and *multiple-input multiple-output* (MIMO) configurations. For structures similar to the HP element investigated in this thesis, a SIMO setup is typically employed (Ewins, 2000). An excitation is then applied in one location at a time, while the response is measured in multiple points.

The FRFs should be measured in a frequency range that is suitable for the application, i.e., it must be wide enough to capture all relevant modes of interest while avoiding unnecessary high-frequency noise. The selected frequency range should ideally encompass the system's fundamental and higher-order natural frequencies that significantly contribute to the dynamic response, ensuring a reliable modal model. The available frequency range is directly correlated to the experimental configuration and the equipment that is used.

An overview of the steps involved in EMA is illustrated in Figure 2.32. Here, a SISO configuration is considered, applied to a cantilever beam discretised into three degrees of freedom. An *impact hammer* is used to excite each DOF individually, while a sin-

gle reference *accelerometer* records the corresponding response. The measured signals are passed through a *data acquisition* (DAQ) system, which performs signal conditioning, such as noise reduction, and applies the discrete Fourier transform to convert time-domain signals into the frequency-domain. For each excitation, a corresponding response is recorded. In the SISO case shown in Figure 2.32, three excitations yield three FRFs. Once modal parameters are identified through curve fitting, mode shapes can be visualised (e.g., through animation) and compared with numerical or experimental data using correlation methods.

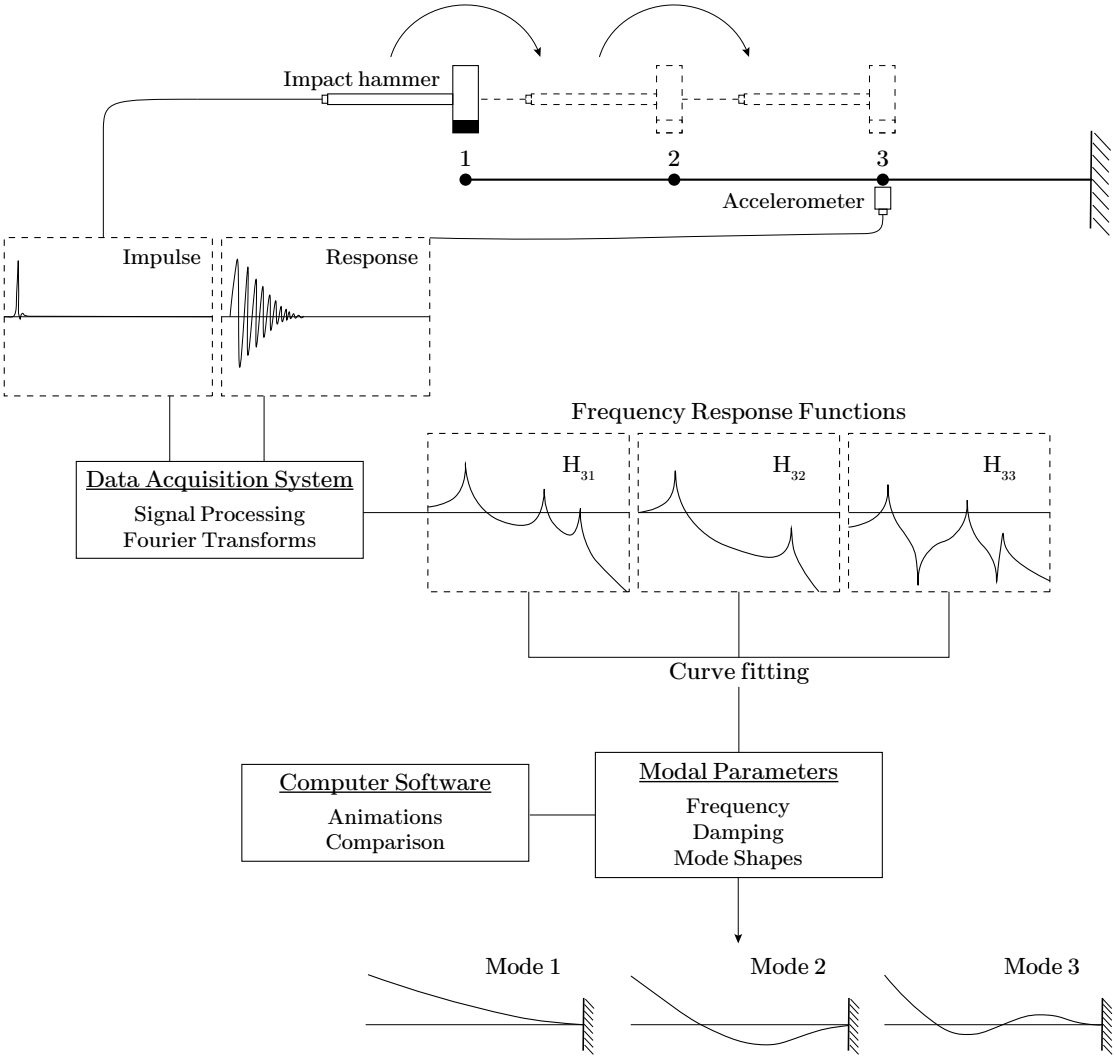

Figure 2.32: Illustration of a general experimental modal analysis procedure using a *single-input single output* configuration.

For modal testing to be valid, two assumptions must hold true:

1. The structure must exhibit linear behaviour, allowing the principle of superposition to be applied.
2. The structure must be invariant over time, which means that the dynamic characteristics will not change during or between tests (Ewins, 2000).

2.5.2 Experimental setup of single-input tests

Assuming a single-input test configuration is adopted, meaning that excitation is applied at only one location at a time, several factors must be considered when selecting an appropriate measurement method and experimental setup. These considerations are discussed in more detail in the following subsections.

2.5.2.1 Boundary conditions

The first consideration is how to support the structure during testing. The decision will greatly influence the outcome and precision of the test results (Ewins, 2000). In general, three configurations are considered in literature:

1. **free**, generally obtained by suspending it in elastic ropes or placing it on inflatable air cushions;
2. **grounded**, either clamped or simply supported; or
3. **in situ**, mounted in its proposed state of use.

Ideally, when using experimental data to validate a finite element model, a free boundary condition should be replicated, as it provides the most accurate results and yields rigid body modes that depend solely on the structure's mass and inertia (Ewins, 2000). In general, all structures exhibit six rigid body modes at a frequency of 0 Hz, corresponding to pure translations (along the x, y and z axes) and rotations (around the x, y and z axes). If the measured rigid body modes occur at frequencies less than 10–20% of the first flexible mode, the free boundary condition can be considered satisfactory, as it will not significantly affect the flexible mode shapes (Ewins, 2000).

2.5.2.2 Transducers

Transducers are used to measure both the input force applied to the system and the resulting response of the system.

The structure may be excited using for instance an *electrodynamic shaker* or an *impact hammer*, with the latter being more commonly employed (Brandt, 2011). Impact hammers are equipped with an internal force transducer and an interchangeable tip that determines the duration and frequency content of the excitation. *Hard tips* produce short impulses with broad frequency content, while *soft tips*, typically made of rubber or vinyl, yield longer impulses with a narrower frequency range (Hewlett-Packard Company, 1986). The hammer should be chosen with regards to the test object and desired frequency range. The mass and tip of the hammer affects its *useful frequency range*, F, and selecting an inappropriate hammer may result in missing important modes (Craig & Kurdila, 2011). The useful frequency range is typically defined as the region where the spectral decay is less than 20 dB, as illustrated in Figure 2.33 (Døssing, 1988). While impact hammers allow for quicker and more flexible testing than shakers, they are less suitable for non-linear systems and may pose a risk of damaging delicate structures (Ewins, 2000).

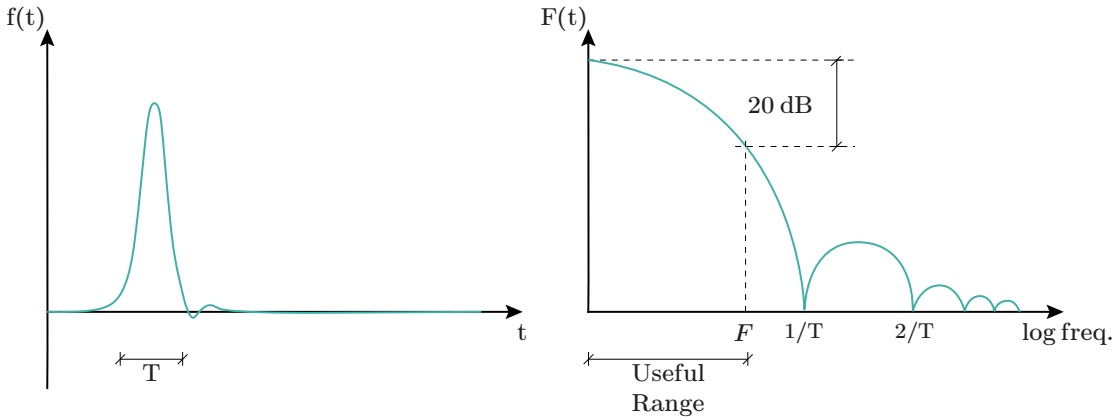

Figure 2.33: Hammer excitation signal (left), and useful frequency range in the force spectrum (right), adopted from (Døssing, 1988).

Acceleration is typically measured using *piezoelectric accelerometers*, which convert motion into an electrical signal. The way accelerometers are mounted is critical, as a poor connection can introduce unwanted resonance or damping effects (Brandt, 2011). A rigid connection to the specimen can generally be achieved using adhesive methods, such as glue or beeswax, which ensure sufficient stiffness without altering the dynamic behaviour significantly. To accurately capture all relevant modes, accelerometers must be strategically positioned to avoid placement on *nodal lines*, i.e., in locations where the structure exhibits no motion for a particular mode shape, as illustrated in Figure 2.34. Placement on such nodes might result in complete omission of certain modes in the measurement data. Using several accelerometers in a SIMO configuration can help mitigate this risk by increasing the likelihood that at least one sensor captures each mode effectively (Ewins, 2000).

Accelerometers are usually either *uniaxial*, measuring response in a single direction (typically normal to the surface), or *triaxial*, capable of capturing motion along three orthogonal axes. Furthermore, accelerometers vary in sensitivity, typically expressed in terms of electrical voltage per unit of acceleration (mV/g). Choosing an accelerometer with insufficient sensitivity can lead to inaccurate measurements, as it may fail to capture low-level vibrations or introduce noise, compromising the quality of the data. Prior to installing the accelerometer, its sensitivity should be checked and calibrated.

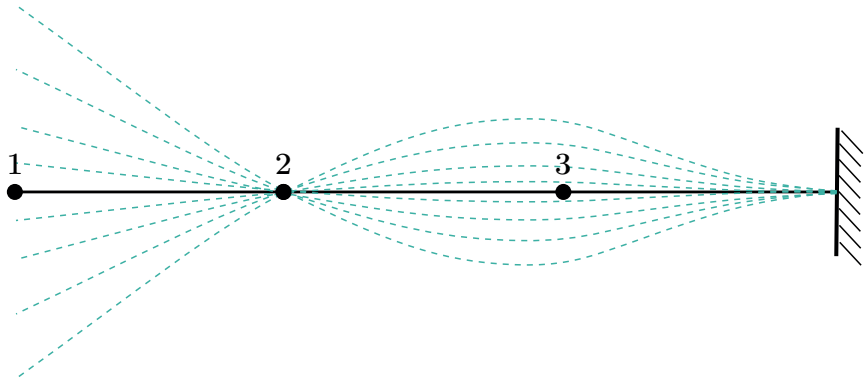

Figure 2.34: Node 2 lies on a nodal point of the second bending mode shape, where no vibration occurs. An accelerometer placed here would fail to register the mode.

2.5.2.3 Test procedures

Common test procedures used in impact testing include the *roving hammer* test, the *roving accelerometer* test, or a combination of both. The most widely adopted approach is the *roving hammer* method (Brandt, 2011). In this setup, one or more accelerometers are mounted at fixed reference points on the structure, as illustrated in Figure 2.32. The structure is then excited sequentially at different nodes using the impact hammer, while the corresponding responses are recorded at the reference accelerometers (Ewins, 2000).

2.5.3 Signal analysis and the Fourier transform

During experimental modal analysis, transducer signals are typically recorded over time, sampled at a specific sampling frequency. However, to extract meaningful dynamic information, it is often helpful to study these signals in the frequency-domain. The human ear, for example, is naturally tuned to detect specific frequencies and can isolate subtle sounds amidst background noise. Likewise, doctors rely on auditory cues in particular frequency ranges to diagnose irregularities in heart or lung function. In modal analysis, the aim is to understand how a structure responds to excitations applied at different frequencies, making frequency-domain analysis indispensable.

The transformation of signals from the time to the frequency-domain is made possible by the Fourier transform (FT). Much of the Fourier transform as it is known today was devised in the early 19$^{\text{th}}$ century. It is named after the French mathematician Jean-Baptiste Joseph Fourier (1768–1830), who in 1822 published his *Théorie analytique de la chaleur* ('The Analytical Theory of Heat'), demonstrating that any periodic function, whether continuous or discrete, can be represented as a sum of sinusoidal components—through a *Fourier series* (Cajori, 1893). The Fourier transform extends this concept to general, non-periodic functions.

The Fourier transform allows any signal to be decomposed into a continuous series (or integral) of sinusoidal components, described by individual amplitudes, phase shifts and frequencies. This decomposition is unique, meaning that only one combination of components exists that fully represents the signal (Hewlett-Packard Company, 1989). Figure 2.35 illustrates this decomposition in a three-dimensional plot with axes representing *amplitude*, *time*, and *frequency*. Viewed in the *time–amplitude plane* (i.e., the time-domain), the original signal is visible. Viewed in the *frequency–amplitude plane* (i.e., the frequency-domain), each sinusoidal component appears as a straight line positioned according to its frequency. This is important; no information is lost nor gained when transitioning to the frequency-domain. The three-dimensional representation remains intact, but is simply viewed from another perspective.

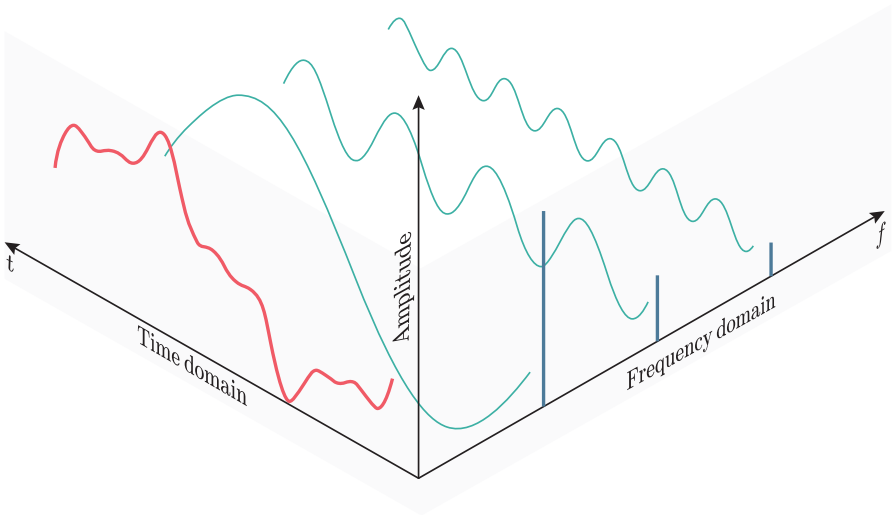

Figure 2.35: Signal in the time-domain (red) decomposed into sinusoidal components (turquoise) using Fourier transformation. The frequency and amplitude of each sinusoidal component can easily be distinguished in the frequency-domain (blue).

In the case of discrete signals, the Fourier transform is expressed as a finite sum of sinusoidal components, known as the *discrete Fourier transform* (DFT), given by:

$$\hat{f}_k = \sum_{j=0}^{n-1} \mathrm{f}_j \mathrm{e}^{-i2\pi \frac{jk}{n}}, \quad k = 0, 1, \ldots, n-1. \tag{2.43}$$

To understand this equation, consider the discrete signal displayed in Figure 2.36. It consists of n samples, each assigned an index j, where $0 \leq j \leq n-1$. Each sample has a function value f_j. The DFT projects these samples onto a set of orthogonal basis functions, i.e., complex exponentials of different frequencies. The result, $\hat{f}_k$, represents the contribution of the k^{th} frequency component in the signal. In other words, $\hat{f}_k$ indicates the amplitude and phase of the sinusoidal component associated with the k^{th} frequency.

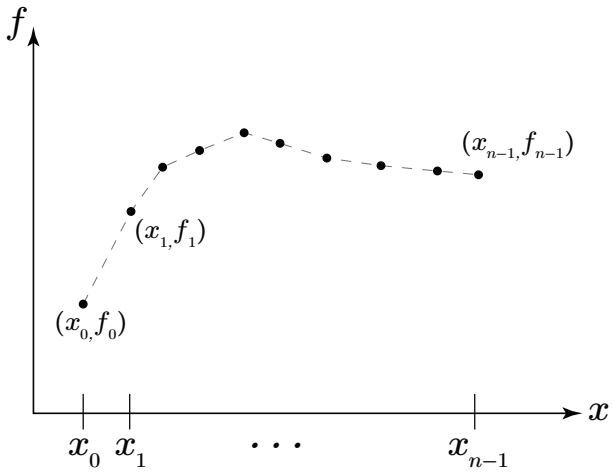

Figure 2.36: Example of discrete signal with n samples.

Equation (2.43) can alternatively be written in matrix format:

$$\hat{\mathbf{f}} = \underline{\mathbf{F}}\mathbf{f}, \tag{2.44}$$

where

$$\hat{\mathbf{f}} = \begin{bmatrix} \hat{f}_0 \\ \hat{f}_1 \\ \vdots \\ \hat{f}_{n-1} \end{bmatrix}, \quad \mathbf{f} = \begin{bmatrix} f_0 \\ f_1 \\ \vdots \\ f_{n-1} \end{bmatrix}, \quad \underline{\mathbf{F}} = \begin{bmatrix} 1 & 1 & 1 & \cdots & 1 \\ 1 & \omega & \omega^2 & \cdots & \omega^{n-1} \\ 1 & \omega^2 & \omega^4 & \cdots & \omega^{2(n-1)} \\ \vdots & \vdots & \vdots & \ddots & \vdots \\ 1 & \omega^{n-1} & \omega^{2(n-1)} & \cdots & \omega^{(n-1)(n-1)} \end{bmatrix}, \tag{2.45}$$

and $\omega = \mathrm{e}^{-i2\pi/n}$ is the primitive n^{th} root of unity.

It becomes immediately clear that for large data sets with many samples, the matrix multiplication involved in computing the DFT is computationally expensive. Specifically, the direct computation requires $\mathcal{O}(n^2)$ operations. The *fast Fourier transform* (FFT) is an algorithm that reduces this complexity to $\mathcal{O}(n \log n)$. It was popularised in 1965 by James Cooley and John Tukey (Dongarra & Sullivan, 2000), and is now a standard feature in virtually all software packages used to compute DFTs.

2.5.4 Signal processing

Signal processing plays an important role in acquiring high-quality data during the EMA. It is typically performed within the provided *data acquisition* (DAQ) system and can be divided into three key stages, outlined in the following subsections:

- **Section 2.5.4.1** — Pre-processing of transducer signals.
- **Section 2.5.4.2** — Application of the DFT to convert signals into the frequency-domain.
- **Section 2.5.4.3** — Evaluation of the processed data to assess its quality and reliability.

2.5.4.1 Pre-processing of transducer signals

Before extracting frequency response functions, the raw time-domain signals must be processed to ensure that they are suitable for frequency-domain analysis. This pre-processing step is particularly important in impact testing, where the accuracy of the computed FRFs depends on the quality of the measured data. Several key aspects of signal conditioning should be considered, including:

Leakage and windowing

The DFT assumes that the signal decays to zero at the boundaries of the sampling window. When this condition is not met, *spectral leakage* can occur, causing artificial spreading of energy across frequencies. This effect is mitigated by applying a *window function*, which tapers the signal smoothly to zero at the beginning and end of the sampling interval, thereby reducing edge discontinuities (Brandt, 2011).

In impact testing, spectral leakage may arise when the system's response does not fully decay within the duration of the measurement. This issue is particularly pronounced in lightly damped structures, where vibrations persist over a longer period. To address this, an *exponential window* is often employed to enforce artificial decay, thereby improving the signal's suitability for frequency-domain analysis (Schwartz & Richardson, 1999).

Aliasing

Aliasing refers to the distortion that occurs when a signal is sampled too slowly to accurately capture its high-frequency components, as illustrated in Figure 2.37. According to the *Nyquist theorem*, a signal must be sampled at a rate greater than twice the highest frequency component f_{max} of the signal, that is, $f_s > 2f_{\text{max}}$ (Craig & Kurdila, 2011). Otherwise, higher frequencies are aliased as lower ones, resulting in misleading data.

To reduce the risk of aliasing, an analogue *anti-aliasing filter* is commonly applied prior to sampling. This filter suppresses frequency components above a certain cut-off threshold, ensuring that only frequencies within the measurable range are retained.

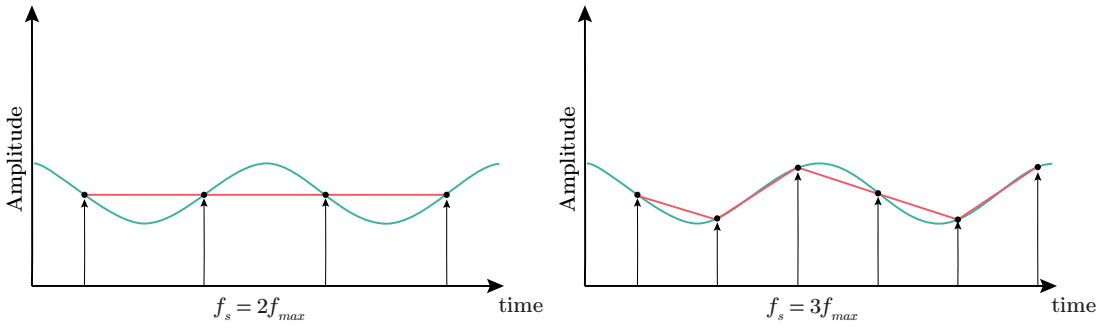

Figure 2.37: Plot showing a recorded signal (green curve) and the sampled signal (red curve) at $f_s = 2f_{max}$ (left) and $f_s = 3f_{max}$ (right). When the sampling rate is too low, as in the left plot, aliasing occurs, resulting in a misleading representation of the original signal. Illustration adopted from Hewlett-Packard Company (1989).

Impact noise and force windowing

External noise can significantly influence the recorded signals during impact testing. A common approach for minimising this influence is *force windowing*, where the signal is truncated shortly after the initial impulse. This ensures that the analysis focuses on the relevant excitation while excluding trailing noise (Craig & Kurdila, 2011; Ewins, 2000).

Averaging

Averaging multiple measurements helps reduce random noise and improve the signal-to-noise ratio. In impact testing, this involves repeating the excitation at the same point and averaging the resulting signals. This process enhances data reliability and provides a basis for evaluating the linearity of the system's dynamic response (Ewins, 2000). Coherence functions (see Section 2.5.4.3) are often used to assess the quality of averaged data.

2.5.4.2 Frequency-domain transformation

The fast Fourier transform of the transducer signals is typically performed automatically within the data acquisition system. To compute frequency response functions, it is recommended to use a *transfer function estimator* (Craig & Kurdila, 2011). The two most commonly used estimators are the H_1 and H_2 estimators. The H_1 estimator helps minimise the effect of noise in the output signal. It is defined as

$$H_1(\omega) = \frac{G_{FX}(\omega)}{G_{FF}(\omega)},$$

where $H_1(\omega)$ is the estimated frequency response function, $G_{FX}(\omega)$ is the *averaged cross-power spectrum* between the input signal F and the output signal X, and $G_{FF}(\omega)$ is the *averaged auto-power spectrum* of the input signal F.

The cross-power spectrum describes the correlation between the input and output signals, indicating how much energy is shared at each frequency. In contrast, the auto-power spectrum reflects the energy content of the input signal alone (Craig & Kurdila, 2011). If the cross-power is much lower than the auto-power, it suggests that noise (which is uncorrelated with the excitation) is present in the response output. In impact testing, the excitation signal is usually well-defined and repeatable, while noise is more likely to occur in the measured response. Under such conditions, the H_1 estimator is generally preferred, as it effectively reduces the influence of output noise (Craig & Kurdila, 2011).

2.5.4.3 Analysing data

The quality of the computed transfer functions should be evaluated prior to extracting modal parameters. This evaluation can be performed using different functions and indicators, such as:

Coherence

In Section 2.5.4.2, the concept of averaging was introduced as a method to improve signal quality. One effective way to evaluate the reliability of the averaged data is by examining the *coherence function*. The coherence function quantifies the degree of linear correlation between the input and output signals under the assumption of a linear and time-invariant system. It is defined over the frequency-domain and should ideally approach unity within the frequency range where resonance occurs. Values significantly lower than 1.0 may indicate the presence of random noise, inadequate excitation energy, or non-linearities in the system response (Døssing, 1988).

Mode indicator function (MIF)

Different *mode indicator functions* (MIFs) are used to identify the number of modes present in the test data. Since not all modes are easily distinguishable in FRF plots, the application of MIFs improves the ability to detect and differentiate between them. One of the most widely used MIFs is the *complex mode indicator function* (CMIF), which is based on the *singular value decomposition* (SVD) of the FRF matrix. Peaks in the CMIF plot correspond to the system's resonance frequencies (Ewins, 2000).

Mode complexity factor (MCF)

The damping behaviour of a structure can be classified as either *proportional* or *non-*

proportional. In the case of proportional damping, the damping matrix is a linear combination of the mass and stiffness matrices, resulting in real-valued mode shapes—as described in Section 2.4.2. All degrees of freedom in a given mode then reach their maximum response simultaneously, with phase differences of either *0°* or *180°*.

However, real structures often exhibit non-proportional damping, where the damping cannot be fully described by the mass and stiffness matrices. This leads to complex-valued mode shapes, introducing phase differences between different degrees of freedom. As a result, not all parts of the structure exhibit synchronised vibration, and nodal lines are no longer stationary (Hewlett-Packard Company, 1986). The complexity of a given mode can be assessed using the *mode complexity factor* (MCF). A high MCF (~ 1) may indicate non-proportional damping, but it can also result from measurement errors or noise. For lightly damped structures, the MCF is generally expected to be low (~ 0) (Hewlett-Packard Company, 1986).

2.5.5 Modal parameter extraction and curve fitting

After the transducer signals have been processed and evaluated, it is of interest to fit the modal model to the obtained FRFs and to extract the corresponding modal parameters.

During a roving hammer test, the structure is excited in n different locations. For each hit, the response is measured in m accelerometers, giving a total of $n \cdot m$ FRF functions. According to the principle of superposition for linear systems, each FRF contributes to the overall dynamic behaviour of the structure. By combining multiple FRFs, one can derive the complete system response and subsequently extract the relevant modal parameters. This is commonly addressed through curve fitting techniques, which can be classified into three categories: *SDOF approaches*, *MDOF approaches*, and *global approaches*.

The SDOF curve fitting approaches are the simplest, examinating one resonance peak on the FRF at a time (Ewins, 2000). They rely on the assumption that modes are sufficiently spaced in frequency, so that the influence of nearby modes is negligible. This simplifies the system into separate, single-mode responses. When modes are closely spaced or damping is high, this assumption no longer holds true, making the SDOF methods less accurate. In these situations, MDOF or global methods should be used. SDOF techniques like *peak picking* and *circle fitting* may nevertheless remain useful. They offer quick estimates of modal parameters and help assess the quality of test data. Further details on SDOF curve fitting approaches can be found in Ewins (2000).

MDOF and global methods simultaneously analyse multiple modes across one or more FRFs, offering a more comprehensive and efficient means of extracting modal parameters (Ewins, 2000). A widely used global curve fitting technique is the *least squares complex frequency* (LSCF) method. It estimates system poles (damped natural frequencies and damping ratios) by fitting the mathematical transfer function model to the measured FRFs using a least squares approach in the frequency domain. The fitting is performed incrementally for increasing *model orders* (also referred to as *modal complexity*), meaning that progressively more modes are included in the model.

To distinguish physical modes from spurious ones, a stabilisation chart is employed. This chart plots the estimated poles for successive model orders, with frequency on the horizontal axis and model order on the vertical axis. Physically meaningful poles,

known as *stable poles*, remain consistent across multiple model orders, showing little variation in both frequency and damping. In contrast, *mathematical poles*, which typically result from noise or numerical artefacts, tend to shift erratically with model order and do not stabilise.

An example of a stabilisation chart is presented in Figure 2.38. In this chart, stability criteria have been applied (e.g., less than 1% variation in frequency and less than 5% in damping) to distinguish stable poles (marked green) from unstable ones (marked with a red cross).

The theoretical foundation of the LSCF algorithm, along with its advantages over for example the *least squares complex exponential* (LSCE) method, is discussed in Guillaume et al. (2003).

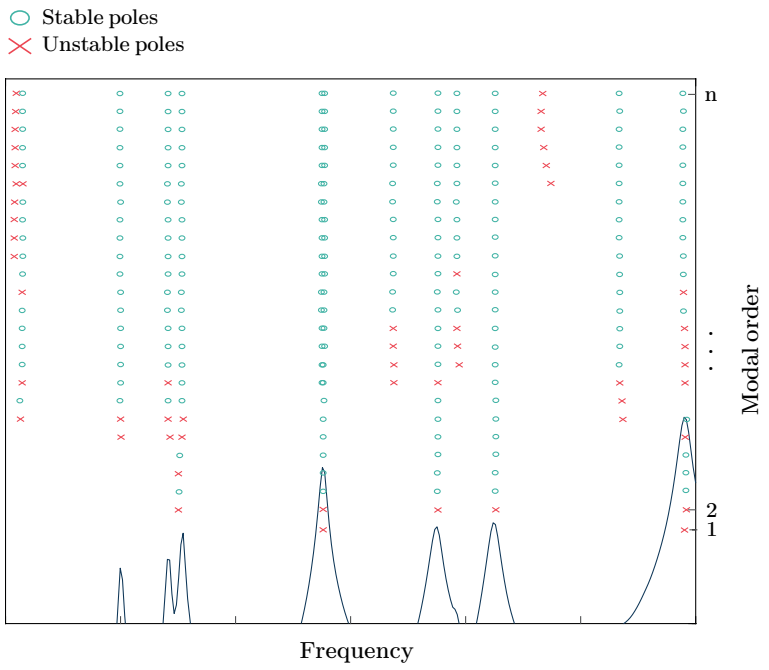

Figure 2.38: Global curve fitters often produce a stabilisation chart similar to the one shown in this figure. A stabilisation chart indicates where and for what modal order stable poles are observed (green circles). It may also be used to see which poles are physical or mathematical (Guillaume et al., 2003).

2.5.6 Comparing numerical and experimental analysis

Various correlation techniques can be applied to compare the experimentally obtained modal parameters with those obtained from numerical simulations. One of the most widely used is the *modal assurance criteria* (MAC), which compares the set of eigenvectors obtained from testing and simulation. In addition, techniques such as the *coordinate modal assurance criteria* (COMAC) can be employed to detect experimental issues, including loose or misaligned accelerometers (Abrahamsson, 2019).

The outcome of such comparisons is used to validate the numerical models. If the results fall within acceptable limits based on the selected correlation method, the model is said to be *verified*. Conversely, if the correlation is unsatisfactory, the model is said to

be *falsified*. Falsified models require calibration, a process that, alongside the modal assurance criteria (MAC), will be discussed in further detail in the following subsections.

2.5.6.1 Modal assurance criteria

The modal assurance criteria (MAC) is based on an eigenvector comparison between numerical and experimental models. The eigenvectors obtained from EMA, ϕ_X, represent the relative displacement of each excited node. Since a finite element model typically includes more nodes than the experimental point cloud, a direct comparison is not always feasible. To ensure a valid comparison, only the eigenvector components corresponding to the experimentally measured degrees of freedom should be extracted from the FE results. These reduced numerical mode shapes are denoted as ϕ_A.

The MAC evaluates the degree of linear correlation between the numerical and experimental eigenvectors, independent of their magnitudes. The comparison of mode pairs is performed using the following equation:

$$\mathrm{MAC}(i,j) = \frac{\left(\phi_{iX}\phi_{jA}\right)^2}{||\phi_{iX}||_2^2||\phi_{jA}||_2^2}. \tag{2.46}$$

A MAC value close to unity indicates a strong correlation, while a value near zero suggests orthogonality and bad correlation. The diagonal elements of the MAC matrix, representing direct mode comparisons, should ideally be close to unity, while off-diagonal elements should be close to zero (Abrahamsson, 2019).

2.5.6.2 Model calibration

If a model is found to be falsified, a calibration process is typically initiated. This is often necessary, as it is uncommon for a numerical model to accurately replicate experimental results when using nominal parameter values alone.

Calibration involves adjusting selected parameters in the numerical model within predefined bounds to improve the agreement between simulation and test results. The core principle is to evaluate a deviation metric that quantifies how the numerical model's output changes in response to parameter variations. The goal is to identify a parameter set that minimises this deviation in a specified search direction (Abrahamsson, 2019).

2.6 Numerical methods for analysing HP elements

The shell and beam theories established for assessing the structural response of HP elements are governed by differential equations. To obtain closed-form solutions, several simplifications were introduced, including assumptions of constant stiffness, uniformly distributed loads, linear elastic material behaviour, and idealised geometry and boundary conditions. While these assumptions allow for analytical treatment, more accurate models may need to account for varying stiffness, complex loading, material nonlinearity, and detailed boundary conditions.

Such detailed models often result in differential equations that are too intricate to solve analytically. To address this, numerical methods have been developed to approximate solutions by discretising the governing equations. The rise of computational power has further enabled the practical analysis of complex structures. Among the various numerical techniques available, the *finite element method* (FEM) is the most widely used approach for solving structural differential equations (Adiels, 2024). This section introduces the fundamental concepts of FEM and demonstrates how it can be used for static assessments and modal analysis of HP elements. Additionally, the challenges and methodologies associated with modelling reinforced concrete in finite element software are discussed.

2.6.1 Finite element method

In the context of differential equations, the unknown variable is a function that possesses infinitely many degrees of freedom, even within a bounded domain. When solving such equations computationally, a direct approach is infeasible since an infinite number of unknowns cannot be handled numerically. The finite element method (FEM) addresses this issue by approximating the function at a discrete set of points, known as *nodes*, within a defined domain. The region between nodes is divided into *elements* of finite size, collectively forming a *mesh*. The behaviour of the function between nodes is approximated using predefined functions, called *shape functions*. These shape functions can be linear, yielding a piecewise linear solution, or may involve higher-order polynomials. Since the shape functions are predetermined, knowing the function's values at the nodes is sufficient to reconstruct its approximate values throughout the domain. This transformation from an infinite to a finite set of unknowns is called *discretisation*, which inherently introduces an approximation error known as a *discretisation error*. It is generally observed that increasing the number of nodes reduces this error, and the solution is said to *convergence* (Ottosen & Petersson, 1992).

The modern formulation of FEM was pioneered in the aerospace industry during World War II, notably through the contributions of John Argyris (Adiels, 2024). The method was subsequently refined by Turner et al. at Boeing in the 1950s and was formally named by Ray William Clough in 1960 in his paper *The Finite Element Method in Plane Stress Analysis*.

According to Ottosen and Petersson (1992), the standard formulation of the finite element method can be divided into four fundamental steps:

1. Establish the strong formulation of the problem.

2. Transform the strong formulation into a weak formulation.

3. Make an element-wise approximation over the entire domain of the unknown function that is to be solved for.

4. Choose weight functions (in accordance with the Galerkin method).

The strong form of the differential equation governing the three-dimensional mechanical equilibrium of an elastic body was given in Equation (2.3). In index notation, it can be written as:

$$-\frac{\partial \sigma_{ij}}{\partial x_j} = f_i \tag{2.47}$$

The weak form is derived by applying the Green–Gauss theorem and introducing a virtual displacement δu_i and the corresponding virtual strain $\delta \epsilon_{ij}$. Utilising the symmetry of the stress tensor, the weak form takes the following expression:

$$\int_V \sigma_{ij}\, \delta\epsilon_{ij}\, \mathrm{d}V = \int_V f_i\, \delta u_i\, \mathrm{d}V + \int_S t_i\, \delta u_i \mathrm{d}S, \tag{2.48}$$

where V and S is the volume and surface area of the body, respectively, and t_i is the traction vector, defined via the Cauchy stress theorem: $t_i = \sigma_{ij} n_j$ (Ottosen & Petersson, 1992). This expression is equivalent to Equation (16.12) in Ottosen and Petersson (1992), where a 'weight vector' $\mathbf{v}$ is used instead of the virtual displacement. Disregarding higher order terms, the strain and its virtual counterpart can be expressed as:

$$\epsilon_{ij} = \frac{1}{2}\left(\frac{\partial(u_i)}{\partial x_j} + \frac{\partial(u_j)}{\partial x_i}\right). \tag{2.49}$$

Boundary conditions may be defined either by prescribing displacements, $u_i = g_i$, along S_g, referred to as *essential boundary conditions* or *Dirichlet boundary conditions*; or by prescribing tractions, $t_i = h_i$, along S_h, known as *natural boundary conditions* or *Neumann boundary conditions* (see Figure 2.39a).

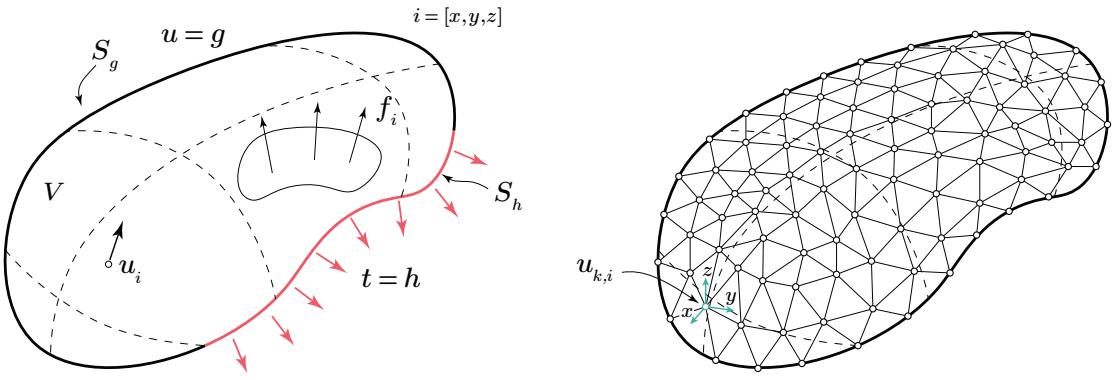

a) b)

Figure 2.39: Three-dimensional elastic body. a) Equilibrium configuration with prescribed displacement along S_g and prescribed traction along S_h, subjected to the body force f_i. b) Mesh discretisation.

The unknown displacement field u_i should be determined such that Equation (2.48) is satisfied. Following step three, the body is discretized into a mesh containing n nodes and m elements, as seen in Figure 2.39b. An ansatz is made, assuming that the displacement solution u_i can be approximated ($u_i \approxeq \tilde{u}_i$) as the sum of predefined shape functions $N^k(x, y, z)$ multiplied by unknown constants a_i^k, where the subscript i represents the vector basis $i = [x\,, y\,, z]$, and the superscript k denotes the node number ($1 \leq k \leq n$). For a more convenient notation, a matrix form may be used, giving

$$\tilde{\mathbf{u}} = \begin{bmatrix} \tilde{u}_x^1 \\ \tilde{u}_y^1 \\ \tilde{u}_z^1 \\ \vdots \\ \tilde{u}_z^n \end{bmatrix} \triangleq \sum_{k=1}^{n} N^k(x, y, z)\, a_i^k = \underline{\mathbf{N}}\boldsymbol{a}, \tag{2.50}$$

$$\underline{\mathbf{N}} = \begin{bmatrix} N^1 & 0 & 0 & \dots & N^n & 0 & 0 \\ 0 & N^1 & 0 & \dots & 0 & N^n & 0 \\ 0 & 0 & N^1 & \dots & 0 & 0 & N^n \end{bmatrix}, \quad \boldsymbol{a} = \begin{bmatrix} a_x^1 \\ a_y^1 \\ a_z^1 \\ \vdots \\ a_z^n \end{bmatrix}.$$

It follows that the strain ϵ can be approximated as:

$$\tilde{\boldsymbol{\epsilon}} = \underline{\tilde{\boldsymbol{\nabla}}}\tilde{\mathbf{u}}, \quad \text{with} \quad \underline{\tilde{\boldsymbol{\nabla}}} = \begin{bmatrix} \partial/\partial x & 0 & 0 \\ 0 & \partial/\partial y & 0 \\ 0 & 0 & \partial/\partial z \\ \partial/\partial y & \partial/\partial x & 0 \\ 0 & \partial/\partial z & \partial/\partial y \\ \partial/\partial z & 0 & \partial/\partial x \end{bmatrix} \tag{2.51}$$

$$\implies \tilde{\boldsymbol{\epsilon}} = \underline{\tilde{\boldsymbol{\nabla}}}\,\underline{\mathbf{N}}\boldsymbol{a} = \underline{\mathbf{B}}\boldsymbol{a}$$

As per step four, Galerkin's method is applied, approximating the virtual displacements as the sum of the shape functions multiplied by arbitrary constants δc. That is $\delta\mathbf{u} = \underline{\mathbf{N}}\delta\mathbf{c}$ and $\delta\boldsymbol{\epsilon} = \underline{\mathbf{B}}\delta\mathbf{c}$. Inserting the approximations of the displacements $\tilde{\mathbf{u}}$, strains $\tilde{\boldsymbol{\epsilon}}$ and their virtual counterparts $\delta\mathbf{u}$ and $\delta\tilde{\boldsymbol{\epsilon}}$ into Equation (2.48), the finite element formulation can be expressed as:

$$\underbrace{\int_V \underline{\mathbf{B}}^{\mathrm{T}}\underline{\mathbf{D}}\,\underline{\mathbf{B}}\,\mathrm{d}V}_{\underline{\mathbf{K}}} \cdot \boldsymbol{a} = \underbrace{\int_V \underline{\mathbf{N}}^{\mathrm{T}}\mathbf{f}\,\mathrm{d}V}_{\mathbf{f}_\mathrm{l}} + \underbrace{\int_S \underline{\mathbf{N}}^{\mathrm{T}}\,\mathbf{t}\,\mathrm{d}S}_{\mathbf{f}_\mathrm{b}}, \tag{2.52}$$

or

$$\underline{\mathbf{K}}\boldsymbol{a} = \mathbf{f}_\mathrm{l} + \mathbf{f}_\mathrm{b}, \tag{2.53}$$

where a constitutive matrix $\underline{\mathbf{D}}$ has been introduced, assuming that the material responds elastically, such that $\boldsymbol{\sigma} = \underline{\mathbf{D}}\boldsymbol{\epsilon}$. Again, boundary conditions may be expressed as either a prescribed traction vector $\mathbf{t} = \mathbf{h}$ along S_h or a prescribed deformation vector $\mathbf{u} = \mathbf{g}$ along S_g, in accordance with Figure 2.39a.

Equation (2.53) forms the basis of the finite element method applied to three-dimensional elasticity problems. It involves a stiffness matrix $\underline{\mathbf{K}}$, derived from predefined shape functions and material properties. Under the assumption of linear elastic material behaviour, the stiffness matrix remains constant and can be computed once for the entire finite element mesh. However, if the material exhibits non-linear behaviour, the tangent stiffness becomes strain-dependent, meaning it varies with the material's load history. In such cases, a non-linear FE implementation is required, in which the stiffness matrix is updated at each incremental load step. Other problems such as contact problems or large deformation problems may also require non-linear FE implementations (Ottosen & Petersson, 1992).

The vector $\boldsymbol{a}$ contains unknown or prescribed parameters that, together with Equation (2.50), describe the nodal displacements throughout the mesh. The displacements may, for instance, be prescribed along boundaries where movement is restricted. Similarly, the vectors $\mathbf{f}_\mathrm{l}$ and $\mathbf{f}_\mathrm{b}$ represent the *body load vector* and *boundary load vector*, respectively. These vectors can either be prescribed, e.g. gravity load assigned to the body load, or unknown due to prescribed displacements. In the latter case the unknown forces are typically referred to as *reaction forces* (Ottosen & Petersson, 1992).

In its current form, Equation (2.53) constitutes a system of n linear equations that can be efficiently solved using computational resources. Given the prescribed boundary conditions, the objective is to solve for the remaining unknown displacements and/or reaction forces such that equilibrium is satisfied. If the displacement is prescribed at a node, the corresponding reaction force is unknown; conversely, if the external force is prescribed, the resulting displacement is unknown.

For an in-depth discussion of the theoretical foundations and practical implementation of the finite element method, the reader is referred to Ottosen and Petersson (1992).

2.6.2 Numerical modal analysis

The finite element method may also be employed to determine the natural frequencies and mode shapes of a structured. As discussed in Section 2.4.2, obtaining these parameters is equivalent to solving an eigenvalue problem of the form:

$$(\mu^2\underline{\mathbf{M}} + \mu\underline{\mathbf{V}} + \underline{\mathbf{K}})\boldsymbol{\phi} = 0, \tag{2.54}$$

where μ is the eigenvalue and $\boldsymbol{\phi}$ the eigenvector. The eigenvalue problem and its numerical approximation methods are classical topics of study, explored in, e.g., Wilkinson (1988). In general, this eigensystem will have complex eigenvalues and eigenvectors. However, if the damping matrix $\underline{\mathbf{V}}$ is neglected, and if $\underline{\mathbf{K}}$ and $\underline{\mathbf{M}}$ are assumed to be symmetric and positive semidefinite, the system will have only real eigenvalues and eigenvectors.

Numerical methods for solving eigenvalue problems are summarised in S. Ramaswamy

(1980). Most structural FEM models involve large, typically narrowly banded matrices. For such problems, the *Lanczos method* and the *subspace iteration method* are among the most effective approaches. The Lanczos method is particularly efficient when only a small subset of eigenvalues from a large system is needed (Bostic, 1994). Many FEM software packages also include *automatic multi-level substructuring* (AMS) eigensolvers, which can offer significant performance advantages over the more common Lanczos method; especially when a large number of eigenmodes is needed for systems with many degrees of freedom (Dassault Systèmes, 2015). Readers interested in a more detailed treatment of numerical eigensolvers are referred to Bostic (1994), Dassault Systèmes (2015), and S. Ramaswamy (1980).

2.6.3 Modelling of reinforced concrete

This section outlines key concepts in modelling the mechanical behaviour of reinforced concrete, the material used in the HP elements examined in this thesis.

Concrete is a heterogeneous material composed primarily of aggregates, cement, and water. It exhibits non-linear mechanical behaviour, with a compressive strength approximately ten times greater than its tensile strength. To compensate for this low tensile capacity, concrete is often reinforced with steel, enabling more efficient material utilisation. The presence of reinforcement adds complexity to the modelling of concrete structures. First, the structural stiffness varies depending on the reinforcement layout and the presence and distribution of cracks. Second, an appropriate modelling approach is necessary to accurately represent the composite interaction between the steel and the surrounding concrete (Plos et al., 2021).

Various approaches can be used to model reinforced concrete, depending on the objective and the required accuracy of the analysis. When assessing a structure under serviceability limit states (SLS), a linear elastic analysis is often sufficient. In such cases, sections are typically assumed to be either fully uncracked (State I) or cracked (State II), with reinforcement embedded into the continuum elements as additional stiffness. Only a few material parameters are needed to perform such analysis, including the modulus of elasticity E, Poisson's ratio ν, and density ρ. Depending on the cracking assumptions, the resulting stresses and deformations are typically overestimated or underestimated. For more accurate assessment of structural responses, such as deformations under serviceability loads or failure modes at the ultimate limit state (ULS), a non-linear material model is required. Such a model must incorporate parameters that describe the complete mechanical behaviour of the material up to failure. In addition, modelling the interaction between reinforcement and concrete may require an interface model, along with a suitable approach for simulating crack initiation and propagation (Plos et al., 2021).

This section outlines methods for modelling reinforced concrete in finite element software, structured into three main parts: the modelling of non-linear concrete material properties (Section 2.6.3.1), the modelling of interaction between steel reinforcement and concrete (Section 2.6.3.2), and the modelling of crack development (Section 2.6.3.3). Together, these topics form the basis for understanding how to accurately model the HP element when evaluating its dynamic and static behaviour numerically. For a more comprehensive discussion on the modelling of reinforced concrete structures, the reader is referred to Plos et al. (2021) and Hendriks et al. (2012).

2.6.3.1 Non-linear material behaviour

Concrete exhibits markedly different behaviour under tension and compression, with distinct failure envelopes for each load type. The strength and stiffness of concrete can also be highly sensitive to the rate at which loads are applied. The non-linear characteristics of concrete will be discussed further below.

Concrete in tension

Tensile failure in concrete typically occurs in two stages: *crack initiation*, followed by *crack propagation* (Hillerborg, 1985). Crack initiation can result from various factors such as temperature fluctuations, shrinkage, or mechanical loading. A crack begins to form when the maximum principal tensile stress at a point exceeds the material's tensile strength, and develops perpendicular to the direction of that principal stress (Hillerborg, 1985).

The models commonly used to describe the tensile behaviour of concrete originate from studies of crack formations under uniaxial tensile tests (Plos et al., 2021). Under uniaxial tensile loading, the tensile stress is nearly uniform across the specimen. As a result, the formation and location of larger macroscopic cracks are primarily governed by naturally occurring flaws, pores, and/or microcracks within the concrete.

Crack propagation is characterised by an increasing energy demand, primarily due to dissipative mechanisms near the crack tip, including heat generation and bond breakage (Hillerborg, 1985). These processes occur within a localised region known as the *fracture process zone* (FPZ). To visualise this, imagine tearing a piece of fabric. Initially, the tear progresses easily, but as it grows, the surrounding fibres begin to stretch and fray, requiring more energy to continue. A similar process occurs in concrete, where additional energy is required to drive crack propagation through the FPZ.

As the crack forms and opens, it continues to transfer stress between its faces through internal cohesive forces (Plos et al., 2021). This cohesive stress σ_{c} describes the concrete's softening behaviour and depends on the history of crack opening width w ($\sigma_{\mathrm{c}} \triangleq \sigma_{\mathrm{c}}(w)$). The stress gradually decreases as the crack widens, until the material fully separates. The total energy dissipated during the formation of a single crack is known as the fracture energy, denoted G_{F}, and is defined per unit area of the formed crack, obtained by integrating the area under the softening curve $\sigma_{\mathrm{c}}(w)$ (cf. Figure 2.40).

Figure 2.40 illustrates a typical stress–displacement curve obtained from a uniaxial tensile test of a concrete specimen. Two models may be used to describe the constitutive relationship between stress and displacement: first, a classical elastic stress–strain relation up to the point where microcracks coalesce and the tensile strength is reached; second, a cohesive stress–crack opening law (Plos et al., 2021). Material parameters such as tensile strength f_{ct} and fracture energy G_{F} can be determined through *wedge splitting tests* (WST), as further demonstrated in Section 3.2.3.3. In numerical analysis, the softening curve can be represented using either a bilinear or exponential function fitted to the WST data. More refined and experimentally validated softening models have been proposed, for example by Cornelissen et al. (1986).

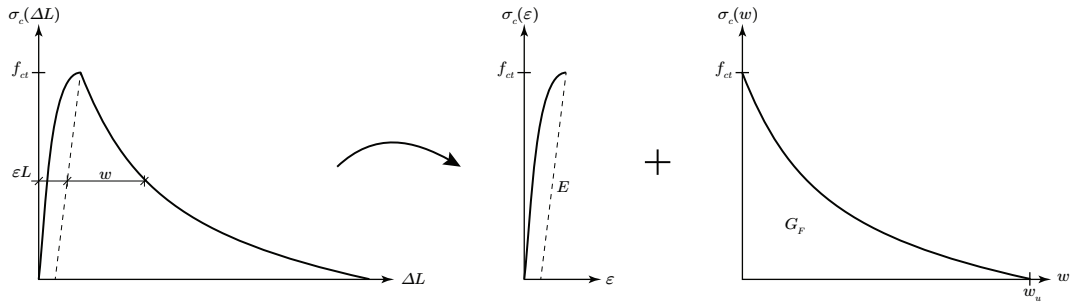

Figure 2.40: The constitutive relation between stress and displacement can be separated into a stress-strain relation and a stress-crack opening relation. The fracture energy G_{F} is defined as the area under the softening curve $\sigma_{\mathrm{c}}(w)$. Illustration adopted from Plos et al. (2021).

Naturally, cracks in a reinforced concrete member are spaced apart. The concrete between these cracks contributes to the overall stiffness of the structure, a phenomenon commonly referred to as *tension-stiffening*. The effect of tension-stiffening is illustrated in Figure 2.41. While its contribution to the structural capacity is minimal, its impact on stiffness can significantly influence the deformation of the structure, even under SLS conditions, as the structure may be partially cracked (Plos et al., 2021).

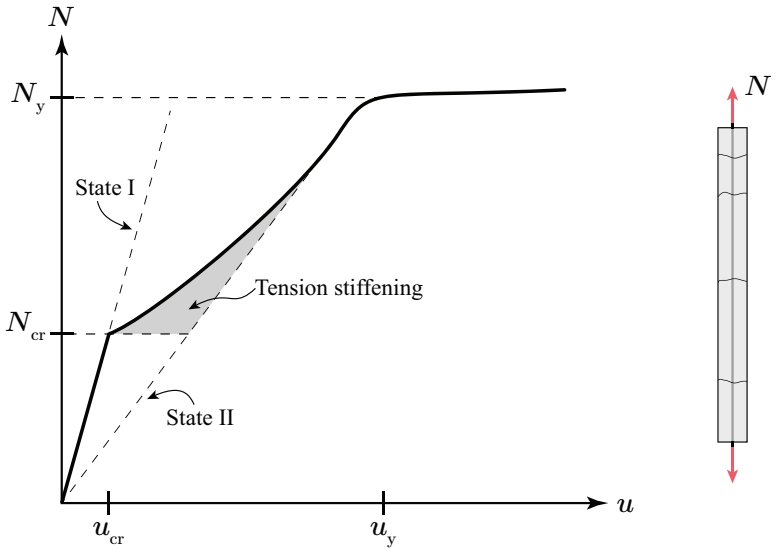

Figure 2.41: Tension stiffening effect in a reinforced concrete prism subjected to a tensile force N. The state I stiffness correspond to a fully uncracked member while state II correspond to a fully cracked member (i.e., all load is transferred through the reinforcement). Illustration adopted from Plos et al. (2021).

Concrete in compression

Softening behaviour can also be observed in compressive tests once the peak strength has been exceeded (Plos et al., 2021). Van, Mier (1984) demonstrated that compressive softening is inherently challenging to model, as the post-peak response is highly dependent on the specimen's geometry. Hendriks et al. (2012) suggest using parabolic

or linear stress–strain relationships regularised with a crushing band width h_{eq}, and a compressive fracture energy related to the tensile fracture energy. Conversely, Hendriks et al. (2012) discourage using models that merely impose a cap on compressive strength, such as elasto-plastic models, as they fail to capture post-peak strength degradation. If such models are employed, additional checks are necessary to ensure that compressive strains do not exceed the ultimate crushing strain, $\varepsilon_{\mathrm{cu2}}$, to avoid overestimating the structure's plastic deformation capacity. Furthermore, Hendriks et al. (2012) caution against using the Thorenfeldt et al. (1987) model, as it lacks regularisation via a crushing band width h_{eq}, leading to mesh size–dependent softening behaviour.

Concrete stiffness

The stiffness of concrete is highly dependent on the rate at which loading is applied, as illustrated in Figure 2.42. In numerical analysis of concrete structures, three different moduli of elasticity (MoE) are typically used: the *static modulus* E_{s}, the *dynamic modulus* E_{d}, and the *effective* or *sustained modulus* $E_{\mathrm{ef}}(t, t_i)$, which accounts for long-term creep effects. The static modulus is the most commonly specified and used stiffness value, and it may be determined through static load tests or calculated using empirical relations or tabulated values provided in the design code.

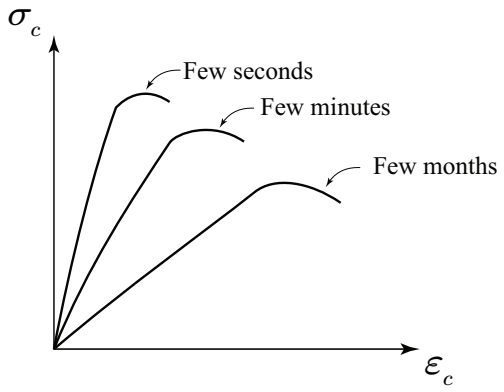

Figure 2.42: The stiffness (and strength) of concrete depends on the rate at which load is applied. Illustration adopted from Collins and Mitchell (1987).

The dynamic modulus E_{d} represents the ratio of stress to strain under vibratory conditions, such as seismic loading, and is generally greater than the static modulus. In practice, it is often approximated from the static modulus using empirical relations provided in design codes. For example, Zhu (2009) recommends taking E_{d} as 115% of E_{s}. Zhu (2009) also demonstrates that the choice of E_{d} significantly affects the eigenfrequencies and dynamic behaviour of the structure, and thus it should ideally be verified through experimental testing. The *resonant frequency method*, specified in ASTM C215, and the *ultrasonic pulse velocity* (UPV) method, as discussed in Prassianakis (2004), are two commonly used non-destructive testing methods. The *impact-echo method*, as outlined by Lu et al. (2013), may also be used.

2.6.3.2 Interaction between concrete and reinforcement

The material response of steel reinforcement is generally well represented by a uniaxial elasto-plastic material model that incorporates hardening behaviour (Hendriks et al.,

2012; Plos et al., 2021). Initially, the steel behaves elastically until its yield strength f_{sy} is reached. Beyond yielding, it continues to deform plastically while maintaining a degree of stiffness, allowing it to carry additional load until failure.

When embedded in concrete, steel reinforcement engages in interaction phenomena that are critical to the composite performance of reinforced concrete structures. The stresses that arise during deformation are primarily transferred through the mechanical interlock and contact forces between the steel and the surrounding concrete. Tepfers (1973) analysed this interaction and demonstrated that for ribbed reinforcement, load transfer is facilitated not only by shear stresses but also by normal forces acting along the interface, as shown in Figure 2.43.

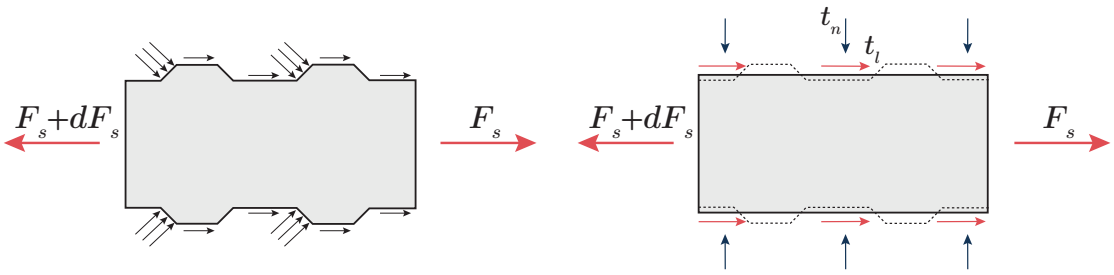

Figure 2.43: Contact stresses on embedded reinforcement (left), and forces represented as traction components on the mean contact surface (right). Illustration adopted from Plos (2000).

The perhaps simplest approach to model the interaction between steel reinforcement and concrete is the *embedded reinforcement model*. In this method, the reinforcement is not represented explicitly with individual degrees of freedom. Instead, it is 'embedded' into existing continuum elements, contributing additional stiffness in the reinforcement's primary direction. Consequently, the reinforcement stresses are computed based on the deformation of the surrounding concrete. While this approach is straightforward to implement, it relies on simplifying assumptions that may affect the accuracy of the results. Most notably, it assumes a *perfect bond* between concrete and steel, i.e., no relative slip occurs between the two materials.

Using embedded reinforcement is often sufficient and simplifies the assembly of the FE model (Plos et al., 2021). However, when anchorage is considered critical or when detailed crack patterns are of particular interest, it may be advantageous to include an explicit interaction model. In such cases, the reinforcement can be modelled using truss or beam elements in combination with a bond-slip material law. A widely used bond-slip model is provided in the CEB fib Model Code (2010), which describes the slipping behaviour through four distinct stages, illustrated in Figure 2.44.

In the first stage, the bond stress increases according to a power function up to the maximum bond stress τ_{max} at a relative slip s_1. In the second stage, the bond stress remains constant at τ_{max} until a slip of s_2 is reached, during which crack opening dominates the behaviour. The third stage is characterised by a linear decrease in bond stress down to a residual value τ_{f} at slip s_3, due to concrete crushing and rib shearing. Finally, for $s > s_3$, the bond stress remains constant at τ_{f}, representing a remaining frictional resistance (DIANA FEA, 2025).

It is important to note that this bond-slip relationship assumes a ductile slipping failure. However, if the concrete is not sufficiently confined, a splitting failure may occur instead. This is a more brittle failure mode, where the concrete cracks along the reinforcement, leading to a sudden loss of bond capacity. The risk of splitting failure should therefore be assessed and ruled out before adopting a slipping failure model (CEB fib Model Code, 2010).

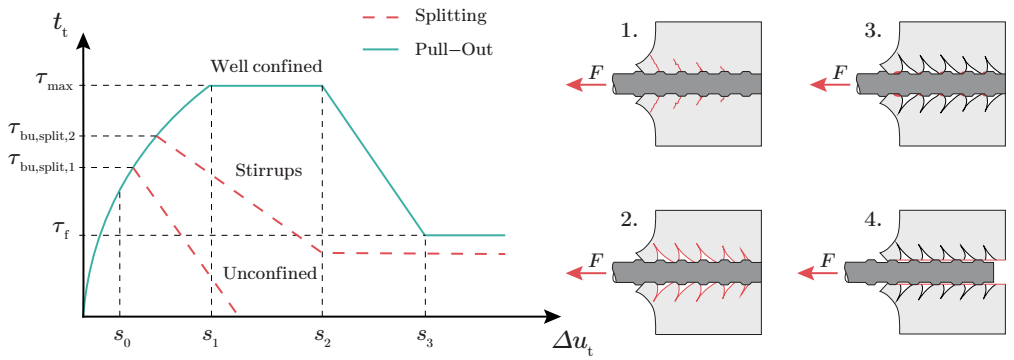

Figure 2.44: Left: Bond-slip back bone curve from the CEB fib Model Code (2010), showing bond stress τ versus slip Δu. The green curve illustrates a ductile slipping failure. The red dashed lines represent the splitting failure of unconfined or moderately confined concrete. $\tau_{\text{bu,split},1}$ and $\tau_{\text{bu,split},2}$ indicate reduced bond capacities due to splitting failure. Stirrups help confine the concrete and provide some residual ductility. Right: illustration of the four slipping stages. Adopted from CEB fib Model Code (2010).

2.6.3.3 Modelling of cracks

Numerous approaches can be employed to model cracked concrete, each offering distinct advantages and limitations. Three commonly used methods include the *discrete crack*, *smeared crack*, and *embedded crack* approaches, as illustrated in Figure 2.45.

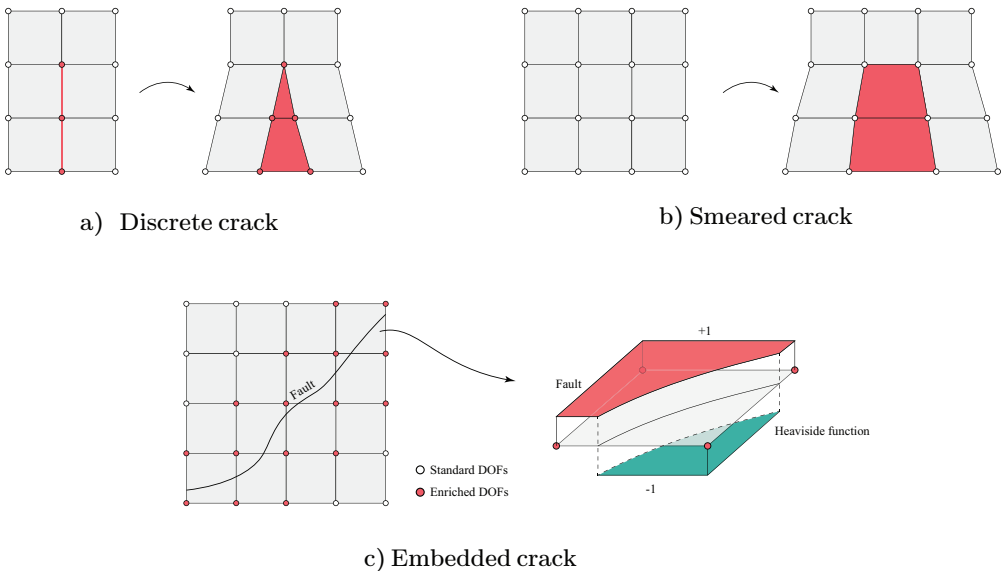

Figure 2.45: Three common crack modelling approaches in FEM.

The smeared crack approach is the most widely available and used method in FE software (Plos et al., 2021). The method does not require any implementation of specific interface elements. Instead, crack discontinuities are 'smeared' across the continuum elements, meaning that the deformation associated with cracking is distributed over the entire element. Consequently, the smeared crack approach does not require prior knowledge of potential crack locations, as is necessary in the other two methods where interface elements or enriched nodes are strategically placed at anticipated crack sites. Cracks can form as soon as the tensile capacity is exceeded at any integration point within the mesh. Thusly, the crack pattern emerges directly from the analysis (Plos et al., 2021). After initiation of a crack in a continuum element, its material response is governed by the specified softening curve (see discussion in Section 2.6.3.1).

On the other hand, the smeared crack approach requires knowledge of the *crack band width*, denoted l_{cr} (Plos et al., 2021). In essence, numerical analysis describes the structural response using strains and stresses, whereas the cohesive law for tensile softening is expressed in terms of a stress-crack width relation, $\sigma\mathrm{c} \triangleq \sigma\mathrm{c}(w)$. At a certain crack width, w_{u}, the two faces of the crack are fully separated and the stress drops to zero. This width corresponds to an *ultimate crack strain*, $\varepsilon_{\mathrm{u,cr}}$, which must be smeared over a finite distance, i.e., the crack band width, l_{cr}. It can be expressed as:

$$\varepsilon_{\mathrm{u,cr}} = \frac{w_{\mathrm{u}}}{l_{\mathrm{cr}}} \propto \frac{G_{\mathrm{F}}}{f_{\mathrm{ct}}\, l_{\mathrm{cr}}}.$$

Thus, to determine $\varepsilon_{\mathrm{u,cr}}$, the crack band width l_{cr}, fracture energy G_{F}, and tensile strength f_{ct} must all be specified. Some finite element software provide automated procedures for determining the crack band width based on the crack orientation. Hendriks et al. (2012) recommend this automated procedure. In the absence of such features, alternative guidance is available in, for example, Plos et al. (2021). According to Plos et al. (2021), if l_{cr} is chosen too small, the response may become 'too brittle'; if it is set equal to the element size of the mesh, the response may become 'too ductile'. Therefore, a sensitivity analysis is recommended. If variations in l_{cr} have minimal effect on the structural response, the analysis can be considered reliable (Plos et al., 2021).

The smeared crack approach can be implemented using various material models, each of which handles the position and orientation of cracks differently. Models reported in the literature include *fixed crack models*, *multi-directional crack models*, *rotating crack models* (see Figure 2.46), as well as various plasticity-based formulations (Plos et al., 2021).

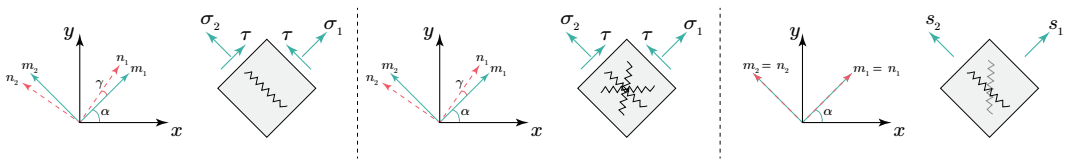

a) Fixed crack model b) Multi-directional crack model c) Rotating crack model

Figure 2.46: Three common material models used in the smeared crack approach.

In a fixed crack model, once a crack initiates, its orientation is permanently aligned perpendicular to the maximum principal tensile stress at the time of initiation. As loading continues and the principal stress directions change, the crack does not reorient, leading to the development of shear stresses along the crack plane. Multi-directional crack models maintain the fixed orientation of existing cracks but introduce the possibility of new cracks forming if the principal stress direction changes beyond a specified threshold. This allows the model to capture more complex crack patterns, while still keeping the assumption of fixed orientations for individual cracks. In contrast, a rotating crack model allows the crack orientation to continuously follow the current principal stress directions, effectively eliminating shear stress along the crack. This approach is particularly useful in situations where the stress field evolves significantly over time, as it provides a more accurate representation of the material's response (Plos et al., 2021).

3 Analysis of HP prototype element

This chapter presents the static and dynamic assessment of the steel-reinforced HP prototype element, shown in Figure 3.1. It documents the process from initial design to experimental testing and numerical validation of the prototype element. The chapter is structured into four main sections:

- **Section 3.1** — Design and fabrication
- **Section 3.2** — Post-fabrication assessment
- **Section 3.3** — Modal analysis
- **Section 3.4** — Static analysis

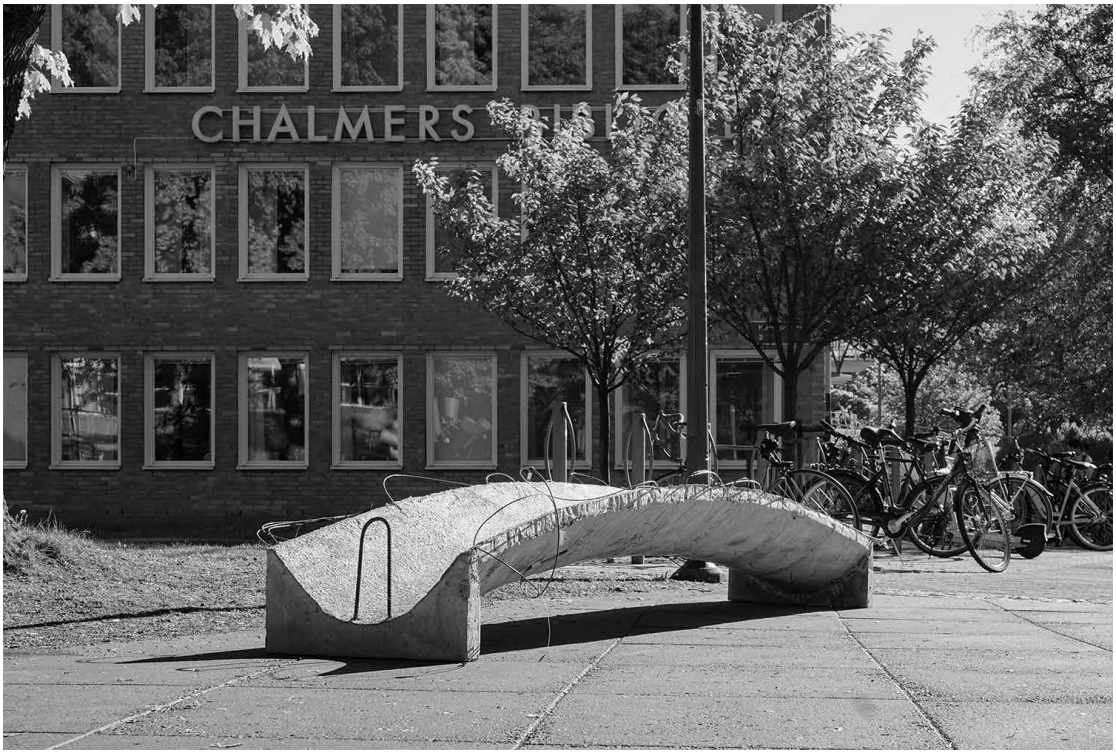

Figure 3.1: Photograph of HP prototype element.

3.1 Design and fabrication

This section outlines the design of the prototype element and provides an overview of the fabrication process. The design and fabrication of the prototype element were carried out prior to the start of the thesis through a collaboration between Chalmers University of Technology, WSP, and NCC.

3.1.1 Design

The prototype element, along with its production drawings, was designed by Alexander Sehlström at WSP. Its design was based on the work of Arlinger (2023), intended to support its self-weight in addition to a uniformly distributed load of $q_k = 2.5$ kN/m^2,

defined on a horizontal plane and projected onto the top surface. The geometry was developed in Grasshopper 3D and exported to Tekla Structures for the preparation of production drawings.

The middle surface of the element conforms to a hyperbolic paraboloid surface parametrised as shown in Figure 3.2, with $\ell = 3$ m, $w = 0.6$ m, and $r = 0.2$ m. Alternatively, using the parametrisation in Equation (2.2), the curvature factors are given as $h_1 = 11.25$ and $h_2 = 0.45$, with $-0.3 \leq y \leq 0.3$ and $-1.5 \leq x \leq 1.5$.

The element has a thickness of 45 mm, including a 10 mm nominal concrete cover. It is reinforced with straight steel reinforcement with end hooks at an approximate distance of 60 mm, complemented with stirrups in the transverse direction at a spacing of 150 mm, as illustrated in Figure 3.3. Additional edge reinforcement is positioned along the perimeter. The total reinforcement accounts for approximately 2.1% of the concrete volume. Optical fibre sensors are installed alongside every second reinforcement bar in the generator direction. Each end of the element is fitted with a 60 mm thick abutment, as shown in Figure 3.4.

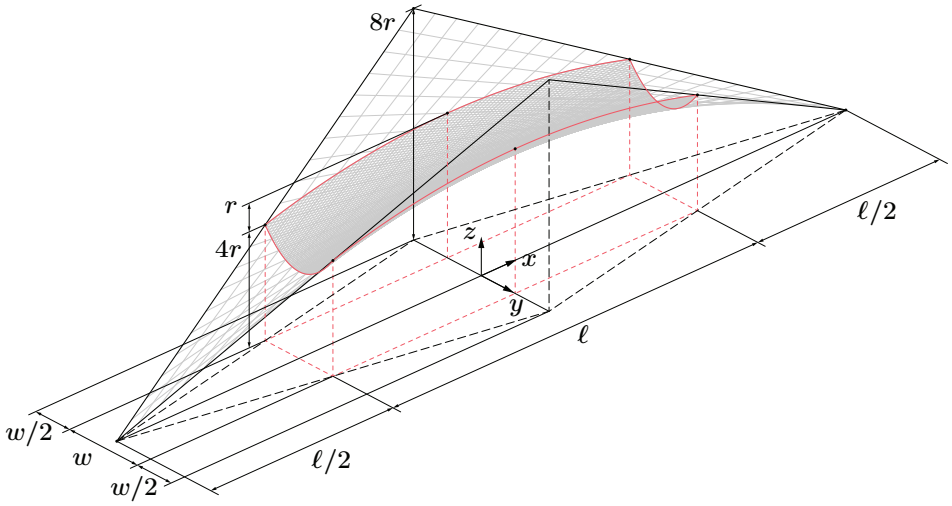

Figure 3.2: Parametrisation of the middle surface of the prototype element.

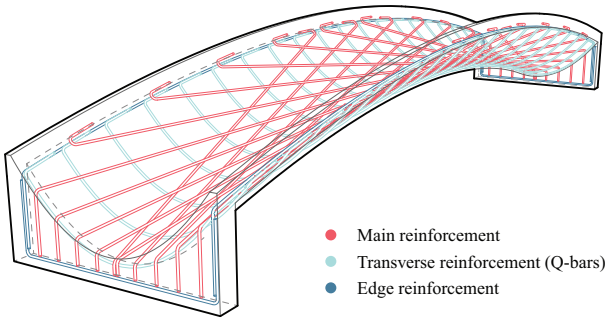

Figure 3.3: Rendered perspective view of the intended reinforcement layout. The main reinforcement (red) is placed in the generator direction. Stirrups (light blue), also referred to as Q-bars, provide transverse tensile capacity and serve as guides for mounting the main reinforcement. The longitudinal edges are reinforced with additional bars (dark blue), which are extended into the abutments and lap spliced to form a closed loop around the edges. All reinforcement bars have a diameter of 6 mm.

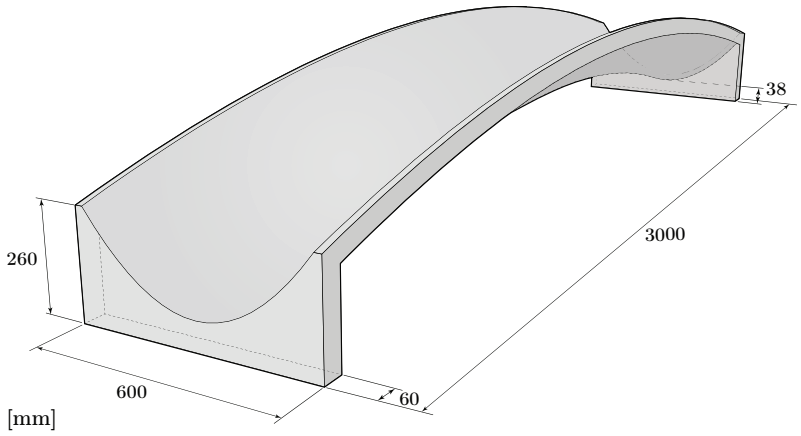

Figure 3.4: Rendered perspective view of the intended HP prototype element.

3.1.2 Fabrication

Prior to casting the prototype element, a formwork was fabricated, into which the reinforcement cage was placed. The fabrication process of the formwork and reinforcement cage consisted of six main stages (cf. Figure 3.5):

1. The supporting wooden formwork was produced and assembled.
2. A thin, flexible chipboard was mounted on top of the supporting structure to create a smooth casting surface. The surface was covered with a plastic sheet to prevent excessive moisture transport.
3. The edge reinforcement bars were positioned, followed by the transverse reinforcement (Q-bars).
4. The main longitudinal reinforcement was positioned and anchored to the underlying reinforcement using plastic cable ties (see Figure 3.6a). Two lifting loops were anchored to the reinforcement cage to facilitate crane lifting (see Figure 3.6b).
5. Fibre optic cables were placed along every other generator reinforcement bar.
6. Edge boards were attached at the ends of the formwork to enclose it.

During fabrication, it was observed that the spacing of the transverse reinforcement (Q-bars) deviated from the design specifications. The specified spacing was defined along a horizontal plane, which was difficult to relate to in practice due to the curved geometry of the formwork. As a result, the Q-bars appeared more closely spaced near the apex of the element and more widely spaced toward the abutments.

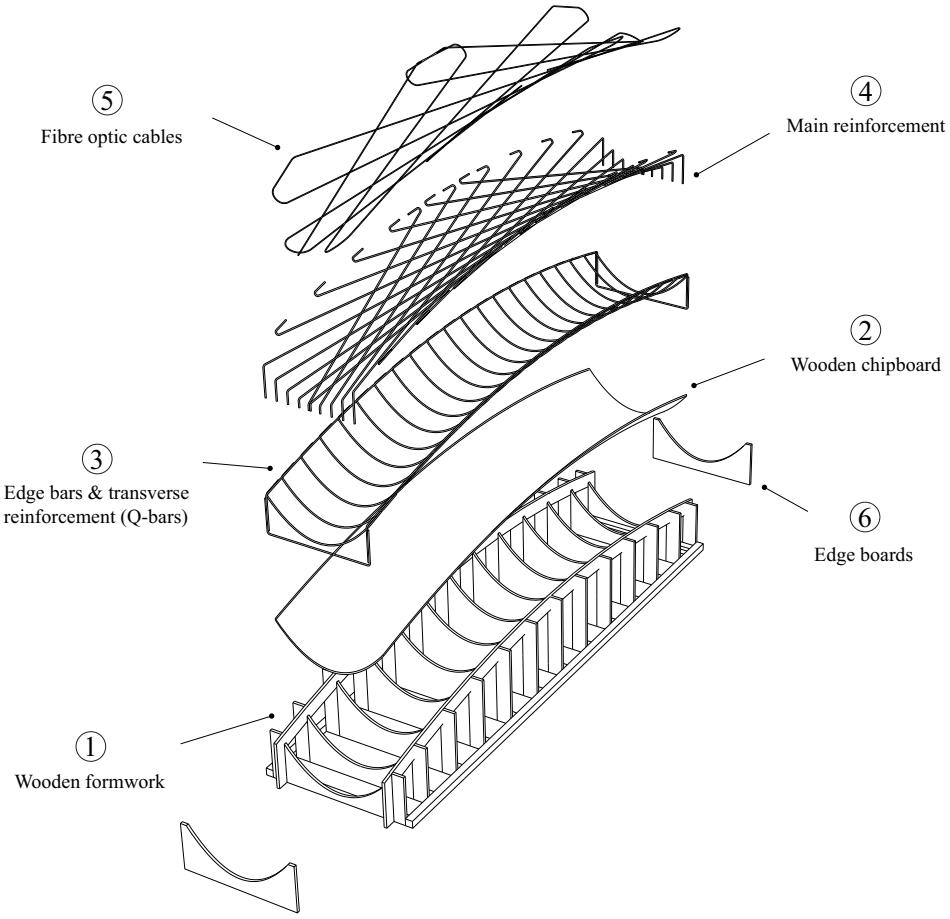

Figure 3.5: Step 1–6 in the fabrication process of the formwork and reinforcement cage.

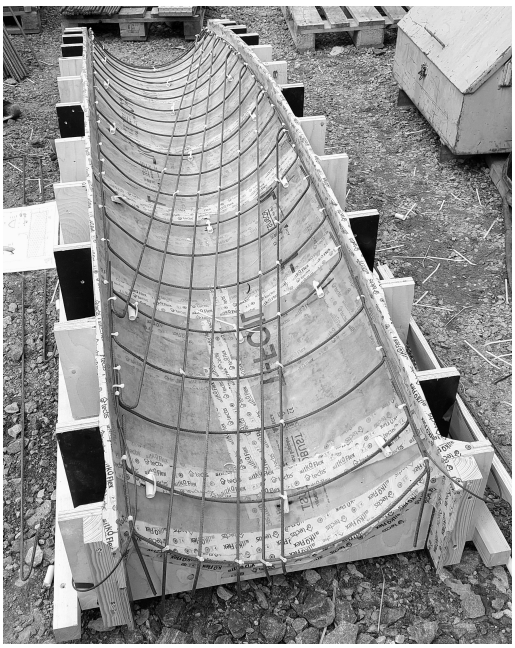

(a) Spacing of main reinforcement on top of Q-bars.

(b) Cast-in lifting loops used to lift the element out of the formwork.

Figure 3.6: Images from the fabrication and demoulding of the element.

The prototype element was cast on 25 June, 2024. The concrete was prepared in a factory and cast outdoors in Örkelljunga, Sweden, at a temperature of around 24°C. Five test cubes were cast from the same concrete batch, for material testing. The concrete was manually placed by shovelling it onto the formwork and then levelled using a wooden screed guide shaped to follow the intended parabolic geometry. No mechanical vibration was applied during casting. The element was cured outdoors at an average ambient temperature of 17°C during the first 28 days, based on meteorological data from SMHI (2024).

After a couple of months, the element was transported to Chalmers University of Technology, where it remained stored outdoors. It was covered with a tarpaulin during the winter to protect it from precipitation. In the early part of this thesis work, on 20 February, 2025, the cast element was removed from the formwork and moved indoors for subsequent testing.

3.2 Post-fabrication assessment

As an initial part of the thesis work, it was of interest to assess the cast prototype element with respect to its geometry and material properties. This section presents a photogrammetry-based evaluation to quantify deviations from the intended geometry, as well as to extract spatial reference data for aligning numerical models. Comparisons of mass, thickness variations, and volume discrepancies are also included. The section concludes with a summary of the material tests and the resulting material properties considered in the numerical analyses.

3.2.1 Photogrammetry

Photogrammetry was employed to generate a 3D model of the HP element. Using a series of overlapping images, a point cloud was obtained, from which a mesh was created. The mesh was used both to evaluate geometric deviations from the intended geometry and to extract datum points for the subsequent modal analysis.

The images were processed using RealityCapture by Epic Games. A total of 572 photographs were imported, of which 435 were successfully aligned. The resulting point cloud, along with the spatial distribution of camera positions, is shown in Figure 3.7.

In addition, a texture map was generated directly in the software, containing the marked reference points of the measurement grid used in the experimental modal analysis. The mesh was imported into Rhino 3D, where reference measurements were taken and used to verify correct scaling.

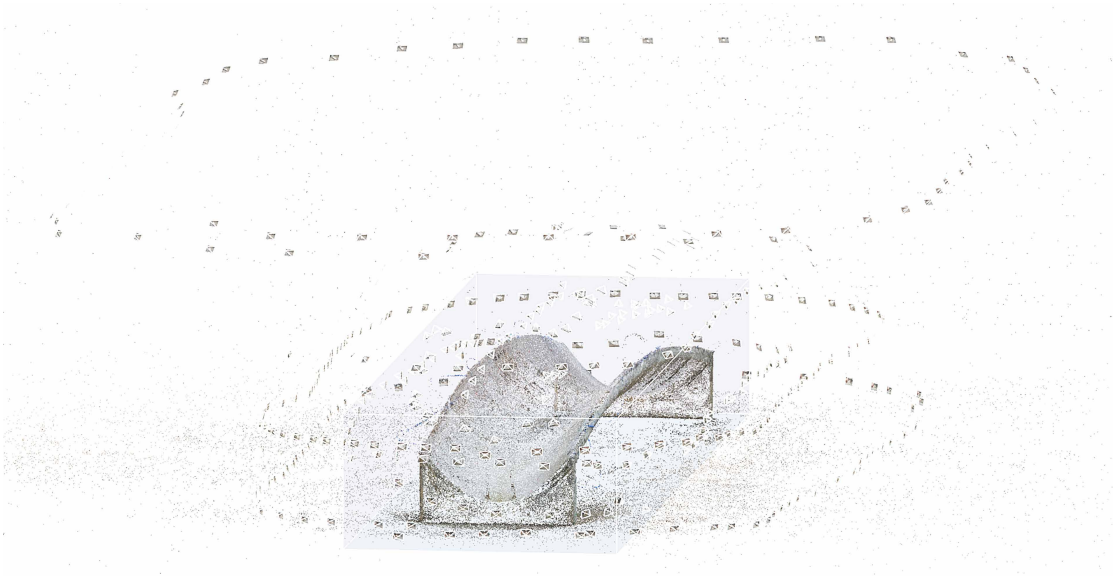

Figure 3.7: The figure showcases the camera alignments as well as the generated point cloud.

3.2.2 Evaluation of cast prototype element

Following the removal of the formwork and the photogrammetry scan, the element underwent a visual inspection to evaluate its condition and a geometric assessment to quantify deviations from the intended geometry. The top and bottom surfaces were deemed satisfactory, with no cracks or damage observed. However, several other discrepancies were identified:

- Significant void in one abutment (see Figure 3.8).
- Geometrical skewness, resulting in an approximately 1.5 cm gap between the abutment and the ground at one place (see Figure 3.8).
- Honeycombing along longitudinal edges, particularly around areas where fibre optic cables protruded, as shown in Figure 3.9.
- Discrepancies in concrete volume and gross weight.
- Variation in thickness.

The gross weight of the element was measured using a crane-mounted scale attached to one of the lifting loops at a time. During weighing, one end of the element was raised approximately 1 cm while the opposite abutment remained on the ground and the reading of the scale was recorded. The procedure was repeated at the opposite lifting loop. Three weight measurements were recorded at each side and averaged, resulting in a gross weight of

$$m = 262 \pm 5\,\text{kg},$$

with a standard deviation of approximately 3 kg. Based on engineering judgment, the overall measurement uncertainty was estimated at ± 5 kg. The measured mass was ex-

pected to be on the higher end, as the weighing was conducted under winter conditions when the element likely exhibited elevated moisture content.

Figure 3.8: Two flaws in the cast prototype element: (i) void in the abutment due to inadequate compaction, (ii) gap between abutment and ground due to a twisting geometry.

Figure 3.9: Honeycombing along edges.

The scanned volume of the element, excluding lifting loops and protruding fibre optic cables, was measured at 0.104 m^3, compared to the intended gross volume of 0.107 m^3. One possible explanation for this discrepancy is that the element's thickness may be less than intended. To investigate this hypothesis, the thickness in the central regions of the scanned geometry was evaluated, as illustrated in Figure 3.10. A rectangular grid of points was projected onto the top surface. Cubic polynomial curves were fitted to the points along the transverse direction to replicate the intended parabolic cross-section. Each point was then projected normal to its respective curve onto the bottom surface to determine the local thickness. The average measured thickness was 46.9 mm, compared to the intended 45.0 mm. This suggests that the main surface of the element (excluding abutments and edges) has approximately 3.7% greater volume than intended, thereby

falsifying the hypothesis of insufficient thickness as the primary cause of the reduced volume.

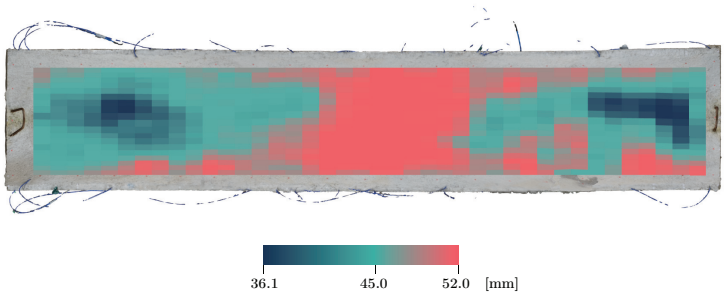

Figure 3.10: Thickness variation across the scanned prototype geometry.

Instead, the approximately 2.8% reduction in total scanned volume is more plausibly attributed to geometric skewness and the presence of a void in one of the abutments. Additionally, material appears to be missing along the edges of the element, where corners are visibly more rounded and less defined than intended. As shown in Figure 3.11, the element exhibits a slight longitudinal twist, likely resulting from inaccuracies in the formwork assembly. The formwork was constructed on a gravel surface, rather than on a levelled surface, which is likely the reason for asymmetry. Specifically, one edge appears to lie slightly lower than the opposite edge, resulting in reduced curvature along that edge, contributing to a reduced volume. By computing the centres of gravity of both the scanned and intended geometries, it was found that they align closely in plan. However, in elevation, the centre of gravity of the scanned geometry is located approximately 25 mm lower, indicating a vertical shift in mass distribution.

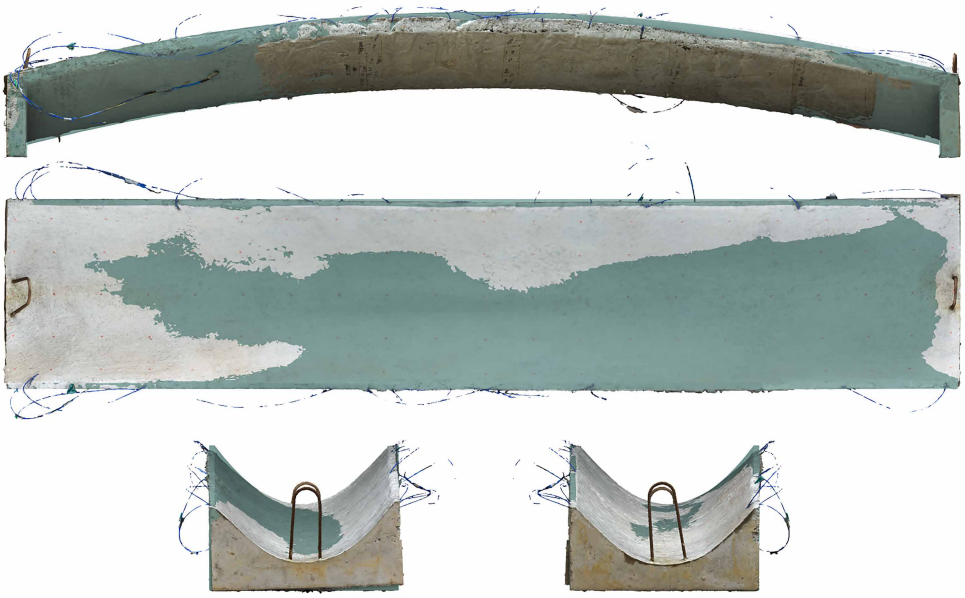

Figure 3.11: Overlay of intended geometry (turquoise) on top of scanned geometry. There is an inherent skewness to the geometry with one edge appearing lower down than on the opposite side.

The mass was additionally estimated by multiplying the volumes of concrete and steel with their respective material densities. The volume of steel reinforcement (including lifting loops) was derived from drawing specifications, while the volume of concrete was calculated by subtracting the reinforcement volume from the scanned gross volume. The resulting values are presented in Table 3.1. The volume of other components, including fibre optic cables and cable ties were neglected.

Table 3.1: Estimated volume and mass of the prototype element based on scanned geometry and reinforcement specifications.

Material	**Volume [m^3]**	**Mass [kg]**
Steel reinforcement	0.002	17.7
Concrete	0.102	245.6
Total	**0.104**	**258.1**

The measured gross weight (262 kg) and the estimated weight based on the scanned geometry (258 kg) can be compared to the nominal mass of 265 kg, which the intended design geometry should have had. Both values are lower than intended, which is consistent with observed discrepancies in the concrete volume. Although the geometry-based estimate relies on assumed material densities, it was considered more accurate than the direct measurement using the crane-mounted scale.

3.2.3 Material properties

The material properties assumed in the structural assessment of the prototype element are based on both experimental testing of five concrete cubes and on nominal values specified in Eurocode. It is important to note that there might be significant discrepancies between the properties of the cubes and those of the actual HP element. The cubes were mechanically vibrated during casting, while the prototype element was not. Three of the cubes were used for compressive strength testing, and were cured together with the HP element under the same environmental conditions. The remaining two cubes, used for wedge splitting tests (WST), were cured indoors in water.

This section examines the material properties of the concrete and steel reinforcement. It begins with a description of the concrete mix design, followed by a summary of the conducted material tests. The section concludes with a summary of the final material properties adopted for analysis. Detailed laboratory reports and the complete concrete mix design are provided in Appendix A.

3.2.3.1 Concrete mix design

The concrete was prepared and mixed by Våxtorps Betong AB, based on specifications provided by Alexander Sehlström at WSP. The mix required a minimum strength class of C25/30 (no upper limit specified) and a maximum aggregate size of $d_{\max} = 8$ mm.

0.7 m^3 of concrete with water-cement ratio 0.615 was mixed using a Portland-composite cement containing ground granulated blast-furnace slag and limestone. The cement, marketed under the product name *Viridis* (CEM II/B-M (S-LL)), was supplied by Schwenk Sverige AB. Admixtures, including an S3 plasticiser and a retarder, were added to achieve the desired fresh concrete properties. The plasticiser improved flowability but

was carefully dosed to prevent excessive flow and segregation. The retarder served to delay the hydration process. Notably, the amount of retarder used exceeded the initially specified dosage by 61.9%, likely as an adjustment to compensate for the relatively high casting temperature of 24°C.

Given the cement's classification as a Portland-composite containing slag and limestone, its strength development over time was expected to differ from that of pure Portland cement. To inform the assessment of long-term strength, Dr. Urs Müller of Schwenk Sverige AB was consulted. Based on his expertise and internal company testing, it was approximated that compressive strength gains beyond 28 days are generally limited for water–cement ratios above 0.5. Estimated increases are approximately 5% between 28 and 56 days, 3% between 56 and 90 days, and 1% between 90 and 182 days (Müller, personal communication, 15 May 2025).

An attempt was made to estimate the CO_2-eq emissions associated with the concrete mix design. It was assumed that the cement component accounts for approximately 85% of the total CO_2-eq emissions, based on guidance from Dr. Nilla Olsson at NCC. The remaining 15% was attributed primarily to the use of fine aggregate. According to environmental product declaration (EPD) data from Schwenk, the Viridis cement has an emission factor of 524 kg CO_2-eq/ton for stages A1–A3 (Schwenk Sverige AB, 2024). Based on this value, the total carbon footprint of the concrete mix was estimated at approximately 184 kg CO_2-eq/m^3. This estimated value may be compared to the industry reference of 225 kg CO_2-eq/m^3 for C25/30 concrete, as specified by Svensk Betong (2022). With an estimated footprint of 184 kg CO_2-eq/m^3, the mix falls between Svensk Betong's Level 1 and Level 2 of climate-improved concrete.

3.2.3.2 Cube strength test

Cube strength tests were performed on three cubes in accordance with SS-EN 12390-3:2019 (Swedish Institute for Standards, 2019). The tested cubes were cured outdoors for 252 days alongside the concrete beam element. A Toni Technik model 2040 test rig was used to load the cubes to failure, as seen in Figure 3.12. All failures were deemed satisfactory, with all four exposed faces showing approximately equal cracking. The test results are presented in Table 3.2.

Table 3.2: Results from the compressive strength tests of specimen 1-3, where ρ is the density of the cubes, N_c is the applied load, and f_{obs} is the calculated stress.

Specimen number [-]	$\boldsymbol{\rho}$ [kg/m^3]	$\mathbf{N_c}$ [kN]	$\boldsymbol{f_{obs}}$ [MPa]
1	2,455	910	51.0
2	2,314	900	49.5
3	2,320	895	50.0
Mean value	**2,363**	**902**	**50.2**

Figure 3.12: Test setup for the compressive strength tests using a Toni Technik model 2040 testing machine.

The resulting compressive strength corresponds to the mean strength after 252 days. In accordance with SS-EN 137207:2005 (Swedish Institute for Standards, 2005), this strength can be converted to the corresponding 28-days mean cube strength $f_{\mathrm{cm,cube}}$, through:

$$f_{\mathrm{cm,cube}} = \frac{f_{\mathrm{obs}}}{\beta_1 \beta_2},$$

where β_1 is a factor that accounts for the dimensions of the cube, and β_2 is a factor that accounts for the effective age j_{20} of the cube. The effective age was evaluated as $j_{20} = 165$ days, based on climate data from Chalmers University of Technology (2025). EN 1992-1-1:2004 (European Committee for Standardization, 2004) express empirical relations that may be used to obtain further material properties based on the 28-days strength. The 28-days and 252-days concrete properties are summarised in Table 3.3.

	$\mathbf{f}_{\mathrm{cm,cube}}$ [MPa]	$\mathbf{f}_{\mathrm{cm}}$ [MPa]	$\mathbf{f}_{\mathrm{ck}}$ [MPa]	$\mathbf{f}_{\mathrm{ctm}}$ [MPa]	$\mathbf{E}_{\mathrm{cm}}$ [GPa]
28-days	43.6	37.1	29.1	2.8	26.9
252-days	50.2	42.7	34.7	3.2	28.0

Table 3.3: Concrete material properties from 28-days and 252-days $f_{\mathrm{cm,cube}}$ in accordance with EN 1992-1-1:2004.

The 28-days characteristic cylinder strength f_{ck} of 29.1 MPa indicates a concrete strength class slightly above the specified C25/30. It should be noted that the conversion factors specified in SS-EN 137207:2005 are based on standard Portland cement properties and may not accurately reflect the behaviour of the SS-L cement used in this study. Therefore, the converted 28-day strength values should be interpreted with caution.

Since the concrete of the prototype element was not vibrated, it is reasonable to assume that its properties differ from those of the test cubes. The impact of compaction of concrete is discussed in Neville (2011) and Zhao et al. (2021), who both report that vibration can increase compressive strength by 20% or more, depending on factors such as vibration frequency, amplitude, duration, and method. It follows that the compressive strength estimated from the test cubes likely overestimates that of the prototype HP element.

The density measurements of the three cubes exhibited a coefficient of variation (CV) of approximately 2.8%, which may be considered relatively low. According to EN 1992-1-1:2004 (2004), the nominal density of plain concrete is $\rho = 2{,}400$ kg/m^3, which is approximately 1.5% greater than the measured average density of the cubes.

3.2.3.3 Wedge splitting test (WST)

A wedge splitting test (WST) was performed to determine the tensile strength f_{ct} and tensile fracture energy G_{F} of the concrete. The test was conducted on two cubes using a MTS 380.10 test rig, as shown in Figure 3.13a, following the recommendations outlined in Nordic Innovation Centre (2005). According to the recommended testing procedure, the cubes should be cast with a groove at the top, in which load bearings can be fitted. However, since the specimens were cast without this groove, it had to be sawn into the cubes afterwards, as shown in Figure 3.13b. In addition, a starter notch was sawn in each specimen to promote controlled crack initiation and localisation.

The machine applied a vertical load onto the roller bearings, which in turn transferred the load horizontally, causing the specimen to split apart. According to Nordic Innovation Centre (2005), the horizontal splitting force can be calculated as:

$$F_{\mathrm{sp}} = \frac{F_{\mathrm{v}}}{2\tan(\alpha)},$$

where F_{v} is the vertical load, and α is the inclination angle of the wedge (with $\alpha = 15°$ in this case). This expression neglects the impact of friction between the wedge and the roller bearings. The friction coefficient μ of the rolling bearings typically ranges from 0.1–0.5%, reducing the splitting force by up to 1.9% for a given vertical load (Shah & Carpinteri, 1991).

A clip gauge was placed in the grove of each specimen, measuring the *crack mouth opening displacement* (CMOD). The results of the test were plotted in a *splitting force-CMOD* curve, as seen in Figure 3.14. The tensile strength was calculated based on the peak splitting force. Assuming a linear stress distribution over the ligament area at onset of cracking, the maximum tensile strength was calculated as

$$f_{\mathrm{ct}} = \frac{M \cdot z}{I} + \frac{F_{\mathrm{sp}}}{A_{\mathrm{lig}}},$$

(a) MTS 380.10 test rig.

(b) Preparation of cubes.

Figure 3.13: Images from the wedge splitting test.

where I is the moment of inertia of the ligament, and A_{lig} is the ligament area. The moment M was calculated as $M = F_{\text{sp}} \cdot x$, where x is the distance between the applied splitting load and the neutral axis z. The fracture energy G_{F}, was calculated as the area below the splitting force-CMOD curve divided by the ligament area. The obtained results are presented in Table 3.4.

Table 3.4: Results from the wedge splitting test of specimen 1 and 2.

Specimen number [-]	**Fracture energy G_{F}** [Nm/m^2]	**Tensile strength f_{ct}** [MPa]
1	216.9	5.18
2	206.5	4.88
Mean value	**211.7**	**5.03**

The obtained results yield unreasonably high values for both tensile strength and fracture energy. As an alternative, the tensile strength can be estimated from the compressive strength, as discussed in Section 3.2.3.2. According to Table 3.3, the expected tensile strength at 252 days is approximately 3.2 MPa; about 36% lower than the value suggested by the wedge splitting test. Hanjari (2006) conducted a comprehensive study on wedge splitting tests and found no indication that the tensile strength of standard concrete could reach values as high as 5.0 MPa. This discrepancy is therefore more likely due to experimental errors, such as misalignment of the bearings, faulty load cells, or excessive friction between wedge and bearings.

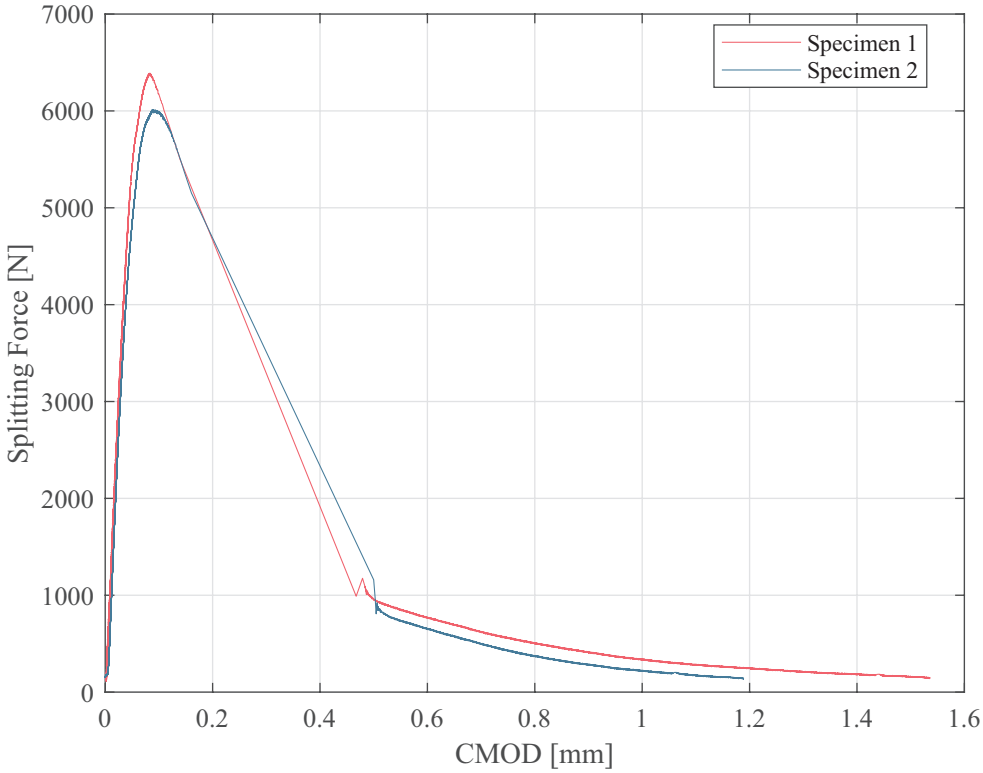

Figure 3.14: Splitting force - CMOD curve for specimen 1 and 2.

The tensile fracture energy can alternatively also be calculated based the compressive strength in accordance with CEB fib Model Code (2010):

$$G_{\mathrm{F}} = 73 f_{\mathrm{cm}}^{0.18} = 143\,\mathrm{Nm/m^2}.$$

The calculated fracture energy of 143 Nm/m² is 32% lower than the value obtained from the WST test and aligns more closely with results reported in the literature and established design codes.

The fracture energy in compression G_{c} can also be obtained in accordance with CEB fib Model Code (2010):

$$G_{\mathrm{c}} = 250 \cdot G_{\mathrm{F}} = 35{,}750\,\mathrm{Nm/m^2}.$$

3.2.3.4 Steel reinforcement properties

K500C-T ribbed reinforcement steel ⌀6 mm was used in the prototype element, with nominal characteristic yield strength $f_{\mathrm{yk}} = 500$ MPa, modulus of elasticity $E_{\mathrm{s}} = 200$ GPa, density $\rho = 7{,}850$ kg/m^3, and Poisson's ratio $\nu = 0.3$, as specified in Annex C of EN 1992-1-1:2004 (European Committee for Standardization, 2004) and in EN 1993-1-1:2005 (European Committee for Standardization, 2005).

3.2.3.5 Summary of material properties

Tables 3.5 and 3.6 provide a summary of the material properties that were considered in the assessment of the prototype element.

Table 3.5: Material properties of the concrete.

$\mathbf{f}_{cm}$ [MPa]	$\mathbf{f}_{ck}$ [MPa]	$\mathbf{f}_{ctm}$ [MPa]	$\mathbf{E}_{cm}$ [GPa]	$\mathbf{G}_F$ [Nm/m^2]	$\mathbf{G}_c$ [Nm/m^2]	$\boldsymbol{\varepsilon_{cu1}}$ [‰]	$\boldsymbol{\nu}$ [-]	$\boldsymbol{\rho_c}$ * [kg/m^3]	$\boldsymbol{\rho_{rc}}$ ** [kg/m^3]
42.7	34.7	3.2	28.0	143	35,750	3.5	0.2	2,363	2,476

*Density of plain concrete according to test data.**Density of reinforced concrete assuming 2.1% reinforcement ratio as per design specifications.

Table 3.6: Material properties of the steel reinforcement (K500C-T).

$\mathbf{f}_{yk}$ [MPa]	$\mathbf{f}_{yd}$ [MPa]	$\mathbf{E}_s$ [GPa]	$\boldsymbol{\rho}$ [kg/m^3]	$\boldsymbol{\nu}$ [-]
500	435	200	7,850	0.3

3.3 Modal analysis

This section presents the methodology and results of the experimental and numerical modal analyses conducted on the prototype element. It is organised into five main parts, presented in Sections 3.3.1 to 3.3.5.

Section 3.3.1 provides an analytical estimation of vertical bending frequencies, as per Euler–Bernoulli beam theory. These frequencies are later used to validate the experimental results and the test procedure. Section 3.3.2 outlines the experimental modal analysis, including the test setup, experimental procedure and the results. Section 3.3.3 presents the numerical modal analysis and investigates the effects of mesh density, reinforcement, and boundary conditions. The outcomes of the experimental and numerical analyses are summarised in Section 3.3.4. Finally, limitations of the current analysis and suggestions for future improvements are discussed in Section 3.3.5.

3.3.1 Analytical modal analysis

The natural frequencies of the first three vertical bending modes were computed in accordance with Euler–Bernoulli beam theory, as described in Section 2.4.4. The results, shown in Table 3.7, are valid for a straight beam with uniformly distributed mass and stiffness. Two cases were considered: (i) a simplified case neglecting the contribution of steel reinforcement entirely, and (ii) a more refined case using effective cross-sectional properties (EI_{ef} and ρ_{ef}) calculated in accordance with EN 1992-1-1:2004 (European Committee for Standardization, 2004), assuming the section remains fully uncracked (State I). In line with Section 3.1.1, the reinforcement ratio of an average cross-section was taken as 2.1%. The beam length was taken as 3.035 m, which corresponds to the arc length spanned by the prototype element.

Table 3.7: Analytically estimated natural frequencies [Hz] of the first three vertical bending modes under two cross-section assumptions.

Case	$\mathbf{EI_y}$ [kNm^2]	$\boldsymbol{\rho}$ [kg/m^3]	**A** [m^2]	$\mathbf{f_1}$ [Hz]	$\mathbf{f_2}$ [Hz]	$\mathbf{f_3}$ [Hz]
(i) No reinforcement	3,612	2,363	0.033	82.9	229	448
(ii) Effective cross-section	3,755	2,476	0.033	82.6	228	447

As seen in Table 3.7, the two cases yield similar natural frequencies. While case (ii) has a greater mass it also has a greater bending stiffness, EI_{y}, thereby resulting in similar natural frequencies. Despite the prototype element being curved and characterised by non-uniform mass and stiffness distributions, its lower vertical bending frequencies are not expected to deviate significantly from these analytical estimates.

3.3.2 Experimental modal analysis (EMA)

The experimental modal analysis (EMA) is summarised in the following subsections:

- **Section 3.3.2.1** — Describes the experimental setup, including boundary conditions, test procedure, transducers, and measurement grid.
- **Section 3.3.2.2** — Explains the execution of the test and how transducer signals

were sampled and processed.

- **Section 3.3.2.3** — Presents preliminary tests conducted to validate the experimental setup.
- **Section 3.3.2.4** — Evaluates the influence of boundary conditions.
- **Section 3.3.2.5** — Presents the extracted modal parameters.

3.3.2.1 Experimental setup

The experimental modal analysis was based on a roving hammer single-input multiple-output (SIMO) setup. It utilised seven accelerometers placed at different reference nodes, and an impact hammer to sequentially excite all measurement points, as shown in Figure 3.15. The details of the experimental setup are summarised below.

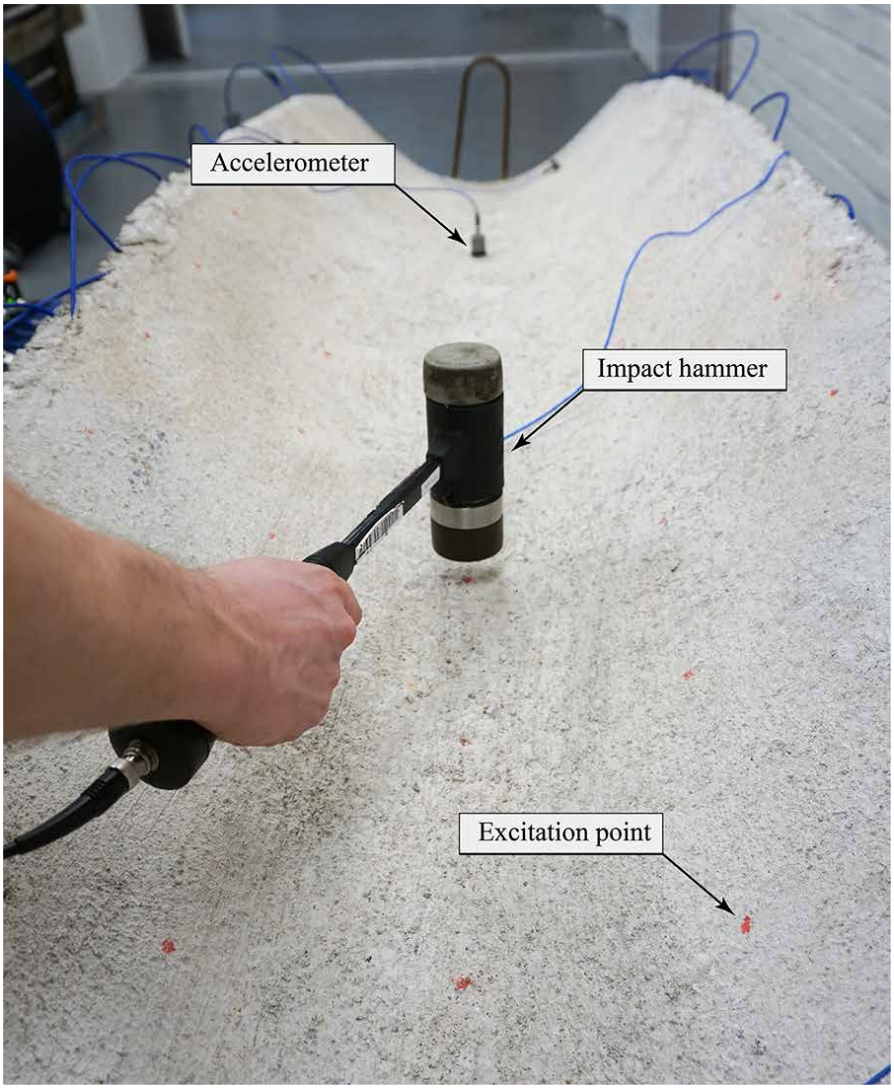

Figure 3.15: Impact testing on the prototype element using an impact hammer. Accelerometers positioned along the surface and connected with BNC cables to the data acquisition (DAQ) system. Red dots indicate excitation points.

Boundary conditions

As stated in Section 2.5.2, free boundary conditions are advantageous when performing experimental modal analysis. Ideally, the element should have been suspended from elastic ropes or springs. This setup was, however, not possible to achieve. Instead, four pressurised Firestone model 116-1 air springs where used to achieve relatively free boundary conditions.

The air springs were positioned below the abutments of the element, as shown in Figure 3.16, mounted onto steel profiles to protect the air valves located beneath the air cushions. A timber frame was used to catch the element in case any air spring failed (which never happened). The steel profiles were fitted into slits in the timber frame to increase buckling strength and to ensure a consistent distance between the springs. Everything was mounted on a thin plywood sheet as shown in Figure 3.16a, which also protected the floor surface from scratches in the event of support movement. Aluminium plates were placed between the springs and abutments, as seen in Figure 3.16b, to level the element and compensate for the slight geometric twist discussed in Section 3.2.2. This ensured a more even distribution of the element's mass across the four springs.

(a) Overview. **(b)** Close-up.

Figure 3.16: Prototype element supported on air springs.

The linear behaviour of the air springs was evaluated by measuring their relative displacement at four different pressure levels. Figure 3.17 compares the results with the manufacturer's data, demonstrating a strong linear correlation between air pressure and stiffness, and close agreement between measured and specified properties.

The degree to which these supports can be considered free is further examined in Section 3.3.2.4.

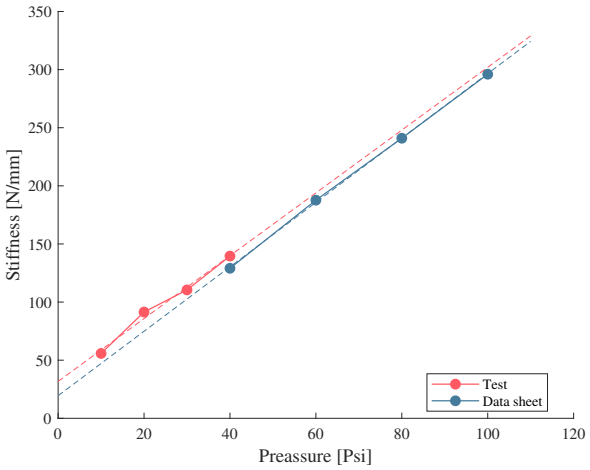

Figure 3.17: Comparison of air springs stiffness from experimental tests and manufacturer data across varying internal pressures. The plot highlights the linear correlation between air pressure and stiffness.

Transducers

Experiments were conducted using two different impact hammers (see Figure 3.18), both manufactured by PCB Piezotronics. The larger PCB 086D20 hammer weighed 1.1 kg and was equipped with a medium-soft tip, which produced a narrower frequency spectrum. The smaller PCB 086B03 hammer weighed 0.16 kg and had a hard steel tip, capable of exciting a broader range of frequencies.

The useful frequency range of each hammer was evaluated in accordance with Section 2.5.2.2 prior to testing. The results indicated that the larger hammer had a useful range of 0–280 Hz, while the smaller hammer covered a range of 0–1,000 Hz.

Figure 3.18: Two hammers were used: PCB 086D20 (left) and PCB 086B03 (right).

Seven accelerometers were used: two triaxial PCB TLD356A16 accelerometers with a sensitivity of 100 mV/g, two uniaxial PCB 352B accelerometers with a sensitivity of 1000 mV/g, and three uniaxial PCB 352C33 accelerometers with a sensitivity of 100 mV/g. All accelerometers were calibrated prior to installation using a Brüel & Kjær type 4294 calibration exciter. The accelerometers were mounted on the prototype element using hot-melt adhesive (hot glue).

Measurement grid

A 5-by-21-point grid (105 points in total) was marked on the top surface of the prototype element, corresponding to a mesh size of approximately 140 by 152 mm. This was achieved by moving a parabolic profile along a rope positioned along the centreline of the surface and marked at 152 mm intervals. The points were marked with a permanent marker, ensuring accurate placement of accelerometers and consistent impact locations for the hammer.

The spatial coordinates of the points were retrieved from the photogrammetry texture map, as illustrated in Figure 3.19. Unit surface normals at the obtained coordinates were computed using Grasshopper 3D. The coordinates and corresponding normals were then used to construct a reference model in DewesoftX, which was used to perform the experimental modal analysis. Local coordinate systems were specified in each node, defined by planes perpendicular to the surface normal and aligned with the global x- and y-axes.

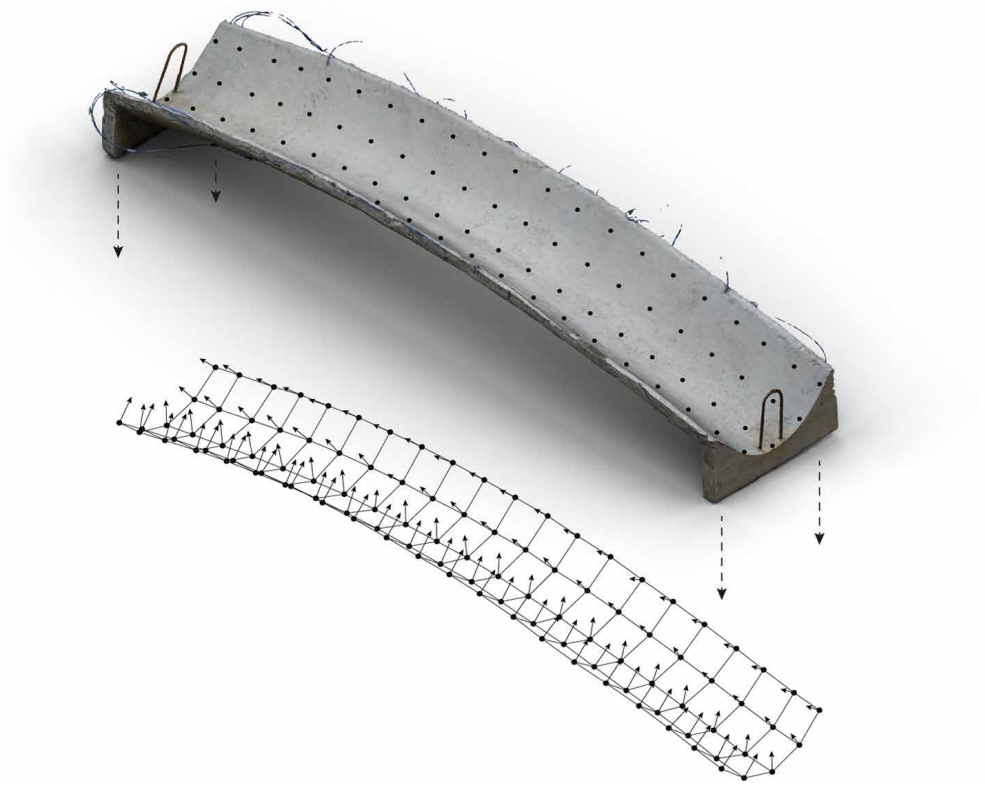

Figure 3.19: Spatial coordinates of the marked points were extracted from the texture map generated by the photogrammetry scan. Surface normals were computed at each point, defining local coordinate systems used in the experimental modal analysis.

3.3.2.2 Experimental procedure

A detailed experimental procedure was developed to ensure the accuracy and reliability of the modal analysis. It is outlined in this section, comprising the following stages:

- Preliminary testing to assess the setup and estimate mode shapes.
- Sensitivity study of support stiffness.
- Modal parameter extraction with a refined test setup.
- Rigid body mode identification and validation.

Preliminary testing was conducted to provide a rough estimate of the mode shapes and to evaluate the test setup. Both hammers were tested to assess whether the quality of the acquired data was sufficient or if an alternative hammer would be required. Additionally, the preliminary tests helped identify suitable accelerometer locations, ensuring they were not placed along nodal lines.

Following the preliminary tests, an additional study was conducted to investigate the influence of different boundary conditions. Specifically, how the spring stiffness of the air cushions could affect damped natural frequencies and mode shapes. Theoretically, stiffer supports reduce system flexibility, causing rigid body modes to occur at higher frequencies, while more compliant supports result in lower-frequency rigid body modes.

Based on insights gained from the preliminary tests and the evaluation of support configurations, the experimental setup was refined. Testing was carried out with the updated setup to identify the system's modal characteristics, including mode shapes, damped natural frequencies, and modal damping ratios.

Lastly, additional testing was conducted in an attempt to identify and categorise all six rigid body modes. It was found during the preliminary testing that three of the six rigid body modes were less distinct and difficult to identify. The experimental configuration was therefore modified to identify the remaining three rigid body modes.

Data acquisition

A Dewesoft Sirius data acquisition (DAQ) system was used to record and process all transducer signals in all experiments. The system featured eight channels in total, with one channel reserved for the impact hammer and the remaining seven used for the accelerometers.

Two measurement configurations were employed. In the first, all seven accelerometers measured acceleration normal to the surface. In the second, one uniaxial and two triaxial accelerometers were used, with a separate channel allocated to each coordinate axis of the triaxial sensors. This latter configuration was employed to identify rigid body modes that were less distinct using the first configuration.

Along with the DAQ system, the DewesoftX software with the *Modal Analysis* package was used. Most of the modal analysis was carried out entirely in this software environment. It included key features such as signal processing, transfer function estimators, coherence plots, mode indicator function plots, averaging of hits, double hit detection, and curve fitting tools for extracting modal parameters.

The prototype element was excited sequentially at each node of the measurement grid.

At each node, six hammer impacts were applied and subsequently averaged to reduce random noise. Trigger and double-hit detection thresholds were configured for both hammers to ensure consistent and high-quality data acquisition. For the larger hammer, the trigger level was set to 1,000 N and the double-hit detection threshold to 70 N. For the smaller hammer, the corresponding values were 200 N and 70 N, respectively. Between impacts, the element was allowed to return to rest, ensuring that all transient vibrations had fully decayed.

Signal processing and sampling parameters

The transducer signals were sampled at 2,000 Hz using 1,024 spectral lines, resulting in a frequency resolution of 0.977 Hz (considering only positive frequency components) and a total sampling time of 1.02 seconds. Consequently, any dynamic effects occurring beyond this time window were not captured in the analysis. To ensure the signals decayed within the sampling period, exponential window functions with a 1% decay rate were applied, assuming that the system was lightly damped. Additionally, anti-aliasing *infinite impulse response* (IIR) filters were employed on all transducer signals.

3.3.2.3 Preliminary testing

Preliminary testing was conducted to evaluate the experimental setup. Five accelerometers were attached to the element in accordance with Figure 3.20, all of which measured the response in the direction normal to the surface. Two test were conducted, one for each hammer.

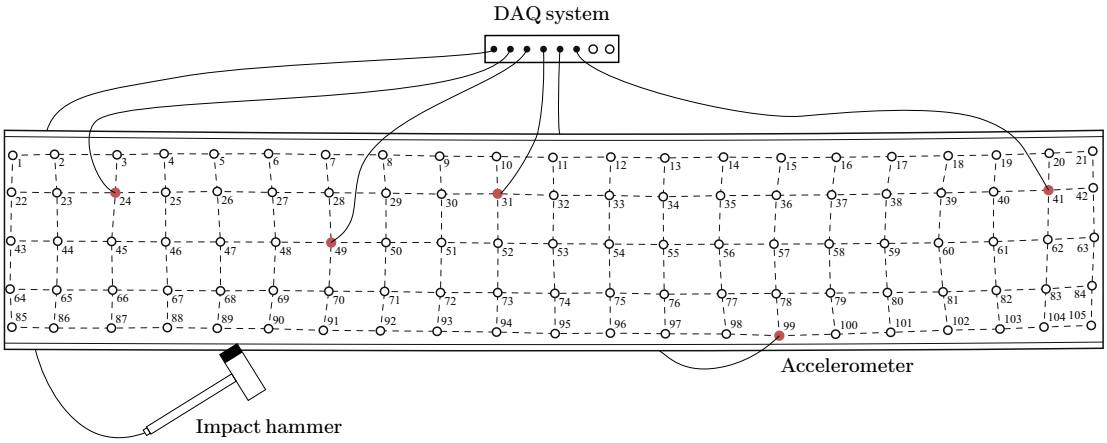

Figure 3.20: Initial experimental setup for the SIMO roving hammer test. The red nodes show the location of accelerometers.

The test provided valuable insight into the expected outcomes of the roving hammer tests. Key observations included:

- The coherence, obtained using the small hammer, was inferior to that of the large hammer.
- Six clear and distinguishable mode shapes were identified below 220 Hz. A seventh mode appeared near 300 Hz, though it was excluded as it exhibited poor definition and coherence.
- Three rigid body modes were clearly observed: translation in the z-direction, and rotation about the x- and y-axes, respectively. The remaining three rigid body modes were less distinct.
- The first six resonance frequencies were nearly identical in both tests, indicating a linear behaviour of the element and that the response is not significantly influenced by the input force magnitude.
- The largest rigid body mode exhibited a frequency ratio of less than 1:5 compared to the first flexible mode, suggesting that the boundary conditions could be considered relatively free.
- Based on the reference grid, it was possible to capture and distinguish between various mode shapes, and no further mesh refinement was deemed necessary.

Based on the results, it was decided to proceed with further testing using only the larger hammer, as it provided significantly better coherence and repeatability between hits compared to the smaller hammer. As the mode shapes of the first six flexural modes had been identified (see Table 3.8), it was possible to refine the placement of accelerometers to avoid placement on nodal lines. Two additional accelerometers were attached to the surface for subsequent testing, as illustrated in Figure 3.21.

Table 3.8: Mode categorisation.

Mode	Rotation axis	Mode description
1	X	1st torsion mode
2	Y	1st bending mode
3	Z + X	1st combined lateral torsional mode
4	Z + X	2nd combined lateral torsional mode
5	Y	2nd bending mode
6	Z + X	3rd combined lateral torsional mode

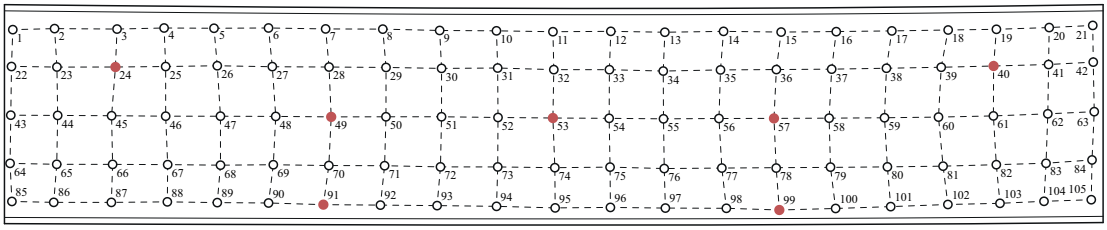

Figure 3.21: Updated experimental setup based on the results from the preliminary test.

3.3.2.4 Influence of boundary conditions

The influence of internal air pressure in the air springs was assessed by comparing damped natural frequencies, damping ratios, and mode shapes across three configurations: 10 psi (0.69 bar), 20 psi (1.38 bar), and 40 psi (2.76 bar), corresponding to approximate spring stiffnesses of 55 N/mm, 90 N/mm, and 140 N/mm, respectively. The tests were conducted using the refined experimental setup derived from the preliminary testing (see Section 3.3.2.3.

The eigenfrequencies of the highest rigid body mode and the first six flexural modes for each configuration are presented in Table 3.9.

Table 3.9: Comparison of eigenfrequencies and damping ratios at different air pressure levels.

Mode	10 psi		20 psi		40 psi	
	Frequency [Hz]	**Damping** [%]	**Frequency** [Hz]	**Damping** [%]	**Frequency** [Hz]	**Damping** [%]
RB*	6.58	–	10.3	–	12.15	–
1	50.55	0.55	50.97	0.58	52.00	0.56
2	71.45	0.52	71.63	0.55	72.48	0.52
3	77.69	0.46	77.75	0.48	78.42	0.46
4	139.80	0.50	138.07	0.71	139.74	0.49
5	188.84	0.90	188.10	0.86	189.75	0.56
6	212.68	0.76	213.00	0.83	212.81	0.47

*Highest rigid body mode.

As expected, the rigid body modes shifted with the varying stiffness of the supports. The highest rigid body mode for each configuration was recorded at 6.58 Hz, 10.3 Hz, and 12.15 Hz, respectively. Ideally, rigid body modes should be as close to 0 Hz as possible to minimise their influence on the flexible modes. In this case, however, the measured resonance frequencies (especially the higher-order ones) appeared to be largely unaffected by the frequency at which rigid body modes occurred.

The first three modes exhibited similar damping ratios across all pressure levels, suggesting they were not significantly influenced by the boundary conditions. In the 10 psi and 20 psi tests, a gradual increase in damping was observed with increasing mode number. This trend was not evident in the 40 psi case, where modes 4–6 showed lower damping values compared to the lower-pressure configurations. This behaviour suggests that higher modes are more sensitive to support stiffness and that damping contributions from boundary interactions are more pronounced under softer support conditions.

In addition to comparing the modal damping ratios and eigenfrequencies, the corresponding mode shapes were compared using the modal assurance criterion (MAC). The results are shown in Figure 3.22.

Each MAC plot exhibits diagonal values that are equal to or very close to unity, while the off-diagonal entries are close to zero. This indicates a strong correlation between the corresponding mode shapes across the different support conditions. The most notable deviation occurs in the comparison between 10 psi and 40 psi, and 20 psi and 40 psi,

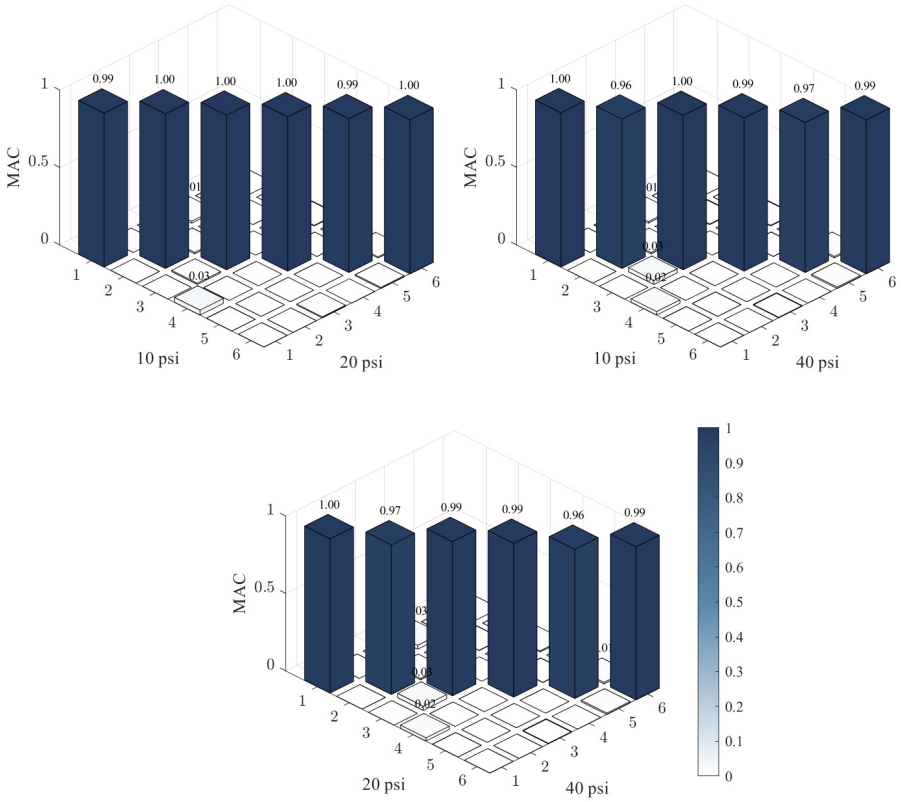

Figure 3.22: MAC comparison between 10, 20, and 40 psi air pressure levels.

particularly for mode 2 and mode 4, where the MAC value drops to 0.96. Although still high, this suggests that there is some influence from the boundary conditions. In contrast, the comparison between 10 psi and 20 psi yields MAC values consistently greater than 0.99 for all modes, demonstrating excellent modal consistency.

In conclusion, the test results indicated that internal air pressures of 10 or 20 psi are preferable over 40 psi for simulating free boundary conditions. The 40 psi configuration introduced additional stiffness, which affected the measured frequencies, mode shapes, and damping ratios. In accordance with Ewins (2000), the frequency of the highest rigid body mode should not exceed 20% of the first flexural mode. Although this criterion was technically not met by the 20 psi configuration, it was decided to proceed with it, as the air cushion manufacturer (Firestone) recommended maintaining a minimum air pressure of 20 psi during operation.

3.3.2.5 Modal parameter extraction

The modal characteristics of the system were determined using the refined experimental setup with air springs pressurised to 20 psi and with seven accelerometers positioned in accordance with Figure 3.21.

The quality of the acquired data and the linearity of the system were initially assessed using coherence and FRF plots, as shown in Figure 3.23. The coherence values for the selected FRFs remained high up to approximately 280 Hz, beyond which a noticeable drop-off occurred. Notably, the coherence approached unity at the resonance peaks below 280 Hz, which is consistent with the previously determined useful frequency range of the impact hammer. Furthermore, the overlaid FRF functions exhibited clear alignment of modal peaks across all plots, indicating that the peaks appeared at consistent frequencies regardless of the excitation intensity. This suggests that the structure behaved linearly, thereby validating the use of experimental modal analysis.

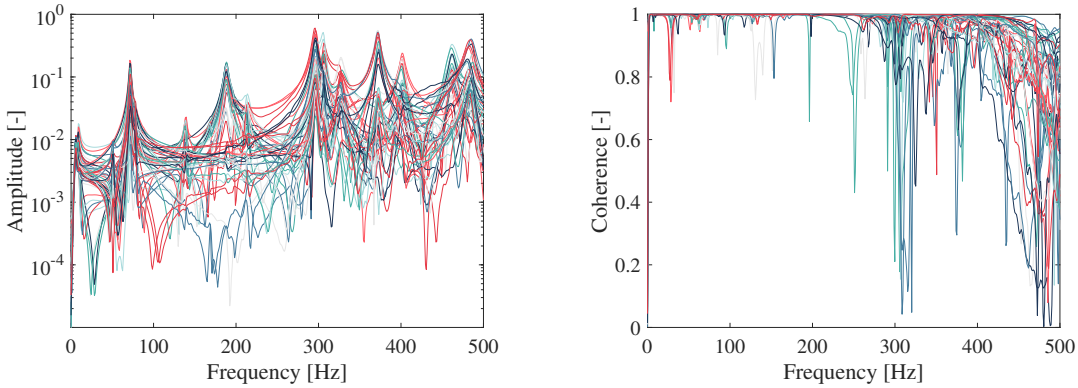

Figure 3.23: Comparison of 50 arbitrarily selected FRFs (left) and their corresponding coherence functions (right).

Modal parameters were obtained from DewesoftX using a least squares complex frequency (LSCF) curve fitting approach, as detailed in Section 2.5.5. A stabilisation chart was generated, as shown in Figure 3.24, highlighting the modal orders for which the estimated damped natural frequencies ω_k and damping ratios ζ_k varied by less than 1% and 5%, respectively.

A modal order of 24 was ultimately selected, as it yielded stable poles for the six flexural modes of interest. The highest rigid body mode and the seventh eigenfrequency were included as residual terms to improve the accuracy of the curve fitting for the first and sixth modes. The complex mode indicator function (CMIF) was used as a validation tool to verify that the identified poles corresponded to the actual system resonances. Figure 3.24 presents both the CMIF plot and the associated stabilisation chart used in the estimation process. A minor peak observed at 169 Hz suggested the presence of a local mode, which was excluded from further analysis.

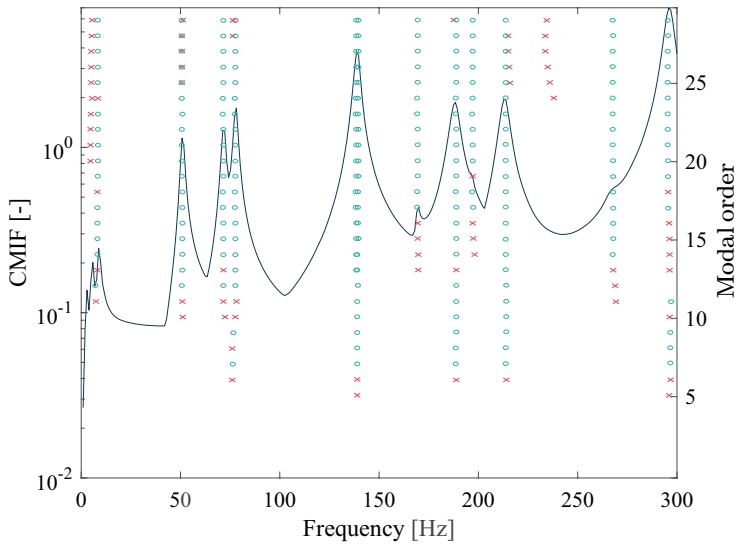

Figure 3.24: Stabilisation chart overlaid CMIF plot. A model order of 24 was found to yield stable poles for all modes of interest, as indicated by the consistent alignment between the stabilisation markers and CMIF peaks.

Four synthesised FRF plots, i.e., FRF plots generated from the derived transfer function model, are shown in Figure 3.25. As seen, the synthesised curves closely replicate the original FRFs, particularly near resonance peaks. This suggests that the obtained mathematical model effectively captures the system's dynamic behaviour within the frequency range of interest. Similar agreement was observed across all 735 individual FRFs acquired during testing.

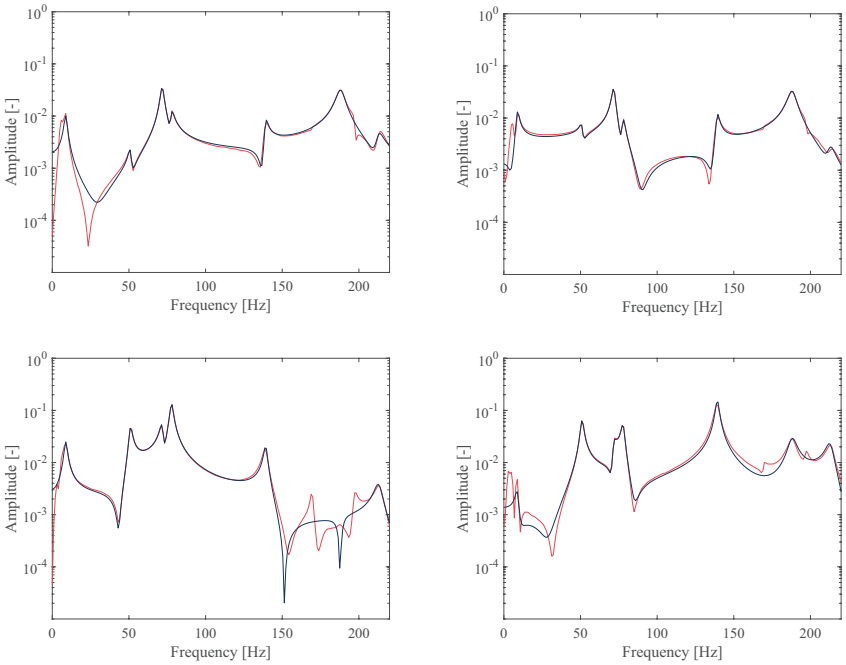

Figure 3.25: Synthesised FRFs (blue) and original frequency response functions (red) at node 40 for four of the seven accelerometers. The plotted region span from 0–220 Hz.

Resulting modal parameters are presented in Table 3.10, along with the corresponding mode complexity factors (MCF). The damping ratios have been corrected to account for the artificial damping introduced by the exponential window function. The corresponding mode shapes are shown in Figure 3.26.

As shown, the MCF is low, approximately 1% for each mode, indicating light damping and likely uncracked concrete. It suggests that the mode shapes are predominantly real and physically meaningful. The small imaginary component indicates near-proportional damping, with points vibrating largely in phase. The low MCF also reflects good data quality, as higher values often result from noise or non-linear effects.

Table 3.10: Modal parameters from LSCF curve fitting.

Mode	Description	Damped frequency [Hz]	Damping ratio [%]	MCF [%]
1	Torsion	50.94	0.57	0.73
2	Bending	71.63	0.56	1.02
3	Lateral torsional	77.74	0.49	1.10
4	Lateral torsional	138.4	0.76	1.03
5	Bending	188.1	1.06	1.05
6	Lateral torsional	212.9	0.81	1.03

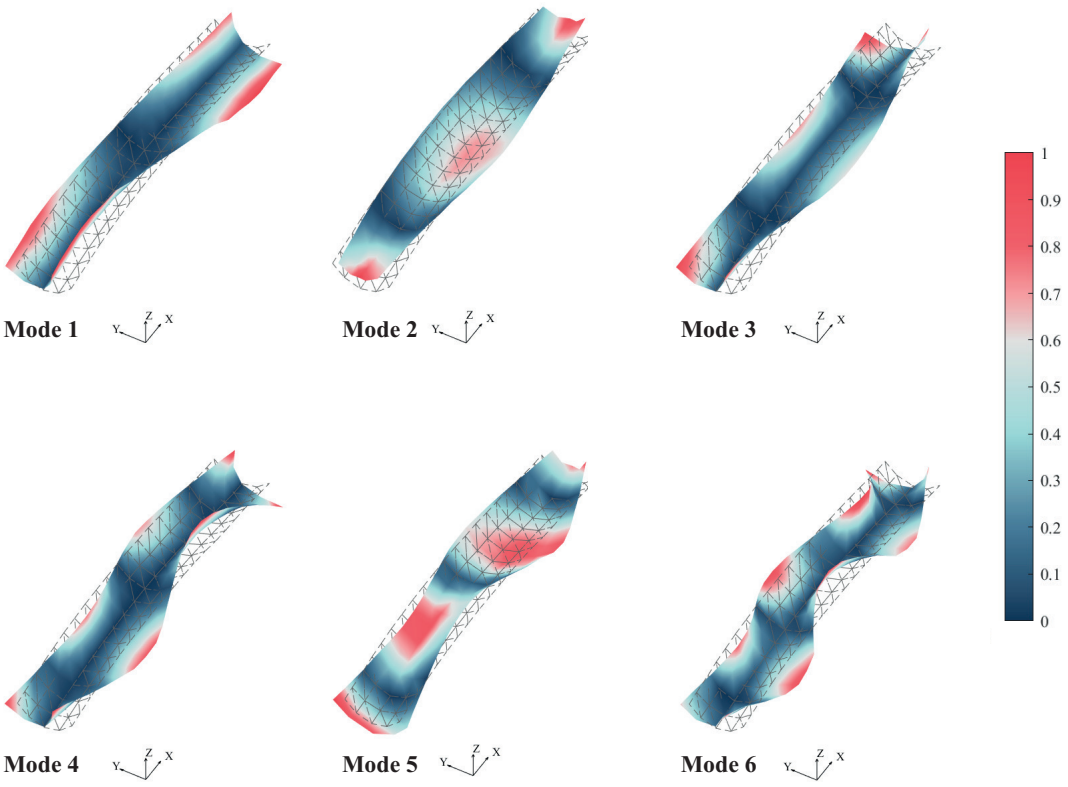

Figure 3.26: First six mode shapes from EMA. Red indicates maximum displacement (positive and negative) and blue indicate zero movement, in the surface normal direction. A reference wireframe mesh is used to visualise the undeformed shape.

By examining the mode shapes, it is evident that modes 1, 2, and 5 primarily exhibit global torsional or bending deformation, while modes 3, 4, and 6 demonstrate more complex coupled responses. It is also notable that several modes are closely spaced in frequency, particularly modes 2 and 3, and modes 5 and 6, suggesting possible mode coupling. The measured damping ratios are relatively consistent for the first three modes, with a slight increase observed in the higher modes. These higher-order modes involve more intricate deformation patterns, likely activating more localised mechanisms for energy dissipation.

According to Gidrão et al. (2024), the damping ratio of uncracked concrete typically ranges from 0.1% to 1.0% and tends to increase in the presence of microcracks, pores, or other irregularities. As noted in Section 3.2.2, the casting quality of the specimen was suboptimal, which may explain why some measured damping values are at the upper end of the expected range.

When comparing modes 2 and 5, interpreted as the first two vertical bending modes, with analytical predictions from an idealised straight Euler–Bernoulli beam model (cf. Section 3.3.1), reasonable agreement is found. For mode 2, the experimental frequency is 72 Hz, while the analytical estimate is 83 Hz (+15.3%). Similarly, mode 5 appears at 188 Hz experimentally versus 229 Hz (+21.8%) analytically. The consistently higher bending frequencies predicted by the analytical model suggest that the straight Euler–Bernoulli beam is dynamically stiffer than the prototype element. This is despite that the Euler–Bernoulli model relies on the static modulus of elasticity for concrete, making it less stiff than expected. There are several possible explanations for this discrepancy. First, the prototype element may exhibit more complex mass and stiffness coupling, where global vibrations involve both bending and in-plane stretching, thereby altering its modal characteristics. Second, the Euler–Bernoulli beam theory neglects shear deformation, which generally results in overestimation of natural frequencies. Lastly, the frequencies obtained from experimental modal analysis are damped natural frequencies and are therefore inherently lower than the undamped frequencies predicted analytically. Considering these factors, the experimentally identified bending modes may be regarded as lying within a realistic frequency range.

Three of the six rigid body modes—specifically, translation along the x- and y-axes and rotation about the z-axis—could not be accurately identified with the initial test setup. To address this, the experimental configuration was revised. All three coordinate axes of the two triaxial accelerometers were utilised, and horizontal excitation was applied in both x- and y-directions along the edges of the element. The resulting rigid body modes are presented in Table 3.11.

Table 3.11: Modal frequencies of rigid body modes.

Mode	Damped frequency [Hz]	Description
1	2.61	Rotation around x-axis
2	4.59	Translation along x-axis
3	5.41	Translation along z-axis
4	7.96	Rotation around z-axis
5	8.87	Rotation around y-axis
6	10.31	Translation along y-axis

3.3.3 Numerical modal analysis

The numerical modal analysis was performed using ABAQUS/CAE (Abaqus). The assessment was divided into three stages. First, a sensitivity study was conducted to examine the effect of reinforcement, element types and mesh densities. Secondly, boundary conditions and material properties were calibrated to align with experimental data. Finally, conclusive numerical modal analysis was performed to determine the natural frequencies and mode shapes of the prototype element.

3.3.3.1 Sensitivity study

The sensitivity study investigated the following questions:

- What impact does reinforcement modelling have on modal results?
- How does the choice of finite element type (e.g., solid vs. shell elements; quadrilateral vs. triangular meshes) influence the results?
- At what mesh density does the solution converge?

By addressing these questions, the study aimed to inform the selection of an appropriate mesh size and to improve the efficiency of the modal analysis. Both 3D solid meshes and 2D plane stress shell meshes were examined, with and without embedded reinforcement. These configurations were associated with a model index, as seen in Table 3.12. For each model, two second-order element types were considered: 10-node tetrahedral and 20-node hexahedral elements for the solid models; and 6-node triangular and 8-node quadrilateral elements for the 2D shell models. Each configuration was analysed at various element sizes: 150, 100, 75, 50, 25, and 10 mm, to assess the convergence of the solution. Figure 3.27 illustrates the two types of models.

Table 3.12: Model configurations.

Model	Element type	Reinforcement
1	3D solid	Yes*
2	3D solid	No
3	2D shell	Yes**
4	2D shell	No

*Explicitly modelled. **Modelled using the *Rebar Layers* option for shell elements in Abaqus.

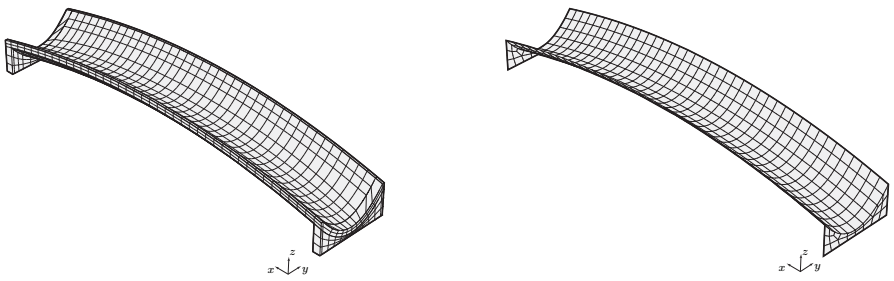

Figure 3.27: 3D solid mesh (left) using hexahedral elements and 2D shell mesh (right) using quadrilateral elements. Both models were generated in Rhino 3D and then imported into Abaqus where they were meshed (here with ~75 mm mesh size).

The free vibration behaviour of each configuration was analysed under free boundary conditions with no assigned damping, using the material parameters listed in Tables 3.5 and 3.6. At early design stages, before reinforcement layouts are finalised, it is common practice to assume a reinforcement ratio and adjust the concrete density accordingly to reflect the total mass. However, estimating the effective stiffness, EI_{eff}, is more complex since it depends on the precise location of the reinforcement bars. For this reason, models that excluded reinforcement used the effective reinforced concrete density ρ_{rc} (see Table 3.5) to compensate for the omitted mass, while the associated stiffness increment was not included in the analysis. In Model 1 and 3, the reinforcement was embedded explicitly, with no interaction defined between individual reinforcement bars.

The results revealed nearly identical trends across all four model configurations. An inverse relationship between mesh size and computed frequencies was observed, as shown in Figure 3.28a. When enlarging the frequency curves, it became evident that the eigenfrequencies consistently decreased with mesh refinement, though the magnitude of change diminished with each refinement step. For instance, in Model 4 using quadrilateral elements, the average frequency difference between 100 mm and 75 mm meshes was 0.021% across the first six modes, while the difference between 75 mm and 50 mm meshes was 0.014%. Overall, for mesh sizes of 75 mm or smaller, the eigenfrequencies were deemed to have converged in all configurations. These findings are consistent with those of Liu et al. (2011), who reported similarly converging frequency trends with decreasing mesh size.

Furthermore, the choice of element type, i.e., tetrahedral versus hexahedral, or triangular versus quadrilateral, appeared to have minimal influence on the resulting modal frequencies (see Figure 3.28b). As shown in Figure 3.29, the mode shapes were virtually identical regardless of the element type used. Nonetheless, both Liu et al. (2011) and Dassault Systèmes (2015) recommend the use of hexahedral and quadrilateral elements, as these generally offer higher accuracy and superior convergence characteristics compared to their respective alternatives. For this reason, 20-noded hexahedral and 8-noded quadrilateral elements were adopted in the subsequent analyses, despite the limited differences observed in this study. It should be noted that the hexahedral meshes were far more difficult to obtain than tetrahedral meshes, as they required pre-partitioning of the model domain.

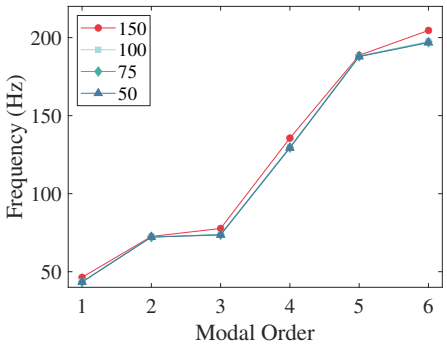

(a) Influence of mesh size.

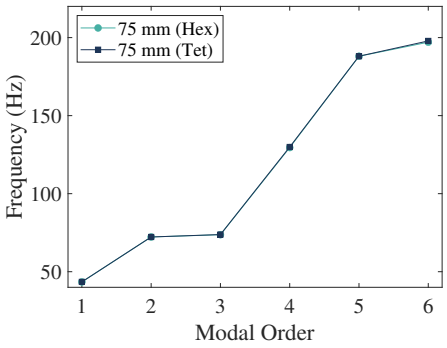

(b) Tetrahedral vs. hexahedral.

Figure 3.28: Modal convergence plots of Model 1. Similar plots were obtained for all four model configurations.

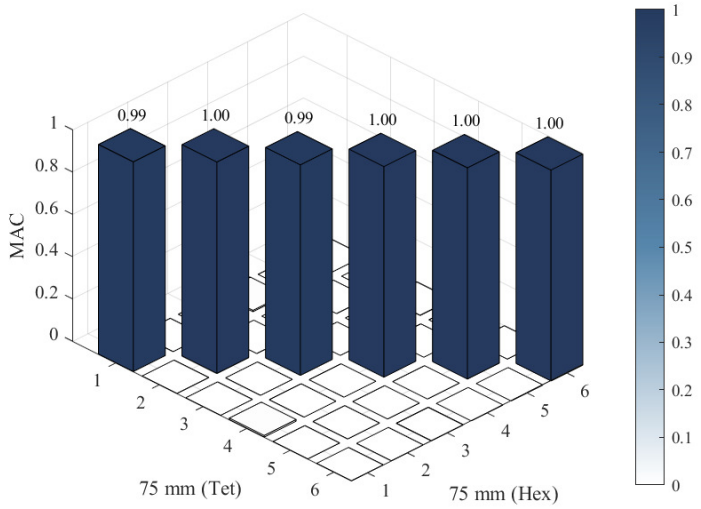

Figure 3.29: MAC comparison of Model 1 with hexahedral and tetrahedral elements.

The first six eigenfrequencies of the four model configurations are listed in Table 3.13. Model 1, assumed to provide the most accurate representation, serves as the reference for evaluating the others. Each model was discretised using an element size of approximately 75 mm with either hexahedral or quadrilateral elements.

Table 3.13: Comparison of mass and the natural frequencies for four considered numerical model setups (see Table 3.12).

	Unit	**Model 1**	**Model 2**	**Model 3**	**Model 4**
Mass	[kg]	270	265	259	272
	[%]	ref	-1.9	-4.1	+0.7
Mode 1	[Hz]	43.45	42.79	42.06	41.86
(Torsion)	[%]	ref	-1.5	-3.2	-3.7
Mode 2	[Hz]	72.25	68.84	69.13	67.02
(Bending)	[%]	ref	-4.7	-4.3	-7.2
Mode 3	[Hz]	73.71	72.49	70.63	70.13
(Lateral torsion)	[%]	ref	-1.7	-4.2	-4.9
Mode 4	[Hz]	129.5	127.3	123.1	122.2
(Lateral torsion)	[%]	ref	-1.8	-4.9	-5.7
Mode 5	[Hz]	188.1	179.9	178.8	174.0
(Bending)	[%]	ref	-4.3	-4.9	-7.5
Mode 6	[Hz]	197.1	193.2	186.1	184.4
(Lateral torsion)	[%]	ref	-1.9	-5.6	-6.4

As shown, there are some differences in total mass between the various models. Model 2 has a mass of 265 kg, which aligns with that of the intended geometry described in Section 3.2.2. This is expected, as the CAD geometry was directly imported into Abaqus.

Model 1 is approximately 5 kg heavier, as the concrete volume displaced by the embedded reinforcement has not been automatically subtracted. Model 4 is also heavier than Model 2, likely due to an increased concrete volume introduced when a shell thickness was assigned. The solid models were created by extruding the mid-surface of the element symmetrically (with the abutments extruded inward). While excess parts were trimmed in the CAD software to ensure a consistent width of 0.6 m, this trimming was not replicated in Abaqus, leading to a larger concrete volume and thus a higher mass. In Model 3, reinforcement was defined using the *Rebar Layers* option for shell elements in Abaqus, specifying bar orientations and spacings. Naturally, this method results in a less precise representation of reinforcement than Model 1, where the reinforcement geometry was explicitly modelled. Deviations in both mass and eigenfrequencies are therefore expected, and the results from Model 3 are generally not directly comparable.

According to the Rayleigh quotient, an increase in mass should lead to lower eigenfrequencies if stiffness remains constant. However, when comparing Model 1 and Model 2, this trend is not observed. Model 1, which includes embedded reinforcement, exhibits higher eigenfrequencies, indicating that the reinforcement contributes to increased stiffness. This effect is particularly evident in the bending modes (2 and 5), which deviate more significantly from Model 2 than the torsional and combined lateral torsional modes (1, 3, 4, and 6). This outcome is reasonable, as bending the element induces axial strain in the generator reinforcement, thereby increasing the overall bending stiffness. In contrast, twisting the element does probably not generate comparable stretching in the reinforcement, particularly since the transverse bars do not form closed loops. Without mechanical interaction between the bars, the torsional stiffness is primarily governed by the shear behaviour of the concrete.

Models 3 and 4 show more significant deviations from Model 1, underestimating the eigenfrequencies by approximately 3.2–5.6% and 3.7–7.2%, respectively. Similar to Model 2, Model 4 exhibits particularly large deviations in the bending modes, while the differences in other modes are comparatively smaller. As previously noted, the reinforcement implementation in Model 3, defined via the *Rebar Layers* feature in Abaqus, is less precise and makes direct comparison less meaningful.

The influence of reinforcement was further examined by comparing the mode shapes of Model 1 and Model 2, as presented in Figure 3.30. The diagonal values of the resulting MAC matrix were all less than 0.01% off from unity, indicating a near perfect correlation between the mode shapes of the two configurations. This suggests that the inclusion of reinforcement had minimal impact on the mode shapes.

In reality, the reinforcement bars were held together using cable ties. Such interaction effects were not considered in this study. Hypothetically, mechanical interaction between the bars could influence the stiffness of the element and, consequently, its dynamic characteristics. This influence may be more pronounced if the bars are welded or otherwise rigidly connected. While it could be of interest to investigate mechanical interactions between reinforcement bars in future studies, the effect is assumed to be negligible in the present case and not further assessed.

It was decided to proceed with numerical analysis using both Model 1 and Model 2. While they produced identical mode shapes, the variation in eigenfrequencies was considered important for further evaluation in comparison with the experimental results.

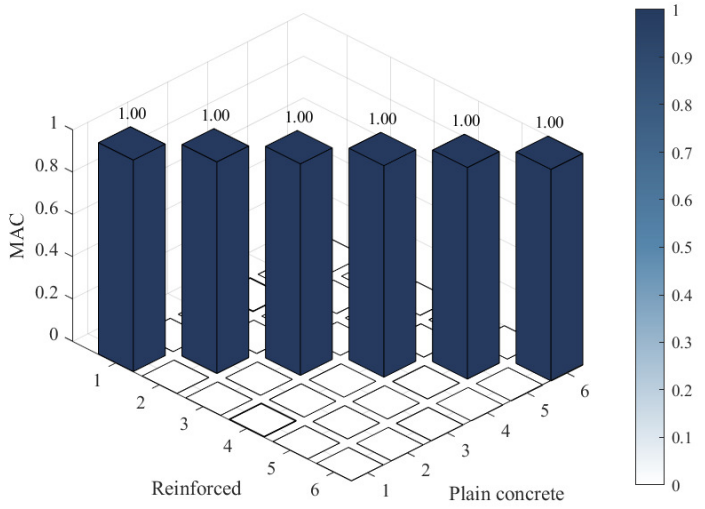

Figure 3.30: MAC comparison of Model 1 (Reinforced) and Model 2 (Plain concrete).

3.3.3.2 Influence of boundary conditions

The prototype element was supported on air springs, as described in Section 3.3.2.1. These springs provide stiffness along the z-axis through the air cushion, and along the x- and y-axes via frictional contact between the spring and the abutment. The vertical stiffness values, evaluated in Section 3.3.2.4, were approximately 55 N/mm, 90 N/mm, and 140 N/mm for air pressures of 10 psi, 20 psi, and 40 psi, respectively. The rigid body modes and first six modal frequencies were analysed numerically using Model 1 (see definition in Table 3.12) for each stiffness configuration. The corresponding results are presented in Table 3.14, based on a single nodal spring element applied at each contact centre between the springs and the abutments, as seen in Figure 3.31. Frictional contributions in the x- and y-directions were neglected in this study.

Table 3.14: Numerical eigenfrequencies [Hz] for varying vertical air spring stiffnesses in the z-direction.

		Spring stiffness $\mathbf{R_z}$		
Mode	**Description**	**55 N/mm**	**90 N/mm**	**140 N/mm**
RB	Highest RBM	7.18	9.18	11.44
1	Torsion	43.96	44.26	44.68
2	Bending	72.59	72.81	73.12
3	Lateral torsion	74.12	74.26	74.47
4	Lateral torsion	130.19	130.27	130.38
5	Bending	188.19	188.24	188.33
6	Lateral torsion	198.16	198.20	198.25

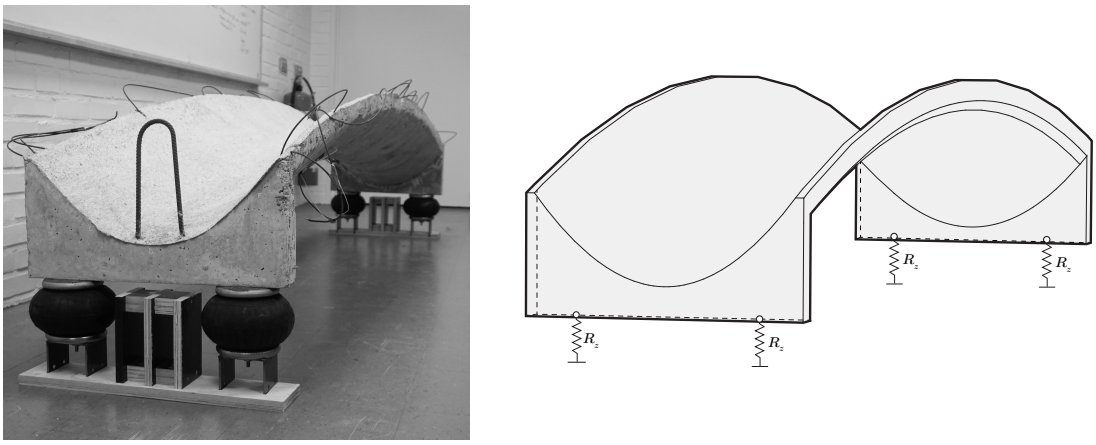

(a) Experimental setup. **(b)** FEA representation.

Figure 3.31: The boundary conditions were modelled using spring elements.

The behaviour closely resemble that observed in the experimental modal analysis. The frequency of the highest rigid body mode is significantly more affected by increased vertical stiffness compared to the flexural modes. Moreover, the influence of stiffness diminishes for higher modes, which is to be expected Brandt (2011). For instance, the frequency of the fundamental mode increases by approximately 1.5% when the spring stiffness is raised from 55 N/mm to 140 N/mm, whereas the change for mode 6 is only about 0.05%.

An additional study was conducted to examine the influence of frictional stiffness between springs and abutments. The rigidity along the x- and y-axes are inherently more complex to estimate and model. It was decided to model the frictional stiffness through springs. Three base cases were considered using springs with stiffness values of 100 N/mm, 200 N/mm and 300 N/mm, based on engineering judgement. The results, presented in Table 3.15, assume a vertical air spring stiffness of 90 N/mm.

Table 3.15: Numerical eigenfrequencies [Hz] for different restraints in the x- and y-directions, with z-direction fixed at 90 N/mm.

	Spring stiffness $\mathbf{R_x = R_y}$				
Mode	**Free**	**100 N/mm**	**200 N/mm**	**300 N/mm**	**Rigid**
RB	9.18	10.47	14.04	16.89	8.88
1	44.26	44.83	45.43	46.09	41.11
2	72.81	72.99	73.17	73.35	86.92
3	74.26	74.32	74.38	74.44	96.33
4	130.27	130.33	130.40	130.47	112.26
5	188.24	188.35	188.46	188.57	145.82
6	198.20	198.27	198.34	198.42	164.03

It was found that the dynamic characteristics changed significantly when the element was fully restrained in the x- and y-directions using infinitely stiff springs. A low correlation is observed in Figure 3.32 between this fully restrained case and those with either no or partial restraint in the x- and y-directions.

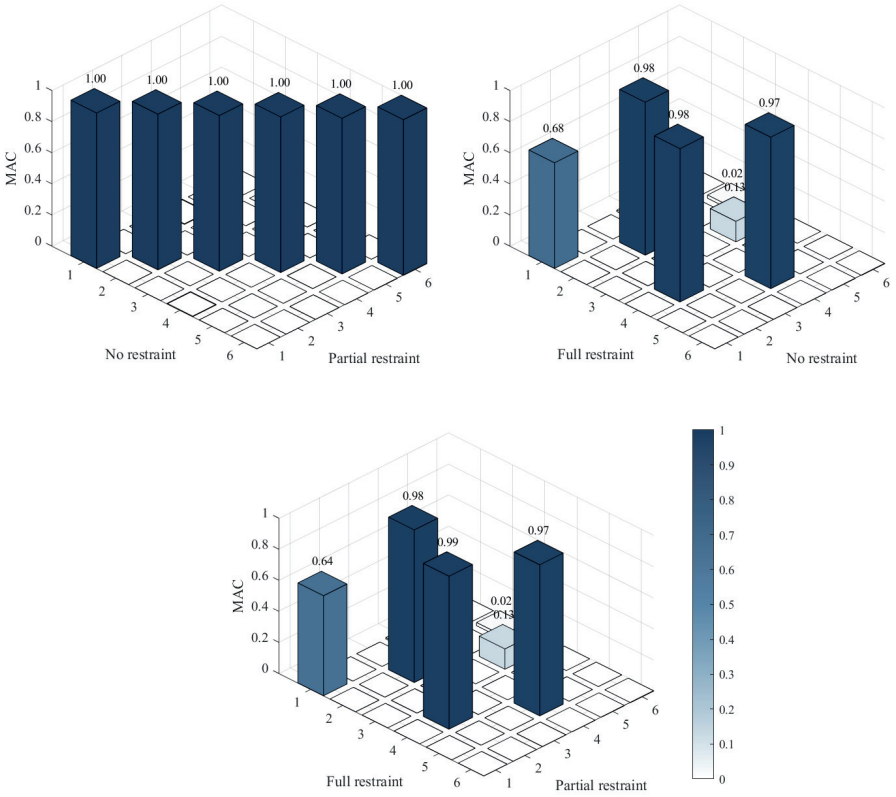

Figure 3.32: MAC matrices comparing the influence of restraining the element in the x- and y-directions. Partial restraint refers to 100 N/mm.

The degree to which the prototype element was restrained in-plane was not further validated in this thesis. Instead, the restraints were calibrated by aligning the rigid body modes of the numerical model with those obtained experimentally. This calibration procedure is explained further in Section 3.3.3.3.

3.3.3.3 Model calibration

Up to this point, the numerical modal analysis has relied on nominal material parameters that likely fail to capture the true behaviour of the prototype element. For example, the concrete has been assigned static stiffness properties, which may underestimate its actual stiffness under dynamic loading. Moreover, the frictional restraint between the abutments and spring supports remains unverified and has been represented by arbitrary spring stiffnesses.

Accurately representing the mass and stiffness distribution of the prototype in the finite element models is inherently challenging for several reasons. First, it was not feasible to construct models that fully accounted for all imperfections and deviations observed in the cast element (see Section 3.2.2). Second, the precise placement of the reinforcement was not documented and could not be reliably verified. Third, the interaction between reinforcement due to tying was not evaluated. Lastly, neither the exact density nor the stiffness of the concrete could be determined with certainty, as these properties are sensitive to factors such as the degree of compaction.

Instead idealised models had to be used, referencing the intended geometry and reinforcement layout. Both Model 1 and Model 2 (see definitions in Table 3.12) were calibrated to align with experimental results. The mass of the cast prototype element was considered to be relatively well established from weigh-ins (see Section 3.2.2). The mass of the FE-models were adjusted to align with this real mass. Stiffness properties of the steel reinforcement was also assumed to be known and fixed. However, stiffness properties of the concrete, including modulus of elasticity and Poisson's ratio, were assumed to be less established. These parameters were adjusted to minimise the error against experimentally observed damped natural frequencies.

Modal damping was excluded from the numerical models, as the calibration focused solely on matching eigenfrequencies obtained from EMA. Although EMA provided modal damping ratios, Abaqus supports only Rayleigh damping, which imposes uniform damping across all modes. Applying an average damping ratio would be physically inconsistent and offer no benefit. Since the models are calibrated against damped natural frequencies from EMA, introducing proportional damping in the FEA would merely redistribute contributions between the mass and stiffness matrices without affecting the overall dynamic stiffness.

Calibration of mass

As discussed in the sensitivity study (Section 3.3.3.1), Abaqus does not automatically subtract the volume of concrete displaced by embedded reinforcement in Model 1. This results in a finite element model with excess mass and stiffness. Several options may be considered to address the mass discrepancy in Model 1:

a) Perform a boolean subtraction of the reinforcement geometry from the concrete in Abaqus, then reduce the concrete density to match the measured total mass of the cast element.

b) Reduce the steel density to compensate for the overestimated mass in regions where concrete and reinforcement overlap, then adjust the concrete density to achieve the correct total mass.

c) Same as option a) or b), but without adjusting the concrete density, i.e., retain the total mass of the idealised element.

d) Reduce only the concrete density to align with the measured total mass.

Although Abaqus supports boolean operations, option a) leads to overly complex geometry requiring extensive partitioning or manual meshing, making it impractical for this study. Option d) uniformly reduces mass across the model, failing to target areas of overlap, and thus yields a less accurate representation of the mass distribution, compared to options b) and c). Ultimately, option b) was adopted. It ensured that the total mass of the numerical model matched that of the prototype element, thereby ruling out incorrect mass as a potential source of deviation in comparisons with the experimental results. While the local mass distribution may still deviate, the alignment in total mass increases confidence that any observed discrepancies are due to other factors than incorrect inertia. Adopting option b) the densities of steel and concrete were adjusted as per Table 3.16 for Model 1. Similarly, the effective density of concrete were adjusted for Model 2, also shown in Table 3.16.

Table 3.16: Adjusted steel and concrete densities to align the total mass of Model 1 and Model 2 with that of the cast prototype element.

Model	Material	Old density [kg/m^3]	New density [kg/m^3]	Change [%]
Model 1	Concrete (ρ_c)	2,363	2,294	-2.9
	Reinforcement (ρ_s)	7,850	5,756	-26.7
Model 2	Concrete (ρ_c)	2,476	2,407	-2.8

Calibration of support conditions

To ensure consistency with experimental observations, the nodal spring stiffnesses R_x, R_y, and R_z were iteratively adjusted so that the rigid body modes computed numerically aligned with those recorded experimentally (see values in Table 3.11). As an example, R_x was modified until the translational RBM in the x-direction matched the experimental value. A similar adjustment was carried out for the y- and z-directions. The resulting calibrated values are shown in Table 3.17.

Table 3.17: Calibrated stiffness values of spring elements.

Spring	Stiffness [N/mm]
R_x	220
R_y	40
R_z	90

Calibration of stiffness

In the same way that the mass of Model 1 was corrected to address the double-counting of overlapping volumes, the modulus of elasticity (MoE) of steel could, in principle, be adjusted to compensate for the additional stiffness introduced by these overlaps. However, based on recommendations from the thesis supervisors, this approach was not pursued. It was recommended to assign a nominal and physical meaningful elasticity to the steel, under the assumption that this property could be assumed with high confidence. In contrast, the dynamic MoE and Poisson's ratio of the concrete was considered to be more uncertain. As such, the stiffnesses of the models were calibrated solely by adjusting the concrete's MoE and Poisson's ratio, potentially leading to an inaccurate representation of stiffness distribution in Model 1.

According to Neville (2011), the Poisson's ratio for normal, uncracked concrete typically ranges from 0.1 to 0.2. The static modulus of elasticity is generally between 27–37 GPa (Al-Emrani et al., 2011), while the dynamic modulus can be expected to be approximately 15% higher.

The stiffness of Models 1 and 2 was calibrated through a gradient-based error minimisation approach. The objective function was defined as the error between numerical natural frequencies and experimentally obtained damped natural frequencies, evaluated over a parameter space defined by Poisson's ratio ($0.1 \leq \nu \leq 0.2$) and concrete modulus

of elasticity ($27 \leq E \leq 33$ GPa). While it would have been possible to include mode shape discrepancies in the minimisation process, this metric was ultimately excluded. Preliminary analyses indicated that variations in concrete stiffness had a negligible effect on mode shapes, rendering their inclusion in the calibration unnecessary.

Figure 3.33 presents contour plots showing how variations in Poisson's ratio and modulus of elasticity influence the frequency error in Model 1, separated by mode type.

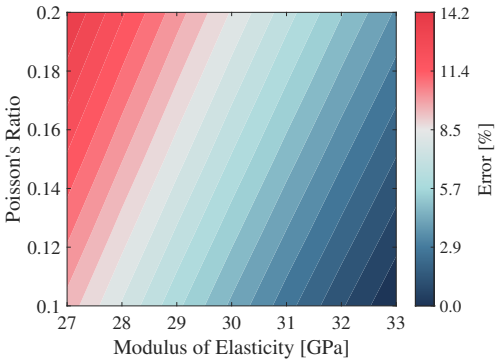

(a) 1st torsion mode.

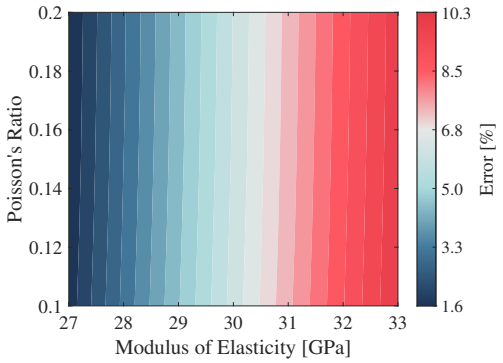

(b) 1st and 2nd bending mode.

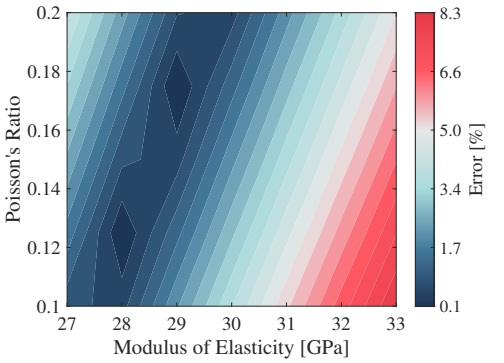

(c) 1st combined lateral torsional mode.

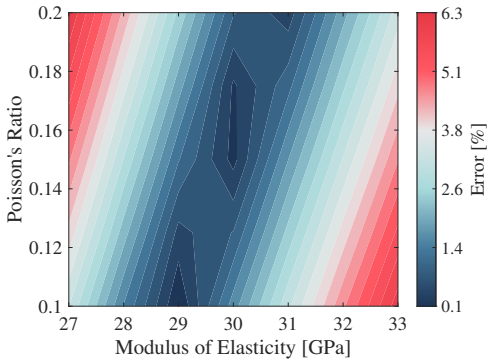

(d) 2nd combined lateral torsional mode.

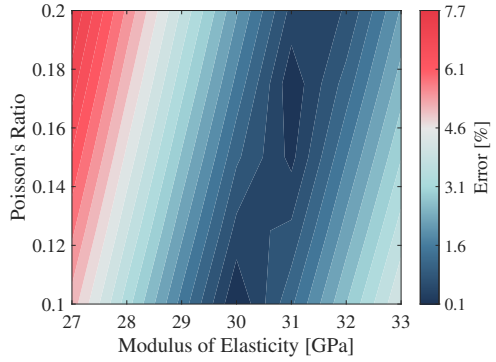

(e) 3rd combined lateral torsional mode.

Figure 3.33: Contour plots of the percentage error in eigenfrequencies when varying Poisson's ratio and modulus of elasticity for Model 1.

The torsional mode (a) and the pure bending modes (b) evidently exhibit contrasting behaviour. The frequency error of the torsional mode decreases for larger values of E and smaller values of ν. Zero error is obtained at $E = 33$ GPa and $\nu = 0.1$. Conversely,

the error of the bending modes decreases for smaller values E, independently of the Poisson's ratio. Zero error is found at around $E = 26$ GPa (outside the bounds of the plot). While bending stiffness is directly proportional to E, the torsional stiffness is proportional to the shear modulus G, given by $G = E/(2(1+\nu))$ for isotropic materials. A larger MoE and smaller Poisson's ratio yields a greater torsional stiffness.

These results suggest that Model 1 is overly stiff in bending and insufficiently stiff in torsion relative to the actual prototype element. As a result, it is not possible to identify a single combination of E and ν that simultaneously minimises both bending and torsional frequency errors; they lie at opposite ends of the parameter space. In other words, Model 1, as currently configured, cannot be tuned to simultaneously capture both behaviours accurately. This suggests that the model fails to reflect key aspects of the physical behaviour, possibly caused by, e.g., anisotropy, interaction effects, or structural details that have not been accurately represented. As a result, there is a risk of masking critical torsional or bending deficiencies, which may have significant implications in design and safety assessments.

The contour plots of the optimisation for lateral-torsional bending modes (Figures 3.33c to 3.33e) exhibit similar trends, with local minima recurring along distinct parameter bands. Again, no single combination of E and ν exist that simultaneously minimises the errors for all lateral torsional modes.

One possible reason why Model 1 cannot simultaneously capture both bending and torsional behaviours accurately is an inaccurate representation of the reinforcement, which may introduce non-physical stiffness anisotropy. As previously discussed, no adjustment was made for overlapping regions of concrete and reinforcement. For completeness, it could have been useful to examine a case where such adjustments were applied. To further evaluate the role of reinforcement, parameter optimisation was also performed for Model 2. As shown in Figure 3.34, the results closely matched those of Model 1. This suggests that the inclusion of reinforcement alone is unlikely to explain why it is not possible to capture the correct bending and torsional behaviours.

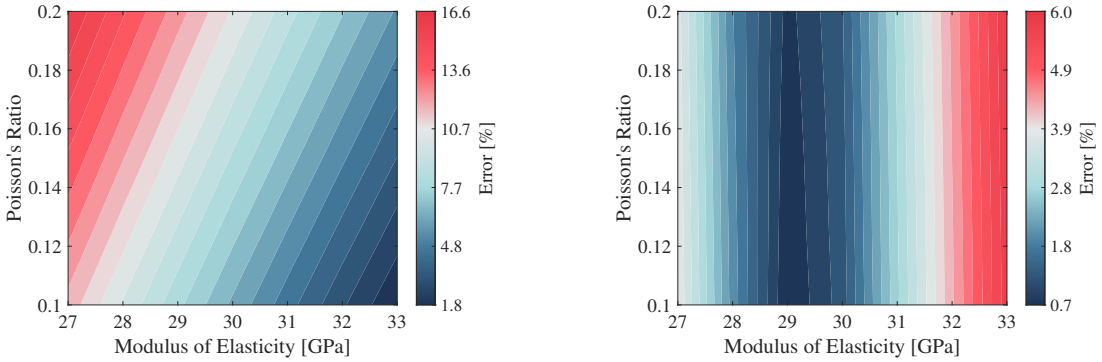

(a) 1st torsion mode.

(b) 1st and 2nd bending mode.

Figure 3.34: Contour plots of the percentage error in eigenfrequencies when varying Poisson's ratio and modulus of elasticity for Model 2.

It is sensible that it is not possible to capture both behaviours accurately in Model 2 as it assumes a homogenous and isotropic stiffness across the whole geometry. It is expected that the reinforcement in the element would introduce some anisotropy and

stiffness variance. This is also observed in the comparison between Model 1 and 2. Notably, Model 1 exhibits inherently higher bending and torsional stiffness. To match the torsional error of Model 1, the shear modulus G in Model 2 must be increased by approximately 3%. Similarly, achieving the same bending error requires increasing the modulus of elasticity E by about 12%.

Alternatively, the inability to simultaneously capture both bending and torsional behaviours may stem from inaccuracies in the geometric stiffness representation. The prototype element may possess higher torsional stiffness or lower bending stiffness than what is reflected in the current finite element models. One potential explanation is the omission of interaction effects between longitudinal and transverse reinforcement, which could contribute to additional torsional stiffness and stiffness coupling. Neglecting this interaction may result in an overestimation of bending stiffness relative to torsion. To confirm this hypothesis, a dedicated sensitivity study would have been required, investigating different levels of connectivity between reinforcement bars. Additionally, geometric imperfections, such as deviations in curvature, asymmetry, or thickness variation introduced during casting, could also alter the stiffness distribution and contribute to the model's inability to accurately capture both bending and torsional behaviour. As observed when comparing the mode shape plots (see Figure 3.39), the EMA results exhibit more pronounced asymmetry in the mode displacements, particularly in the bending modes, compared to the numerical models. This discrepancy is likely attributable to the aforementioned geometric imperfections.

The modulus of elasticity and Poission's ratio were tuned to minimise the average error for the six observed modes for both models. The average error for the two models, shown in Figure 3.35, will inevitably be biased towards specific parameter combinations. Since there are two bending modes but only one torsional mode, the optimisation favours parameter sets that better fit the bending behaviour, thereby shifting the minimum average error closer to the bending-optimal region. At the same time, because the torsional mode occurs at a lower frequency, its error carries relatively more weight in the optimisation. An absolute error of 1 Hz constitutes a larger percentage error in a low-frequency mode than in a high-frequency mode. As a result, the same absolute deviation is penalised more heavily in lower modes, increasing their influence on the optimisation outcome.

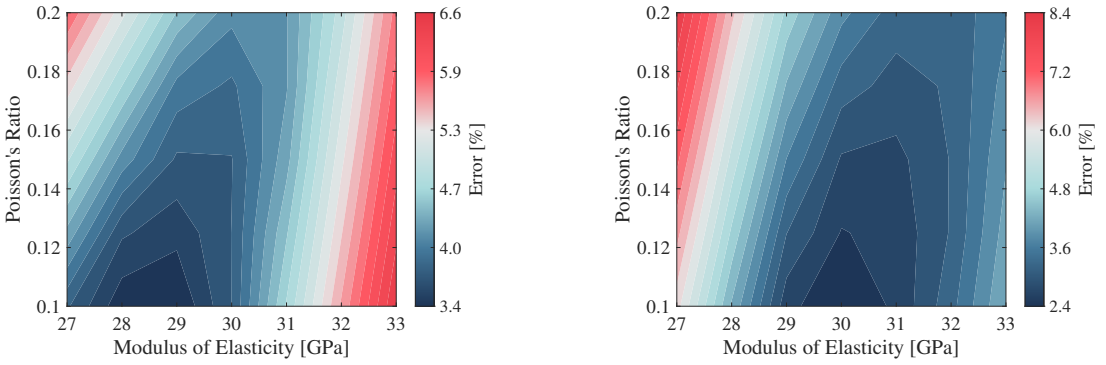

(a) Model 1.

(b) Model 2.

Figure 3.35: Contour plots of the average percentage error in eigenfrequencies when varying Poisson's ratio and modulus of elasticity for Model 1 and 2.

Model 1 was calibrated to achieve an average frequency error of 3.35% across the six modes using $E = 29$ GPa and $\nu = 0.1$. Model 2 reached a lower average error of 2.36% with $E = 30$ GPa and $\nu = 0.1$.

A MAC plot comparing both model configurations with the experimental data is shown in Figure 1.35. The comparison between Model 1 and Model 2 yielded identical mode shapes, as indicated by values of unity along the diagonal. Both models also demonstrate good agreement with the experimental results. The first bending mode (mode 2) exhibited the lowest correlation with a MAC value of 0.9202 for Model 1, and 0.9208 for Model 2. Four modes (modes 1, 3, 4, and 6) displayed MAC values exceeding 0.95 and can thus be considered closely correlated, in line with the criteria proposed by Abrahamsson (2019). The two bending modes (modes 2 and 5) yielded MAC values of approximately 0.92 and 0.94, respectively, for both models—above the commonly accepted threshold of 0.8 for poor correlation but slightly below the 0.95 cut-off for close correlation. According to Abrahamsson (2019), this range falls within a so-called 'grey zone', where correlation is neither clearly strong nor weak.

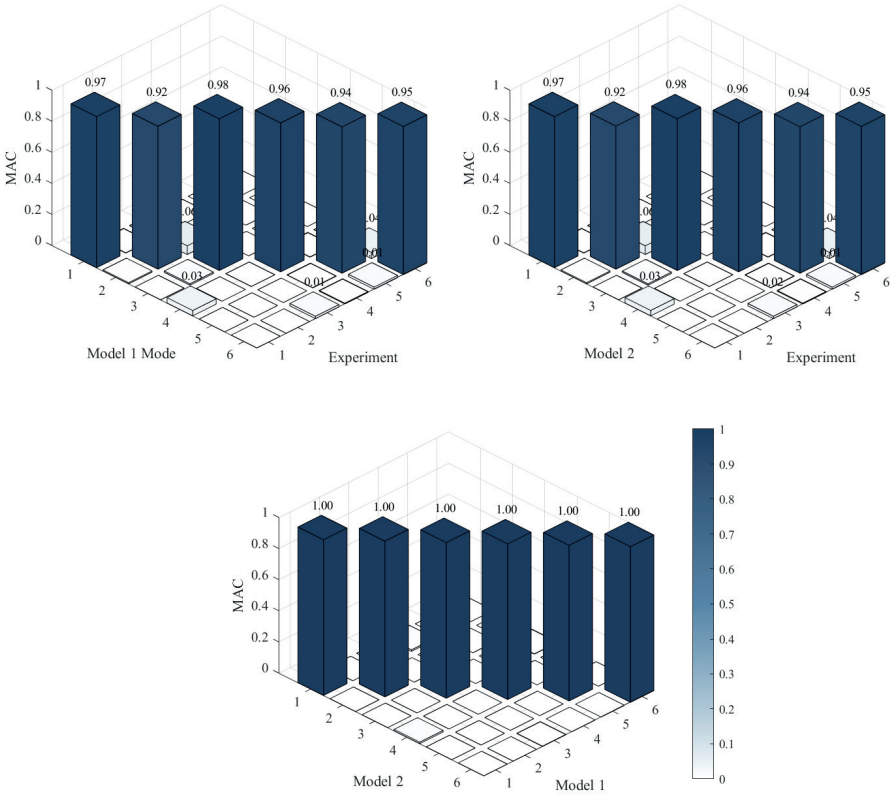

Figure 3.36: MAC matrices of experimental results the updated material parameters of model 1 and 2.

3.3.3.4 Modal parameter extraction

The eigenfrequencies and corresponding mode shapes were extracted from Abaqus using Model 1 (see definition in Table 3.12), which employed 3D solid elements with spring supports, as illustrated in Figure 3.37. The model was calibrated as described in Section 3.3.3.3, with the modulus of elasticity set to $E = 29$ GPa and Poisson's ratio to

$\nu = 0.1$. Spring stiffness values R_x, R_y, and R_z were applied according to Table 3.17. Damping was omitted from the analysis, following the discussion in Section 3.3.3.3. Tables 3.18 and 3.19 display the frequency values of the first six flexural modes and six rigid body modes, respectively. The corresponding mode shapes of the six flexural modes are depicted in Figure 3.38

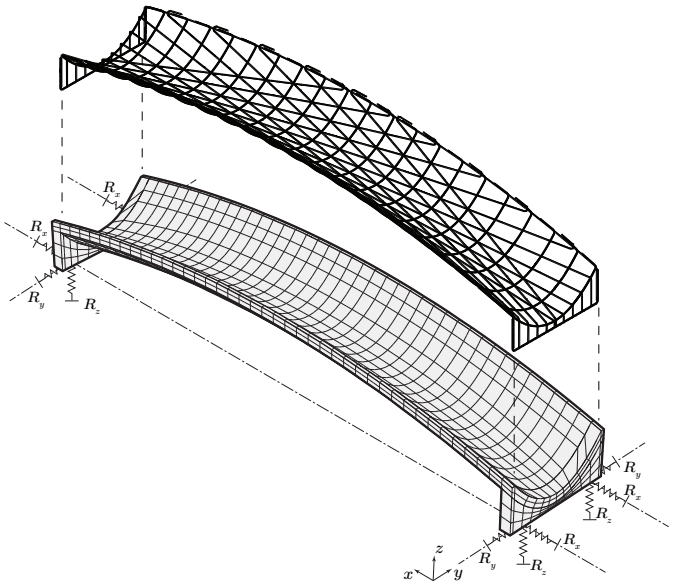

Figure 3.37: Finite element model of Model 1, partially restrained in four nodes by spring elements in the x, y, and z-direction. 20-noded hexahedral element types (C3D20R) were used with an approximate size of 75 mm.

Table 3.18: Eigenfrequencies of first six flexural modes.

Mode	Frequency [Hz]	Mode description
1	47.89	1st torsion mode (x-axis)
2	75.89	1st bending mode (y-axis)
3	79.60	1st combined lateral torsional mode (z- and x-axis)
4	138.6	2nd combined lateral torsional mode (z- and x-axis)
5	196.0	2nd bending mode (y-axis)
6	209.2	3rd combined lateral torsional mode (z- and x-axis)

Table 3.19: Eigenfrequencies of rigid body modes.

RBM	Frequency [Hz]	Type
1	2.89	Rotation around x-axis
2	5.90	Translation along z-axis
3	6.40	Rotation around z-axis
4	7.77	Translation along y-axis
5	8.15	Translation along x-axis
6	10.56	Rotation around y-axis

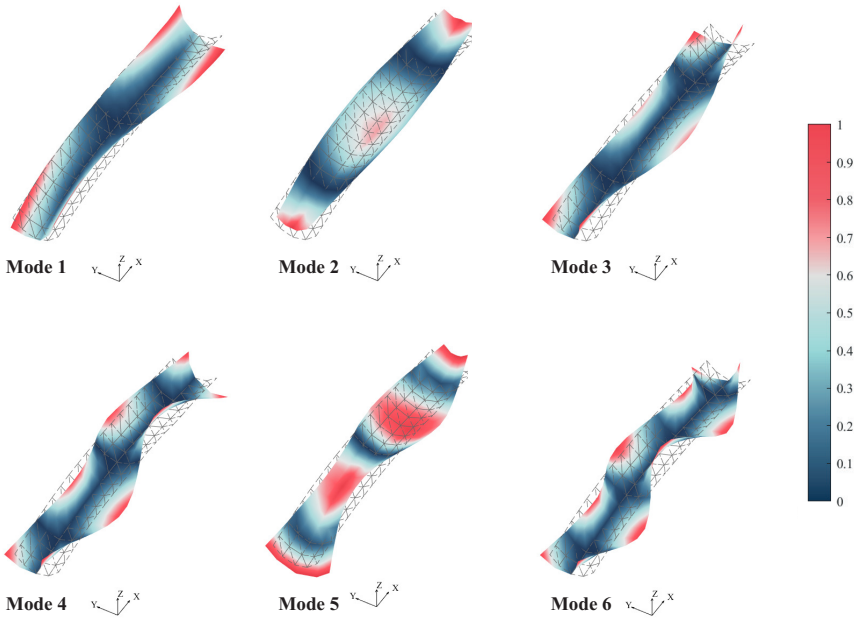

Figure 3.38: First six mode shapes. Red indicates maximum displacement (both positive and negative) and blue indicate zero movement. A reference wireframe mesh is used to visualise the undeformed shape.

3.3.4 Summary of results

This section provides a summary of the results obtained from the experimental modal analysis (EMA) (Section 3.3.2) and numerical modal analysis (NMA) (Section 3.3.3) of the prototype element. The first six mode shapes from each analysis are presented in Figure 3.39, and the corresponding natural frequencies are listed in Table 3.20. A MAC comparison between the experimental and numerical mode shapes is shown in Figure 3.40. The section concludes with a list of key observations from the two assessments. Note that all natural frequencies obtained from the experimental analysis are *damped*, whereas those from the numerical analysis are *undamped*.

Table 3.20: Comparison of natural frequencies between numerical and experimental results.

Mode	**Description**	**Numerical*** [Hz]	**Experimental**** [Hz]	**Difference** [%]
RB	Highest RBM	10.56	10.31	-2.37
1	Torsion	47.9	50.9	+6.26
2	Bending	75.9	71.6	-5.67
3	Lateral torsion	79.6	77.7	-2.39
4	Lateral torsion	138.6	138.4	-0.01
5	Bending	196.0	188.1	-4.03
6	Lateral torsion	209.2	212.9	+1.78

*Undamped. **Damped.

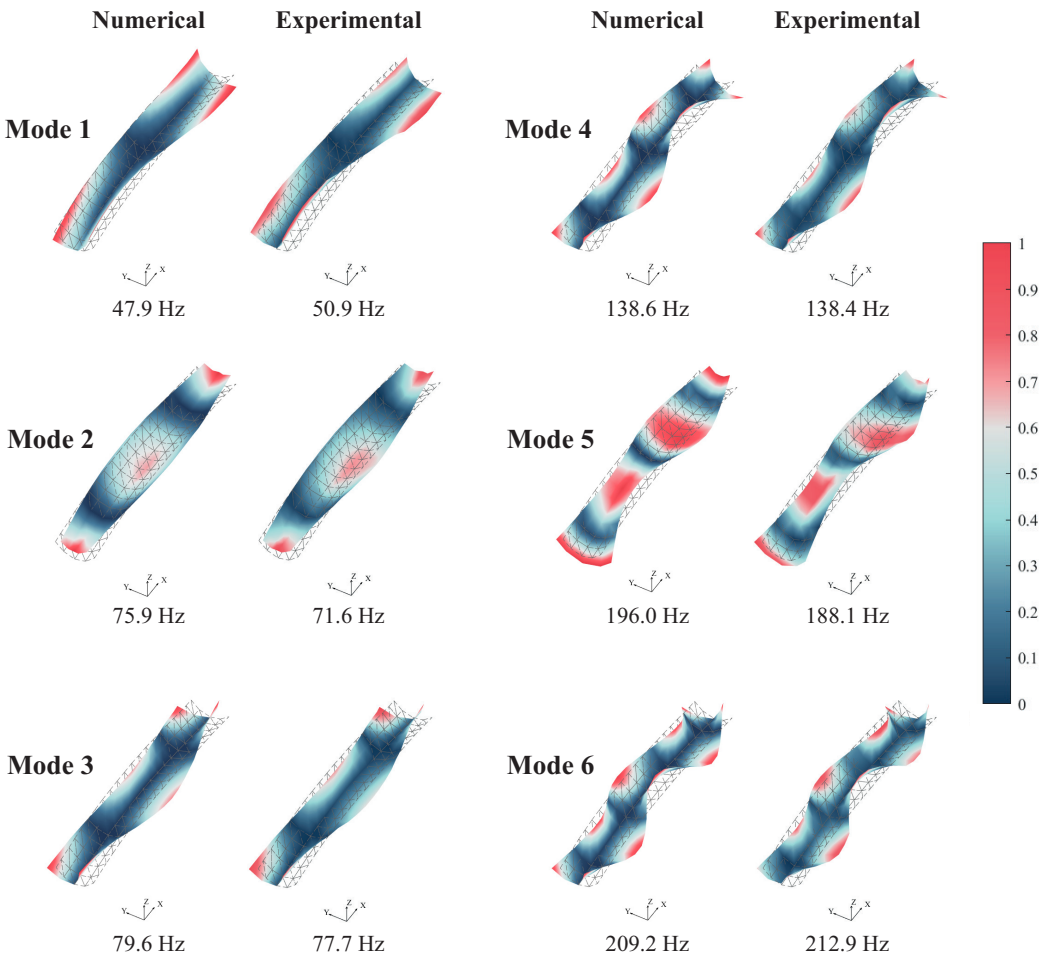

Figure 3.39: Mode shape comparison between experimental and numerical analysis.

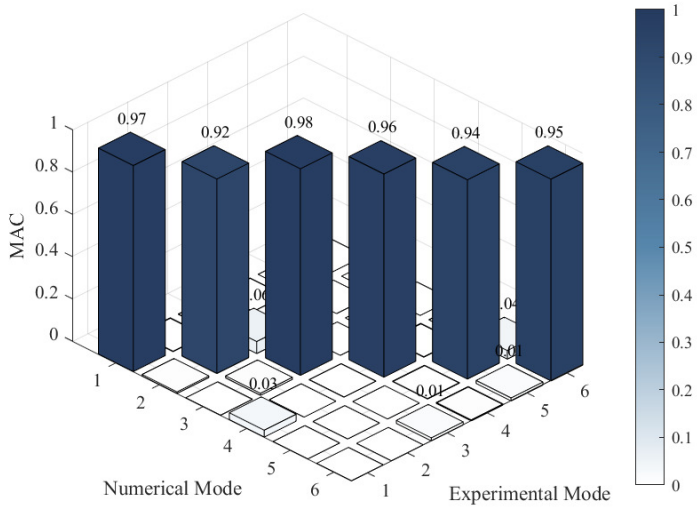

Figure 3.40: MAC comparison between experimental and numerical results.

A summary of the key observations is provided below:

Experimental modal analysis (EMA):

- Six distinct flexural modes were identified below 220 Hz, with the lowest mode occurring at 50.9 Hz. Among these, one torsional mode, two pure bending modes, and three coupled lateral-torsional modes were observed. A seventh mode was detected at around 300 Hz, past the upper limit of the impact hammer's useful frequency range, and was excluded due to poor coherence.
- The structure exhibited linear dynamic behaviour, with coherence values approaching unity across all resonance peaks below 300 Hz.
- Two closely spaced mode pairs were identified: the first separated by less than 5 Hz, and the second by less than 15 Hz, suggesting possible mode coupling.
- All six rigid body modes were successfully identified, with the highest occurring at 10.31 Hz, equivalent to 20.3% of the fundamental mode frequency. Although this mode could be lowered further through support tuning, its influence on the flexural modes was found to be negligible.
- The modal complexity factor (MCF) ranged from 0.73% to 1.1% (see Table 3.10), indicating well-defined and predominantly real mode shapes.
- Modal damping ratios ranged from 0.56% to 1.1% (see Table 3.10), consistent with typical values for lightly damped concrete structures.
- Both vertical bending modes occurred at frequencies lower than those predicted using a straight, idealised, Euler-Bernoulli beam (see Section 3.3.3.1).

Numerical modal analysis (NMA):

- The NMA results were relatively insensitive to mesh refinement, with eigenfrequencies converging at mesh sizes of approximately 75 mm. Additionally, the choice of element type (e.g., tetrahedral versus hexahedral) had minimal influence on results. Some discrepancies were observed between models using 3D solid and 2D shell elements; 3D solid elements were ultimately adopted.
- Inclusion of reinforcement had limited impact on mode shapes but noticeably influenced eigenfrequencies, especially bending mode frequencies (see results in Section 3.3.3.1).
- The dynamic response was notably sensitive to the assumed boundary conditions. While vertical support stiffness had limited influence beyond the rigid body modes, frictional restraint in the horizontal directions (x and y) had a more pronounced effect on both eigenfrequencies and mode shape correlation (see Figure 3.32).
- Regardless of the configuration of material parameters, the numerical models were unable to accurately capture the bending and torsional behaviour observed in the EMA, simultaneously.

3.3.5 Discussion

Much of the results obtained from the experimental and numerical modal analyses have been discussed in their respective sections (Sections 3.3.2 and 3.3.3). This concluding discussion shifts focus from individual results to an assessment of the overall modelling approach, highlighting areas of mismatch between numerical and experimental results, and proposing potential underlying causes and improvements. It outlines key limitations, and suggests strategies to improve future simulations and experimental setups. The aim is to support more reliable interpretation of modal behaviour through better-integrated numerical and experimental analyses.

The analyses showed that the first six mode shapes and corresponding natural frequencies of the prototype element, as identified in the numerical modal analysis (NMA), closely matched those observed in the experimental modal analysis (EMA). This alignment supports the general validity of the modelling approach. However, several limitations and opportunities for improvement were identified.

Although strong correlation was achieved for the first six mode shapes, the numerical models were unable to simultaneously reproduce the bending and torsional behaviour observed in the EMA, regardless of material parameter configurations of the concrete. This indicates that applied idealised assumptions regarding geometry, reinforcement properties, and boundary conditions may not fully capture the real structural response.

A key simplification was the use of an idealised geometry, whereas the actual specimen exhibited geometric imperfections introduced during casting, including asymmetry, curvature deviations, and thickness variations. These aspects likely influenced the stiffness distribution, particularly for coupled modes. Future studies could improve accuracy by basing numerical models on scanned geometries, thereby incorporating geometric irregularities that are otherwise neglected. An alternative or complementary approach could involve introducing stochastic perturbations in the numerical model, by randomly varying the stiffness and mass properties of individual elements to simulate the effects of air voids and material inconsistencies. Different levels of variability could be studied systematically. Such perturbations could also be applied in a spatially controlled manner, focusing on specific regions where irregularities are likely to occur—for example, to simulate thickness variations or known voids near the abutment—by adjusting parameters within predefined zones.

Reinforcement was considered only in simplified terms—either fully included or omitted—and interactions between the bars or with the surrounding concrete were not explicitly modelled. Future work could explore more realistic assumptions, for example by introducing interface elements to simulate the mechanical interlocking between individual bars. Investigating such interactions may improve understanding of the reinforcement's contribution to stiffness and modal characteristics.

Experimental modal analysis on a specimen without reinforcement could help isolate the reinforcement's influence on modal properties. This approach would require improved production control to ensure that observed differences are not caused by manufacturing defects. Similarly, performing modal analysis on the reinforcement cage alone could provide additional insights, particularly regarding its directional stiffness contributions. It is currently assumed that the reinforcement has limited effect on the torsional stiffness of the element, and this hypothesis could be further evaluated through

such targeted investigations.

The material properties used in the numerical analysis were estimated or calibrated rather than directly measured. Parameters such as the dynamic modulus of elasticity and Poisson's ratio of the concrete were inferred, introducing a degree of uncertainty. A more rigorous approach would involve laboratory testing of the cast concrete to experimentally determine these values. Techniques such as ultrasonic pulse velocity (UPV) or the impact-echo method (cf. Section 2.6.3.1) could be applied directly to the prototype element, or to separate plain-concrete cubes or cylinders to avoid interference from reinforcement. If material properties were obtained experimentally, the current calibration step—where concrete stiffness is manually tuned—could be eliminated. This would allow for the use of physically justified input parameters, meaning that any remaining deviations between numerical and experimental results would likely stem from other modelling assumptions rather than uncertainties in the material behaviour. Such an approach could help identify the true sources of discrepancies. In addition, the prototype element exhibited inconsistent compaction and geometric irregularities, which may have contributed to the observed differences. Casting additional specimens with improved quality control, e.g., with better vibration during casting, could help reduce variability and isolate specific effects.

The conducted experimental modal analysis relied on the assumptions that the studied HP prototype element behaves as a linear and time-invariant system. While concrete structures are known to exhibit time-dependent behaviour such as stiffness development and shrinkage strain accumulation, these effects were assumed minimal over the short testing period of a few days. Furthermore, the relatively low-energy excitations employed in this study ensured the structure remained uncracked and within its linear-elastic range. The assumptions of linearity and time-invariance were further supported by the observed consistency of modal parameters across repeated tests with different hammers on separate days. These findings support the validity of using EMA to evaluate the modal characteristics of the HP prototype element. Future investigations could provide further validation of these assumptions by analysing the system's response under higher excitation amplitudes and at different concrete ages, thereby assessing the onset of non-linear behaviour and the effects of time-dependent material evolution on dynamic performance.

To improve comparison with numerical models, it is valuable to identify a broader set of vibration modes. The experimental assessment was limited to the first six modes due to the frequency range of the impact hammer. A harder hammer tip could extend the excitation range and reveal higher-frequency modes, offering a broader basis for validation. Alternative excitation methods, such as shaker excitation, could provide more energy at higher frequencies and enable identification of additional modes.

Moreover, a clearer separation between rigid body and flexural modes is desirable to improve the reliability of modal identification. To further minimise the influence of unintended boundary restraints and friction effects, the specimen could be suspended during testing to more closely approximate free–free boundary conditions. This setup would reduce the impact of air cushion dynamics and provide a clearer characterisation of the element's intrinsic dynamic properties.

3.4 Static analysis

The dynamic response of the HP prototype element was investigated in Section 3.3 through modal analysis. This section focuses on the element's performance under static loading, evaluated through analytical calculations, experimental testing, and numerical simulations.

The section is organised into five main parts, presented in Sections 3.4.1 to 3.4.5. Section 3.4.1 presents analytical stress estimations, using Pucher's membrane shell method (cf. Section 2.2.1), and Lundgren's beam theory for cylindrical shells (cf. Section 2.2.2). Section 3.4.2 outlines the experimental static load testing. Section 3.4.3 explores both linear and non-linear FEA, examining sensitivity to mesh resolution, boundary conditions, and reinforcement modelling approaches. Section 3.4.4 provides a comparative summary of the findings from all three assessments. Finally, Section 3.4.5 discusses the outcomes and limitations.

The main objective of these investigations is to assess the prototype element's static response under incremental loading, addressing the following key questions:

- **How does the element respond to increasing static load, and what governs its failure?**
  – How do stress and strain fields evolve during loading? Where do cracks initiate, and at what locations do concrete crushing and steel yielding occur? What defines the ultimate load-bearing capacity?
- **How does reinforcement affect the element's static behaviour?**
  – What is its effect on deformation characteristics and ultimate load capacity?
- **To which extent can analytical and numerical models predict the experimentally observed behaviour?**
  – How closely do the models replicate experimental outcomes, and where do discrepancies arise?

To address these questions, the prototype element was studied using analytical, numerical, and experimental approaches. Due to practical constraints, the second question—concerning the influence of reinforcement—could only be investigated numerically. Two static load cases were considered (see Figure 3.41): one involving a uniformly distributed gravitational load applied across the surface (LC1), and another consisting of two concentrated point loads positioned along the centreline of the element, 900 mm apart (LC2).

LC1 was implemented by placing cement bags on top of the element, corresponding to an approximate loading of $q_z = 0.869$ kN/m^2 (per unit area of the top surface). This relatively low load level was assumed to be non-destructive, i.e., insufficient to initiate cracking or plastic straining, and was therefore unlikely to interfere with the subsequent point load test conducted up to failure. Furthermore, the uniformly distributed load was expected to provide a favourable loading condition that promoted membrane action, thereby enforcing the intended shell behaviour and minimising localised bending effects. This setup also reflects a realistic loading scenario from a potential application standpoint, where the element would be subjected to UDLs from overlying fill materials. Lastly, it enabled meaningful comparison with membrane shell theory and

Euler-Bernoulli beam theory for cylindrical shells.

LC2 used two concentrated loads ($Q_1 = Q_2$) which were applied via a hydraulic piston rig, incrementally increased until failure. While this loading induces localised bending—contrary to the preferred membrane action in shell structures—it was chosen as the most practical and controlled method to achieve failure, providing precise force data at each step compared to less controlled alternatives like stacking cement bags.

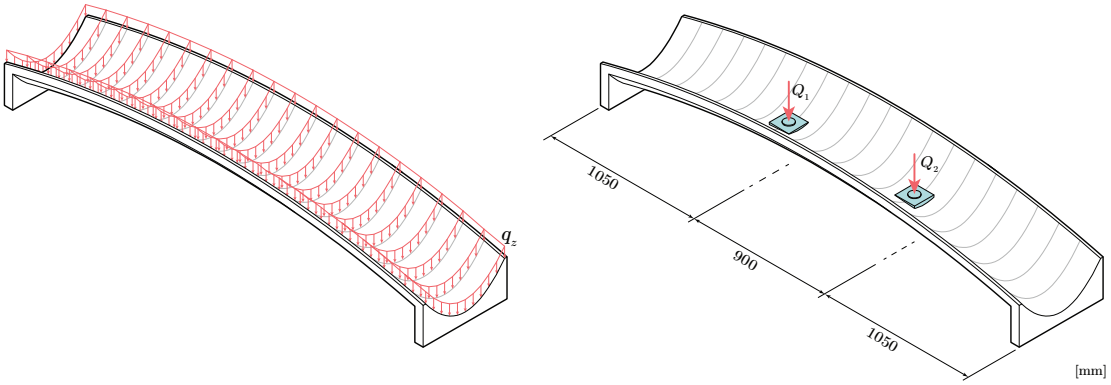

LC1 - Uniformly distributed loads

LC2 - Point loads

Figure 3.41: Illustration of the two load cases considered during static load testing.

To minimise bending and promote in-plane membrane action, the element was restrained longitudinally within the test rig, as illustrated in Figure 3.42.

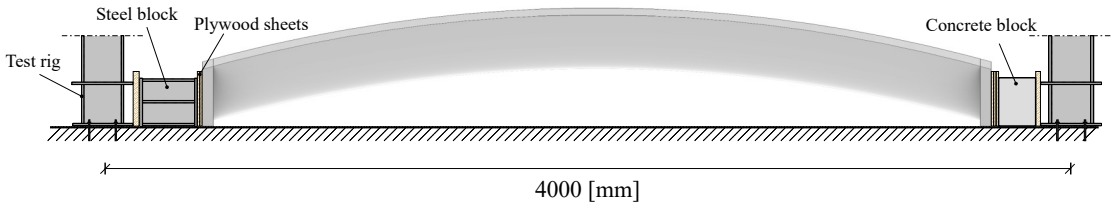

Figure 3.42: Illustration of support conditions considered during static load testing. The prototype element was placed within the test rig, with steel blocks, concrete blocks and plywood sheets added to minimise the gap between the element and the test rig, and to ensure adequate load transfer.

3.4.1 Analytical static analysis

This section provides an analytical estimate of the internal stresses within the HP element under a vertical distributed load of $p_z = -0.869$ kN/m^2, applied to its top surface (LC1). The analysis is conducted in two stages: firstly, by using the method for arbitrary membrane shells developed by Pucher (1934); and secondly, by employing the Euler–Bernoulli beam theory for cylindrical shells suggested by Lundgren (1949).

3.4.1.1 Membrane shell theory

A plan projection of the HP prototype's middle surface is shown in Figure 3.43. The straight-line generators are oriented at an angle $\pm\gamma$ given as

$$\tan\gamma = \sqrt{\frac{h_2}{h_1}} = \sqrt{\frac{0.45}{11.25}} \implies \gamma = \tan^{-1} 0.2 \approx 11.3°.$$

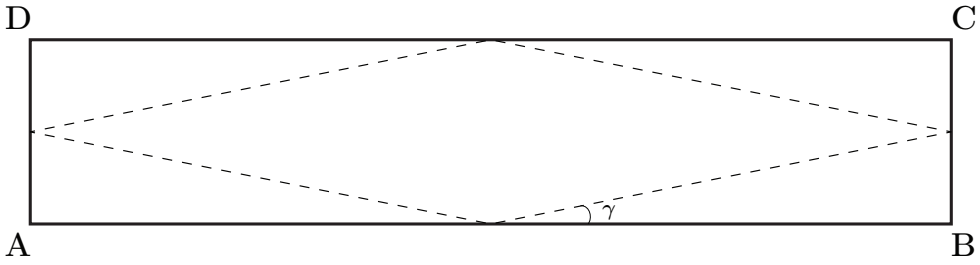

Figure 3.43: Plan projection of the prototype element's middle surface.

Pucher's method yields an admissible solution in which the element is fully compressed (cf. Section 2.2.1.3), with projected stress resultants given as:

$$\bar{n}_x = -\frac{q\,h_1}{2}, \quad \bar{n}_y = \bar{n}_{xy} = 0.$$

This solution assumes that the external load p acts solely in the z-direction ($p = p_z$), and that the projected load $\bar{p}_z$ is constant over the projected surface ($\bar{p}_z = -q = \text{const.}$). In practice, the surface load from the cement bags potentially induces a hydrostatic pressure with non-zero components in the x- and y-directions. Additionally, the projected load $\bar{p}_z = \frac{\mathrm{d}A}{\mathrm{d}x\,\mathrm{d}y} \cdot p_z = C(x,y) \cdot p_z$ varies spatially, as shown in Figure 3.44. Nonetheless, these simplifications are necessary to obtain a closed-form analytical solution. The function $C(x,y)$ is assumed constant and taken as the ratio of the total surface area to the total projected area, giving:

$$q = -1.255 \cdot p_z = 1.130\,\text{kN/m}^2.$$

The projected normal stress resultant $\bar{n}_x$ is constant on the projected surface:

$$\bar{n}_x = -6.35\,\text{kN/m}.$$

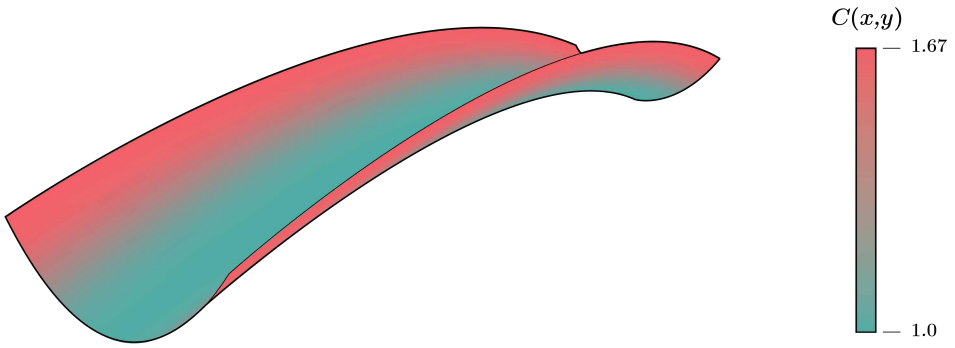

Figure 3.44: Spatial variation of the function $C(x, y) = \frac{\mathrm{d}A}{\mathrm{d}x\,\mathrm{d}y}$ over the surface.

In accordance with Flügge (1962), the surface stress resultant n_x is related to the projected stress by the local inclination of the surface, and can be expressed as:

$$n_x = \frac{\cos(\theta_y)}{\cos(\theta_x)} \cdot \bar{n}_x = D(x, y) \cdot \bar{n}_x,$$

where the angles θ_x and θ_y are defined as per Figure 2.8. The spatial variation of $D(x, y)$, shown in Figure 3.45, reveals a symmetrical stress distribution that increases toward the central axis of the shell and toward the supported edges. Integration of the stresses along the supported edges yields a total thrust of $N_x = -4.02$ kN at each end. As discussed in Section 2.2.1.3, any attempt to reduce the thrust at one supported edge results in an equal increase in thrust at the opposite edge.

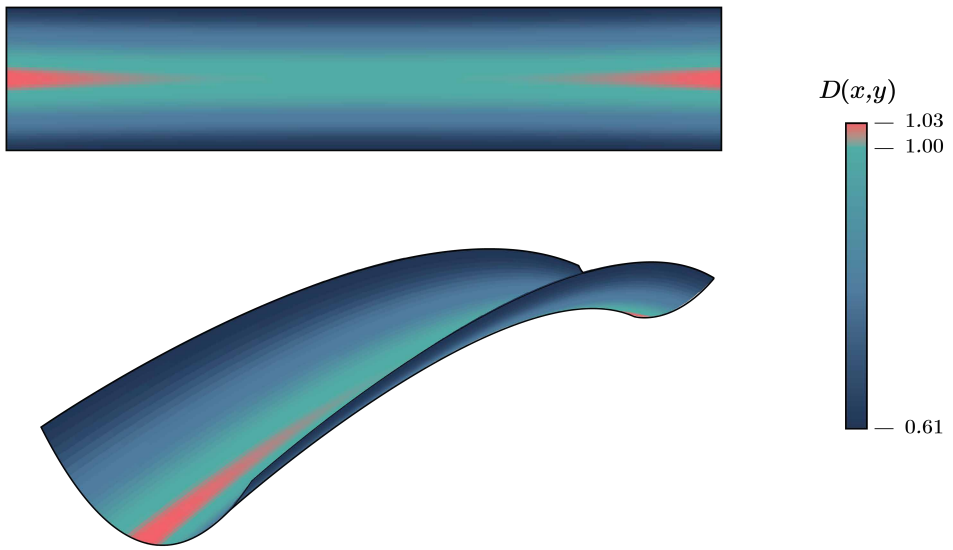

Figure 3.45: Spatial variation of the function $D(x, y) = \frac{\cos(\theta_y)}{\cos(\theta_x)}$ over the surface.

3.4.1.2 Euler-Bernoulli beam theory for cylindrical shells

This section presents stress estimations based on the Euler–Bernoulli beam theory for cylindrical shells proposed by Lundgren (1949), following the theoretical framework introduced in Section 2.2.2.

The beam representation of the HP prototype element, shown in Figure 3.46, has a longitudinal arc length of $l = l_{\text{arc}} = 3.035$ m. The beam is assumed to be subjected to a constant surface load p_z, equivalent to a line load q per unit arc length along the beam's longitudinal direction. This line load is obtained by multiplying p_z with the transverse arc length:

$$q = p_z \int_{-\eta}^{\eta} \mathrm{d}s_y \approx -0.647\,\text{kN/m}.$$

The beam is assumed to have a constant thickness of $t = 45$ mm, yielding a uniform second moment of area of $I_{yy} = 1.161 \cdot 10^{-3}$ m^4 about the local y-axis.

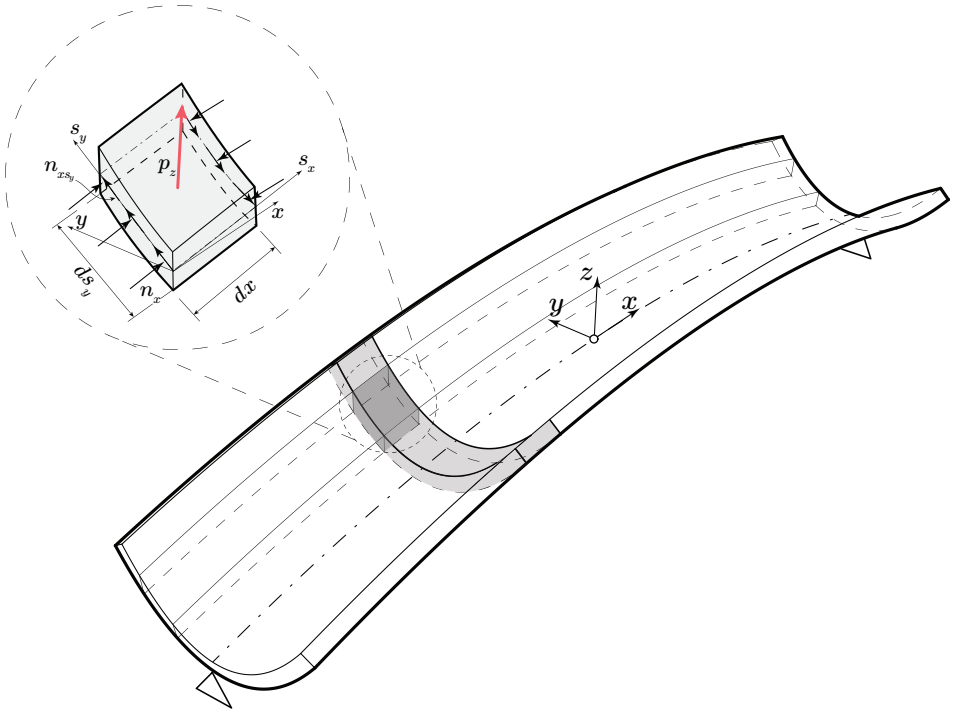

Figure 3.46: Beam representation of HP prototype element.

The spatial distributions of the resulting normal membrane stress resultant n_x and transverse shear stress resultant n_{xs_y} are presented in Figure 3.47. The decomposition of the shear stress resultant n_{xs_y} into its global components n_{xy} and n_{xz} is shown in Figure 3.48.

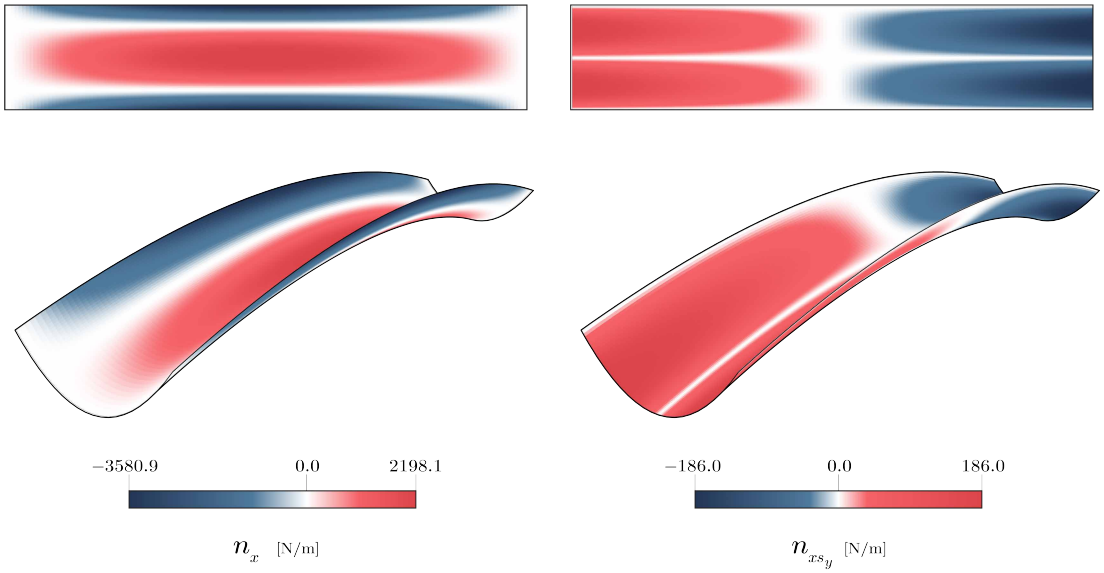

(a) Normal stress resultants n_x [N/m] **(b)** Shear stress resultants n_{xs_y} [N/m]

Figure 3.47: Distribution of membrane stresses in the beam due to external load $\bar{p}_z$.

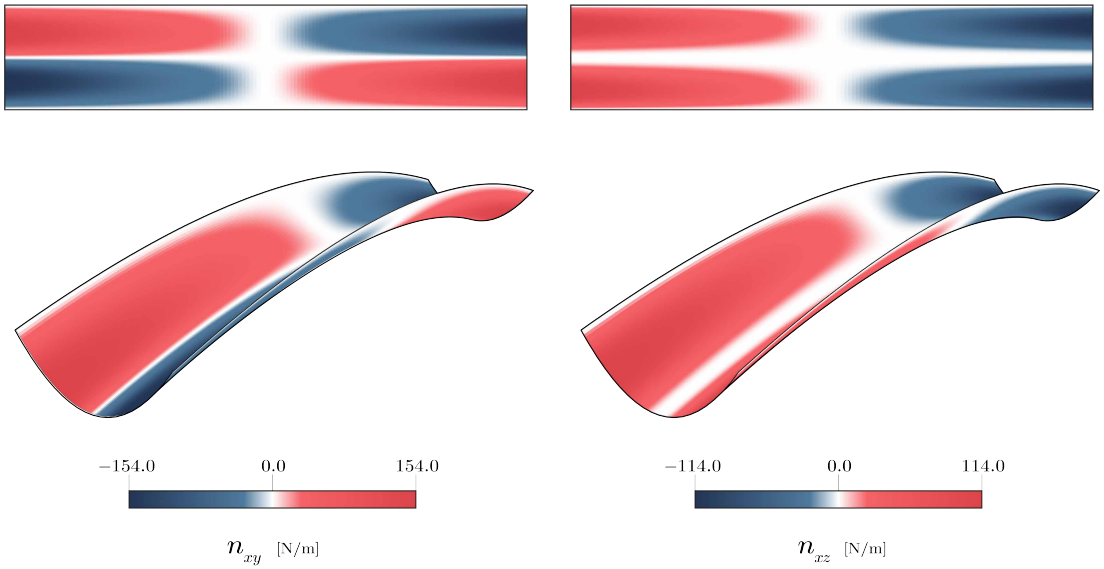

(a) Shear stress resultants n_{xy} [N/m] **(b)** Shear stress resultants n_{xz} [N/m]

Figure 3.48: Distribution of shear stress n_{xs_y}, decomposed into global y- and z-components.

3.4.2 Experimental static analysis

Experimental static load testing for LC1 and LC2, as defined in Figure 3.41, was conducted on 3 June 2025. This section outlines the testing methodology and presents some preliminary results. The content is organised into four sections:

- **Section 3.4.2.1** — Describes the two load cases in detail.
- **Section 3.4.2.2** — Covers how boundary restraints and supports were realised during testing.
- **Section 3.4.2.3** — Covers the acquisition of strain data using digital image correlation (DIC) and distributed fibre optic sensing (DFOS).
- **Section 3.4.2.4** — Summarises the observed test results.

3.4.2.1 Loading

A description of the two load cases is given below:

Load case 1 (LC1)

Non-destructive testing of the element under a uniformly distributed load was conducted by placing ten cement bags, each weighing approximately 20 kg, evenly across the main surface (see Figure 3.49). This corresponded to an applied load of approximately 0.869 kN/m^2.

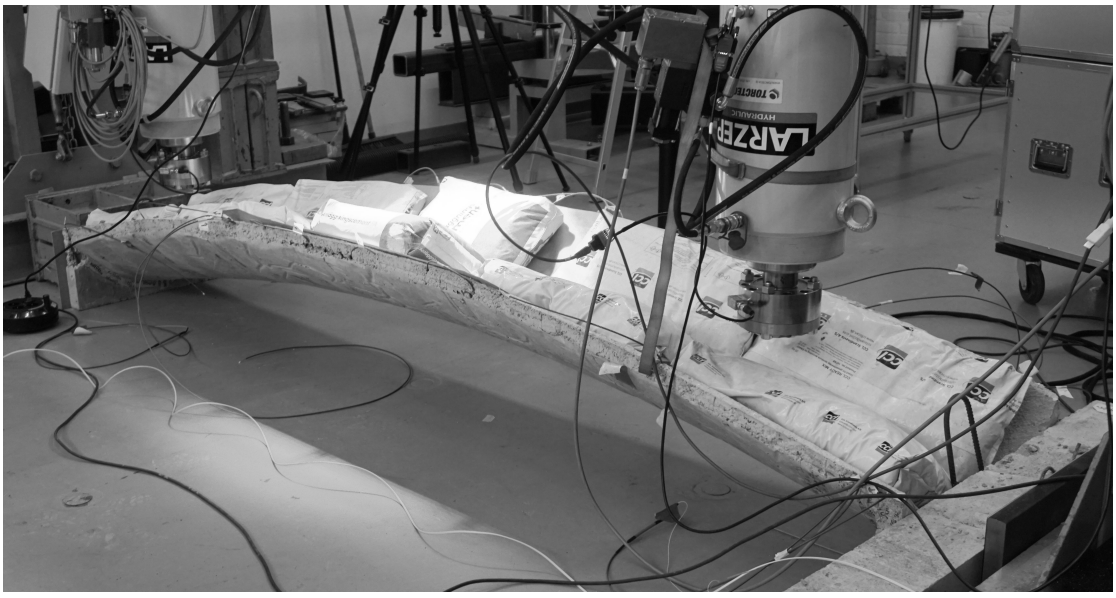

Figure 3.49: Application of uniformly distributed load (LC1). Ten cement bags, each weighing around 20 kg, were evenly placed across the main surface of the element.

Load case 2 (LC2)

The element was loaded to failure via two concentrated loads, each applied through a Larzep hydraulic piston, positioned 900 mm apart, symmetrically about the element's midpoint, as per Figure 3.41. Custom 140-by-140 mm plywood load distributors were fabricated to transfer and spread the loads onto the curved surface geometry. Each load distributor featured an extruded cross geometry on its top surface, designed to

interface with SKF *GX50* bearings. These bearings were subsequently connected to the hydraulic pistons. To improve contact and mitigate local stress concentrations, the load distributors were placed on top of a foam sheet, as shown in Figure 3.50.

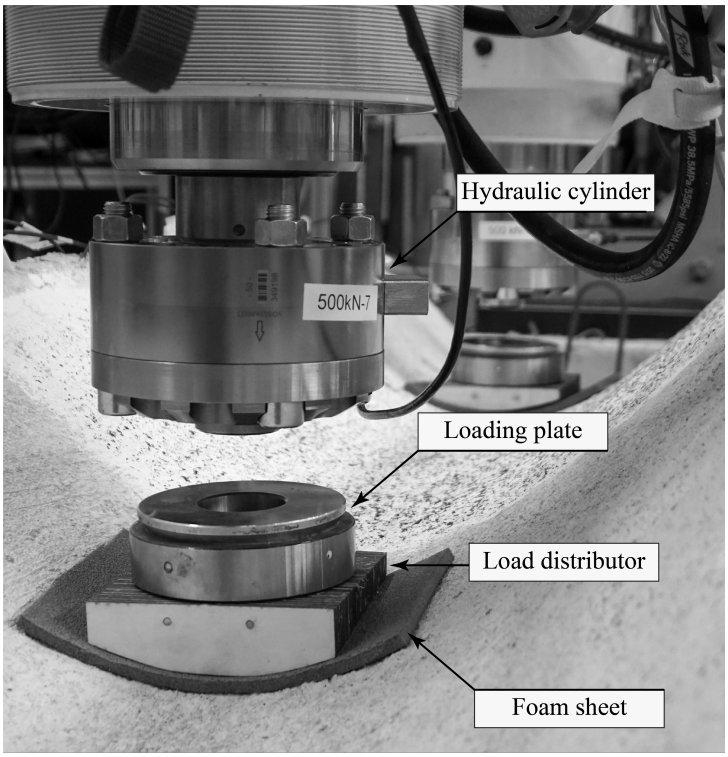

Figure 3.50: Application of concentrated loads (LC2). A plywood load distributor was positioned beneath each hydraulic cylinder. A thin foam layer was placed between the load distributors and the concrete surface to improve load transfer. The cylinders were positioned 900 mm apart.

One of the hydraulic pistons was displacement-controlled, while the second was programmed to track and replicate the displacement of the first. To stabilise the setup and account for initial plastic deformations in the foam sheets, preliminary load cycling was conducted, with a preload of 1 kN applied to each piston. The primary loading phase commenced at a displacement rate of 1.5 mm/min, reaching approximately 37 kN over 9 minutes. The rate was then increased to 5 mm/min, maintained until failure. This increase was necessary to prevent the DIC system from exceeding its memory capacity. The total duration of the test was approximately 21 minutes.

3.4.2.2 Boundary conditions

The element was vertically supported on a concrete floor and longitudinally confined within the test rig, as shown in Figure 3.42. To reduce the gap between the element and test rig, a steel block and a concrete beam were positioned on opposite sides of the element. Gaps were further closed using plywood sheets, MDF boards, and wooden wedges. Additional steel plates and wooden wedges were positioned under the abutments to level the element and correct for the geometric twist described in Section 3.2.2. An overview of the boundary conditions is provided in Figure 3.51.

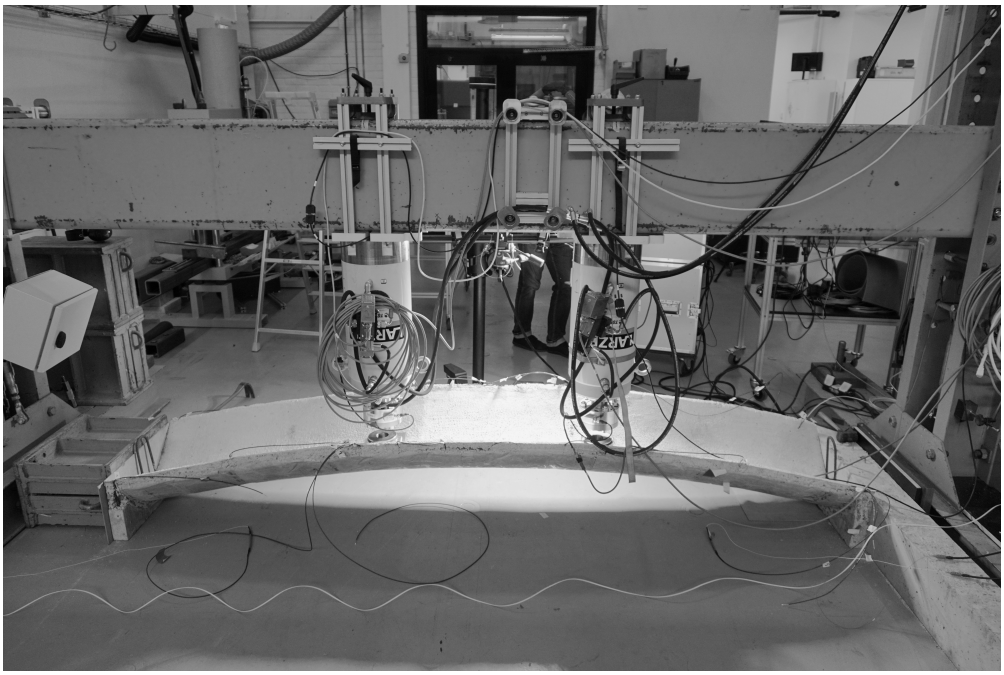

Figure 3.51: Prototype element rested on a concrete surface and restrained within the test rig.

3.4.2.3 Strain measurements

Strain measurements were obtained using distributed fibre optic sensing (DFOS). Additionally, for LC2, digital image correlation (DIC) was employed to monitor surface strains on the top face of the element between the two concentrated load points. The configuration and implementation of each strain measurement methods is summarised below.

Distributed fibre optic sensing (DFOS)

Four *BRUsens DSS V9* DFOS cables were cast into the element, labelled in accordance with Table 3.21, and positioned as shown in Figure 3.52. Each DFOS cable was aligned parallel to a reinforcement bar, with the bars placed at varying depths across the section thickness. The offset values reported in Table 3.21 assume that the cables remained centered along the centroidal axes of their respective reinforcement bars. The exact positions of the reinforcement and DFOS cables were not documented during casting, and their placement should therefore be considered approximate.

Table 3.21: Classification and characteristics of the four DFOS cables embedded in the prototype element.

Name	**Colour**	**Offset*** [mm]	**Total length** [mm]
Transversal		−6	6,404
Diagonal W-E		−3	14,477
Diagonal E-W		+3	16,013
Perimeter		±0	6,031

*Offset from middle surface.

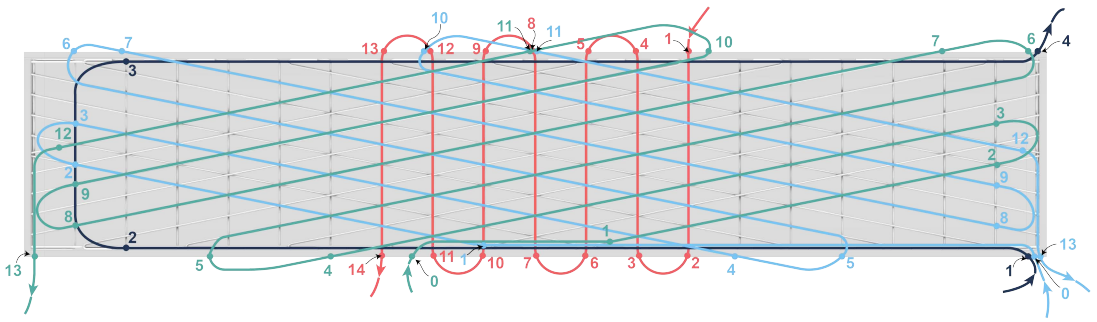

Figure 3.52: Assumed positions of the four DFOS cables within the prototype element.

The four cables were connected to an ODiSI 6108 fibre optic interrogator by Luna Innovations. Strain data was recorded at a sampling rate of 3.125 Hz with a spatial resolution of 1.3 mm. Prior to testing, any existing strain signals in the fibres were tared.

Digital image correlation (DIC)

DIC was used during LC2, serving two main purposes: to monitor the development of cracks and strain in the region between the concentrated loads, and to capture the vertical mid-point deflection of the specimen.

A stochastic speckle pattern was painted onto the surface, as shown in Figure 3.53. First, a base layer of matte white paint was applied to the surface and left to dry for one day. Subsequently, a rubber mat was dipped in black paint and gently dabbed onto the surface, creating a high-contrast stochastic pattern.

Two charge-coupled device (CCD) cameras were used to record the deformations of the speckle pattern. Both cameras were calibrated using a calibration cross prior to testing. Blue LED light was used to illuminate the DIC pattern, enhancing the contrast of black and white, providing better data quality. Images were recorded at 1 Hz and processed in ZEISS INSPECT Correlate.

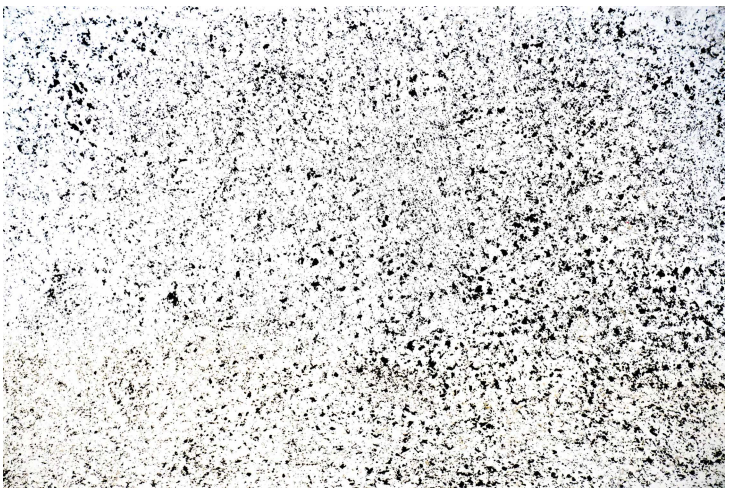

Figure 3.53: Close-up image of the stochastic speckle pattern painted onto the top surface of the prototype element.

3.4.2.4 Preliminary Results

This section summarises preliminary outcomes from the static load testing. At this stage, the data has been processed and compiled for initial interpretation, but no detailed assessment of measurement reliability, error margins, or repeatability has yet been conducted. A more thorough evaluation will be required to confirm the robustness and accuracy of the findings.

Uniformly distributed load (LC1)

The strains induced by placing cement bags on top of the prototype element were recorded using the cast-in distributed fibre optic sensors. The measured strain profiles after applying ten cement bags uniformly across the surface are presented in Figure 3.54 for each of the DFOS cables.

To interpret these graphs, it is suggested to use Figure 3.52 as a reference key. Each graph includes a series of numbered vertical lines that correspond to specific positions along the DFOS cables. These positions are also indicated as dots in Figure 3.52. It should be noted that these positions have not been experimentally verified, but are based on the intended design of the element.

The measured strain levels were generally low, approximately 10 $\mu\epsilon$ (micro strain) in magnitude, resulting in notable noise in the recorded data. The strain along the Transversal DFOS cable was close to zero, indicating that stress does not distribute significantly in the transverse direction. Two distinct peaks with elevated strain levels were observed in the data of the Transversal DFOS cable. These peaks correspond to parts of the fibre located outside the element and were likely caused by damage incurred during transportation or handling.

For the diagonal cables (Diagonal E-W and Diagonal W-E), the fibres were predominantly in tension along most of their length, transitioning into compression near the free edges. While the overall strain profiles were similar, a slight asymmetry can be observed between the two diagonals.

The Perimeter fibre indicated full compression along the free edges, with a pronounced increase in compressive strain toward the middle of the span, diminishing gradually toward the supports.

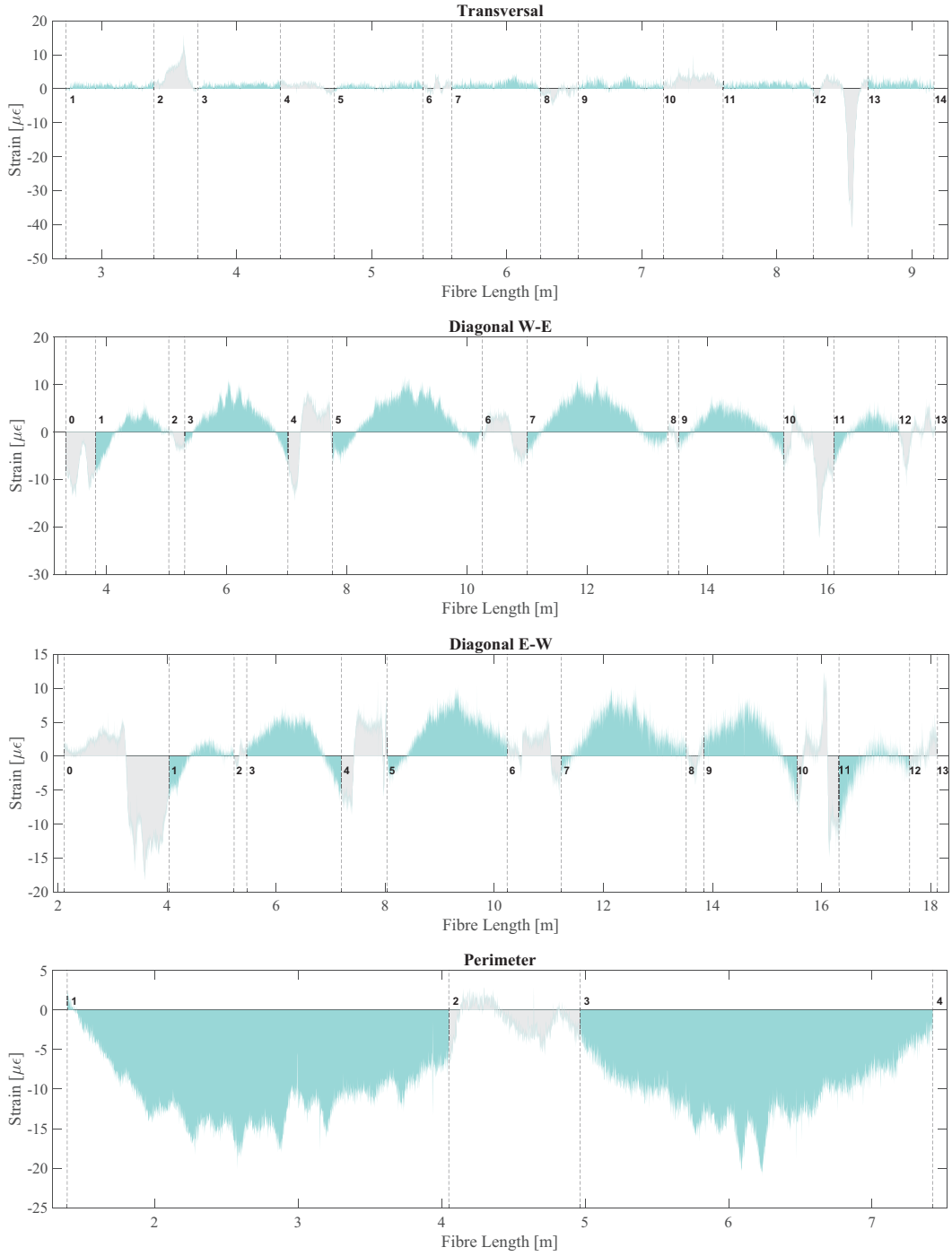

Figure 3.54: Strain measurements along the four DFOS cables under cement bag loading (LC1). Vertical dashed lines mark known positions along each cable. Figure 3.52 serves as a reference key for locating these positions within the element. Gray-shaded zones denote regions that are either outside the element or simply not aligned with reinforcement bars.

Concentrated loads (LC2)

The strains induced by the two hydraulic cylinders were measured using both the cast-in DFOS cables and DIC.

Using two CCD cameras, it was possible to capture 3D-deformations with the DIC. By correlating these deformations with load data from the hydraulic cylinders, the midpoint deflection of the element was plotted as a function of the total applied load, as shown in Figure 3.55. The displacement was averaged across 28 nodes located near the geometric midpoint of the top surface. The graph presents both the individual displacements of each node and the mean displacement.

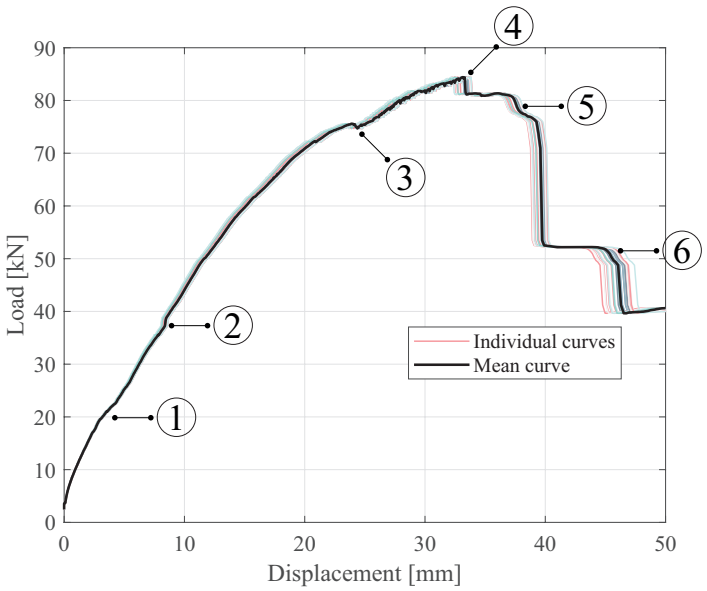

Figure 3.55: Load–displacement response from LC2. Vertical displacements were measured at 28 nodes near the geometric midpoint on the element's top surface using DIC. Coloured curves show individual node responses; the black curve represents the average displacement. Six distinct stages were identified: (1) First crack formation, (2) Increased loading rate, (3) Longitudinal crack formation, (4) Ultimate load reached, (5) Compressive failure of both free edges, (6) Punch-through of cylinder.

Six distinct stages were observed in the load-displacement response graph:

(1) The first visible crack formed at the centre of the element at approximately 19 kN. By 31 kN, five cracks had developed. Despite this, the response remained nearly linear, indicating no significant stiffness reduction.

(2) At 37 kN, a sudden jump in the curve occurred, attributed to a deliberate increase in loading rate from 1.5 mm/min to 5.0 mm/min—rather than a structural event.

(3) With continued loading, a longitudinal crack appeared in a region along one of the upper edges of the parabolic cross-section. This area was under high compressive stress and exhibited poor compaction, making it a natural point for local failure to initiate.

(4) The element reached its ultimate load at 84 kN. Failure occurred through brittle fracturing of the poorly compacted concrete along the highly compressed upper

edge, at the same location where the longitudinal crack had formed. Large pieces of concrete detached, and the edge reinforcement showed signs of local buckling.

(5) Similar brittle fracturing of poorly compacted concrete occurred at the opposite upper edge.

(6) In the final stage, full punching shear failure occurred beneath the cylinder aligned with the previously damaged edge, causing the load to puncture completely through the element's surface.

Figure 3.56 shows selected images taken after the completion of the load test.

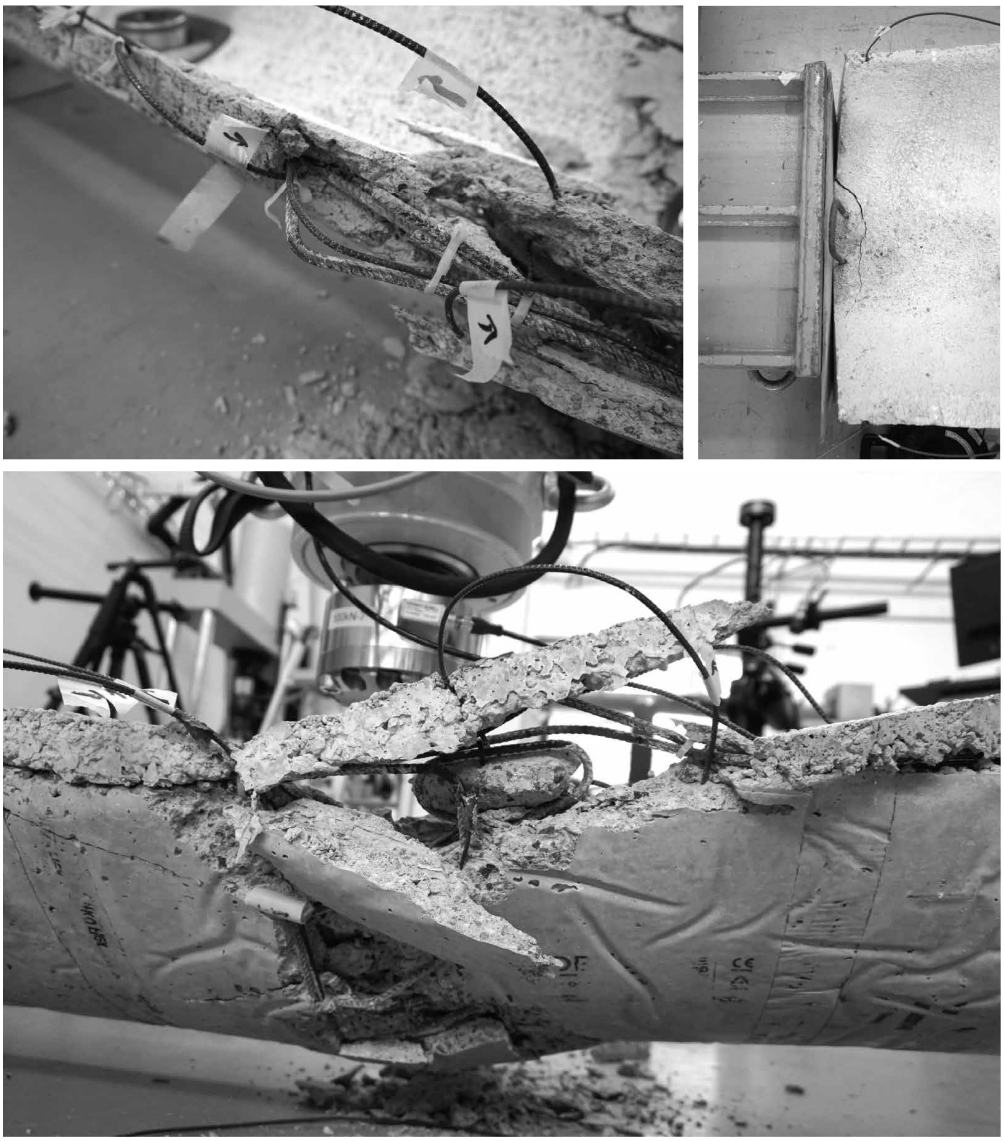

Figure 3.56: Selected images from the static load test with two concentrated loads (LC2). Top left: Buckling of reinforcement and brittle fracturing of poorly compacted concrete along the upper edge. Top right: Crack formation near the support region. Bottom: Full punch-through failure beneath one of the loading cylinders.

Figure 3.57 shows the strain distribution on the top surface between the point loads at Stage (3), captured using DIC. Five transverse cracks are visible, each centred above

a transverse reinforcement bar. Notably, the upper edge exhibits elevated strain levels in the same region where concrete fracturing occurred during Stage (4). Figure 3.58 shows the DIC mesh recorded at stage (2) and (3).

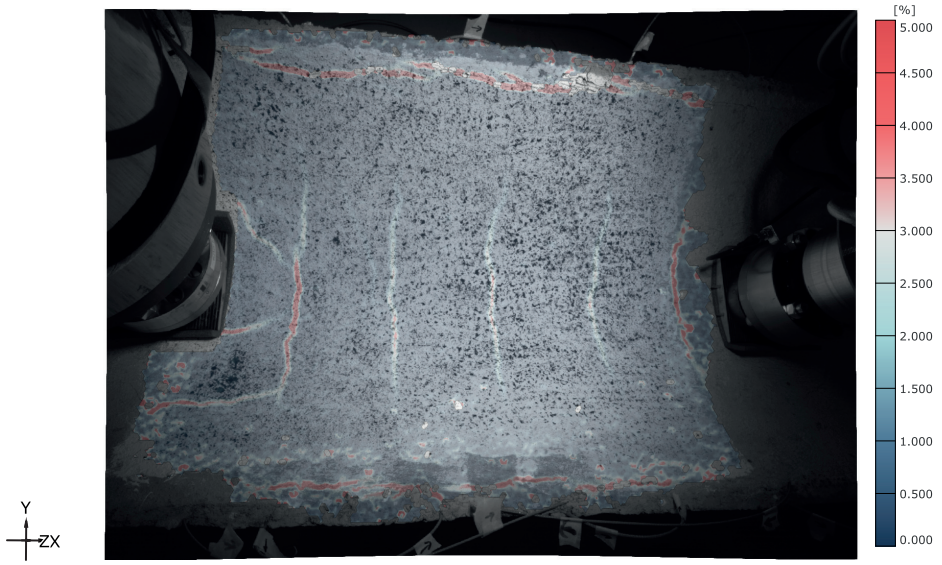

Figure 3.57: DIC snapshot at an applied load of 75 kN, corresponding to Stage (3) in Figure 3.55. Five transverse cracks from Stage (1) are clearly visible between the load cells. A developing longitudinal crack near the upper edge—characteristic of Stage (3)—is also evident.

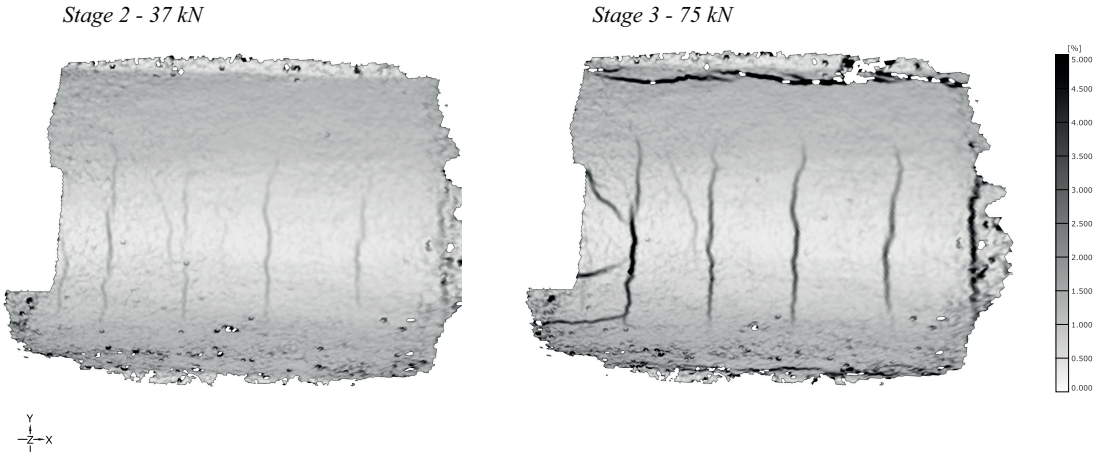

Figure 3.58: DIC crack patterns at a total applied load of 37 kN and 75 kN, corresponding to Stage (2) and (3) in Figure 3.55.

Figure 3.59 present the strain distribution along each of the four DFOS cables at three distinct load steps:

- Step 1 — corresponds to a load of 15 kN, recorded prior to Stage (1) and before any visible cracking of the element.
- Step 2 — represents a load of 38 kN, measured just after the load rate was increased during Stage (2).

- Step 3 — refers to a load of 75.7 kN, recorded immediately after Stage (3), coinciding with the formation of cracks along the longitudinal edge.

For interpretation of the graphs, refer to Figure 3.52, which shows the layout and position numbering of the DFOS sensors.

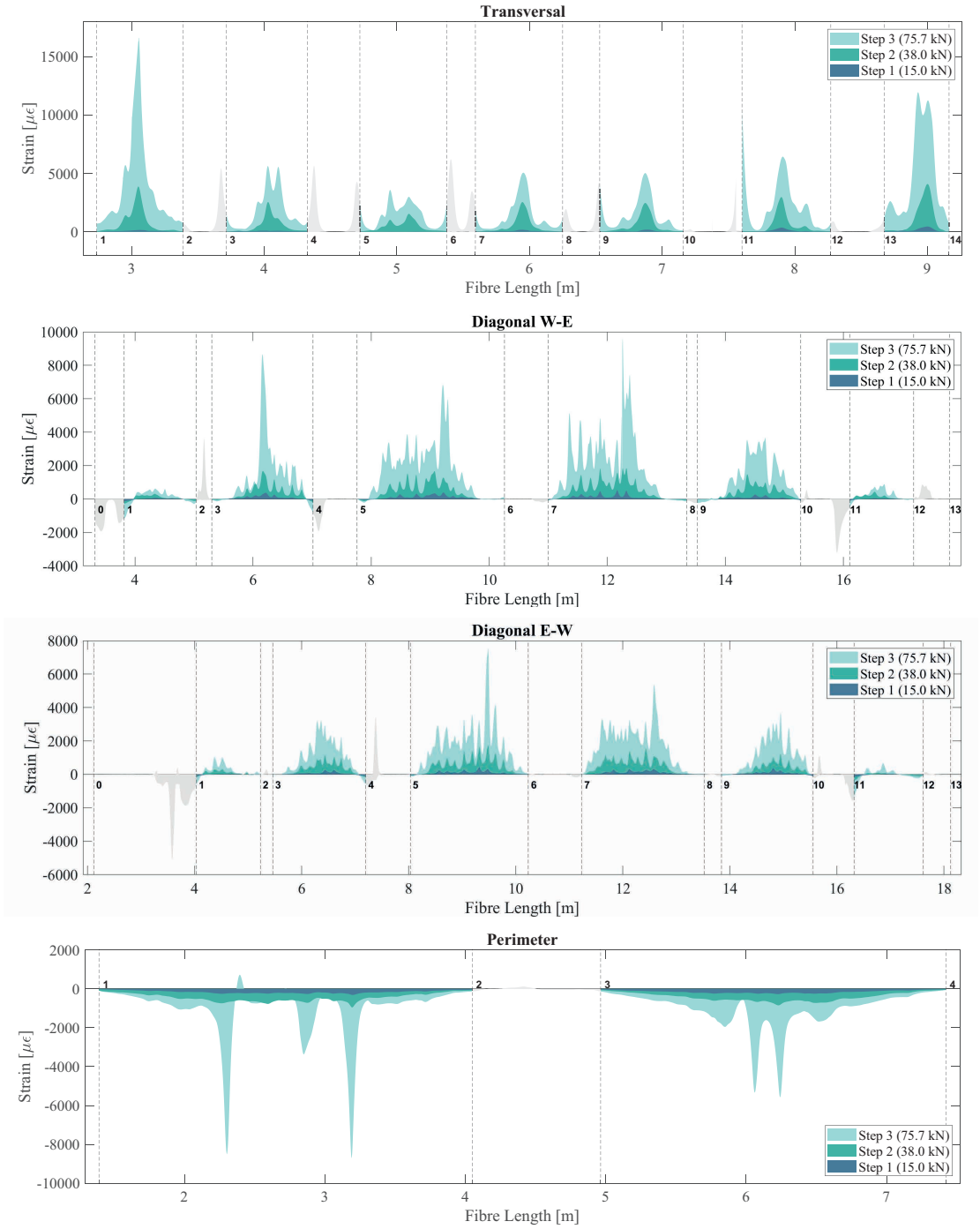

Figure 3.59: Strain measurements along the four DFOS cables under application of concentrated loads (LC2). Vertical dashed lines mark known positions along each cable. Figure 3.52 serves as a reference for locating these positions in the physical element. Gray-shaded zones denote regions that are either outside the element or simply not aligned with reinforcement bars.

As shown in Figure 3.59, strain levels along the Transversal DFOS cable remained close to zero during the initial load step, prior to visible cracking, indicating minimal stress in the transverse direction. Slightly elevated strains were recorded between points 13–14 and 11–12, which is consistent with their proximity to the applied point loads. In load steps 2 and 3, following the onset of cracking, tensile strains in the transverse direction increased significantly. Given a steel yield strength of 500 MPa, yielding is expected at approximately 2,500$\mu\epsilon$. Since the DFOS cables are embedded directly along the reinforcement bars, it is possible that yielding occurred in all transverse bars during load step 3—assuming a high degree of strain compatibility. Yielding may also have initiated as early as step 2 in the bars between points 1–2 and 13–14, which are located close to the applied loads.

The fibres along the main reinforcement bars (Diagonal W-E and Diagonal E-W) exhibited small strain peaks already during load step 1, suggesting the presence of microcracking. These strain levels increased in steps 2 and 3, indicating further crack development. In contrast to the strain behaviour observed for LC1, no negative strain was recorded at the ends of the diagonals, suggesting that they remained predominantly in tension. The largest straining was recorded between points 5–6 and 7–8.

As in LC1, the fibres along the perimeter predominantly exhibited negative strain, indicating compression at these edges. Notably, pronounced peaks appeared during load step 3, likely corresponding to localised zones of concrete fracturing and steel buckling.

3.4.3 Numerical static analysis

This section presents the static numerical analysis performed using DIANA FEA (Diana). Section 3.4.3.1 outlines the modelling methodology, covering mesh generation, boundary conditions, material definitions, and loading schemes. A sensitivity study is then described in Section 3.4.3.2, investigating the effects of mesh density, reinforcement modelling, and boundary condition assumptions on the results.

3.4.3.1 Finite element model

Both 3D solid elements and 2D shell elements were considered during the numerical modal analysis in Abaqus. While solid meshes can offer improved accuracy, they also demand significantly greater computational effort for meshing and processing. To keep the non-linear stress analysis manageable within the scope of this thesis, 2D shell elements were used in Diana. Unlike Abaqus, which has a *Rebar Layers* feature, Diana allows for the direct embedding of explicitly modelled 1D reinforcement, thereby making 2D shell elements a viable option.

To gain confidence in the use of 2D shell elements, an initial modal analysis was performed in Diana, replicating the setup used earlier in Abaqus (see Section 3.3.3). The resulting modal characteristics closely matched those obtained in Abaqus, thereby further justifying the use of 2D shell elements for subsequent non-linear stress analysis.

The base mesh, including the 1D reinforcement splines, was generated in Rhino 3D/-Grasshopper and imported into Diana as STEP files. This mesh could then be further refined within Diana. Care was taken to construct the mesh such that the reinforcement bars were aligned with the mesh edges, as illustrated in Figure 3.60. This alignment ensured consistent interaction between the reinforcement and the surrounding concrete,

reducing the likelihood of numerical artefacts at the interface.

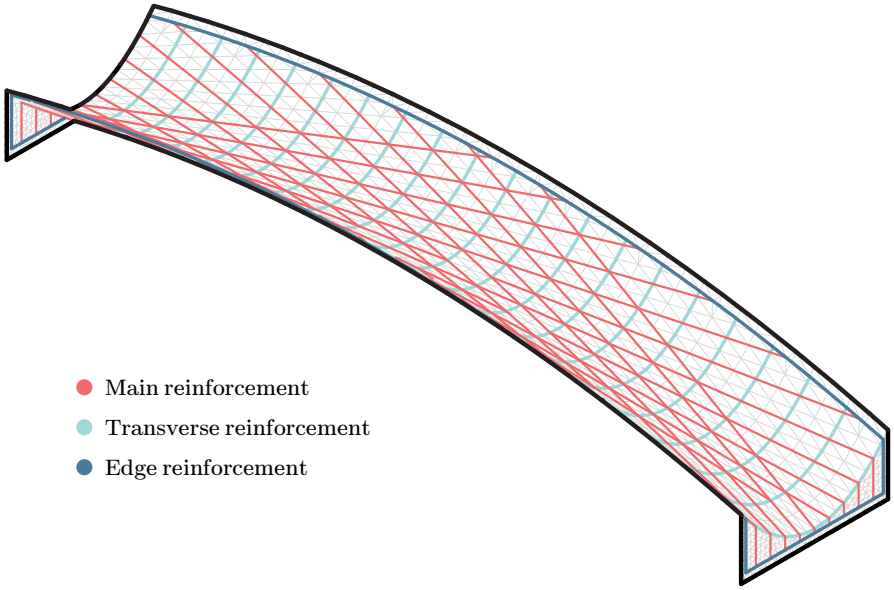

Figure 3.60: Base mesh used in the finite element stress analysis.

The concrete continuum was modelled using six-noded curved triangular shell elements (CT30S). These elements neglect transverse normal stresses through the thickness of the shell ($\sigma_{zz} = 0$) and assume that straight normals to the mid-surface remain straight after deformation, consistent with the Reissner-Mindlin plate theory (Mindlin, 1951; Reissner, 1945). As a result, the in-plane strains ε_{xx}, ε_{yy}, and γ_{xy} vary linearly through the shell thickness, while the transverse shear strains γ_{xz} and γ_{yz} remain constant. Each node has five degrees of freedom, including three for translations and two for rotations. To avoid membrane locking and shear locking, a reduced integration scheme is implemented by default in Diana (DIANA FEA, 2025).

The reinforcement bars were modelled as straight truss elements, meaning they could only carry axial forces and undergo axial straining.

The considered element properties are summarised in Table 3.22.

Table 3.22: Summary of element definitions.

Element	Element class	Material	Geometry
Main surface	Regular curved shells (CT30S)	Concrete	$t = 45$ mm
Abutments	Regular curved shells (CT30S)	Concrete	$t = 60$ mm
Reinforcement	Truss	Steel	⌀=6 mm

Concrete material model

All material parameters used to define the non-linear concrete model are summarised in Table 3.23. The cohesive law relating stresses to crack widths was based on a non-linear tension softening model developed by Hordijk et al. (1986). The compressive post-peak behaviour was represented using a parabolic softening curve.

Table 3.23: Non-linear concrete material parameters.

Input parameter	Symbol	Input	Unit
Young's Modulus	E_c	28.0	[GPa]
Poisson's ratio	ν	0.2	-
Density	ρ	2,363	[kg/m^3]
Crack orientation	-	Rotating	-
Tensile curve	-	Hordijk	-
Tensile strength	f_{ctm}	3.2	[MPa]
Mode-I tensile fracture energy	G_F	143	[N/m]
Crack bandwidth orientation	-	Rots	-
Compressive curve	-	Parabolic	-
Compressive strength	f_{ck}	34.7	[MPa]
Compressive fracture energy	G_C	35,750	[N/m]

Reinforcement material model

An ideal plastic von Mises material model was adopted for the steel reinforcement, neglecting strain hardening.

Two approaches were used to model the interaction between concrete and reinforcement: a fully bonded embedded reinforcement model, and a bond-slip formulation derived from the CEB-FIB Model Code (CEB fib Model Code, 2010).

Theoretical membrane behaviour of HP shells (see Section 2.2.1) indicate that tensile stresses would primarily develop in the transverse direction, toward the free edges. Consequently, bond performance was considered most critical along the transverse reinforcement bars (Q-bars).

The CEB-FIB Model Code specifies different bond stress–slip relationships depending on the bond condition and the expected failure mode (pull-out or splitting). In this study, the *all other bond conditions* case was adopted. Since the concrete cover was less than 5$\varnothing$, splitting failure was assumed, in accordance with Table 6.1-1 in CEB fib Model Code (2010).

The assumed steel reinforcement properties and the corresponding bond–slip parameters from the model code are summarised in Table 3.24.

Diana requires a shear stiffness modulus, DSSX, which represents the initial slope of the bond-slip curve at the origin. Assuming an initial sampling point at $s_0 = 0.1$ mm, the stiffness was calculated as:

$$\text{DSSX} = \frac{\tau_0}{s_0} = 25.13\,\text{N/mm}^3,$$

where the initial shear stress τ_0 is obtained from the power-law expression:

$$\tau_0 = \left(\frac{s_0}{s_1}\right)^{\alpha} \cdot \tau_{\text{max}}.$$

The normal stiffness modulus, DSNY, accounts for the potential crushing of concrete at the interface between reinforcement bars and concrete. Following the approach suggested by Eriksen and Kolstad (2016), it was estimated as:

$$\text{DSNY} = \frac{E_\text{c}}{\varnothing} \cdot 10^3 = 4.7 \cdot 10^6 \,\text{N/mm}^3.$$

Table 3.24: Parameters of the bond-slip reinforcement material model.

Input parameter	Symbol	Input	Unit
Young's Modulus	E_s	200	[GPa]
Poisson's ratio	ν	0.3	-
Density	ρ	7,850	[kg/m^3]
Non-linear model	-	Von Mises plasticity	-
Hardening function	-	No hardening	-
Yield stress	f_yk	500	[MPa]
Normal stiffness modulus	DSNY	4,700	[N/mm^3]
Shear stiffness modulus	DSNX	25.13	[N/mm^3]
Bond-slip interface failure model	-	CEB-FIB 2010 bond-slip function	-
Maximum shear stress	τ_max	6.31	[MPa]
Ultimate shear stress	τ_f	2.53	[MPa]
Linearized initial slip section	s_0	0.01	[mm]
Relative slip section	s_1	0.76	[mm]
Relative slip section	s_2	0.76	[mm]
Relative slip section	s_3	2.00	[mm]
Exponent alpha	α	0.40	-

Boundary conditions

The applied boundary conditions are illustrated in Figure 3.61. Vertical restraints were applied by fixing all bottom nodes of the abutments in the global z-direction. To prevent rigid body motion, one node was additionally restrained in the global y-direction.

Different approaches were considered for restraining translations in the global x-direction. In the physical test setup, the element was positioned within a test rig, partially restraining it against outward displacements. It is likely that some initial freedom of movement existed due to imperfect contact, with restraint progressively developing as the interfaces settled under load. No strain measurements were recorded at the supports, making it difficult to quantify their actual stiffness. Instead, two limiting cases were analysed numerically: one representing rigid restraint and the other assuming no restraint (free displacement), to capture the potential range of boundary behaviour.

The rigid restraint was simulated by introducing spring elements along the bottom nodes of the abutments, as well as along the central portions of the ends of the main surface, corresponding to the regions where interface elements were present in the physical experiments. The springs were assigned high compressive stiffness and effectively zero tensile stiffness, as illustrated in Figure 3.62. At each abutment, 32 springs were used.

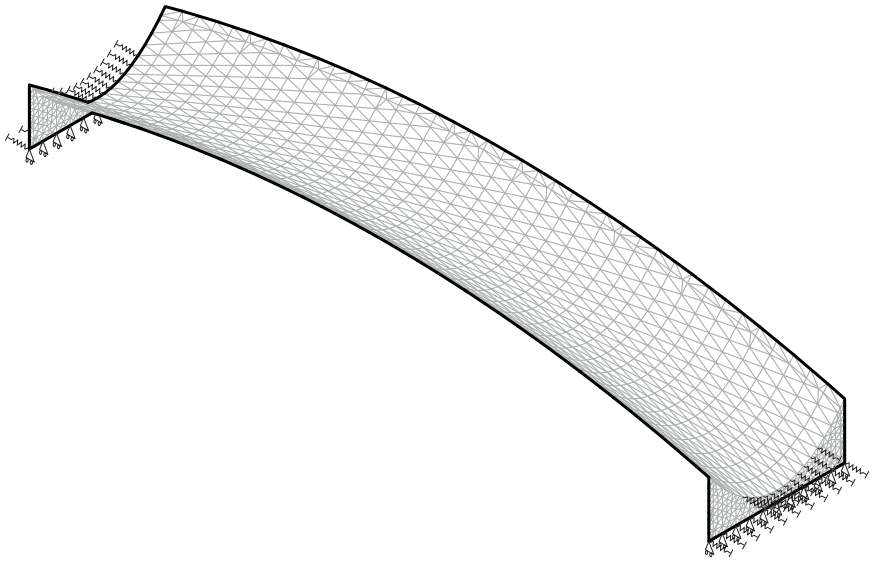

Figure 3.61: Finite element model with compression-only springs in the x-direction, full restraint in the z-direction along the bottom edges of the abutments, and a single node fixed in the y-direction.

Under a vertical load of 50 kN per load cylinder, the spring supports are expected to deform approximately 0.1 mm, based on the assigned compressive stiffness and assuming the load is fully transferred as axial thrust.

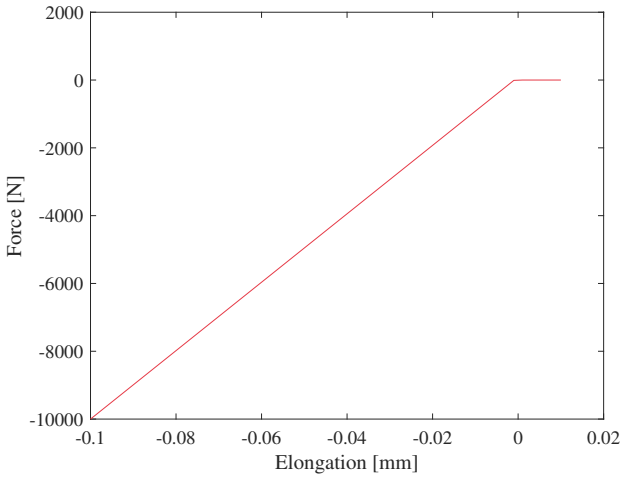

Figure 3.62: Force-elongation diagram of spring elements in the x-direction.

The unrestrained support condition was simulated by restricting the bottom edge of one of the abutments in the longitudinal direction.

Loading

LC1, representing the scenario in which cement bags are placed on top of the element, was simulated by applying a uniformly distributed gravitational load of $q = 0.869$ kN/m^2 across the element's top surface (see Figure 3.63a). The analysis was conducted in two load steps, ranging from zero to full load, under the assumption of a linear elastic response.

LC2, simulating a scenario where the element is subjected to two concentrated point loads spaced 900 mm apart, was modelled by distributing a load over two defined element sets, as illustrated in Figure 3.63b. Each set approximated an area of 130-by-150 mm, corresponding to the footprint of the load distributors used during physical testing (cf. Figure 3.50). The load was applied incrementally in steps of 1.0 kN until failure. A Newton-Raphson iteration scheme was used with a maximum number of iterations set to 400. Convergence was monitored using both force and energy norms, specified as 0.01 and 0.001 respectively. To improve convergence behaviour under nonlinear conditions, the *line search algorithm* was activated in Diana.

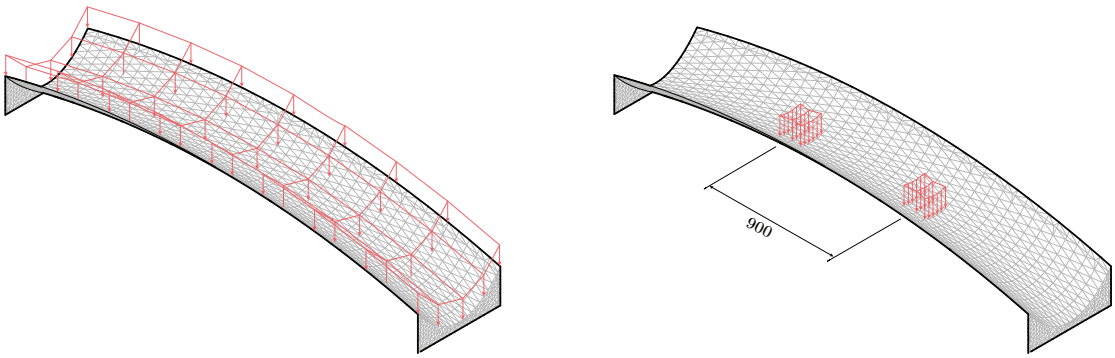

(a) LC1 - Uniformly distributed loads **(b)** LC2 - Concentrated loads

Figure 3.63: Numerical representation of loading scenarios in the static analysis.

3.4.3.2 Sensitivity study

A sensitivity study was conducted to study the following questions:

- At what mesh density does the numerical solution converge?
- How do boundary conditions influence the structural response?
- How do different approaches to reinforcement modelling influence the structural response?

Influence of mesh discretisation

The initial base mesh imported into Diana consisted of triangular elements with approximate side lengths of 75×75×30 mm. Due to their irregular aspect ratios, these elements may be considered relatively skewed, which can lead to poor Jacobian conditioning and affect numerical stability and convergence. The use of second-order shape functions likely mitigated some of the adverse effects associated with element distortion. No formal mesh quality metrics were evaluated. However, initial inspections of the stress and strain fields did not reveal indications of spurious peaks or discontinuities, suggesting acceptable mesh performance for the analyses conducted.

A convergence study was performed by refining the base mesh within Diana. The study was carried out for LC1 with a total applied load of 3 kN/m^2. The results, presented in Figure 3.64, show both the maximum vertical deflection ($|u_{\max}|$) and the maximum normal stress in the global x-direction ($|S_{xx,\max}|$) as functions of mesh refinement. Acceptable convergence was observed after two levels of refinement, corresponding to element side lengths of approximately 19 mm. Further refinement yielded marginal

improvements while significantly increasing the computational cost of the analysis.

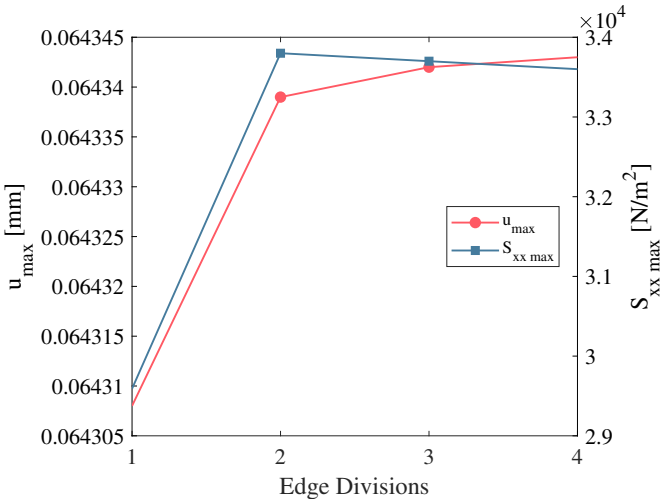

Figure 3.64: Convergence study of mesh refinement.

Influence of boundary conditions

As discussed in Section 3.4.3.1, the prototype element was expected to be partially restrained in the longitudinal direction. A numerical sensitivity study was carried out to assess how the structural response varies with different levels of longitudinal restraint. The study specifically focused on LC2, assessing the impact of longitudinal restraint on ultimate load capacity, deformation characteristics, stress development, and crack patterns. A complementary, linear elastic analysis of LC1 was also performed by comparing stress distributions under different restraint scenarios. As demonstrated by Arlinger (2023), the element is expected to exhibit beam-like behaviour when unrestrained, and shell-like behaviour when fully restrained in the longitudinal direction.

In addition to the two restraint configurations described in Section 3.4.3.1, a third level of restraint was evaluated. This configuration employed springs with stiffness reduced by a factor of 10 compared to the 'rigidly restrained' case, reflecting a more realistic stiffness based on engineering judgement. Under a vertical load of 50 kN per cylinder, and assuming full transfer of the load as compressive thrust, this stiffness would result in approximately 1 mm total deformation at each abutment. A summary of the three considered boundary configurations is provided in Table 3.25.

Table 3.25: Boundary condition configurations with corresponding spring stiffness values in the global x-direction.

Label	Support stiffness R_x [kN/mm]	Bond-slip direction	Description
BC1	0	Main reinforcement	Unrestrained
BC2	10	Main reinforcement	Partially restrained
BC3	100	Transverse reinforcement	Rigidly restrained

Linear elastic simulations were performed for LC1 using fully embedded reinforcement, considering configurations BC1–BC3. The resulting normal stress distribution

in the x-direction ($\sigma_{xx} = S_{xx}$) is shown in Figure 3.71 across the top surface of the element. As illustrated, the fully unrestrained configuration (BC1) exhibits a beam-like response: the central portions of the parabolic cross-section, located below the neutral axis, experience tensile stresses; while the edges, above the neutral axis, are in compression. Normal stresses in the x-direction are near zero at the supports and increase toward the midspan, consistent with the behaviour of a simply supported beam.

Increasing the longitudinal restraint significantly alters the stress distribution. In the rigidly restrained case (BC3), compressive stresses develop in the central region of the supports while tensile stresses appear toward the upper regions of the supported edges. Loads are carried in compression from the free edges toward the abutments along the generator directions. Normal stresses in the x-direction (both tensile and compressive) decrease with increased degree of longitudinal restraint. Notably, the maximum tensile stress is reduced by a factor of 20 when comparing the unrestrained case to the rigidly restrained configuration.

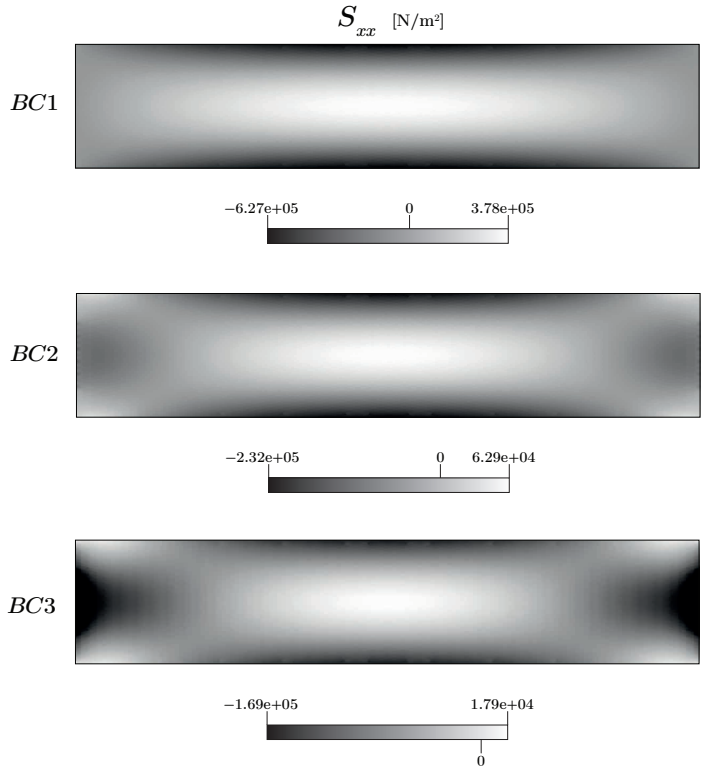

Figure 3.65: Normal stresses S_{xx} across the top surface from linear elastic simulations of LC1 for the three boundary conditions in Table 3.25. From top to bottom: BC1 (unrestrained), BC2 (partially restrained), BC3 (rigidly restrained).

For LC2, which was analysed using non-linear simulations, it would have been preferable to model all reinforcement using bond–slip relationships to more accurately capture strain distributions and crack development. However, preliminary analyses revealed significant convergence issues when yielding occurred in one of the reinforcement directions. Despite the use of very small load increments near the onset of yielding, the solver failed to converge beyond the yield point when bond–slip models were assigned to all reinforcement bars.

To improve numerical stability, bond–slip modelling was applied to only one reinforce-

ment direction at a time. For each of the three boundary condition configurations, two separate analyses were conducted: one with the bond–slip model assigned to the transverse reinforcement (with all other reinforcement modelled as fully bonded), and another with bond–slip applied to the main longitudinal reinforcement. The resulting reinforcement stress distributions were compared between the two configurations.

Ultimately, the bond–slip model was assigned in the critical reinforcement direction, i.e., the one exhibiting the highest tensile stresses. For BC1 (unrestrained boundary condition), this corresponded to the main longitudinal reinforcement. For BC3, bond–slip was applied exclusively to the transverse reinforcement. Due to persistent convergence issues, bond–slip could only be applied to the main longitudinal reinforcement in BC2, even though higher tensile stresses were observed in the transverse bars.

Figure 3.66 presents the vertical displacement at the midpoint of the top surface under varying load levels for the three longitudinal restraint configurations.

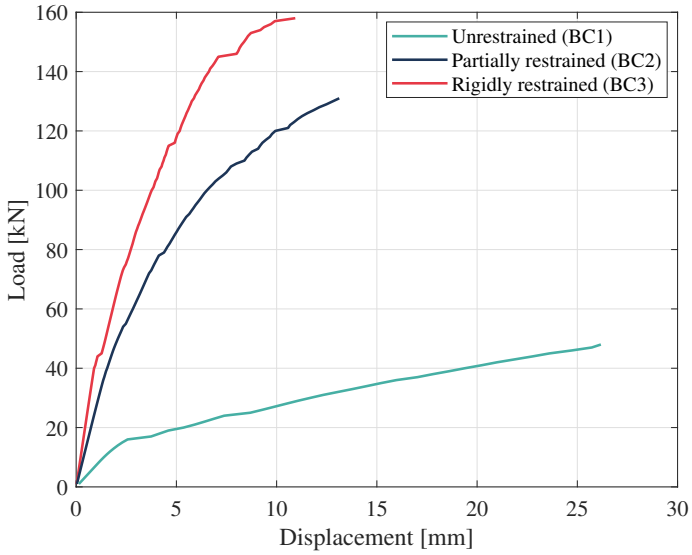

Figure 3.66: Midpoint vertical displacement at the top surface under increasing load for LC2, obtained from non-linear simulations with the three longitudinal restraint configurations defined in Table 3.25. The load value corresponds to the total externally applied load.

The results indicate that the load-bearing capacity of the element under rigidly restrained support conditions (BC3) is approximately three times greater than in the unrestrained case (BC1). This outcome aligns with expectations, as rigid longitudinal restraint facilitates the development of compressive membrane action, enhancing structural efficiency. In contrast, the unrestrained configuration is not compatible with membrane shell theory, leading to increased bending stresses to satisfy equilibrium. As expected, the partially restrained configuration (BC2) exhibits deformation characteristics and ultimate load capacity intermediate between those of the unrestrained (BC1) and rigidly restrained (BC3) cases. Studying the fully restrained case, cracks are initiated at a load of around 45 kN, compared to 18 kN for the unrestrained case.

Figure 3.67 illustrates the crack strain and principal stress distributions on the top and

bottom surfaces of the element at 95% of the ultimate load for each of the three boundary condition configurations.

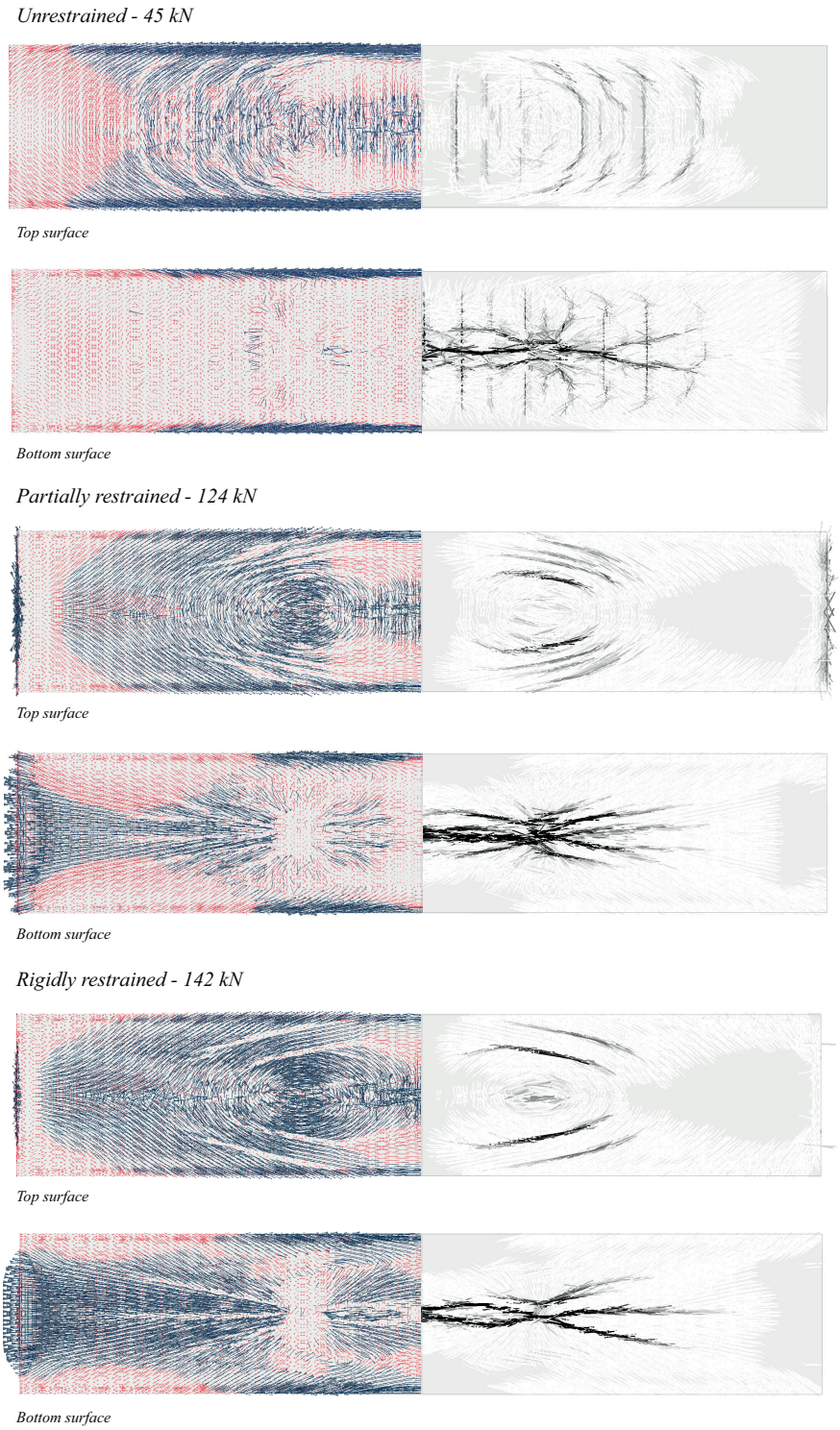

Figure 3.67: Principal stress distributions (left) and crack strain patterns (right) on the top and bottom surfaces at 95% of the ultimate load in LC2, for the three boundary condition configurations defined in Table 3.25. Configurations BC1, BC2, and BC3 are shown from top to bottom. In the principal stress plots, red indicates tension and blue indicates compression. In the crack plots, black represents regions with higher crack strain, while white indicates no cracking.

The unrestrained configuration (BC1) exhibits a series of evenly spaced cracks ($s_r \approx 150$ mm) aligned with the transverse reinforcement. In the central region of the surface, the cracks are primarily oriented transversely, suggesting that the element undergoes global bending about its y-axis. The presence of transverse reinforcement locally weakens the section, promoting crack initiation at these locations. Near the concentrated load points, the cracks rotate and spread toward the free edges, indicating localised bending response about the x-axis. This combination of global and local bending is further supported by the distribution of principal stresses: the bottom layer of the element is in tension in the central region (being below the neutral axis) and in compression along the free edges (above the neutral axis).

The rigidly restrained configuration (BC3) shows a crack pattern on the top surface characterised by radial cracks extending from the two concentrated loads. These cracks are aligned along the main longitudinal reinforcement, following the straight-line generator directions. Again, the presence of reinforcement likely weakens the cross-section, serving as a location for onset of cracking. On the bottom surface, cracking is more localised and concentrated at the centre of the element, aligned with the primary span direction.

The crack pattern, together with the distribution of principal stresses, suggests that the concentrated loads are carried in tension toward the free edges and in compression toward the supported ends. This behaviour reflects the cable and arch action mechanisms predicted by membrane shell theory for HP shells, and is similar to the one observed for LC1. At the free edges, the tension is redirected as compression in the generator directions toward the abutments, creating a state of local edge compression necessary for equilibrium. Notably, the principal stress vectors in the top and bottom layers appear orthogonal, indicating a through-thickness rotation of the principal stress directions.

The crack pattern and principal stresses of the partially restrained configuration (BC2) should be interpreted with caution. Yielding occurred in the transverse reinforcement bars, which were modelled as fully embedded. As such, the absence of bond-slip behaviour limits the accuracy of strain predictions.

Influence of reinforcement

To evaluate the influence of reinforcement on the overall load-bearing capacity, additional non-linear simulations were performed for LC2 (see definition in Figure 3.41) using BC3. Three different reinforcement configurations were analysed:

- No reinforcement.
- Reinforcement only along the straight-line generator directions (main reinforcement).
- Base case reinforcement configuration, matching the intended reinforcement layout in the physical specimen.

A load–displacement curve is shown in Figure 3.68, plotting the midpoint vertical displacement of the top surface for the three reinforcement configurations. All reinforcement was modelled as fully bonded.

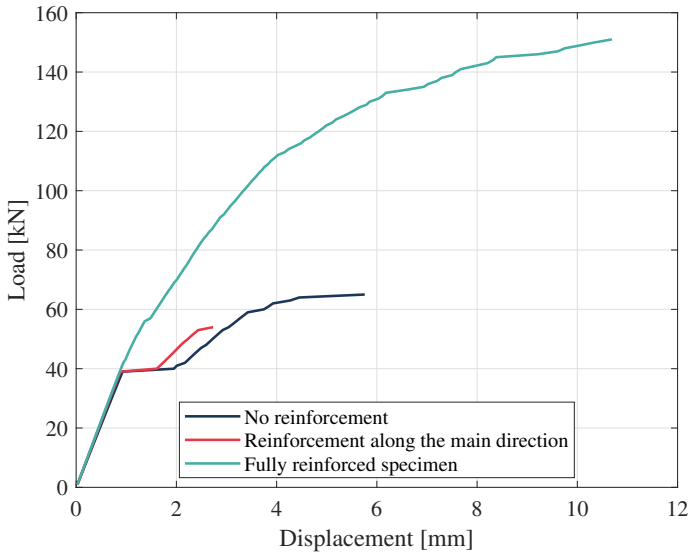

Figure 3.68: Load–displacement response at the midpoint of the top surface for LC2 and BC3, comparing three reinforcement configurations: no reinforcement, reinforcement along generator directions only, and the base case configuration. The load value corresponds to the total externally applied load.

As shown in Figure 3.68, the configuration without reinforcement exhibited a higher load-bearing capacity than the case with reinforcement only in the generator directions. This result is plausible; cracks were observed to form along the generator reinforcement bars (cf. Figure 3.67), suggesting that reinforcement in these zones may locally weaken the concrete continuum. In contrast, the base case configuration, which includes transverse reinforcement, achieved approximately twice the ultimate load capacity. This improvement is attributed to the ability of the transverse reinforcement to carry tensile forces toward the edges and yield under loading, thereby enhancing ductility and crack-bridging capacity. While all configurations showed similar initial stiffness up to the onset of crack formation (around 40 kN), the full reinforcement case maintained a more stable and ductile response post-cracking. The other two configurations softened markedly after cracking, regained some stiffness with further deformation, but ultimately failed at lower loads.

A sensitivity study was also conducted to assess how different modelling approaches for the concrete–reinforcement interface affect the ultimate load-carrying capacity under LC2. Three configurations were considered: (i) all reinforcement fully embedded, (ii) bond-slip behaviour assigned to the transverse reinforcement while all other bars were embedded, and (iii) bond-slip assigned to the main reinforcement, with all others embedded. Figure 3.69 presents the vertical displacement at the midpoint of the top surface for both the unrestrained (BC1) and rigidly restrained (BC3) boundary conditions.

As illustrated, the approach to modelling the interaction between concrete and reinforcement had limited influence on the global deformation characteristics and ultimate load-bearing capacity. However, the development of crack patterns and strain fields proved significantly more sensitive to how and where bond-slip behaviour was assigned. As discussed previously, bond-slip models should ideally be applied to all reinforcement bars expected to experience significant tensile straining and yielding. In the fully unre-

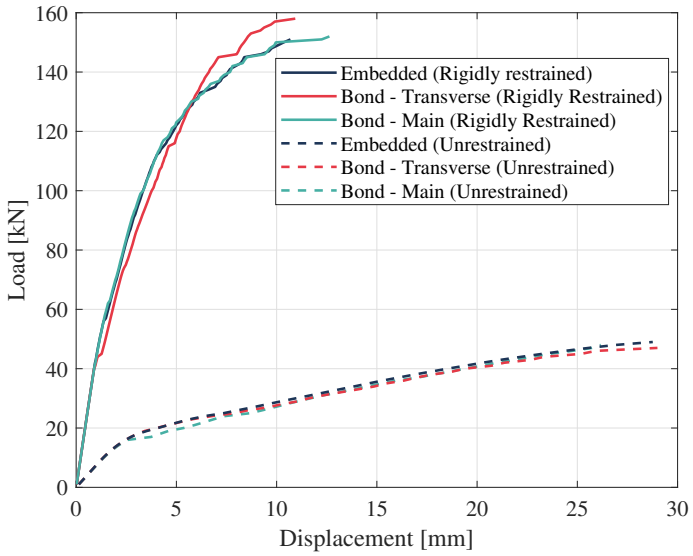

Figure 3.69: Load–displacement response at the midpoint of the top surface for LC2 with boundary conditions BC1 (dashed) and BC3 (solid), using three different reinforcement modelling approaches: fully embedded reinforcement (blue), bond–slip interaction in the main reinforcement only (green), and bond–slip interaction in the transverse reinforcement only (red).

strained configuration, yielding primarily occurred in the main reinforcement, whereas in the partially and rigidly restrained cases, yielding was concentrated in the transverse reinforcement.

3.4.4 Summary of results

This section provides a comparative summary of the findings from the analytical (Section 3.4.1), experimental (Section 3.4.2), and numerical (Section 3.4.3) static analyses. The discussion is structured around two load cases: the uniformly distributed load (LC1) and the four-point bending load (LC2) (see load case definitions in Figure 3.41).

Note that the experimental results are preliminary and should be interpreted with caution.

Uniformly distributed load (LC1):

LC1 comprised a uniformly distributed surface load of $p_z = 0.869$ kN/m^2 applied to the top face of the structural element. This case was assessed through experimental testing, analytical methods, and numerical simulations. The main observations are summarised below:

- Experimental strain measurements obtained using distributed fibre optic sensing (DFOS) indicated low strain magnitudes, typically averaging around 10 $\mu\epsilon$.
- The DFOS data suggested limited load transfer in the transverse direction. However, higher strains were recorded in the main reinforcement (oriented along the straight-line generators) and the longitudinal edge reinforcement. The main reinforcement primarily experienced tension, while the edge reinforcement was subjected to compression.

- A comparison between DFOS-measured strains and FEA results (see Figure 3.70) revealed good agreement when the element was modelled as longitudinally unrestrained. In this case, while the numerical strain magnitudes were generally higher than the experimental values, the distribution and pattern of the strains—particularly along the Diagonal E–W, Diagonal W–E, and Perimeter fibre paths—closely matched those recorded by DFOS. Conversely, the model with rigid longitudinal restraint exhibited poor agreement with the experimental strain data.
- Parametric numerical studies incorporating varying degrees of longitudinal restraint showed that the normal stress component S_{xx} (both tensile and compressive) progressively decreased as the longitudinal support stiffness increased (see Figure 3.71). Notably, tensile stresses reduced by a factor of approximately 20 when transitioning from a fully unrestrained to a rigidly restrained longitudinal boundary condition.
- The membrane shell theory developed by Pucher (1934) yielded an admissible stress solution in which the element was entirely under compression in the x-direction. The normal stress σ_{xx} increased toward both the centre of the cross-section and toward the supported edges, reaching a maximum of approximately 145 kN/m^2 (see Figure 3.45).
- The Euler-Bernoulli beam theory for cylindrical shells, as formulated by Lundgren (1949), predicted non-zero normal stress σ_{xx} along with shear stresses τ_{xy} and τ_{xz} (see Figures 3.47 and 3.48). The resulting stress distribution featured compressive σ_{xx} near the upper edges of the cross-section (up to 80 kN/m^2) and tensile stresses in the central region (up to 49 kN/m^2).
- A comparison between the analytical Euler-Bernoulli solution and numerical models (see Figure 3.71) revealed notable differences in the predicted stress fields for σ_{xx}. In the fully restrained numerical model, the analytical solution yielded tensile stresses approximately 2.7 times greater and compressive stresses around 4.7 times greater. When compared to the fully unrestrained numerical case (see Figure 3.71), the analytical model produced about 1.3 times higher compressive stresses, while the numerical model predicted tensile stresses roughly 7.7 times greater. Despite discrepancies in magnitude, the stress distribution patterns of σ_{xx} showed better qualitative agreement with the unrestrained numerical model than with the fully restrained case. For the shear stress components τ_{xy} and τ_{xz}, the overall stress fields from the analytical and fully restrained numerical models appeared similar in distribution, though differences in magnitude remained.

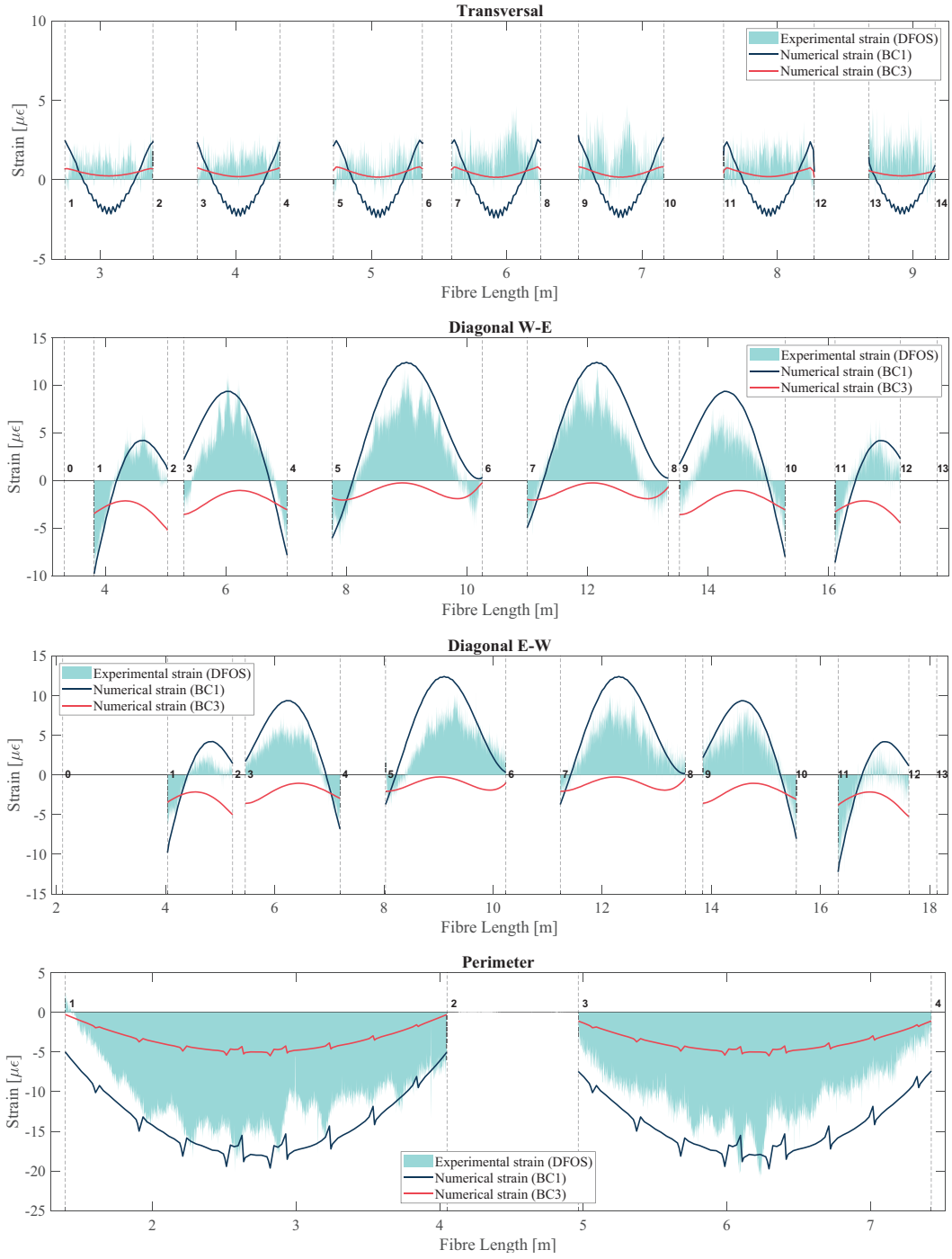

Figure 3.70: Comparison of DFOS-measured strains and numerically simulated strains for LC1. The numerical model is analysed under two boundary conditions: fully unrestrained (BC1) and rigidly restrained (BC3) in the longitudinal direction. Numerical strains are extracted by projecting the strain tensors onto the tangent vectors of the corresponding DFOS fibre paths. Vertical dashed lines indicate known positions along each cable; see Figure 3.52 for a reference map of these locations within the element.

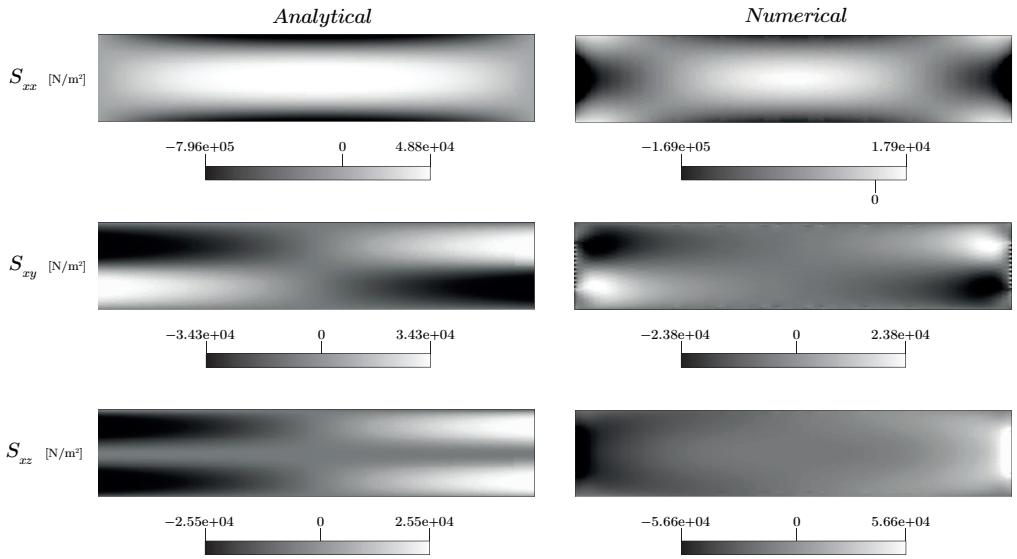

Figure 3.71: Comparison of normal stresses S_{xx} and shear stresses S_{xy} and S_{xz} from analytical and numerical simulations of LC1. The analytical results are based on the Euler-Bernoulli beam theory for cylindrical shells developed by Lundgren (1949), while the numerical results are obtained from simulations using boundary condition BC3.

Concentrated loads (LC2)

LC2 involved the application of two concentrated loads spaced 900 mm apart, loading the element to failure. This load case was investigated through experimental testing and non-linear numerical simulations. The key findings are summarised below:

- The prototype element failed at a total applied load of 84 kN. Numerical simulations predicted failure at 158 kN under rigid longitudinal restraints and at approximately 48 kN when fully unrestrained. A comparison is shown in Figure 3.72.
- Longitudinal cracking developed along the upper edge region—an area exhibiting signs of poor concrete compaction—ultimately culminating in brittle compressive failure.
- The failure mechanism comprised a combination of compressive crushing along the free edges and pronounced bending and shearing under one of the hydraulic pistons, leading to a shear-punching failure.
- Distributed fibre optic sensing (DFOS) cables installed along the transverse and primary longitudinal reinforcement recorded significant tensile strains, exceeding the yield strength of the reinforcement steel (see Figure 3.59). The DFOS cable placed along the edge reinforcement exhibited pronounced peaks in compressive strain at locations coinciding with observed failure zones.
- A comparison between DFOS-measured strains and numerical results revealed generally good agreement in overall strain distribution when using a fully unrestrained boundary condition (BC1) in the simulation (cf. Figure 3.73). However, the numerical model consistently underestimated strain magnitudes, particularly at peak locations along the edge reinforcement where localised failure occurred. These strain concentrations were not captured in the FEA, suggesting it did not

fully capture the non-linear behaviour of the free edges.

- DIC results indicated that the central portion of the element experienced cracking in the transverse direction. Five distinct cracks were observed, each aligned with a transverse reinforcement bar located directly beneath (see Figure 3.58). A similar crack pattern was also reproduced in numerical simulations of the unrestrained case (see Figure 3.67).
- Numerical sensitivity studies highlighted several key factors influencing the structural response. The degree of longitudinal restraint had a significant impact on ultimate load capacity, with fully restrained models exhibiting more than three times the capacity of fully unrestrained ones. Additionally, transverse reinforcement was found to be critical, enhancing ductility and increasing ultimate capacity by approximately a factor of three for LC2. The modelling approach for the reinforcement-concrete interface (embedded vs. bond-slip) showed limited influence on overall load capacity and global deformation, but had a more pronounced effect on local strain and stress distributions, as well as on crack pattern development.

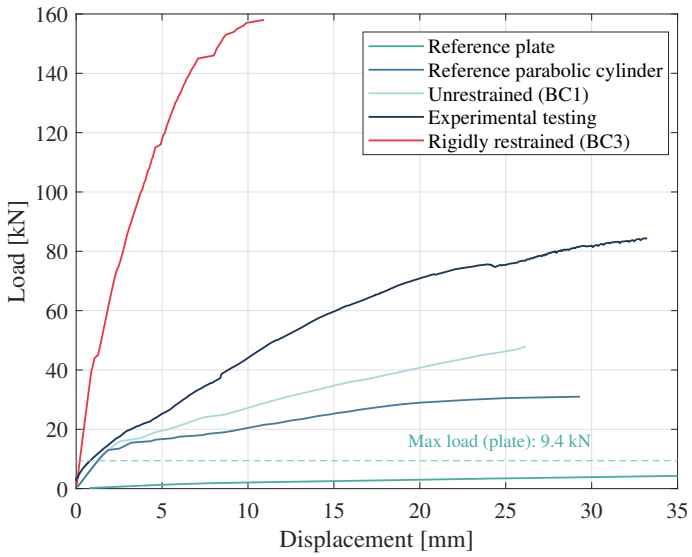

Figure 3.72: Load–displacement response at the midpoint of the top surface for LC2, comparing numerical simulations and experimental testing. For reference, responses of a plate and a parabolic cylinder—both matching the prototype element's thickness, length, and width—are included. The parabolic cylinder has a secondary moment of area equal to that of the prototype element's cross-section

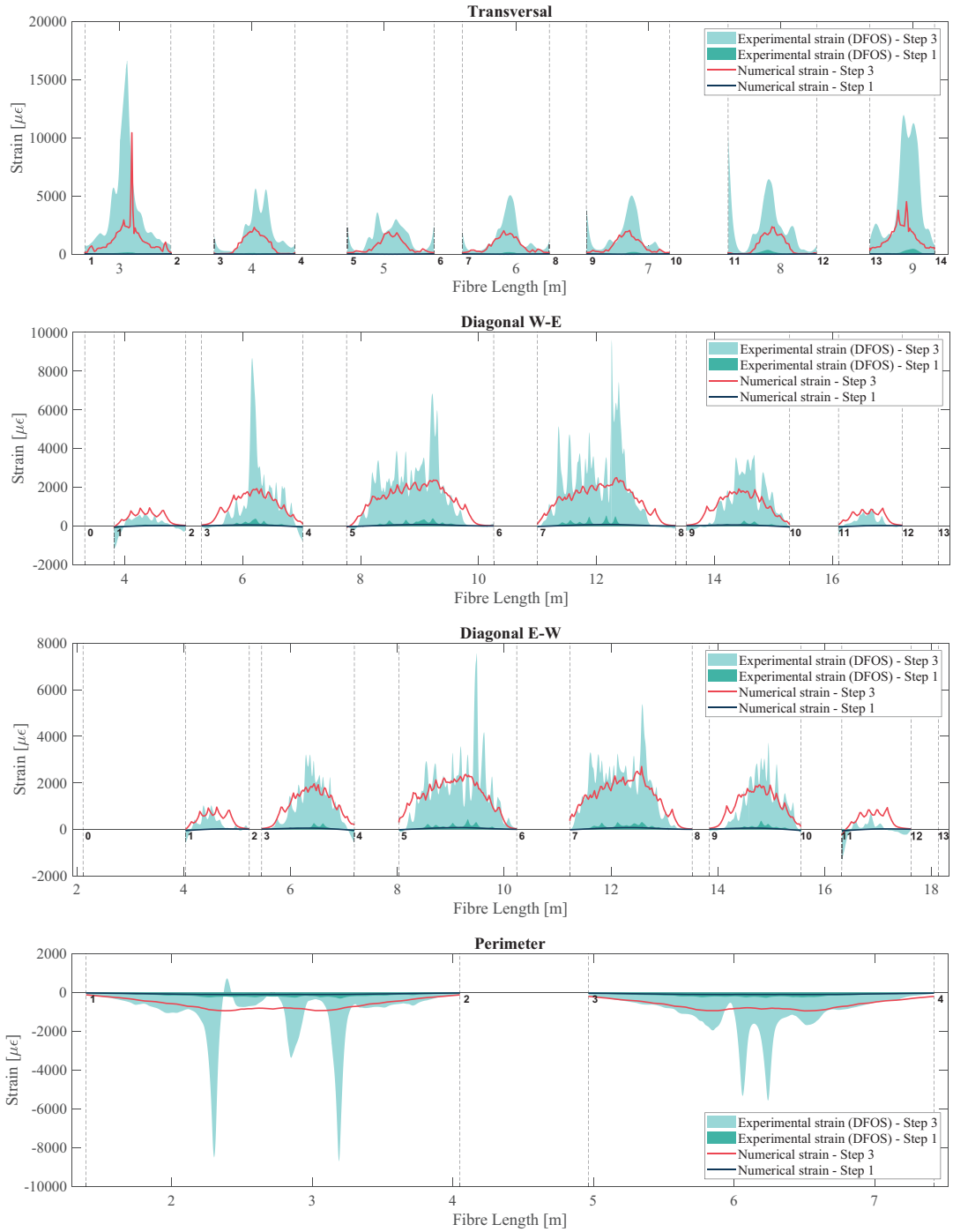

Figure 3.73: Comparison of DFOS-measured strains and numerically simulated strains for LC2 at two load steps (see definition in Section 3.4.2.4). The numerical model is fully unrestrained in the longitudinal direction (BC1). Numerical strains are extracted by projecting the strain tensors onto the tangent vectors of the corresponding DFOS fibre paths. Vertical dashed lines indicate known positions along each cable; see Figure 3.52 for a reference map of these locations within the element.

3.4.5 Discussion

As with the modal analysis, many of the key findings from the analytical, experimental, and numerical static assessments have already been discussed in their respective sections (Sections 3.4.1 to 3.4.3). The purpose of this concluding discussion is to compare the results across the different methods, highlight potential limitations, and suggest strategies for improving both future simulations and experimental setups.

The experimentally obtained results should be regarded as preliminary. Further work is required to process, assess, and interpret the data to draw robust and well-founded conclusions. One particularly valuable avenue for future analysis is the comparison between strains obtained from digital image correlation (DIC) and those recorded by the distributed fibre optic sensors (DFOS). Such a comparison would serve two purposes: to evaluate the consistency and reliability of the respective measurement systems; and to investigate how strain varies through the thickness of the element at locations where spatial overlap between DIC and DFOS data exists.

At present, the strain measurements from DFOS are interpreted under plane strain assumption, implying uniform strain along the thickness. However, this assumption is unlikely to hold in regions of high curvature or in cracked sections, where strain gradients are expected. By examining regions where multiple DFOS cables are embedded at different heights and spatially coincide, it may be possible to quantify through-thickness strain variation and evaluate the validity of the plane strain assumption. This would not only enhance the interpretation of current results but perhaps also inform improved sensor placement strategies in future tests.

A prerequisite for any meaningful comparison between DFOS and DIC data, particularly for assessing through-thickness strain variation, is precise knowledge of the DFOS cable positions within the concrete cross-section. Unfortunately, this information is not available for the current specimen. The cables were installed along the reinforcement, whose layout was assumed to match the design drawings. However, it is known that the actual placement of reinforcement deviated from its intended position, introducing uncertainty regarding the exact location of the DFOS cables.

This lack of positional accuracy presents a significant limitation. Ideally, the sensor positions should have been documented during fabrication through laser scanning or photogrammetry. Without this information, it becomes challenging to reliably relate measured strains to specific positions within the element and to compare them directly with numerically calculated strains.

For future studies, careful documentation of DFOS placement is essential to enable such advanced analyses. As for the existing dataset, it is important to estimate the potential margin of error in cable positioning. This would allow for a more informed interpretation of the strain measurements and facilitate a more meaningful comparison with numerical results.

The numerical analysis revealed a high sensitivity to the modelling of boundary conditions, particularly the degree of longitudinal restraint at the supports. This aspect may not have been accurately represented in the current simulations and warrants further investigation. The results indicated that variations in support stiffness significantly influenced key aspects of the static response, including ultimate load capacity, stress

distribution, deformation patterns, and crack development.

In the present model, longitudinal restraint was applied through 32 discrete springs on each side of the element, positioned at the top and bottom of the abutment. No intermediate springs were included, meaning that stresses could only be transferred along these two edges. This simplification likely introduced unrealistic stress concentrations and did not accurately reflect the actual load transfer mechanisms in the physical test setup, where interaction likely occurred along the full interface.

Although this approach was initially assumed to have limited effect on the global response, future studies may consider incorporating intermediate springs or using contact/interface elements to more realistically simulate the restraint provided by the test rig. An attempt was made to simulate the contact behaviour directly, but this led to convergence issues and significantly increased computational demands.

Moreover, the lack of experimental strain measurements at the supports limits the ability to calibrate restraint stiffness in the numerical model. Future experiments should include instrumentation at the supports to quantify the actual level of longitudinal restraint, which would allow for more accurate model calibration and improved understanding of the element's true boundary conditions.

Future static simulations could benefit from the use of geometric symmetry to reduce computational complexity. In all cases analysed within this thesis, the geometry, boundary conditions, and loading were assumed to be symmetric. As such, modelling only half of the element, while applying appropriate symmetry boundary conditions, would have been a valid simplification. This approach could significantly reduce computational cost, enabling more refined or extended analyses, such as additional load steps, finer mesh resolution, or more advanced boundary condition modelling.

In addition, accurately capturing the interaction between concrete and steel reinforcement remains a key challenge in non-linear modelling. Ideally, bond-slip models should be applied to all reinforcement elements experiencing significant tensile strains, to account for the relative displacement between steel and concrete. Attempting this resulted in severe convergence issues, and it was only possible to assign bond-slip models to a limited subset of the reinforcement bars.

To address this limitation, future work should include targeted sensitivity studies on both bond-slip formulations and concrete crack models. Such studies would provide deeper insight into how strain localisations and crack patterns evolve in response to varying interface behaviour and material assumptions. They would also help identify which regions of the structure are most affected by bond-slip interactions, and under what conditions simplifications may or may not be justified. This would ultimately support the development of more robust and predictive numerical models of steel-reinforced HP elements.

The quality and type of finite elements used in the numerical analysis also warrant further attention. In this study, 6-noded triangular shell elements were employed, which at times appeared visually skewed. Such irregularities may result in ill-shaped elements with poor Jacobian conditioning, potentially compromising the accuracy and stability of the results. A more thorough mesh quality assessment would be valuable in evaluating the reliability of the simulations. In addition, it may be beneficial to explore alternative

element formulations, including higher-order elements or even transitioning to three-dimensional solid elements, particularly in regions of stress concentration.

As in the case of the modal analysis, the numerical models were constructed based on an idealised geometry and perfectly symmetric loading. In reality, the physical specimen exhibited concrete fracturing along the upper edges of the parabolic cross-section—most likely at locations affected by poor compaction during casting. These defects represent a significant deviation from the ideal model and are believed to have contributed to premature local failure. To more accurately capture such behaviour, future studies could incorporate local material imperfections or stochastic variability into the model. Sensitivity analyses exploring the influence of these local weaknesses on failure mode, load-bearing capacity, and crack development would provide more realistic and robust predictions of the static response.

4 Conclusion

This thesis set out to investigate the static and dynamic behaviour of oblong, beam-like hyperbolic paraboloid (HP) concrete elements through full-scale testing, while also evaluating the predictive capabilities of analytical and numerical models. Through a combination of experimental work and numerical simulations, the study has contributed new insights into the performance and modelling of HP elements.

Experimental modal analysis (EMA) and static load testing were performed on a full-scale HP prototype element, enabling a detailed characterisation of its vibrational and statical response.

The EMA employed a single-input multiple-output (SIMO) roving hammer configuration, from which key dynamic properties—including natural frequencies, mode shapes, and damping ratios—were extracted. The consistency of modal parameters across repeated measurements indicated predominantly linear and time-invariant behaviour, thereby supporting the validity of EMA for evaluating dynamic performance. Numerical sensitivity studies evaluated the effects of reinforcement, boundary conditions, and mesh density on the simulated dynamic response. Overall, numerical predictions showed strong agreement with experimental results, particularly after calibration of boundary conditions and material properties, affirming their applicability for simulating the dynamic performance of HP elements.

The static load tests provided a comprehensive evaluation of the element's performance under both service and ultimate loading conditions. Load Case 1 (LC1) demonstrated the system's behaviour under distributed, quasi-realistic service conditions using cement bags laid across the surface. Load Case 2 (LC2) enabled a controlled failure scenario through four-point bending with two concentrated loads applied via hydraulic cylinders. The integration of distributed fibre optic sensing (DFOS) and 3D digital image correlation (DIC) enabled high-resolution strain mapping and enhanced understanding of local and global response during loading.

Finite element simulations, successfully reproduced key aspects of the experimental behaviour, including crack development, deflection profiles, and ultimate load capacity. Sensitivity studies explored the influence of modelling approaches, reinforcement modelling, and boundary conditions on the structural response. Complementary analytical calculations further contextualised the stress distribution, indicating that shell- and beam-based idealisations can offer useful, though approximate, design estimates.

Preliminary findings suggest that failure occurred through a combination of transverse bending and punching shear, initiated by concrete degradation at the upper edges of the parabolic cross-section. This degradation was likely caused by inadequate compaction. The observed deflection mode and ultimate capacity lay between those predicted by two extreme numerical cases: one with full longitudinal restraint and one fully unrestrained.

Ultimately, this thesis has delivered a detailed experimental assessment of the structural response of a HP prototype element, contributing to a broader framework for evaluating similar structural systems. The insights gained provide a foundation for continued technical development and future research, supporting the more informed and effective application of HP structures in contemporary construction practice.

5 Outlook and future work

Several suggestions for future work have been outlined throughout this thesis, particularly in the dynamic and static assessment discussions (Sections 3.3.5 and 3.4.5). These suggestions focused on improving the dynamic and static assessments of the HP prototype element, including refinements to experimental setups and numerical modelling approaches. This final section expands these suggestions to outline broader research directions and development opportunities. Thereby, the focus shifts from the individual prototype element level to larger-scale considerations, such as assessing application-oriented performance, exploring statistical variability through repeated testing, and identifying steps toward real-world implementation of HP elements.

The thesis work was delimited to the assessment of a single prototype element, with dimensions chosen for easy handling and compatibility with available laboratory facilities. Future studies should include multiple elements to enable statistical studies, verify behaviour consistency, and increase confidence in observed trends.

Furthermore, it is essential to transition from prototype-scale investigations to studies involving application-scale elements. The prototype's 3-meter span does not reflect the longer spans envisioned in real-world use cases. Experimentally investigating elements with realistic sizes will offer deeper insights into how structural behaviour scales with size. Future studies should also assess the dynamics and statics of connected elements, placed side by side or structurally joined. Understanding the interaction between connected elements is crucial for applications in large-span floors or bridge decks.

Experimental investigations reflecting real-world installation boundary conditions and loading conditions are important. From a dynamic perspective, it is particularly relevant to examine the influence of external factors—such as infill materials, live loads, and pedestrian activity—on modal properties like natural frequencies and damping. Consideration of footfall-induced vibrations and acoustic responses is necessary for residential or public applications. Shaker tests can also be employed to simulate dynamic effects from trains or wind, enhancing the understanding of operational behaviour. Similarly, for static performance, experimentally evaluating structural behaviour under expected boundary conditions and service loads would provide more application-relevant insights.

A promising direction for future research is the experimental investigation of prestressed HP elements that omit conventional steel reinforcement. Numerical studies by Eddin et al. (2024) and Loutfi et al. (2024) have shown promising results for CFRP-reinforced prestressed HP elements in residential applications, but experimental validation is needed to characterise their structural stiffness, cracking response, and modal properties. These studies are essential to support the broader implementation of prestressed and CFRP-reinforced HP elements.

Several fabrication-related questions require further investigation. While full-scale production methods for HP elements were previously developed by, e.g., J. Wilhelm Silberkuhl and Herbert Müller (see Section 1.1), these historical approaches may benefit from re-examination. Integrating digital fabrication tools, automated reinforcement placement, and robotic casting could improve precision and scalability, at a reasonable

cost. Optimising formwork systems for adjustability in span, curvature, or width, to suit diverse design contexts, is a key focus area. The viability and cost-effectiveness of reusable or modular formwork also require further study. In addition, improvements in casting quality, vibration methods, and reinforcement placement may rely on automation. Optimising concrete mix design remains essential to balance structural performance with environmental considerations, particularly to reduce CO_2 emissions without compromising durability or workability.

References

Abrahamsson, T. (2019). *Structural dynamics and linear systems*. Chalmers University of Technology.

Adiels, E. (2024). *Differential geometry and structural action of vaults and shells* [Doctoral dissertation, Chalmers University of Technology].

Airy, G. B. (1863). On the strains in the interior of beams. *Philosophical Transactions of the Royal Society of London*, *153*, 49–80. https://doi.org/10.1098/rstl.1863.0003

Al-Emrani, M., Engström, B., Johansson, M., & Johansson, P. *Bärande konstruktioner del 1*. Göteborg, 2011.

Almegaard, H. Pucher, isler and form finding of shells [Nordic Society for Structures in Architecture Meeting ; Conference date: 24-06-2014 Through 24-06-2014]. English. In: Nordic Society for Structures in Architecture Meeting ; Conference date: 24-06-2014 Through 24-06-2014. 2014.

Arlinger, E. (2023). *Design and evaluation of doubly-curved shell-like concrete slab elements: Pre-stressed structurally optimized elements and their potential to reduce the climate impact* [Master's thesis, Chalmers University of Technology].

Bao, X., & Chen, L. (2012). Recent progress in distributed fiber optic sensors. *Sensors*, *12*(7), 8601–8639. https://doi.org/10.3390/s120708601

Beleș, A. A., & Soare, M. V. (1971). *Das elliptische und hyperbolische paraboloid im bauwesen*. VEB Verlag für Bauwesen.

Bostic, S. W. (1994). *Lanczos eigensolution method for high-performance computers* (tech. rep.). NASA Langley Research Center.

Brandt, A. (2011). *Noise and Vibration Analysis : Signal Analysis and Experimental Procedures*. John Wiley & Sons, Incorporated.

Broyles, J., Shepherd, M., & Brown, N. (2023). Evaluation of the dynamic response for scaled models of shaped concrete floor slabs. *Building Acoustics*, *30*. https://doi.org/10.1177/1351010X231157613

Cajori, F. (1893). *A history of mathematics*. Macmillan & Company. https://books.google.se/books?id=bfgRxVzjbMYC

Caughey, T. K., & O'Kelly, M. E. J. (1965). Classical normal modes in damped linear dynamic systems. *Journal of Applied Mechanics*, *32*(3), 583–588. https://doi.org/10.1115/1.3627384

CEB fib Model Code. (2010). *Model code 2010: First complete draft – volume 1*. International Federation for Structural Concrete (fib).

Chalmers University of Technology. (2025). Göteborg/chalmers johanneberg [Accessed: 2025-04-25]. https://www.temperatur.nu/chalmers

Cocco, L. P., Giannetti, I., & Russo, M. (2024). *The silberkuhl system (1958–1970): Exploring form, construction, and structural conception of hp-shell by parametric modeling*. Springer Nature Switzerland AG.

Collins, M., & Mitchell, D. (1987). *Prestressed concrete basics*. Canadian Prestressed Concrete Institute.

Cornelissen, H., Hordijk, D., & Reinhardt, H. (1986). Experimental determination of crack softening characteristics of normalweight and lightweight concrete. *HERON*, *31*(2). https://resolver.tudelft.nl/uuid:08c29b39-5c60-4ab6-b9d5-643d11007f7c

Craig, J., Roy R., & Kurdila, A. J. (2011). *Fundamentals of structural dynamics.* Wiley-Blackwell.

Dassault Systèmes. (2015). *Abaqus 2016 online documentation* [Generated: Sun July 5, 2015 at 1:06:48, Build ID: 2015_07_02-15.44.29 46006]. Dassault Systèmes.

DIANA FEA. (2025). *Diana documentation release 10.1* [Accessed: 2025-04-14]. DIANA FEA. https://manuals.dianafea.com/d1010/en/index.html

Do Carmo, M. P. (2016). *Differential geometry of curves and surfaces* (2nd). Dover Publications.

Dombrowski, M., Merz, P., Osman-Letelier, J. P., & Schlaich, M. (2021). Transverse structural behaviour of doubly curved beam-like shells. *Proceedings of the IASS Annual Symposium 2020/21 and the 7th International Conference on Spatial Structures: Inspiring the Next Generation*.

Domokos, G. (1989). The equilibrium equations of membrane shells expressed in general surface coordinates [Presented by Prof. Dr. J. Peredy]. *Department of Mechanics, Technical University, Budapest*.

Dongarra, J., & Sullivan, F. (2000). Guest Editors Introduction to the top 10 algorithms. *Computing in Science & Engineering*, *2*(01), 22–23. https://doi.org/10.1109/MCISE.2000.814652

Døssing, O. (1988). *Structural testing part i: Mechanical mobility measurements*. Brüel & Kjær.

Eddin, A. E., Merz, P., Dombrowski, M., Heidemann, L., Reinhold, S., Loutfi, J., & Zeitler, B. (2024). Building acoustic analysis of doubly curved beam-like shell floors made of cfrp prestressed concrete and its integration into an interdisciplinary optimisation tool. *Proceedings of the IASS 2024 Symposium: Redefining the Art of Structural Design*. https://app.iass2024.org/files/IASS_2024_Paper_339.pdf

Eriksen, M., & Kolstad, M. T. (2016, June). *Investigation of cracking behavior in reinforced concrete panels with bond-slip reinforcement* [Master's thesis]. Norwegian University of Science and Technology (NTNU) [Supervisor: Max Hendriks; Co-supervisor: Reignard Tan].

European Committee for Standardization. (2004). EN 1992-1-1:2004 - Eurocode 2: Design of concrete structures – Part 1-1: General rules and rules for buildings.

European Committee for Standardization. (2005). EN 1993-1-1:2005 – Eurocode 3: Design of steel structures – Part 1-1: General rules and rules for buildings.

Ewins, D. J. (2000). *Modal testing : Theory, practice and application*. Baldock : Research Studies Press, cop. 2000.

Farshad, M. (1992). *Design and analysis of shell structures* (Vol. 16). Springer. https://doi.org/10.1007/978-94-017-1227-9

Flügge, W. (1962). *Stresses in shells* (Illustrated). Springer Science & Business Media.

Foraboschi, P., Mercanzin, M., & Trabucco, D. (2014). Sustainable structural design of tall buildings based on embodied energy. *Energy and Buildings*, *68*, 254–269. https://doi.org/10.1016/j.enbuild.2013.09.003

Gidrão, G., Krahl, P., Bosse, R., Silvestro, L., Scoczynski Ribeiro, R., Terezinha dos Santos Lima, G., & Carrazedo, R. (2024). Internal damping ratio of normal- and high-strength concrete considering mechanical damage evolution. *Buildings*, *14*. https://doi.org/10.3390/buildings14082446

Government Offices of Sweden. (2024, September). Framtidsinvesteringar och tillväxtreformer för ett rikare och tryggare Sverige [Retrieved from Government Offices of Sweden]. Retrieved January 28, 2025, from https://www.regeringen.se/

pressmeddelanden/2024/09/framtidsinvesteringar-och-tillvaxtreformer-for-ett-rikare-och-tryggare-sverige/

Guillaume, P., Verboven, P., Vanlanduit, S., der Auweraer, H. V., & Peeters, B. (2003). A poly-reference implementation of the least-squares complex frequency-domain estimator. *Proceedings of IMAC-XXI: Conference & Exposition on Structural Dynamics*. https://www.researchgate.net/publication/265423092_A_poly-reference_implementation_of_the_least-squares_complex_frequency-domain_estimator

Hanjari, K. Z. (2006). *Evaluation of wst method as a fatigue test for plain and fiber-reinforced concrete: Experimental and numerical investigation* [Master's Thesis]. Department of Civil and Environmental Engineering, Division of Structural Engineering, Concrete Structures.

Hendriks, M. A. N., den Uijl, J. A., de Boer, A., Feenstra, P. H., Belletti, B., & Damoni, C. (2012). *Guidelines for nonlinear finite element analysis of concrete structures* (Technical Report No. RTD 1016-1:2016) (1st edition). Rijkswaterstaat Centre for Infrastructure. Delft, The Netherlands.

Hewlett-Packard Company. (1986). *The fundamentals of modal testing: Application note 243-3* (tech. rep. No. Application Note 243-3) (Author not specified). Hewlett-Packard Company. https://www.hpmemoryproject.org/an/pdf/an_243-3.pdf

Hewlett-Packard Company. (1989). *The fundamentals of signal analysis: Application note 243* (tech. rep.) (Author not specified). Hewlett-Packard Company. https://research.ebsco.com/linkprocessor/plink?id=b1523751-ea6e-3942-ba0c-b90de904570f

Hillerborg, A. (1985). The theoretical basis of a method to determine the fracture energy G_F of concrete. *Materials and Structures*, *18*(4), 291–296. https://doi.org/10.1007/BF02472919

Hodge, P. G. (1959). *Plastic analysis of structures*. McGraw-Hill.

Hordijk, D. A., Cornelissen, H. A. W., & Reinhardt, H. W. (1986). Experimental determination of crack softening characteristics of normalweight and lightweight concrete. *Heron*, *31*(2), 45–56.

Kärrholm, G., & Samuelsson, A. (1972). Analysis of a prestressed cable-roof anchored in a space-curved ring beam. *IABSE Congress Report*. http://doi.org/10.5169/seals-9586

Kreger, S., Rahim, A., Garg, N., Klute, S., Metrey, D., Beaty, N., Jeans, J., & Gamber, R. (2016). Optical frequency domain reflectometry: Principles and applications in fiber optic sensing, 98520T. https://doi.org/10.1117/12.2229057

Leissa, A. W. (1973). *The free vibration of rectangular plates* (tech. rep. No. NASA SP-160). NASA Scientific and Technical Information Office. https://ntrs.nasa.gov/citations/19730018197

Liu, W. B., Gheni, M., & Yu, L. (2011). Effect of mesh size of finite element analysis in modal analysis for periodic symmetric struts support. *Fracture and Strength of Solids VII*, *462*, 1008–1012. https://doi.org/10.4028/www.scientific.net/KEM.462-463.1008

Loutfi, J., Dombrowski, M., Merz, P., Eddin, A. E., & Schlaich, M. (2024). Interdisciplinary optimisation tool for doubly curved beam-like shell floors made of cfrp prestressed concrete. *Proceedings of the IASS 2024 Symposium: Redefining the Art of Structural Design*. https://app.iass2024.org/files/IASS_2024_Paper_405.pdf

Lu, X., Sun, Q., Feng, W., & Tian, J. (2013). Evaluation of dynamic modulus of elasticity of concrete using impact-echo method. *Construction and Building Materials*, *47*, 231–239. https://doi.org/https://doi.org/10.1016/j.conbuildmat.2013.04.043

Lundgren, H. (1949). *Cylindrical shells: Cylindrical roofs* (Vol. 1). Danish Technical Press, Institution of Danish Civil Engineers.

McCormick, N., & Lord, J. (2010). Digital image correlation. *Materials Today*, *13*(12), 52–54. https://doi.org/https://doi.org/10.1016/S1369-7021(10)70235-2

Mindlin, R. D. (1951). Influence of rotatory inertia and shear on flexural motions of isotropic, elastic plates. *Journal of Applied Mechanics*, *18*, 31–38.

Ministry of the Environment and Government Offices of Sweden. (2020). Sweden's long-term strategy for reducing greenhouse gas emissions [Retrieved from Government Offices of Sweden on 2025-01-28]. https://unfccc.int/sites/default/files/resource/LTS1_Sweden.pdf

Neville, A. M. (2011). *Properties of concrete* (5th). Pearson Education Limited.

Nordic Innovation Centre. (2005). NT BUILD 511: Wedge Splitting Test Method (WST) – Fracture Testing of Fibre-Reinforced Concrete (Mode I) [Project 04032 (1672-04)].

Örebroporten. (2025). Svalan [Accessed: April 7, 2025]. https://www.orebroporten.se/fastighet/svalan/

Osman-Letelier, J. P., Goldack, A., Schlaich, M., Lordick, D., & Grave, J. (2017). Shape optimization of concrete shells with ruled surface geometry using line geometry. *International Association for Shell and Spatial Structures (IASS)*.

Ottosen, N., & Petersson, H. (1992). *Introduction to the finite element method*. Pearson Education (US).

Plos, M. (2000). *Finite element analyses of reinforced concrete strucutres*. Chalmers University of Technology.

Plos, M., Johansson, M., Zandi, K., & Jiangpeng, S. (2021). *Recommendations for assessment of reinforced concrete slabs: Enhanced structural analysis with the finite element method* (tech. rep.). Chalmers University of Technology, Department of Architecture and Civil Engineering, Division of Structural Engineering, Concrete Structures. Göteborg, Sweden.

Prassianakis, I., & Prassianakis, N. (2004). Ultrasonic testing of non-metallic materials: Concrete and marble. *Theoretical and Applied Fracture Mechanics*, *42*(2), 191–198. https://doi.org/https://doi.org/10.1016/j.tafmec.2004.08.007

Pucher, A. (1934). Über den spannungszustand in gekrümmten flächen. *Beton und Eisen*, *33*(19), 298–304.

Ramaswamy, G. S. (1984). *Design and construction of concrete shell roofs* (Revised). R.E. Krieger.

Ramaswamy, S. (1980). *Towards optimal solution techniques for large eigenproblems in structural mechanics* [Doctoral dissertation, Massachusetts Instutute of Technology].

Ramsden, K. (2020, November). Cement and concrete: The environmental impact [Retrieved from Princeton University]. Retrieved January 28, 2025, from https://psci.princeton.edu/tips/2020/11/3/cement-and-concrete-the-environmental-impact

Rayleigh, J. W. S. (1877). *The theory of sound* (Vol. 1). Macmillan.

Reissner, E. (1945). The effect of transverse shear deformation on the bending of elastic plates. *Journal of Applied Mechanics*, *12*, A68–A77.

Rogers, C. W. (2023). Tacoma narrows bridge collapses [Accessed: 2025-04-06]. https://research.ebsco.com/linkprocessor/plink?id=b1523751-ea6e-3942-ba0c-b90de904570f

Scheffler, T. (2017, September). Development and application of precast hyperboloid shells in east and west germany from the 1950s to the 1980s. In A. Bögle & M. Grohmann (Eds.), *Proceedings of the iass annual symposium 2017: Interfaces: Architecture, engineering, science*.

Schwartz, B. J., & Richardson, M. H. (1999). Experimental modal analysis. *CSI Reliability Week, Orlando, FL*.

Schwenk Sverige AB. (2024, January). Environmental Product Declaration: CEM II/B-M (S-LL) 52.5 N (Viridiscement) [Declaration number: NEPD-5724-5012-EN, issued by The Norwegian EPD Foundation]. Retrieved May 21, 2025, from https://schwenk.se/cements/viridiscement-cem-ii-b-m-s-ll-525-n/

Sehlström, A. (2021). *Prestress and its application to shell, fabric, and cable net structures* [Doctoral dissertation, Chalmers University of Technology]. Department of Architecture; Civil Engineering, Chalmers University of Technology.

Sehlström, A., Olsson, K., & Williams, C. (2022). Should torroja's prestressed concrete alloz aqueduct be thought of as a beam or a shell? *Engineering Structures*, *264*. https://doi.org/10.1016/j.engstruct.2022.114425

Shah, S. P., & Carpinteri, A. (1991). *Fracture mechanics test methods for concrete: Report of technical committee 89-fmt fracture mechanics of concrete: Test methods*. Chapman; Hall.

SMHI. (2024, July 31). *Juli 2024 – övervägande regnigt men längst i norr torrt och varmt*. SMHI. Retrieved April 24, 2025, from https://www.smhi.se/klimat/klimatet-da-och-nu/manadens-vader-och-vatten-i-sverige/manadens-vader-och-vatten-i-sverige/2024-07-31-juli-2024---overvagande-regnigt-men-langst-i-norr-torrt-och-varmt

Svensk Betong. (2022). Vägledning Klimatförbättrad Betong – Utgåva 2.0 [Vägledning framtagen i samverkan med Fossilfritt Sverige och Betonginitiativet]. Retrieved May 21, 2025, from https://www.svenskbetong.se/

Swedish Institute for Standards. (2005). SS 137207:2005 – betongprovning – hårdnad betong – tryckhållfasthet – omräkningsfaktorer.

Swedish Institute for Standards. (2019). SS-EN 12390-3:2019 - provning av hårdnad betong - del 3: Tryckhållfasthet hos provkroppar.

Swedish National Board of Housing, Building and Planning. (2025, January). Behov av bostadsbyggande 2024–2033 [Retrieved from Boverket]. Retrieved January 28, 2025, from https://www.boverket.se/sv/samhallsplanering/bostadsmarknad/bostadsmarknaden/behov-av-bostadsbyggande/behov-2024/

Tepfers, R. (1973). *A theory of bond applied to overlapped tensile reinforcement splices for deformed bars* (Vol. 73:2). Division of Concrete Structures, Chalmers University of Technology.

The Swedish Environmental Protection Agency. (2024, December). Sveriges klimatmål och klimatpolitiska ramverk [Retrieved from Naturvårdsverket on 2025-01-28]. https://www.naturvardsverket.se/amnesomraden/klimatomstallningen/sveriges-klimatarbete/sveriges-klimatmal-och-klimatpolitiska-ramverk/

Thorenfeldt, E., Tomaszewicz, A., & Jensen, J. J. (1987). Mechanical properties of high strength concrete and application to design. *Proceedings of the Symposium: Utilization of High Strength Concrete*, 149–159.

Timoshenko, S., & Krieger, S. W. (1959). *Theory of plates and shells* (2nd). McGraw-Hill.

van, Mier, J. (1984). *Strain-softening of concrete under multiaxial loading conditions* [Doctoral dissertation, Built Environment]. Technische Hogeschool Eindhoven. https://doi.org/10.6100/IR145193

Wang, Z., Zhang, X., Dai, C., Wang, Y., Liu, Q., Jiao, M., Li, Q., Mi, L., & Mao, W. (2025). Application of digital image correlation technology in investigating mechanical-related issues of lithium batteries. *Journal of Power Sources*, *642*, 236965. https://doi.org/https://doi.org/10.1016/j.jpowsour.2025.236965

Wilkinson, J. H. (1988). *The algebraic eigenvalue problem*. Oxford University Press.

Williams, C. (2014). What is a shell? In S. Adriaenssens, P. Block, D. Veenendaal, & C. Williams (Eds.), *Shell structures for architecture: Form finding and optimization* (1st, pp. 21–31). Routledge. https://doi.org/10.4324/9781315849270

Zhao, K., Zhao, L., Hou, J., Zhang, X., Feng, Z., & Yang, S. (2021). Effect of vibratory mixing on the slump, compressive strength, and density of concrete with the different mix proportions. *Journal of Materials Research and Technology*, *15*, 4208–4219. https://doi.org/https://doi.org/10.1016/j.jmrt.2021.10.033

Zhu, B. (2009). On the dynamic modulus of elasticity of concrete in anti-earthquake design of concrete dams. *Water Res. Hydropower Eng.*, *40*(11), 19–22.

Image credits

Unless else specified, all pictures used in this thesis are either the author's own or are in the public domain.

Figure 1.1a
Unknown. (n.d.). *Magazzino Merci Rinascente* [Photograph]. Retrieved from L'industria italiana del Cemento 3 (March 1962) - Pietroboni, G. "Copertura con volte sottili prefabbricate" (pp. 147–155). Reproduced with permission.

Figure 1.1b
©Hansjürgen Mannweiler. (1968). *Delta-Kindergarten, Halle-Neustadt with HP Delta shells* [Photograph]. Reproduced with permission from Halle-Neustadt Bildarchiv. https://haneu-bildarchiv.de/

Figure 2.19
©Dombrowski et al. (2021). *Qualitative assessment of internal stress distribution in the transverse direction* [Illustration]. Reproduced with permission from Max Dombrowski.

Figure 2.23
Unknown. (1940). *Tacoma Narrows Bridge collapse* [Photograph]. Wikimedia Commons. Public domain. https://commons.wikimedia.org/wiki/File:Tacoma-narrows-bridge-collapse.jpg

List of software

All software used in this thesis is properly licensed for academic use.

ABAQUS/CAE

Dassault Systèmes Simulia Corp. (2024). *ABAQUS/CAE* (Version 2024) [Computer software]. https://www.3ds.com/products-services/simulia/products/abaqus/

DewesoftX

Dewesoft (2025). *DewesoftX* (Version 2024.5) [Computer software]. https://dewesoft.com/products/dewesoftx

DIANA

DIANA FEA bv. (2025). *DIANA* (Version 10.10) [Computer software]. https://dianafea.com/product/diana-fea/

RealityCapture

Epic Games, Inc. (2025). *RealityCapture* (Version 1.5.1.118081 RC) [Computer software]. https://www.capturingreality.com/realitycapture

Rhinoceros 3D

Robert McNeel & Associates. (2025). *Rhinoceros 3D* (Version 8.0) [Computer software]. https://www.rhino3d.com/

ODiSI 6000 Application Software

Luna Innovations Inc. (2025). *ODiSI 6000* (Version 2.4.2) [Computer software]. https://lunainc.com/odisi-software-download

ZEISS

Carl Zeiss Industrielle Messtechnik GmbH. (2025). *Correlate Pro* [Computer software]. https://www.zeiss.com/metrology/en/software/zeiss-correlate.html

Appendices

A Concrete properties

This appendix contains the concrete mix design (in Swedish) along with laboratory reports from the performed cube strength and wedge splitting tests.

Våxtorps Betong

Lassrapport

Följesedel **117943**
Fabrik **Våxtorp**
Blandare **BL1**

Ordernr	4295	**Lass**	0,7 m³	**Producerad**	**2024-06-25 12:00**
Lassnr	1	**Antal satser**	1	**Startad**	**11:56**

Grundrecept	**C253008 - C25/30-08**	**C 25/30 8mm 0,65**
Tilläggsrecept	ECO cem	ECO CEMII/B-M
	S3 - S3-SKY. 558	Flyttillsats SKY 558
	RET - RET 0,1%	Retarder 0,1%

Kund	**140107**	**NCC SVERIGE AB**
Arbetsplats	44	Ljungaskolan, Kungsvägen 22 286 34 Örkelljunga
Bil	22 / ENX397	

Silo	Material	Bör kg	Är kg	Diff %	Fukt bör %	Fukt är %	Abs %	Temp °C	kg/m³ Totalt	kg/m³ Effektivt vatten	kg/m³ Mängd yttorr
2	0-8LBC	345	365	5,9	4,5	4,5	0,2	14,0	525,2	21,6	503,6
3	0-8STA	478	485	1,4	4,4	(A) 4,3	0,2	14,0	697,8	27,4	670,4
6	4-8	530	510	−3,7	0,0	0,0	0,4	14,0	733,8	−2,9	736,7
2	VIRIDIS	210	209	−0,5				30,0	300,7	0,0	300,7
2	SKY 558	0,31	0,36	14,3				15,0	0,5	0,4	0,1
1	RET	0,21	0,34	61,9				15,0	0,5	0,4	0,0
1	KV	94,3	93,0	−1,4				8,0	133,8	133,8	0,0
	Spädvatten	11,0	3,0						4,3	4,3	
Totalt, kg		1 657	1 666	0,5					2 398	185	2 213
Totalt, liter		696	691	−0,8					995		
inkl. luft		700	695	−0,8							

	VCTekv	Konsistens	Blandningstid	Betongtemp
Bör	0,650	59	50	0
Är	0,615	45	56	18

	Bör	Är
Sättmått	90	
Lufthalt	0,5	
Temp	0	
Densitet	2398	
VCTekv	0,65	
Sign		

Kub nr.	Antal dygn	Densitet	Hållfasthet	Datum	Sign

DATE
2025-03-05

AUTHOR
David Selse; Erik Wigh

CUBE STRENGTH TEST REPORT

Overview

This document reports on the cube strength tests carried out for the thesis work *Dynamic and static response of beam-like hyperbolic paraboloid concrete elements* by David Selse and Erik Wigh. The tests were conducted on 4 March 2025 and carried out according to SS-EN 12390:2019.

Standard

SS-EN 12390-3:2019

Test specimens

Cube strength tests were carried out on three cubes, referred to as specimen *1*, *2* and *3*.

All cube specimens had side lengths *d = 150 mm*, within less than 2% tolerance. In accordance with SS-EN 12390-1, all tolerances regarding designated size, flatness, and perpendicularity were satisfied. The specimens were regarded as valid for testing. No cracks or damages were found on the specimens.

The method of curing deviate from the suggestion given in SS-EN 12390-2, which recommends curing in water at temperatures of (20 ± 2) °C, or in a chamber at (20 ± 2) °C and relative humidity ≥ 95%. The standard allows also other forms of curing. In this case, the cubes were cured together with the hyperbolic concrete shell in the outdoor environment.

The actual age of specimens at the time of test was 252 days. In accordance with conversion factors specified in SS 137207:2005 an effective hardening age j_{20} was determined as 165 days, based on daily average exterior temperatures recorded at Chalmers during the curing period.

Table 1 provides mass and density properties of the three test specimens.

Table 1 – Mass properties of the three test specimens

ID	*1*	*2*	*3*	***Mean***
d1 [mm]	147,245	150,1	150,7	**149,3483**
d2 [mm]	147,47	150,1	150	**149,19**
d3 [mm]	147,32	149,8	150,2	**149,1067**
Volume [m^3]	0,003199	0,003375	0,003395	**0,003323**
Cross-section Area [m^2]	0,021714	0,02253	0,022605	**0,022283**
Mass [kg]	7,8533	7,8088	7,8763	**7,846133**
Density [kg/m^3]	2454,97	2313,722	2319,785	**2362,826**

Date and location of testing

The testing was carried out on 2025-03-04 at the concrete laboratory of Chalmers University, campus Johanneberg.

Testing setup, and results

The testing machine satisfies the requirements given in SS-EN 12390-4 regarding flatness, size, roughness and stiffness of auxiliary platens. Spacing blocks were not used during the test.

Pressure was applied at a constant rate of 0,6 ± 0,2 MPa/s ($N/mm^2 \cdot s$) as prescribed in SS-EN 12390-3.

All specimens failed according to what is described as a satisfactory failure.

Table 2 presents maximum load at failure and the corresponding compressive strength of the three specimens.

Table 2 – Recorded compressive strength of the three test specimens

ID	*1*	*2*	*3*	***mean***
F_{max} [kN]	910	900	895	**901,6667**
f_{cm} [Mpa] (to nearest 0.1)	51,0	49,5	50,0	**50,2**

Declaration

I hereby confirm that the test was carried out in accordance with SS-EN 12390-3:2019

Name: Erik Wigh

Signature: 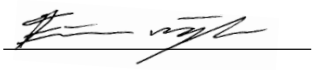

Göteborg, 2025-03-05

DATE
2025-03-05

AUTHOR
David Selse; Erik Wigh

WEDGE SPLITTING TEST (WST) - REPORT

Overview

This document reports on the wedge splitting tests carried out for the thesis work *Dynamic and static response of beam-like hyperbolic paraboloid concrete elements* by David Selse and Erik Wigh. The tests were carried out on 3 March 2025, according to *NORDTEST (NT) Method*[1].

General information

The tests were carried out in the *Structures Lab* at Sven Hulthins gata 8 at Chalmers University of Technology. A research engineer Sebastian Almfeldt provided supervision and assistance in all moments of the testing, including handling of specimens and test equipment. The purpose of the testing was to determine the fracture properties of the concrete material used in the casting of the HP element studied in the thesis. The fracture energy, i.e. the energy needed for crack propagation per area unit, was obtained by integrating the splitting force – CMOD curve, divided by the ligament area. The tensile strength was determined by solving the force moment equilibrium at the peak applied force.

Description of the material tested

Two 150x150x150 cube specimens were cast on the 25 of June and later cured in water at temperatures of (20 ± 2) °C. The age of the specimens at the time of test was 251 days.

Test method

The tests were performed in a test system provided by MTS Systems available at the *Structures Lab* at Chalmers University of Technology (cf. Figure 1). Tests were carried out on two cubes with dimensions 150x150x150 (within 1% error). It is recommended to cast the cubes with a groove at the top. However, since this had not been done, the grooves were sawn afterwards. The dimensions of the grooves intentionally deviated from the recommended dimensions of 30 mm width and 22 mm depth. The actual dimensions were 29 mm width and 25 mm depth. These dimensions followed the recommendation of the research engineer Almfeldt for better fitting of bearings and clip gauges. A starter notch was sawn across the centerline of the groove to a depth of approximately 74 mm from the bottom of the cube. Figure 2 shows a drawing of the specimens with their grooves and starter notches.

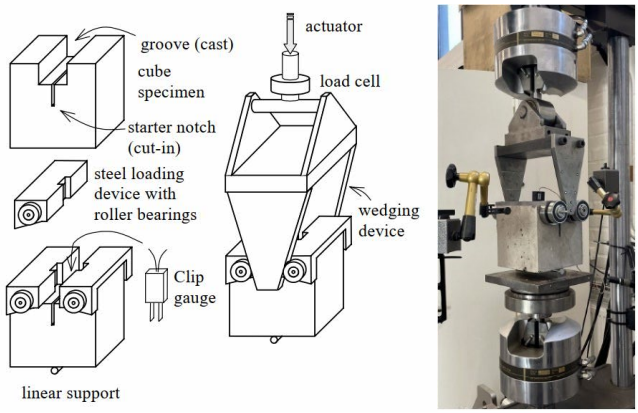

Figure 1 – Left: Schematic view of the equipment and test setup. Right: Principle of load application.

[1] Wedge Splitting Test Metod. NordTest Method NT Build 511. ISSN 1459-2762 (2005)

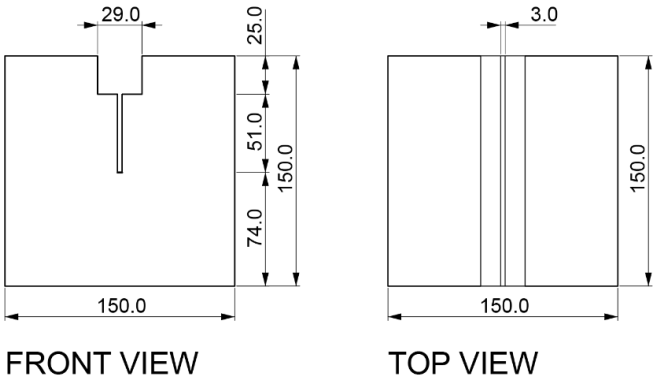

Figure 2 – Dimensions of specimens with grooves and staring notches.

The dimensions of the specimens were initially recorded. Each specimen was placed centrally on the support according to Figure 1. Two load devices with roller bearings were placed inside the groove, transferring the vertical load of the machine horizontally and effectively splitting the specimen apart. The crack mouth opening displacement (CMOD) was measured through a clip gauge placed in the groove, between the loading devices. The gauge expanded as the groove opened up.

The wedge was lowered onto the specimen and pre-loaded to a load of 80 N for both specimens. The load was then applied at a constant rate of approximately 0.25 mm/min throughout the full test duration. A load-CMOD curve was recorded by measuring the applied vertical load F_{v} and the CMOD. The vertical load was converted to a horizontal splitting force according to:

$$F_{\mathrm{sp}} = \frac{F_v}{2\tan(\alpha)}.$$

Where α, is the inclination of the wedge.

The work of fracture W_{F} was found by integration of the splitting force-CMOD curve. The fracture energy G_{F} was then calculated by dividing the work of fracture by the ligament area A_{lig}.

$$G_{\mathrm{F}} = \frac{W_{\mathrm{F}}}{A_{\mathrm{lig}}}.$$

Test results

The splitting load-CMOD curves are presented in Figure 3.

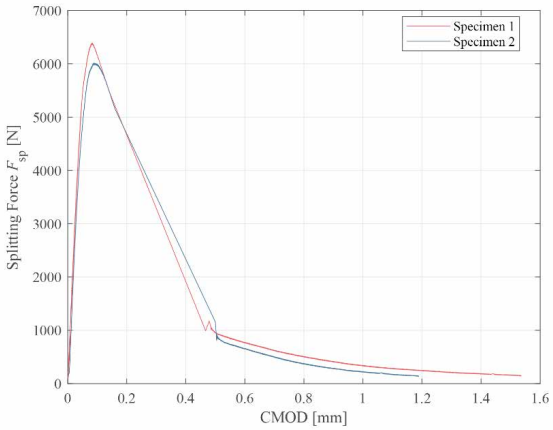

Figure 3 – Splitting force - CMOD curve for specimen 1 and 2.

Table 1 presents the energy dissipated during fracture for the two cubes, along with the recorded tensile strength.

Table 1 1 – Recorded fracture energy and tensile strength of the two test specimens

ID	*1*	*2*	***mean***
G_F [Nm/m²]	216.9	206.5	**211.7**
f_{ct} [MPa]	5.18	4.88	**5.03**

Declaration

I hereby confirm that the test was carried out in accordance with *NORDTEST (NT) Method.*

Name: Erik Wigh

Signature: 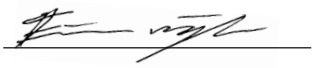

Göteborg, 2025-03-05

DEPARTMENT OF ARCHITECTURE AND
CIVIL ENGINEERING
CHALMERS UNIVERSITY OF TECHNOLOGY
Gothenburg, Sweden 2025
www.chalmers.se

CHALMERS
UNIVERSITY OF TECHNOLOGY